Measuring and modelling lung microstructure with hyperpolarised gas MRI

Ho-Fung Chan

Supervised by

Professor Jim Wild

Dr. Guilhem Collier

A thesis submitted in fulfilment of the requirements for
the degree of Doctor of Philosophy

POLARIS Group

Academic Unit of Radiology

Infection, Immunity, and Cardiovascular Disease

Faculty of Medicine, Dentistry & Health

The University of Sheffield

March 2018

Abstract

This thesis is concerned with the development of new techniques for measuring and modelling lung microstructure with hyperpolarised gas magnetic resonance imaging (MRI). This aim was pursued in the following five chapters:

1. Development of a framework for lobar comparison of lung microstructure measurements derived from computed tomography (CT) and ^{3}He diffusion-weighted MRI evaluated in an asthmatic cohort. Statistically significant linear correlations were obtained between ^{3}He diffusion-weighted MRI and CT lung microstructure metrics in all lobar regions.

2. Implementation of compressed sensing (CS) to facilitate the acquisition of 3D multiple b-value ^{3}He diffusion-weighted MRI in a single breath-hold for whole lung morphometry mapping. Good agreement between CS-derived and fully-sampled whole lung morphometry maps demonstrates that CS undersampled ^{3}He diffusion-weighted MRI is suitable for clinical lung imaging studies.

3. Acquisition of whole lung morphometry maps with ^{129}Xe diffusion-weighted MRI and CS. An empirically-optimised ^{129}Xe diffusion time ($\Delta=8.5$ ms) was derived and ^{129}Xe lung morphometry values demonstrated strong agreement with ^{3}He equivalent measurements. This indicates that ^{129}Xe diffusion-weighted MRI is a viable alternative to ^{3}He for whole lung morphometry mapping.

4. Implementation of an in vivo comparison of the stretched exponential and cylinder theoretical gas diffusion models with both ^{3}He and ^{129}Xe diffusion-weighted MRI. Stretched exponential model diffusive length scale was related to cylinder model mean chord length in a non-linear power relationship; while the cylinder model mean alveolar diameter demonstrated excellent agreement with diffusive length scale.

5. Investigation of clinical and physiological changes in lung microstructure with ^{3}He and ^{129}Xe diffusion-weighted MRI. Longitudinal studies with ^{3}He and ^{129}Xe diffusion-weighted MRI were used investigate changes in lung microstructure in cystic fibrosis and idiopathic pulmonary fibrosis. Lung inflation mechanisms at the acinar level were also investigated with ^{3}He and ^{129}Xe diffusion-weighted MRI acquired at two different lung volumes.

Acknowledgements

Firstly, I would like to thank my supervisor Jim Wild for the opportunity to undertake my PhD research with the POLARIS group in Sheffield. Jim's guidance and support has been invaluable during my PhD and has helped me develop into a successful researcher. I am also grateful for the many opportunities to attend conferences and present my work to the wider research community. I would like to express my gratitude to my second supervisor Guilhem Collier for all his help with my research experiments. It was a pleasure to learn from Guilhem and he was always willing to discuss any research problems and experimental results. I also want to thank Juan Parra-Robles for his help at the start of my PhD, and insightful discussion of diffusion modelling results.

Throughout my PhD, I have had the pleasure of working alongside many wonderful colleagues and friends in the POLARIS group. They have all made helpful contributions to my research, and in chronological order I would like to thank Neil Stewart, Paul Hughes, Laura Saunders, Madhwesha Rao, Graham Norquay, Felix Horn, Helen Marshall, Andy Swift, Laurie Smith, Bilal Tahir, Nick Weatherley, Adam Maunder, Chris Johns, Martin Brook, Alberto Biancardi, and Oliver Rodgers.

Within the wider Academic Radiology department, I would like to thank the team of radiographers, in particular Jody Bray and David Capener, for their assistance in MR scanning and hyperpolarised gas administration for the numerous patient studies. I am also very appreciative of the Academic Radiology administration team, in particular Leanne Armstrong and Jen Rodgers, for recruiting patients for scanning, and ensuring the department and POLARIS building runs smoothly everyday.

I want to thank my fellow POLARIS football team-mates, within and outside the group, and the board games group of friends who have helped me maintain a good work-life balance during my PhD. Special thanks to my flatmates, Wungtei and Neil, who I have thoroughly enjoyed sharing a flat with in Sheffield. I also want to thank my Kiwi mates in London, Christoph and Paul, for all the hiking trips and occasional Arsenal matches.

Finally, I am grateful for all the love and support from my parents, Simon and Alice, and my sister, Wing. Their constant encouragement from New Zealand has been instrumental in the completion of my PhD and this thesis.

Contents

List of Figures

List of Tables

Chapter 1

Introduction

The potential for imaging pulmonary ventilation with inhaled hyperpolarised gas magnetic resonance imaging (MRI) was first demonstrated in 1994 with the noble gas isotope xenon-129 (^{129}Xe) in excised mouse lungs [1]. Within a few years, the feasibility of in vivo human lung imaging with inhaled helium-3 (^{3}He) [2, 3] and ^{129}Xe [4] was demonstrated. Through advancements in optical polarisation and imaging techniques, hyperpolarised gas MRI has now become a robust imaging technique used for the functional assessment of various aspects of lung physiology in a range of pulmonary diseases. One of the most novel and proven aspects of hyperpolarised gas MRI is its sensitivity to changes in lung microstructure through the measurement of restricted Brownian gas diffusion. With the development of theoretical gas diffusion models [5, 6], in vivo measurements of alveolar length scales, that are analogous to direct histological morphometry measurements, can now be extracted from hyperpolarised gas diffusion-weighted MR imaging.

The principle goal of this thesis was to develop new techniques to measure and model lung microstructure with hyperpolarised gas MRI. Specific objectives were:

- The development of a 3D diffusion-weighted MRI sequence to acquire higher resolution diffusion data in a single breath-hold with hyperpolarised ^{3}He.

- Extend these image acquisition techniques to hyperpolarised ^{129}Xe gas.

- Further development of existing diffusion models to derive in vivo parameters of lung microstructure, and validation of these quantitative models with both hyperpolarised gases, and against each other.

This thesis is organised into seven separate chapters. **Chapter 2** provides a brief introduction into the basics of lung physiology with a focus on lung morphometry. A review of the different techniques used to image lung microstructure is also presented. **Chapter 3** covers

the theoretical background of MR physics, hyperpolarised gas MRI, and diffusion-weighted MRI. These two chapters provide the reader with an overview of the hyperpolarised gas MR imaging techniques used in the subsequent chapters of original research.

Chapter 4 is the first chapter of original research, and presents a framework for lobar comparison of lung microstructure measurements derived from computed tomography (CT) and ^{3}He diffusion-weighted MRI evaluated in an asthmatic cohort. A statistical comparison of the lung microstructure metrics between the two imaging modalities for all lobar regions is implemented.

In **Chapter 5** the implementation of the MR imaging acceleration technique of compressed sensing (CS) for 3D multiple b-value ^{3}He diffusion-weighted MRI is explored. The feasibility of CS with 3D ^{3}He diffusion-weighted MRI is first investigated through retrospective CS undersampling simulations. Prospective CS diffusion-weighted MRI datasets are then acquired, and CS-derived whole lung morphometry maps are validated against fully-sampled measurements to demonstrate the clinical potential of this technique. Finally, the possibility of a 3D multi-interleaved CS sequence for the simultaneous acquisition of multi-parametric maps of lung microstructure and function is explored.

Chapter 6 builds upon the 3D CS acquisition techniques introduced in Chapter 5 to acquire ^{129}Xe whole lung morphometry maps in a single breath-hold. A ^{129}Xe diffusion time is empirically-optimised and benchmarked against ^{3}He measurements. ^{129}Xe lung morphometry maps derived from two theoretical gas diffusion models are compared against ^{3}He equivalent measurements to assess the viability of this empirically-optimised diffusion time for ^{129}Xe whole lung morphometry with different diffusion models.

Chapter 7 presents an in vivo comparison of the stretched exponential and cylinder theoretical gas diffusion models in a range of patient groups with the newly developed 3D ^{3}He and ^{129}Xe diffusion-weighted MR imaging sequences. The estimates of alveolar dimensions from each diffusion model are compared to determine possible relationships between the lung morphometry parameters.

Chapter 8, the last chapter of original research, contains three different clinical and physiological investigations of lung microstructure with ^{3}He and ^{129}Xe diffusion-weighted MRI. Lung microstructural changes in early cystic fibrosis (CF) lung disease are investigated with ^{3}He diffusion-weighted MRI in a longitudinal study of children with mild CF. In a separate longitudinal study, a cohort of idiopathic pulmonary fibrosis (IPF) patients are imaged with ^{3}He and ^{129}Xe to investigate if lungs with IPF demonstrate changes in diffusion-weighted MRI metrics. Finally, ^{3}He and ^{129}Xe diffusion-weighted MRI acquired at two different lung volumes are used to investigate lung inflation mechanisms at the acinar level.

Chapter 2

Imaging lung microstructure

The purpose of this chapter is to review imaging techniques, across multiple modalities and length scales, which are used to measure lung microstructure. The imaging modalities of stereology through microscopy, bronchoscopy-based imaging, computed tomography (CT), and magnetic resonance imaging (MRI) will be covered and their different applications will be discussed.

2.1 Lung structure and function

The main function of the lungs is to provide efficient gas exchange between airspaces and the pulmonary vasculature. Gas exchange occurs in the alveoli, where oxygen (O_2) diffuses into capillaries and carbon dioxide (CO_2) is removed. The complex structure of the human lung is optimised for this function, with an effective gas exchange surface area of approximately 130 m^2 [7]. The right lung consists of three lobes (upper, middle, and lower) split by right oblique and horizontal fissures; while the left lung consists of only two lobes (upper and lower, split by the left oblique fissure), due to the cardiac notch area that accommodates the heart.

2.1.1 Static lung volumes and spirometry

The lung can be characterised by sub-divisions that correspond to four lung volumes and four lung capacities (Figure 2.1). Tidal volume (TV) is the volume of air between resting inspiratory and expiratory levels during normal breathing conditions. Inspiratory reserve volume (IRV) is the maximum volume that can be inspired from resting inspiratory level; while expiratory reserve volume (ERV) is the maximum volume that can be expired from resting expiratory level. The vital capacity (VC) is a combination of ERV+TV+IRV, and represents the total volume that can be inspired or expired. Inspiratory capacity (IC) is the

total volume that is inspired from resting expiratory level and is the sum of TV and IRV. All the aforementioned volumes or capacities can be measured with spirometry, the most commonly used pulmonary function test (PFT). Spirometry also includes the measurement of forced vital capacity (FVC) and forced expiratory volume after 1 second (FEV$_1$). Forced spirometry metrics are typically quoted as predicted values or 'z-scores', that are derived from empirical reference equations representing normative values from a representative sample of healthy subjects with similar characteristics (e.g. age, sex, height, and ethnicity).
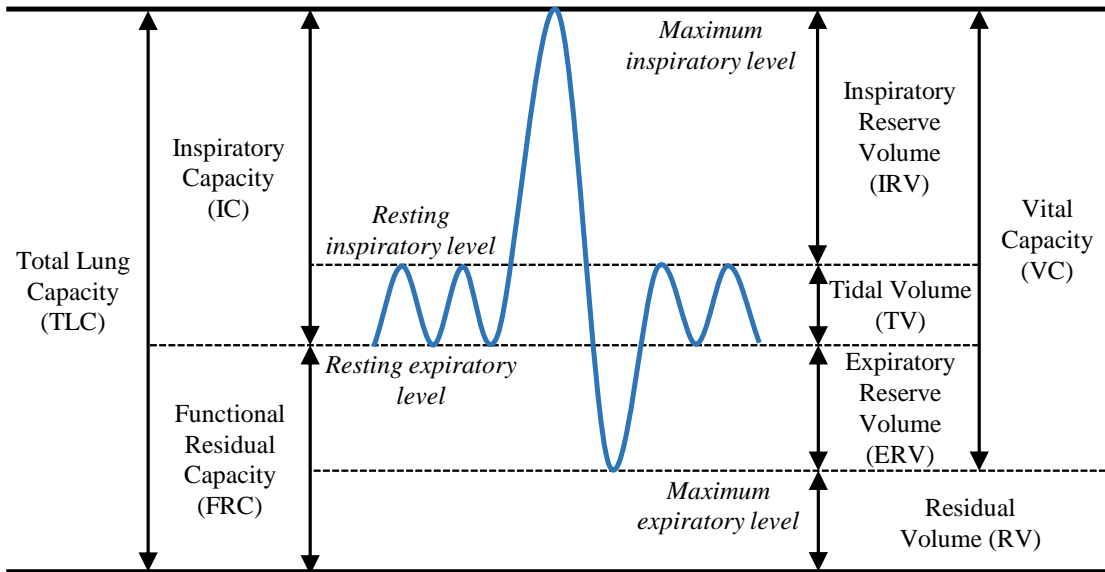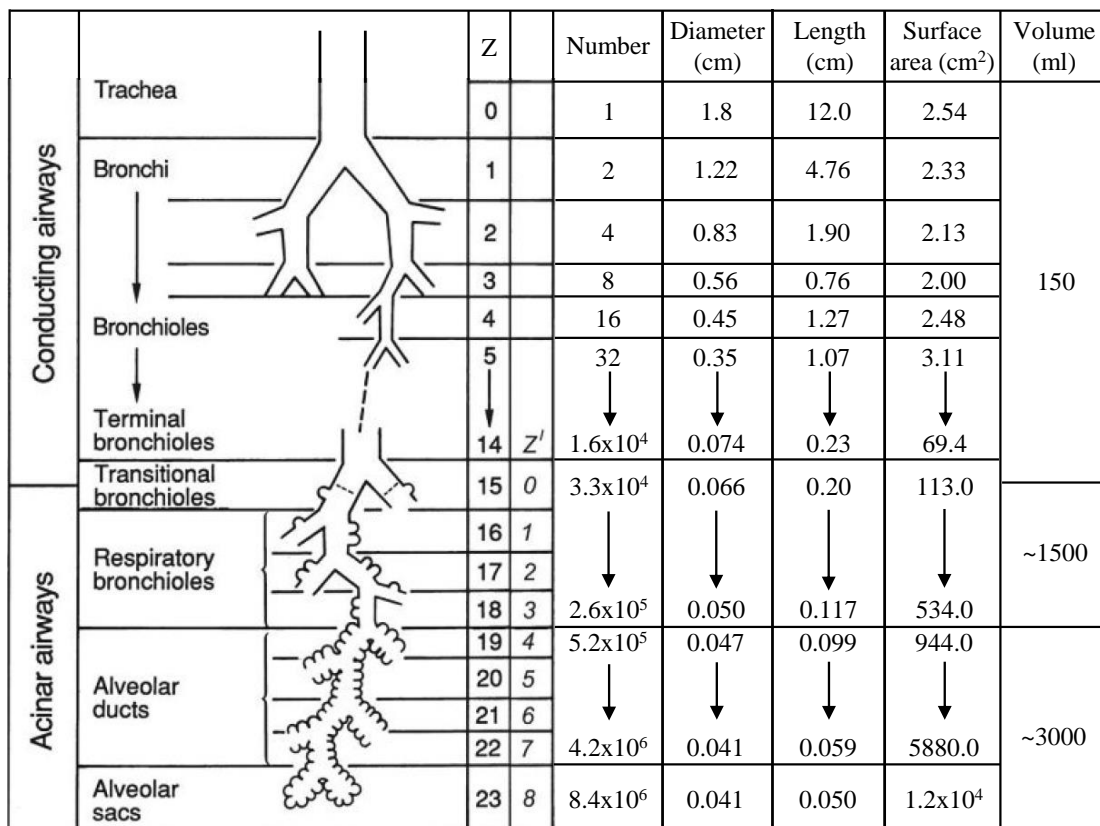
Figure 2.1: Diagram of the different lung volume sub-divisions. A volume-time graph depicts a typical spirometry test where steady tidal breathing is followed by forced maximum inspiration and expiration. The majority of sub-divisions can be calculated from this test, and an alternative test (e.g. body plethysmography) can be used to derive the sub-divisions of FRC, RV, and TLC.

The remaining lung volume and capacities can be determined from alternative methods, and are derived from the measurement of functional residual capacity (FRC). FRC is the volume of the lung at resting expiratory level, and represents the volume at which the elastic force of the chest wall and elastic recoil of the lungs are equal, and the lung is considered at equilibrium. Three common techniques used to measure FRC are body plethysmography (FRC$_{pleth}$), multiple-breath He dilution (FRC$_{He}$), and multiple-breath N$_2$ washout (FRC$_{N_2}$). In healthy lungs, all three methods show good agreement; however, in obstructive lung diseases, gas dilution methods (FRC$_{He}$ and FRC$_{N_2}$) potentially underestimate FRC [8]. FRC$_{pleth}$ is considered the most accurate method for measuring FRC, and entails the measurement of thoracic cage gas volume through Boyle's law. After FRC is determined, the residual volume (RV) is derived by subtracting FRC with ERV, and represents the volume of gas remaining after maximum expiration. Finally, total lung capacity (TLC), the volume of the lung after maximum inspiration, is calculated as the sum of FRC and IC.

2.1.2 Lung morphometry

The lung airways start at the trachea with a single trunk, and the airways branch according to a dichotomous pattern [9]. The lung airways consists on average 23 airway generations, and are separated into two main zones: the conducting zone containing airways up to the 14th generation, and the transitional and respiratory zone where gas exchange occurs (Figure 2.2). The conducting zone does not participate in gas exchange and has little air volume ($\sim$150 ml); in contrast, the transitional and respiratory zones represent over 90% of the lung air volume [10]. Typical adult lung morphometric data for each airway generation is summarised in Figure 2.2.

	Z		Number	Diameter (cm)	Length (cm)	Surface area (cm²)	Volume (ml)
Trachea	0		1	1.8	12.0	2.54	
Bronchi	1		2	1.22	4.76	2.33	
	2		4	0.83	1.90	2.13	
	3		8	0.56	0.76	2.00	150
Bronchioles	4		16	0.45	1.27	2.48	
	5		32	0.35	1.07	3.11	
Terminal bronchioles	14	Z'	1.6×10^4	0.074	0.23	69.4	
Transitional bronchioles	15	0	3.3×10^4	0.066	0.20	113.0	
Respiratory bronchioles	16	1					$\sim$1500
	17	2					
	18	3	2.6×10^5	0.050	0.117	534.0	
Alveolar ducts	19	4	5.2×10^5	0.047	0.099	944.0	
	20	5					
	21	6					$\sim$3000
	22	7	4.2×10^6	0.041	0.059	5880.0	
Alveolar sacs	23	8	8.4×10^6	0.041	0.050	1.2×10^4	

Figure 2.2: Weibel model of human lung airways with associated airway dimensions for an average adult lung volume of 4800 ml at 3/4 maximum inflation [9]. Adapted from Weibel [7].

The transitional and respiratory zones start with the respiratory bronchioles and the distal structural unit of the lung that participates in gas exchange is defined as the pulmonary acinus (Figure 2.3a). The morphometry of the acinus was characterised with silicone rubber casts of adult lungs by Haefeli-Bleuer and Weibel [11], and a summary of typical pulmonary acinus morphometric data is presented in Table 2.1. The volume of an average adult lung acinus is 185 mm³. The inner diameter of intra-acinar airways range from 270 to 500 µm; while the outer diameter is relatively constant at $\sim$700 µm for all acinar airway generations [11].

Alveoli first appear on respiratory bronchioles and increase in number with each subsequent airway generation, until the airways terminate into alveolar sacs that consist entirely of alveoli (Figure 2.3b). The mean diameter of an alveolus, equivalent to the inner diameter of the alveolar sacs, is found to be approximately 250 µm [9, 11]. The number of alveoli in both lungs was initially determined to be ∼300 million across a range of lung volumes [9]; however, more accurate counting methods have determined that number to be closer to 480 million and related to lung volume [12].
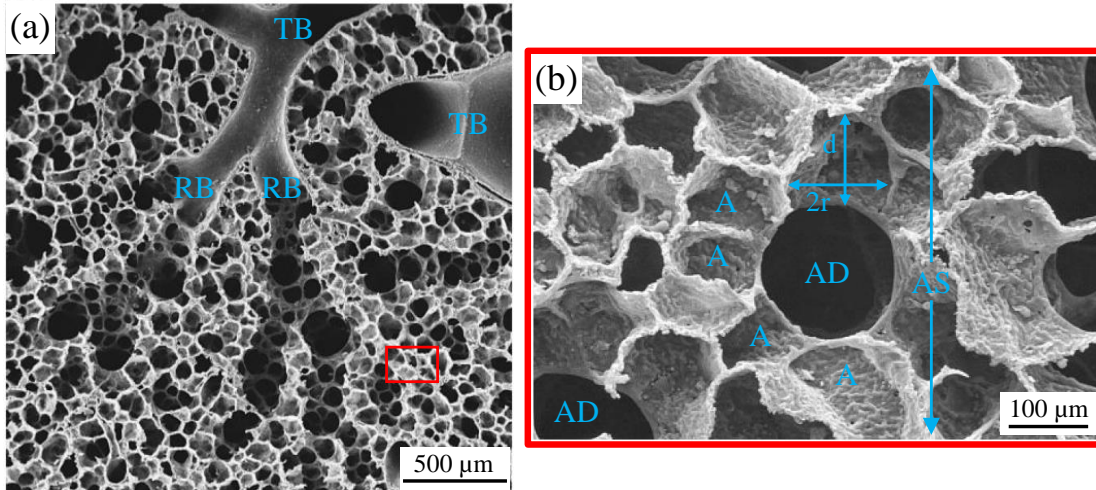
Figure 2.3: Scanning electron micrograph of human acinus. (a) The terminal bronchioles (TB), the terminal conducting airways, branch into respiratory bronchioles (RB). Airways distal to RB are surrounded by alveoli and form the pulmonary acinus. (b) Scanning electron micrograph of an alveolar sac (AS). The approximate equivalent area is denoted by the red rectangle in (a). The alveolar sac consists of an alveolar duct (AD) that is surrounded by multiple alveoli (A). Each alveolus can be characterised by a depth (d) or diameter (2r), and both parameters are on average ∼250 µm. Adapted from Weibel [7].

Table 2.1: Summary of pulmonary acinus and intra-acinar airway morphometric data. Data derived from [11] and [12].

Morphometric parameter		Mean ± SD
Acinus Volume (ml)		0.185 ± 0.079
Acinus duct [a]	Length (µm)	730 ± 258
	Outer diameter (µm)	699 ± 122
	Inner diameter (µm)	323 ± 60
Alveolar sac	Length (µm)	1012 ± 323
	Outer diameter (µm)	656 ± 127
	Inner diameter (µm)	251 ± 40
Number of alveoli (millions) [b]		240 ± 89

[a] Acinar airway duct includes the respiratory bronchioles and alveolar ducts

[b] Mean alveoli number for a single lung

2.1.3 Lung stereology

Lung stereology is the gold standard for measuring lung morphometry, and is based on histological methods and mathematical foundations. Stereology utilises unbiased tissue sampling and assumption-free methods to quantify lung microstructure through the analysis of 2D representative samples of the 3D lung tissue structure with light or electron microscopy. Excised lung tissue samples are typically prepared for histological measurements by a series of lung fixation, tissue processing, embedding and staining methods that ensures the sample is adequate for quantitative analysis [13]. Stereological parameters that describe lung structure are well established, and provide quantitative data on lung microstructure such as the morphometry of the pulmonary acinus [9, 11, 14, 15].

Commonly used or 'standard' stereology parameters that characterise lung morphometry are mean linear intercept (chord) length (Lm), parenchyma surface-to-volume ratio (S/V), and alveoli number density (N_a) [16]. Lm is defined as the mean length of segments or 'chords' along random test lines between sequential alveolar wall intersections (Figure 2.4). Lm can be estimated either directly through the frequency distribution of intercepts from random test lines, or indirectly by counting the number of intersection points [17]. The entire airspace is characterised with Lm, and is related to the estimated volume and surface area of the airspace by:

$$Lm = \frac{4V_a}{S_a} \tag{2.1}$$

where V_a is the volume of the airspace that includes the alveoli and alveolar ducts, and S_a is the surface area of the alveoli.
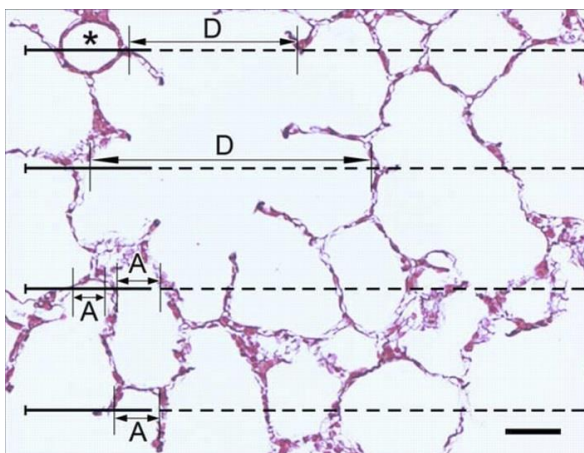
Figure 2.4: Estimation of mean linear intercept length (Lm) based on intercept distribution. Random test line segments (solid line) are followed by a guard line (dashed line). Each time the test line intersects the alveolar wall, the distance (chord length) to the next wall is measured. Double-headed arrows correspond to boundaries of measurements within the alveolar airspace (A) or ductal airspace (D). Reproduced from Knudsen et al. [17].

The estimation of Lm provides a rapid and reliable method to assess chronic obstructive pulmonary disease (COPD) or emphysema [18, 19]. However, Lm only represents airspace enlargement, and does not necessarily reflect the underlying geometry of alveolar structures which may change with lung physiology (e.g. inflation) [17]. Lm may therefore be unsuitable

for distinguishing between emphysema and other conditions, such as healthy ageing lung, for which increased Lm has been reported [20]. In more recent stereological analyses, alveolar surface area is used in conjunction with Lm to quantify emphysema airspace enlargement and alveolar wall destruction [21, 22]. Even though lung stereology is considered the gold standard for quantifying lung morphometry, the histological foundation prevents in vivo whole lung or volumetric measurements of lung morphometry. This limitation is one of the motivations for the development of non-invasive imaging techniques for in vivo volumetric measurements of lung morphometry.

2.2 Imaging techniques

2.2.1 Optical coherence tomography

Optical coherence tomography (OCT) is an optical tomography technique that uses optical interferometry to visualise the airway microstructure at near histological level resolution in real-time [23–25]. The advantages of OCT include no exposure to ionising radiation and high spatial resolution. OCT can acquire subsurface mucosa images of 1–15 µm resolution with a depth penetration of 2–4 mm by directing a near-infrared light beam onto the target tissue and capturing the back-scattered light from the tissue [23]. The amount of back-scattered light varies for different tissues; this allows interferometry to resolve the light signals and differentiate layers of tissue.

Figure 2.5: Fifth-generation airways images obtained using CT and OCT. Images (A, C) were obtained from a normal subject (FEV$_1$ 118% predicted), and (B, D) were obtained from a subject with FEV$_1$ 52% predicted. The percentage of airway wall area measured using CT (A, B) is 5% different, while with OCT (C, D) the difference was 29%. Reproduced with permission from Coxson et al. [26]. Copyright American Thoracic Society.
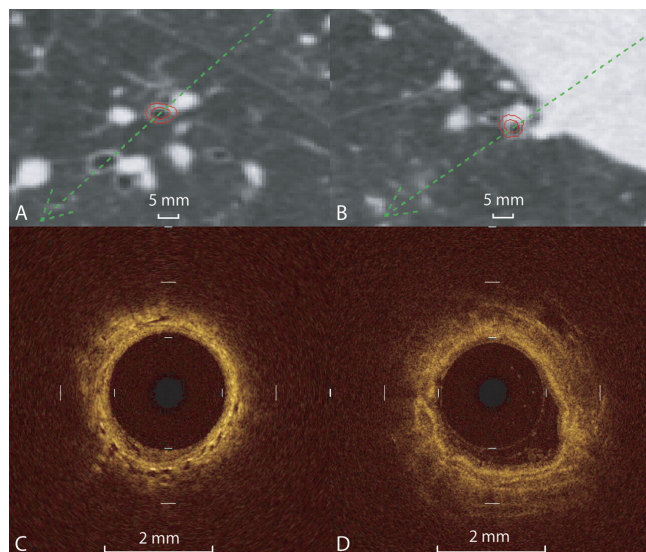
Clear images of small airways, unresolved in advanced CT scanners, can be obtained with OCT. In Coxson et al. [26], airway wall dimensions were obtained with OCT to monitor airway wall changes in COPD and asthma. Airway wall dimensions, such as airway wall and lumen area, in medium to large airways were shown to correlate well with CT and

lung function tests. In fifth generation airways, OCT was superior to CT in measuring the difference in airway wall thickness [26] (Figure 2.5). More recent advancement in OCT techniques involving needle probes have been used to image alveoli, with image resolutions of ~12 µm [27]. The imaging of individual alveoli was not previously feasible due to low image resolution and alveoli access limitations. McLaughlin et al. [27] imaged the alveoli of excised rat and fetal lamb lungs with this technique, and good matching with corresponding histological sections was observed (Figure 2.6). In the same work, dynamic OCT images were also acquired with OCT needle probes, allowing the tracking of individual alveoli in simulations of lung inflation and deflation.
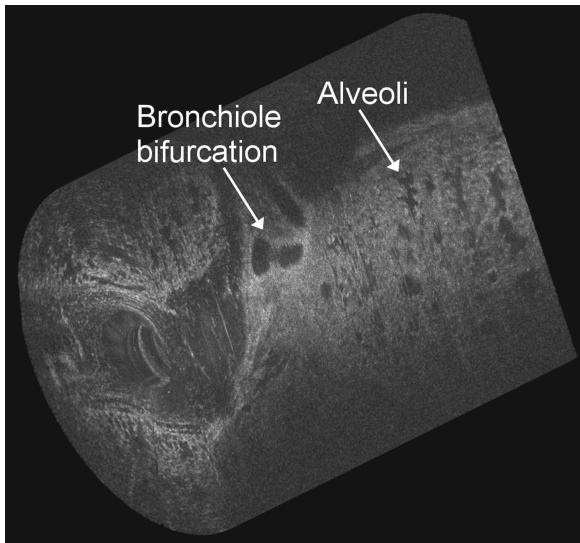
Figure 2.6: 3D visualisation of fetal lamb lung with OCT needle probes showing alveoli and bifurcation of bronchioles. Reproduced from McLaughlin et al. [27].

Optical coherence tomography is a local microscopy technique that provides partially-invasive high resolution, real-time in vivo images of lung microstructure as an alternative to lung stereology. However, its limited optical penetration depth and lack of volumetric imaging restricts the more widespread use of OCT in research and clinical settings.

2.2.2 Computed tomography

Computed tomography (CT) is a non-invasive imaging technique developed in the early 1970s, and its invention is credited to Hounsfield [28] and Cormack [29]. The first prototype CT scanner, developed by Hounsfield [28] in the UK, acquired images with a $80{\times}80$ pixel resolution in a 4–5 minute examination. Modern scanners such as multi-detector row CT (MDCT) can now acquire high resolution 3D images of the lungs within a single breath-hold. Reconstructed CT images represent the linear attenuation coefficient map or densitometry of the scanned subject. The amount of x-rays absorbed by the lung tissue is directly proportional to its density, and provides excellent contrast in CT images. CT is currently considered the clinical gold standard imaging modality for structural assessment of the lungs; however, the ionising radiation dose (standard CT ~8 mSv; low dose CT ~1.5 mSv [30]) can limit its use in

longitudinal pulmonary studies. Healthy lung tissue has a mean value of approximately -800 HU [31, 32], and changes to the density distribution can be indicative of structural changes in the lung tissue due to disease. The enlargement of airspaces and destruction of alveolar walls can be detected through changes in CT attenuation values [33].
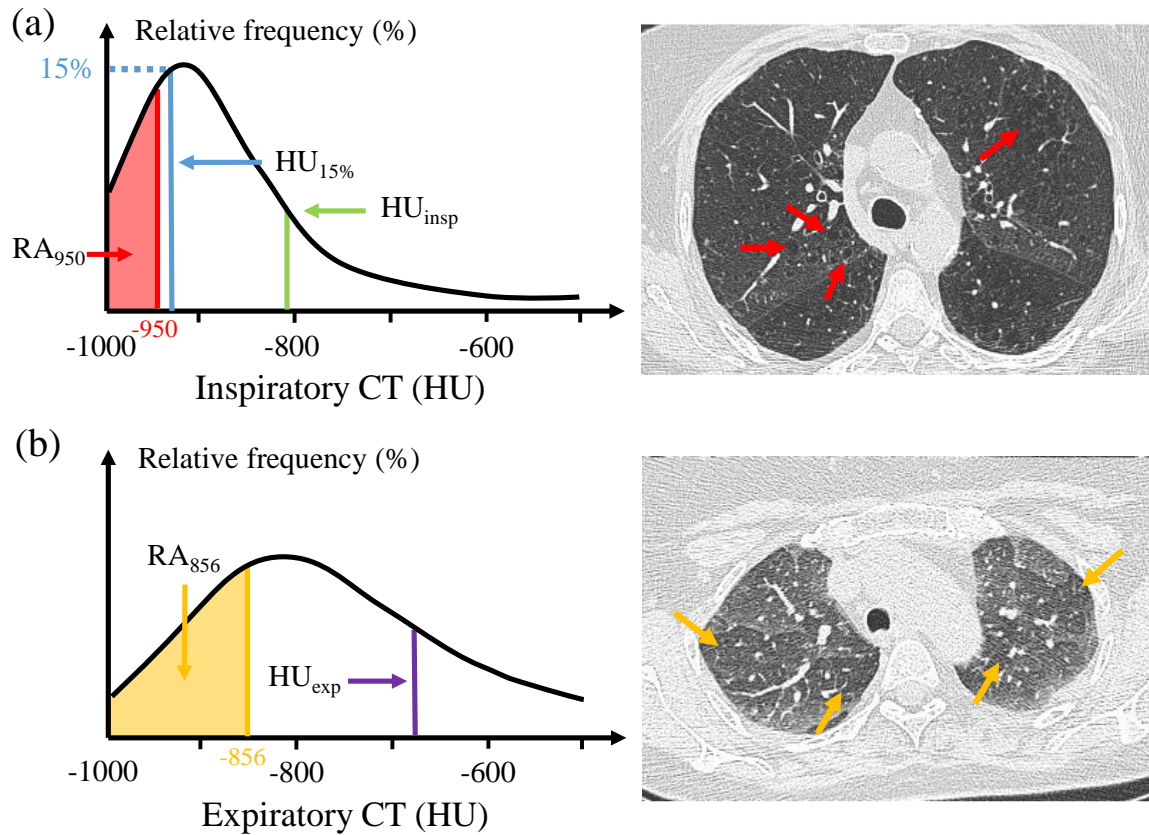
Figure 2.7: Representative densitometry attenuation curves from inspiratory and expiratory CT. (a) Common inspiratory CT metrics are: mean HU (HU_{insp}); percentage of voxels with a value less than -950 HU (RA_{950}); 15th percentile cut-off point corresponding to 15% of voxels with the lowest density ($HU_{15\%}$). Example inspiratory CT image from a COPD patient with regions of emphysema (red arrows). (b) Common expiratory CT metrics are: mean HU (HU_{exp}); percentage of voxels with a value less than -856 HU (RA_{856}). Example expiratory CT image from a COPD patient with evidence of gas trapping (yellow arrows).

A primary application of pulmonary CT imaging is therefore lung parenchyma density analysis for emphysema evaluation [34–36]. Common methods for quantifying emphysema from inspiratory and expiratory CT (see Figure 2.7) include: mean lung density, emphysema index with -950 HU threshold [37], lowest 5th percentile [35] or 15th percentile [38], and gas trapping index at -856 HU in expiratory CT images [39]. The quantification of lung surface area from CT tissue density is an alternative method to quantify emphysema, and shows good correlation with histological estimations allowing for the monitoring of emphysema progression [40]. Fractal analysis are computer-based, texture methods that use complex metrics to differentiate normal lung from emphysematous regions, and are capable of detecting early emphysema by measuring size of regional airspace enlargement [36, 41]. COPD phenotypes

can be differentiated using CT-based parametric response mapping (PRM) derived from CT attenuation maps providing information of COPD disease distribution within the lungs [42]. Inspiratory and expiratory CT volumes are registered and each image voxel is classified by specific expiration and inspiration thresholds.

The development of CT analysis software packages (e.g. VIDA Diagnostics (Coralville, IA, USA) and CALIPER (Mayo Clinic, Rochester, MN, USA)) have enabled automated segmentation of the lungs for density and airway analysis. With MDCT, the 3D airway tree down to the sixth generation can be visualised and quantified. Airway wall area percent and lumen area significantly correlates with FEV_1, and stronger correlations are observed in the more distal airways [43]. Quantitative assessment of lungs with interstitial lung disease (ILD) is challenging due to the complex morphological patterns of ILD. Through the development of automated analysis tools, the different radiological patterns of ILD can be characterised reliably for longitudinal monitoring of disease progression [44, 45].

CT densitometry analysis can however be influenced by factors that may affect the accuracy of disease analysis. In Soejima et al. [46], CT evaluation of emphysema was shown to be altered by age, lung remodelling and smoking-related inflammation effects. Scanning parameters such as radiation dose and slice thickness have also been shown to affect attenuation values and densitometry distribution curves [47, 48]. Lung volume can additionally influence densitometry analysis; where correlations between CT measurements and PFTs are stronger for expiratory CT volumes than for inspiratory due to the appearance of abnormal permanent enlargements of airspaces at the smaller lung inflation state [49–51].

2.2.3   Micro-CT

Even with the advancements in CT scanner technology, the smallest airways visualised with high resolution in vivo CT of human lungs are 1.5–2 mm in size [52], corresponding to approximately the seventh to ninth generation of airways [9]. Studies of distal airways or acinus morphometry have therefore been restricted to silicone rubber casts of the lungs [11] or through 3D mathematical models of the human acinus [53–55]. These models simulate the acinar structure through an airway-tree growing algorithm and compare well with lung morphology obtained from histology. The emergence of micro-CT technology allows 3D lung structures to be imaged at a resolution of 5 µm [56]. At this resolution, previously unseen lung microstructure, such as the 3D acinus structure (Figure 2.8), can be imaged [57, 58].

Micro-CT imaging provides an alternative method for the assessment of pulmonary acinus and parenchyma morphometry. With mice lungs, morphometric measurements from micro-CT were validated against conventional histology, and comparable measurements were obtained [59, 60]. The additional 3D information of micro-CT enables 3D visualisation and quantification of the acinus that is not possible with histology. Micro-CT has been used to quantify emphysema
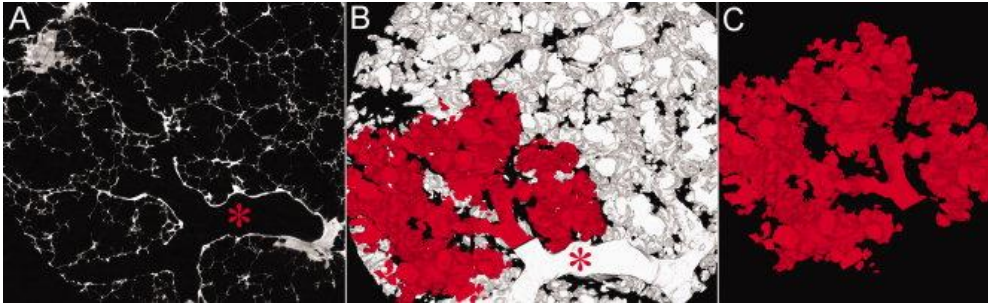
Figure 2.8: Pulmonary acinus imaged with micro-CT. (A) Axial slice with a voxel size of 4 µm^3 with a terminal bronchiole (red star). (B) The micro-CT data was converted into binary images and the acinus was then segmented from the volume data set (C). Reproduced with permission from Litzlbauer et al. [58]. Copyright John Wiley and Sons.

in mice [61, 62] and human lungs [63, 64]. Mouse lungs can be imaged in vivo; however, due to their size, human lungs are currently imaged from excised lung specimens.
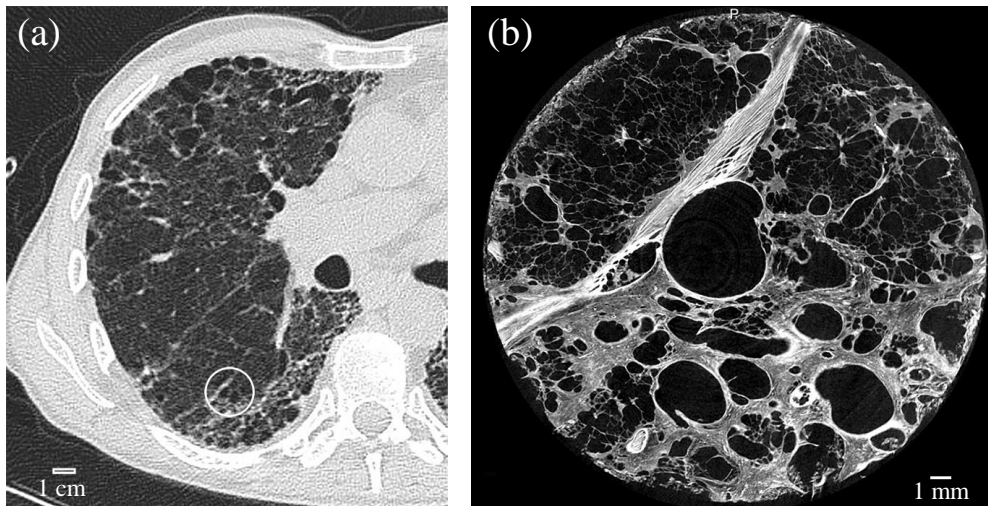
Figure 2.9: Images from an explanted idiopathic pulmonary fibrosis (IPF) lung that demonstrates overt cyst formation and honeycombing. (a) CT image with a distorted region (circle) with inlying cysts along a blood vessel. (b) Micro-CT image of the circled CT region shows a large area of increased attenuation containing multiple cysts. Reproduced with permission from Mai et al. [65]. Copyright Radiological Society of North America.

Micro-CT imaging is typically used in conjunction with in vivo MDCT, and has been used to investigate the relationship of small airways and emphysematous destruction in COPD [66–68]. In early stage COPD, a decrease in the number of small airways (∼2 mm diameter) was observed with CT, alongside a reduction in cross-sectional surface area of terminal bronchioles with micro-CT. This loss and narrowing of small airways was also shown to precede emphysematous destruction in early COPD. Other studies with micro-CT and MDCT imaging have investigated morphometric changes in end-stage cystic fibrosis [69] and idiopathic pulmonary fibrosis [65] (Figure 2.9).

Micro-CT imaging is currently limited by resolution, respiratory artefacts (for in vivo imaging), and poor signal-to-noise ratio (SNR). In small animals, computer-controlled respiratory gating can facilitate the acquisition of in vivo micro-CT images [70]. With more advancements in micro-CT technology, there is potential for in vivo imaging of human lungs in the near future, but the increased radiation dose needed for high resolution imaging will always be a limitation of this modality.

2.2.4   Magnetic resonance imaging

Conventional proton (^{1}H) magnetic resonance imaging (MRI) detects subtle changes in the nuclear spin of hydrogen atoms in an applied magnetic field, and provides high contrast imaging without the use of ionising radiation. MRI was first proposed as a medical imaging diagnostic tool in 1971, when mouse tumours were discovered to exhibit different relaxation times when compared to normal tissue [71]. For an overview of the theoretical background of MR image acquisition, the reader is referred to Section 3.2.

[1]H MR imaging of the lung is relatively difficult, when compared to other organ systems, due to the inherent low tissue density of the lungs (0.1–0.2 g/cm^3), translating to low MR signal [72]. Imaging can be further complicated by cardiac and respiratory motion, and the bulk magnetic susceptibility difference observed at lung-air interfaces due to paramagnetic oxygen in air and diamagnetic tissue. This susceptibility difference creates microscopic inhomogeneous magnetic field gradients at the surfaces of airways and alveoli, causing a very short apparent transverse relaxation time (T_2^*). A T_2^* value of $\sim$2 ms [73] has been observed at $B_0 = 1.5$ T, with an even shorter T_2^* of $\sim$0.5 ms [74] found at $B_0 = 3$ T due to the increase in magnetic field inhomogeneity. Therefore, MRI sequences with short echo times (TE<1–2 ms) are required to image the lung parenchyma [72].

While CT is considered the gold standard when it comes to measuring lung tissue density, techniques have been developed to quantify regional proton lung density from MR images to reduce ionising radiation exposure. Lung proton (water) density is calculated in each image voxel by relating the voxel signal with the signal of a water phantom [75, 76]. Lung proton density calculated from MRI is shown to linearly correlate with CT signal in a study of canine lungs, indicating its potential as an alternative to CT tissue density [77]. Lung proton density reflects the tissue and blood content of the lung, however, is influenced by coil inhomogeneity and T_2^* decay [78]. T_2^* in the lung is shown to vary considerably with lung volume (1.2 $\pm$ 0.1 ms at total lung capacity when compared to 1.8 $\pm$ 0.2 ms at functional residual capacity); therefore T_2^* correction of MR signal is required for accurate quantification of lung density [78]. Maps of lung proton density can also be generated from fitting multiple MR images, obtained with different inversion times, to the inversion recovery signal equation [79]. From these density maps, mean, 15th percentile and relative lung area below a threshold

were determined in healthy and COPD subjects, and compared to equivalent CT metrics. MRI and CT measures were strongly correlated and suggests lung MR signal mapping is a viable alternative to CT for emphysema assessment.
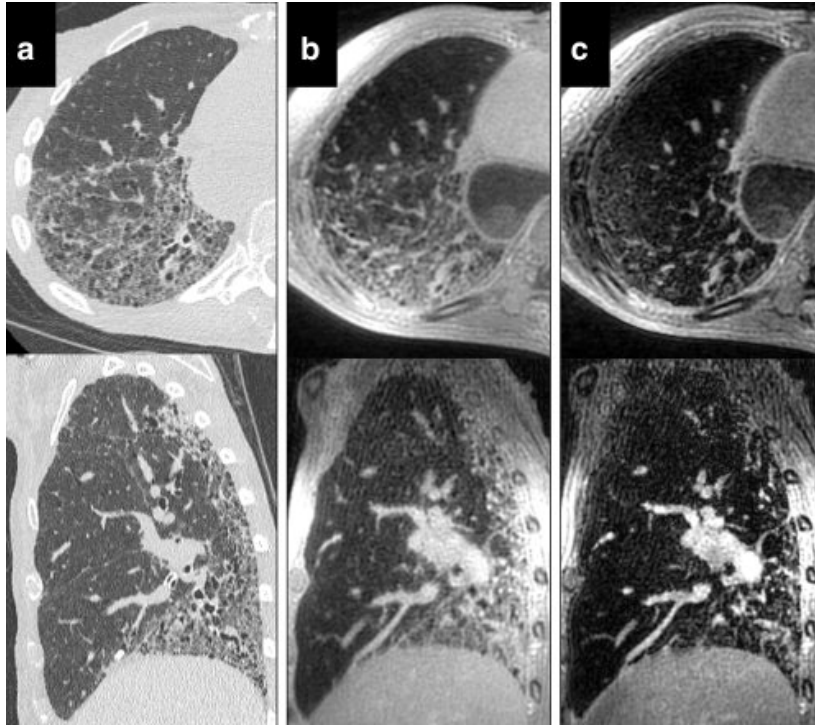
Figure 2.10: Comparison of 3D UTE lung slices with HRCT. (a) Axial and sagittal slices of HRCT. (b) 3D UTE images. (c) Second echo of UTE sequence (TE = 2.1 ms). Both HRCT and 3D UTE show similar fibrosis patterns, which is not seen in the longer echo MRI slices. Reproduced with permission from Johnson et al. [80]. Copyright John Wiley and Sons.

The short T_2^* of lung is a significant constraint in pulmonary MR imaging, however, sequences with radial trajectories can reduce echo times and minimise some of this T_2^* dephasing effect [81]. Ultra-short echo time (UTE) sequences with TE<0.1 ms can increase lung MRI signal such that the tissue density contrast is comparable to that of CT. In UTE, the data acquisition can start without delay after the RF pulse during the ramping up of the gradient [82]. These acquisition strategies enable UTE sequences to have very short echo times and significant improvement in pulmonary image quality is observed (Figure 2.10) [80]. UTE-derived tissue density measurements are shown to agree with CT tissue density in healthy subjects [83], and patients with emphysema or COPD [84, 85]. Imaging of neonatal lungs is also possible through free-breathing UTE acquisitions with retrospective gating [86], and UTE-derived tissue density are also in good agreement with CT measures of tissue density [87].

2.2.5 Hyperpolarised gas MRI

The inhalation of hyperpolarised noble gas isotopes (^{3}He and ^{129}Xe) enables functional assessment of pulmonary ventilation, structure, and gas exchange (see Section 3.3). Noble gas isotopes have low MR signal at thermal equilibrium, but their signal can be enhanced up to five orders of magnitude larger through optical polarisation techniques [88]. One of the most powerful and proven aspects of hyperpolarised gas MRI is its sensitivity to gas diffusion through random Brownian motion of the inhaled hyperpolarised gas atoms. The free diffusion coefficients of ^{3}He and ^{129}Xe in air (at atmospheric pressure and standard temperature) are 0.86 cm^2/s and 0.14 cm^2/s, respectively [89]. Over a time-scale of several milliseconds, ^{3}He and ^{129}Xe gas atoms can travel ∼1 mm. In the lungs, where the alveoli are the smallest restricting structure with a diameter of ∼0.2 mm [9], the gas atoms can encounter the alveolar tissue walls multiple times. The confinement by the alveolar walls leads to gas diffusion restriction and the measured apparent diffusion coefficient (ADC) is hence reflective of the underlying alveolar dimension and sensitive to changes in lung microstructure.

The first hyperpolarised gas diffusion measurements with ^{3}He were reported for healthy volunteers at 1.5 T, where a mean ADC of around 0.25 cm^2/s was obtained [90]. Further studies in healthy volunteers obtained a similar mean ^{3}He ADC of ∼0.2 cm^2/s [91, 92]. In these same studies, lungs with emphysema were demonstrated to have approximately 2.5 times larger mean ^{3}He ADC (∼0.5 cm^2/s [91, 92]), indicating good sensitivity to lung tissue destruction (Figure 2.11). In emphysematous lungs, ADC is shown to significantly correlate with pulmonary function tests (FEV$_1$ [92, 93], diffusing capacity of the lung for carbon monoxide (D$_{LCO}$) [94, 95]), and established metrics of emphysema from CT (mean lung density [95], and emphysema index [93]). Crucially, ADC demonstrates significant correlation with histologically-derived mean linear intercept [96, 97], and surface area to lung volume ratio [96]. Subsequent hyperpolarised gas diffusion studies have utilised ^{3}He ADC to elucidate early emphysematous changes in smokers [94, 98], bronchodilator effects in severe COPD [99], postural and anatomical gradients within the lung [100], and changes related to lung growth [101], ageing [102], lung inflation [103–105], asthma [106], radiation induced lung injury [107] and pulmonary fibrosis [108].

Studies with hyperpolarised gas diffusion-weighted MRI have predominantly utilised ^{3}He over ^{129}Xe due to its higher gyromagnetic ratio translating to approximately a three-fold MR signal advantage in equivalent experimental conditions. However, with the shortage and rising cost of ^{3}He gas [110], recent hyperpolarised gas MRI research has focused on the transition from ^{3}He to the more cost-effective ^{129}Xe gas. In vivo ^{129}Xe ADC values in healthy subjects lungs (0.035–0.040 cm^2/s) [111–113] are 5–6 times smaller than the respective ^{3}He ADC value, reflecting the lower diffusivity of the ^{129}Xe gas. In patients with emphysema, ^{129}Xe ADC is elevated with global values of ∼0.055 cm^2/s reported [113, 114]. Other studies with ^{129}Xe
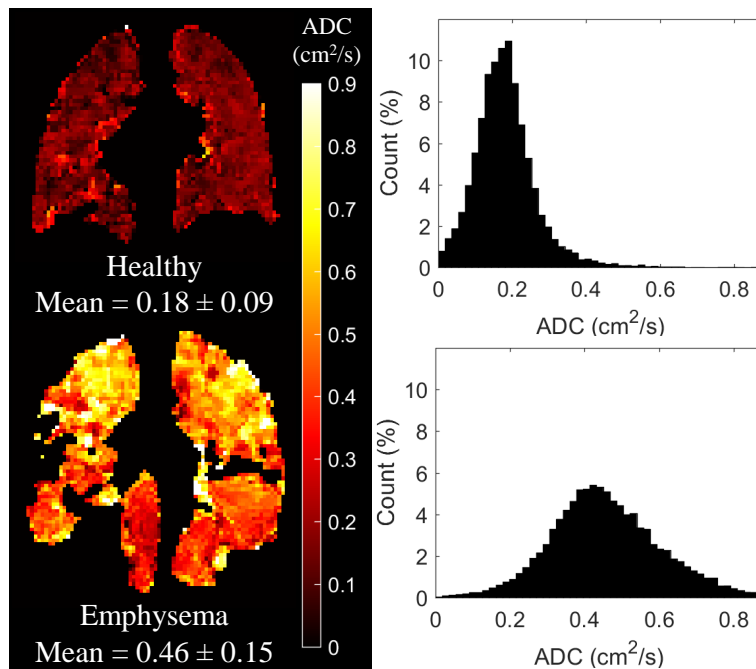
Figure 2.11: Single slice [3]He ADC map and corresponding whole lung histogram from a healthy subject and emphysema patient. Higher ADC values observed in the emphysema patient reflect increased [3]He diffusion due to lung microstructure damage. Reproduced with permission from Wild et al. [109]. Copyright Springer Nature.

ADC have demonstrated significant correlation with histology [115], and elevated ADC in ex-smokers with COPD [116]. Importantly, [129]Xe ADC demonstrates excellent linear correlation with [3]He ADC in subjects across a range of microstructural length scales [116–118].

All the aforementioned hyperpolarised gas diffusion-weighted MRI studies have utilised short diffusion times ([3]He Δ<2 ms; [129]Xe Δ<10 ms) corresponding to a theoretical free diffusion length of less than 1 mm; enabling the diffusion MR experiment to probe a single acinar airway. It is however possible with longer diffusion times to probe diffusion length scales in the lungs associated with inter-acinar connectivity and disease processes that lead to different gas mixing and wash-out times. The problem with longer diffusion times in the order of tens of milliseconds is that T_2^* decay ($T_2^* \sim$25 ms for both [3]He and [129]Xe in the lungs at 1.5 T [119, 120]) can significantly attenuate the MR signal before application of the second diffusion gradient pulse. Various pulse sequences have been proposed to address this that involve storing the diffusion-encoded magnetisation in the longitudinal direction ($T_1 \sim$20 s in the lungs [121]), such that measurements of long time scale diffusion can be made [122–126]. In all these studies, the reported ADC values were approximately an order of magnitude less than those measured with short diffusion times. Long time scale diffusion measurements are thought to be more representative of inter-acinar connectivity rather than alveolar morphometry in short diffusion time experiments [127]. Preliminary comparisons of short and long time scale diffusion measurements suggest there may be difference in sensitivity to diseases that affect different aspects of lung microstructure [106].

Theoretical models of hyperpolarised gas diffusion

The average ADC value over the lung is clearly an indicator of mean alveolar size and hence disease severity in the case of emphysema. However, the diffusion regime of hyperpolarised gases in the lungs results in a non-Gaussian phase dispersion and non-mono-exponential signal decay that is not accounted for in the calculation of ADC. The non-Gaussian dispersion causes difficulties when extracting quantitative information about lung microstructure from in vivo diffusion-weighted MR imaging, and as such there is no direct one-to-one correspondence between measured ADC value and histological lung morphometry parameters. Theoretical models of gas diffusion have been proposed to extract lung morphometry measurements from the diffusion MR signal. To date, only cylindrical geometrical models [5, 128], stretched exponential models [129], and q-space transforms [130] have been used to provide in vivo estimates of alveolar length scales from hyperpolarised gas diffusion measurements akin to those obtained from histology. A fundamental requirement for the application of these models is that multiple (>2) b-value diffusion measurements are acquired to sufficiently sample the non-mono-exponential diffusion signal.
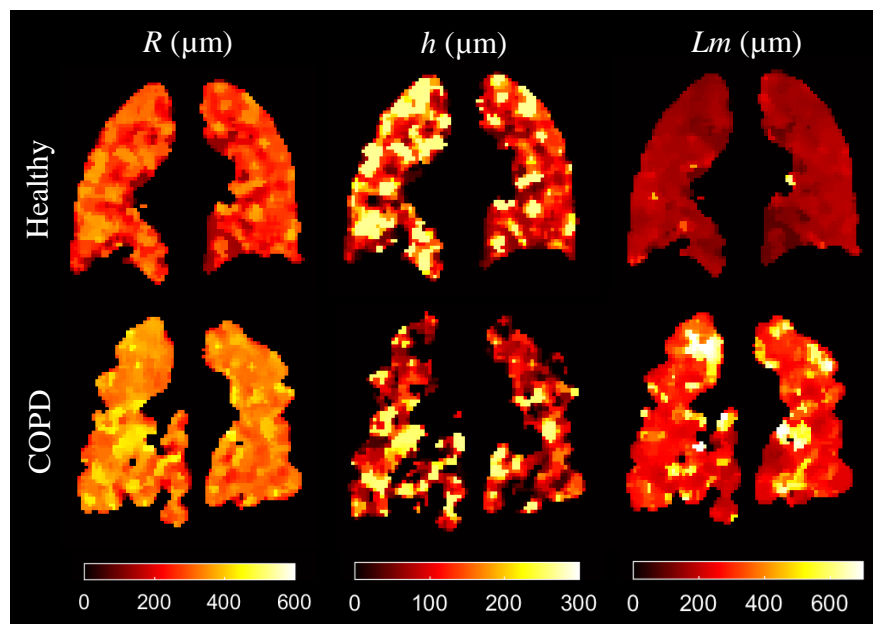
Figure 2.12: Example healthy subject and COPD patient ^{3}He lung morphometry maps of R, h, and mean linear intercept (Lm) derived from the cylindrical geometric model. Reproduced with permission from Wild et al. [109]. Copyright Springer Nature.

The first reported in vivo measurements of lung geometrical parameters at the acinar level were by Yablonskiy et al. [5] using a theoretical analytical model of infinitely long cylinders based upon the Weibel model of airway geometry (see Section 3.5.2). Multiple b-value measurements were used to estimate alveolar duct diameters from a model of anisotropic diffusion in healthy subjects and emphysema patients (Figure 2.12). The cylindrical geometrical model was subsequently updated to permit the evaluation of lung morphometry parameters (mean linear

intercept (Lm), surface-to-volume ratio (S/V), and alveoli density (Na)) from acinar airway radii (R) and alveolar depth (h) parameters [6, 128] (see Figure 3.26 for a schematic of cylinder model parameters). Lm measurements derived from ^{3}He diffusion MRI have been found to be strongly correlated with histological measurements of Lm in specimens of healthy and emphysematous lungs [6]. Various groups have since used this model to study changes in lung microstructure associated with smoking-related early emphysema [131, 132], age [133], lung inflation [134], and adult lung growth [135]. More recently, the cylindrical geometry model was adapted for ^{129}Xe [136], and ^{129}Xe lung morphometry parameters were comparable to ^{3}He and demonstrated in healthy volunteers and COPD patients [137–139].

An alternative theoretical model of hyperpolarised gas diffusion signal behaviour in the lungs is the stretched exponential model [129, 140, 141] (see Section 3.5.2 for more details). This mathematical model does not include any assumptions about the lung geometry to derive in vivo estimates of alveolar length scales. In the stretched exponential model, a probability distribution of diffusive length scales is derived, representative of the distribution of microscopic dimensions of the airways (i.e. the diffusion-restricting boundaries) contained within a given voxel. The shape of this distribution is comparable to that of intercept lengths measured in histology, and is used to derive a mean diffusion length scale (Lm_D). Example stretched exponential model data is presented in Figure 2.13. The first in vivo Lm_D values were reported in a population of asthmatic subjects, and Lm_D was shown to significantly correlate with %-predicted functional residual capacity (FRC) measurements from spirometry, in addition to mean CT density [129].
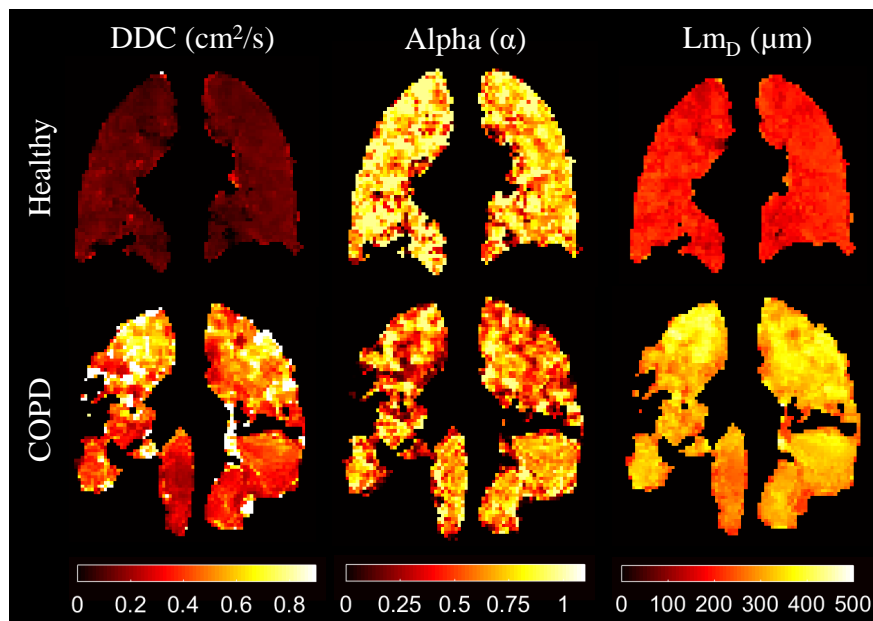
Figure 2.13: Example healthy subject and COPD patient ^{3}He parameter maps of effective distributed diffusion coefficient (DDC), heterogeneity index (α) and mean diffusion length scale (Lm_D) derived from the stretched exponential model. Reproduced with permission from Wild et al. [109]. Copyright Springer Nature.

Global spectroscopic measurements of hyperpolarised gas diffusion can also provide an alternative means to obtain lung microstructural information. At the expense of spatial information, diffusion-weighted spectroscopy experiments offer shorter acquisition times and require less hyperpolarised gas than the imaging-based methods discussed above, and therefore may be ideally suited for longitudinal monitoring of paediatric patients. Multiple b-value diffusion-weighted spectroscopy data can be analysed using q-space theory [142] to derive displacement probability profiles and root-mean-square displacements (X_{rms1} and X_{rms2}) in healthy children and adults, and COPD patients [130]. X_{rms1} and X_{rms2} correspond to two different diffusion length scales in the lung, and both values correlated well with age and conventional ADC measurements, suggesting that these displacements may be similarly sensitive to lung microstructural changes. q-Space was used in a study of alveolarisation in children, and X_{rms} results suggested that neo-alveolarisation occurs through childhood [143, 144]. However, due to the long diffusion times (>5 ms) used, the ^{3}He atoms are sampling structures beyond the alveoli. Therefore the validity of the X_{rms} results need to be further demonstrated. Recent developments in ^{3}He MR q-space imaging have utilised an under-sampled radial stack-of-stars acquisition to obtain 3D spatially resolved maps of X_{rms} [145].

2.3 Conclusion

Multiple imaging modalities and techniques can been used to measure lung microstructure across a range of resolutions from a single alveolus to whole lung coverage. Hyperpolarised gas MRI, a non-invasive and non-ionising radiation technique, is of particular interest to this work, and the development of new hyperpolarised gas MR imaging techniques is the emphasis of subsequent chapters.

Chapter 3

Theoretical background

This chapter covers the theoretical background of the experimental work presented in the subsequent chapters, and is divided into five sections: nuclear magnetic resonance (Section 3.1), magnetic resonance imaging (MRI) (Section 3.2), hyperpolarised gas MRI (Section 3.3), sub-Nyquist imaging (Section 3.4) and diffusion-weighted MRI (Section 3.5). The majority of material is derived from the following textbooks [146–150].

3.1   Nuclear magnetic resonance

The physical phenomenon of nuclear magnetic resonance (NMR) was first observed and measured by Rabi [151] in 1938, and this work was expanded upon by Bloch [152] and Purcell [153] in 1946 where the effects of spin precession in a magnetic field were quantified. This section aims to provide an overview of the fundamentals of NMR theory.

3.1.1   Spin and polarisation

Spin angular momentum or spin is an intrinsic property of all nuclei, and the detection of this nuclear spin within a magnetic field forms the principle of NMR. The overall spin of an atomic nucleus is given by its spin quantum number ($\vec{I}$) and is dependent on the number of protons and neutrons within the nucleus. Atomic nuclei, such as ^{1}H, ^{3}He, and ^{129}Xe, that have non-zero nuclear spin ($\vec{I} > 1/2$) are suitable for NMR. At ground state, nuclei with non-zero spin have an associated magnetic moment ($\vec{\mu}$):

$$\vec{\mu} = \gamma \hbar \vec{I} \tag{3.1}$$

where γ is the gyromagnetic ratio that is unique to each nuclei, and $\hbar$ is the reduced Planck's constant ($h/2\pi$). When observed along an arbitrary axis (z) associated with an applied

magnetic field ($\vec{B} = B_0\hat{z}$), the spin quantum number (I_z) can have $2I + 1$ values or levels ranging from $-I$ to $+I$. In the absence of an external magnetic field, these levels are degenerate because each level is energetically equivalent and equally populated. This degeneracy is lifted when spins interact with an external magnetic field $\vec{B}$, and the energy levels are separated according to the Zeeman interaction. The Hamiltonian H (energy) operator describing this interaction for a constant B_0 along the z-axis:

$$H = -\gamma\hbar B_0 I_z \tag{3.2}$$

The difference in energy (ΔE) between each level is therefore given by:

$$\Delta E = \gamma\hbar B_0 = \hbar\omega_0 \tag{3.3}$$

where ω_0 is the Larmor frequency:

$$\omega_0 = \gamma B_0 \tag{3.4}$$

From a quantum mechanics perspective, the Larmor frequency corresponds to the photon frequency associated with the transition between energy levels. For a spin-1/2 nucleus (e.g. protons), spins experience two energy levels due to the Zeeman interaction (Figure 3.1), corresponding to 'spin-up' $I_z = +1/2$ and 'spin-down' $I_z = -1/2$ levels.

Figure 3.1: Energy level diagram for spin-1/2 nucleus (with a positive gyromagnetic ratio) experiencing a Zeeman interaction due to a magnetic field B_0. The energy separation between the levels is given by $\Delta E = \gamma\hbar B_0$, corresponding to a larger relative spin population in the lower energy ground state ($m = +1/2$).
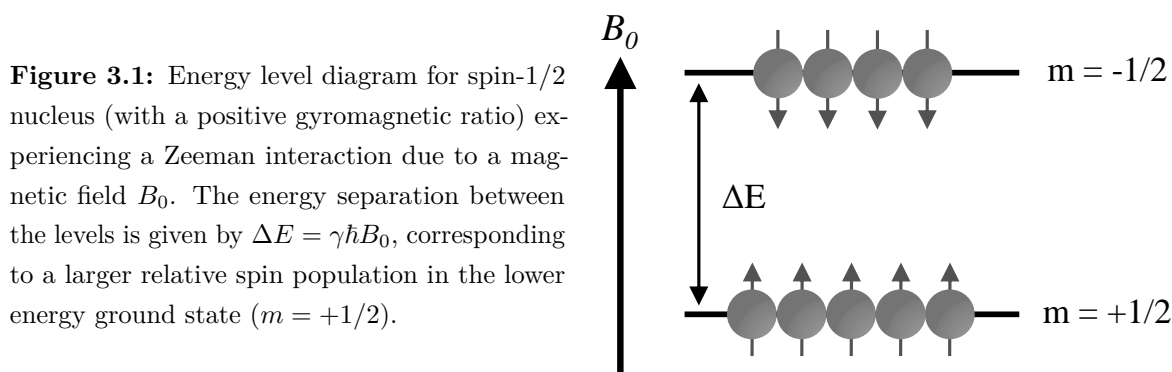
When an ensemble of nuclei with quantum number $I_z = m$ at thermal equilibrium is considered, the Boltzmann law of statistical mechanics states that the populations (P_m) of the different energy levels (E_m) are proportional to:

$$P_m \propto \exp(-E_m/kT) = \exp(\gamma\hbar m B_0/kT) \tag{3.5}$$

where k is the Boltzmann constant, and T is the temperature. The net magnetisation of a

sample containing N spins per unit volume can be described by:

$$M = N\gamma\hbar\frac{\sum\limits_{m=-I}^{I} m\exp(\gamma\hbar mB_0/kT)}{\sum\limits_{m=-I}^{I} \exp(\gamma\hbar mB_0/kT)} \tag{3.6}$$

At room temperature, the energy difference ΔE is over five magnitudes smaller than the Boltzmann energy (kT), therefore, a linear expansion of Equation 3.6 can be performed to derive:

$$M = \frac{N\gamma^2\hbar^2 I(I+1)}{3kT}B_0 \tag{3.7}$$

For a spin-1/2 nucleus, the net magnetisation can be simplified to:

$$M = \frac{N\gamma^2\hbar^2}{4kT}B_0 = N\mu P \tag{3.8}$$

where μ is $\gamma\hbar/2$ (Equation 3.1), and P is the Boltzmann polarisation that describes the population difference between the two energy levels. Protons, therefore have very small polarisation at thermal equilibrium $(P \sim 5 \times 10^{-6})$, but the net magnetisation is compensated by the large proton spin density within water $(6.7 \times 10^{22}$ atoms/cm$^3)$. In the case of a gas at room temperature, such as ^{3}He and ^{129}Xe, the spin density is three orders of magnitude lower $(2.7 \times 10^{19}$ atoms/cm^3 [88]), and therefore techniques such as 'hyperpolarisation' are used to increase their net magnetisation for the purposes of MRI (see Section 3.3.1).

3.1.2 Excitation and relaxation

Excitation and rotating frame

A nuclear spin, with an associated magnetic moment $(\vec{\mu})$, in the presence of a magnetic field $\vec{B}$ will experience a torque (τ) that results in a change in microscopic angular momentum:

$$\tau = \frac{d\vec{I}}{dt} = \vec{\mu} \times \vec{B} \tag{3.9}$$

When Equation 3.9 is combined with Equation 3.1, the equation of motion of a spin is:

$$\frac{d\vec{\mu}}{dt} = \gamma\vec{\mu} \times \vec{B} \tag{3.10}$$

In the semi-classical description of magnetisation, the change of macroscopic angular momentum is described by the net magnetisation vector $\vec{M}$, a sum of all magnetic moments

per unit volume, to derive:

$$\frac{d\vec{M}}{dt} = \gamma \vec{M} \times \vec{B} \tag{3.11}$$

Equation 3.11 can be considered in a rotating coordinates system, where the static laboratory frame (x, y, z) rotates at an angular frequency ω, and is denoted by primed coordinates (x', y', z'):

$$\frac{\partial \vec{M}}{\partial t} = \gamma \vec{M} \times \vec{B}_{eff} = \gamma \vec{M} \times \vec{B} + \frac{\omega}{\gamma} \tag{3.12}$$

In a static magnetic field along the z-axis ($\vec{B} = B_0 \hat{z}$), if $\omega = \omega_0 = -\gamma/B_0$, the effective field B_{eff} disappears, and the magnetisation $\vec{M}$ is constant. This indicates that, with respect to the laboratory frame, $\vec{M}$ precesses at the Larmor frequency (Equation 3.4).

A radiofrequency (RF) pulse with a frequency (ω), will create an oscillating magnetic field $\vec{B}_1$ in the perpendicular direction to B_0. The application of the RF pulse will displace the magnetisation vector from the z-axis by an angle α. This angle is the flip angle, and is given by:

$$\alpha = \omega t = \gamma \vec{B}_1 t \tag{3.13}$$

The total magnetic field is now a sum of the static field B_0 along z-axis and the rotating field $\vec{B}_1$:

$$\vec{B} = B_1(\cos \omega t \ \hat{x} - \sin \omega t \ \hat{y}) + B_0 \hat{z} \tag{3.14}$$

If the rotating frame system is chosen such that B_1 is static along the x' direction, Equation 3.12 becomes:

$$\frac{\partial \vec{M}}{\partial t} = \gamma \vec{M} \times \vec{B}_{eff} = \gamma \vec{M} \times [(B_0 - \frac{\omega}{\gamma})\hat{z}' + B_1 \hat{x}'] \tag{3.15}$$

Equation 3.15 indicates that, in the laboratory frame, in the presence of a static (B_0) and rotating (B_1) magnetic field, the magnetisation precesses around both fields (Figure 3.2a). Within the rotating frame, when $\omega = \omega_0$ this is called *on resonance*, and the effective magnetic field is reduced to $B_1 \hat{x}'$ and $\vec{M}$ rotates around $\hat{x}'$ at a frequency ω_1 (Figure 3.2b). When $\omega \neq \omega_0$, *off resonance* behaviour occurs, and the effective longitudinal ($\hat{z}'$) field in the rotating frame is non-zero ($B_0 - \omega/\gamma$), and the magnetisation precesses around B_{eff} at an effective frequency (ω_{eff}).
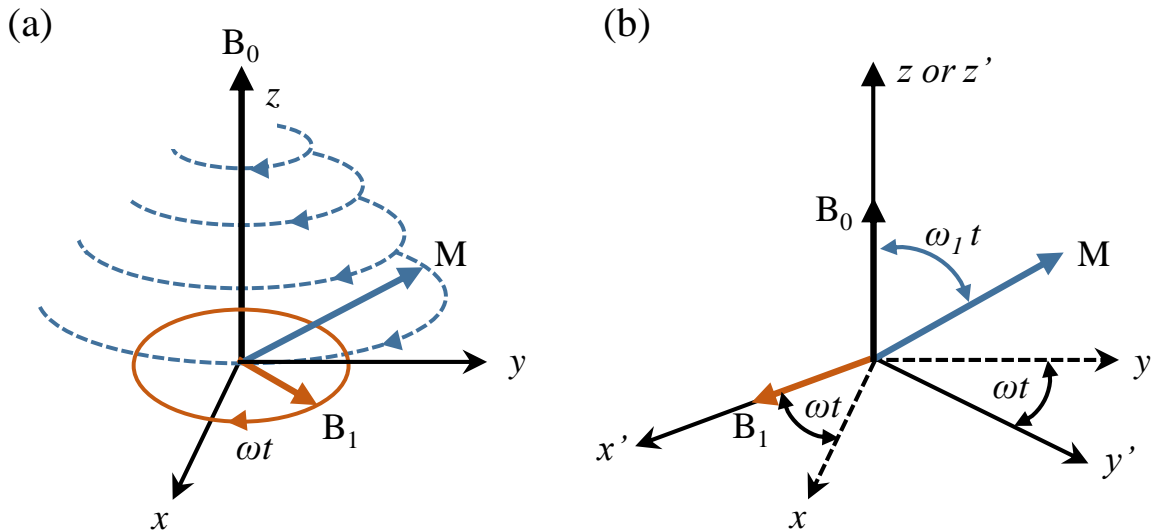
Figure 3.2: Evolution of the nuclear spin magnetisation in the presence of a longitudinal static field B_0, and transverse rotating field B_1 when $\omega = \omega_0$ or on resonance. (a) In the laboratory frame, the magnetisation vector M precesses simultaneously about B_0 at ω_0, and B_1 at ω_1. (b) In the rotating frame, where a rotation about the z-axis is set to $-\omega$, the fields B_0 and B_1 are stationary, and the magnetisation M precesses about B_1 (aligned to the x'-axis) at ω_1.

Relaxation and Bloch equations

Equation 3.15 suggests that after the application of a RF pulse, the net magnetisation vector $(\vec{M})$ is displaced from equilibrium and precesses indefinitely; however, in reality, the net magnetisation is returned to its equilibrium state through relaxation processes. Within a static magnetic field pointing along the z-axis ($\vec{B} = B_0\hat{z}$), Equation 3.11 can be modified to include relaxation processes to form the Bloch equation [152]:

$$\frac{d\vec{M}}{dt} = \gamma\vec{M} \times \vec{B} + \frac{1}{T_1}(M_0 - M_z) - \frac{1}{T_2}\vec{M}_{xy} \tag{3.16}$$

This equation describes the relationship between parallel or longitudinal (M_z), and perpendicular or transverse ($\vec{M}_{xy}$) magnetisation components, and two relaxation parameters (T_1 and T_2) related to the interaction of spins with the surrounding lattice and with each other, respectively. From Equation 3.16, the rate of change in longitudinal magnetisation (M_z) is characterised by the spin-lattice relaxation time, T_1:

$$\frac{dM_z}{dt} = \frac{1}{T_1}(M_0 - M_z) \tag{3.17}$$

The solution for Equation 3.17 is in the form of an exponential growth that describes the change in longitudinal magnetisation from initial value, $M_z(0)$, to equilibrium value, M_0:

$$M_z(t) = M_z(0)e^{-t/T_1} + M_0(1 - e^{-t/T_1}) \tag{3.18}$$

where after a duration T_1, the initial longitudinal magnetisation has recovered to approximately 63% of the equilibrium M_0.

The individual spins in the transverse plane experience local magnetic fields that are a combination of the external (B_0) applied field and the fields created by neighbouring spins. Each spin experiences a slight variation in local fields that leads to different local precession frequencies, and causes spin isochromats to disperse and dephase in coherence over time leading to a reduction of net transverse magnetisation. The overall rate of reduction is defined as the spin-spin relaxation time, T_2, and is described by:

$$\frac{d\vec{M}_{xy}}{dt} = \gamma \vec{M}_{xy} \times \vec{B}_{ext} - \frac{1}{T_2}\vec{M}_{xy} \tag{3.19}$$

The solution to Equation 3.19 describes the exponential decay of the magnitude of the transverse magnetisation; which reduces to approximately 37% of the initial transverse magnetisation after a T_2 time constant:

$$\vec{M}_{xy}(t) = \vec{M}_{xy}(0)e^{-t/T_2} \tag{3.20}$$

In addition to spin-spin interactions, inhomogeneities in the external B_0 field, caused by intrinsic magnetic field inhomogeneities or susceptibility differences, introduce additional dephasing of the transverse magnetisation and further reduces the spin-spin relaxation time. The effective relaxation time, T_2^* is a combination of T_2 and the inhomogeneity relaxation time, T_2', such that:

$$\frac{1}{T_2^*} = \frac{1}{T_2} + \frac{1}{T_2'} \tag{3.21}$$

It is possible to recover the dephasing caused by T_2' through a spin echo sequence where an additional RF pulse rephases the spins and effectively reverses the dephasing caused by external field inhomogeneity. However, the intrinsic dephasing caused by spin-spin interactions is permanent and not recoverable. $\vec{M}_{xy}$ in Equation 3.19 can also be decomposed into its M_x and M_y components as follows:

$$\frac{dM_x}{dt} = \omega_0 M_y - \frac{1}{T_2}M_x \tag{3.22}$$

$$\frac{dM_y}{dt} = -\omega_0 M_x - \frac{1}{T_2}M_y \tag{3.23}$$

where ω_0 is the Larmor frequency. The exponential solutions are described by:

$$M_x(t) = e^{-t/T_2}(M_x(0)\cos\omega_0 t + M_y(0)\sin\omega_0 t) \tag{3.24}$$

$$M_y(t) = e^{-t/T_2}(M_y(0)\cos\omega_0 t - M_x(0)\sin\omega_0 t) \tag{3.25}$$

The combination of Equations 3.18, 3.24, and 3.25 describe a 'corkscrew' trajectory for the magnetisation vector initially tipped into the transverse plane. The transverse components precess at the Larmor frequency and decay due to T_2; while the longitudinal component relaxes to equilibrium value with T_1. Equations 3.24, and 3.25 can also be represented in a complex representation ($M_+ = M_x + iM_y$):

$$M_+(t) = e^{-t/T_2} e^{-i\omega_0 t} M_+(0) \tag{3.26}$$

The application of an RF pulse to tip the magnetisation from equilibrium produces its own rotating RF field (B_1), which in the rotating frame is parallel to $\hat{x}'$, such that $\vec{B} \equiv \vec{B}_{eff}$ as per Equation 3.15. The Bloch equations, in primed coordinates, can now be described by:

$$\begin{aligned}
\frac{dM_{x'}}{dt} &= (\omega_0 - \omega)M_{y'} - \frac{1}{T_2}M_{x'} \\
\frac{dM_{y'}}{dt} &= (-\omega_0 + \omega)M_{x'} + \omega_1 M_{z'} - \frac{1}{T_2}M_{y'} \\
\frac{dM_{z'}}{dt} &= \omega_1 M_{y'} + \frac{1}{T_1}(M_0 - M_{z'})
\end{aligned} \tag{3.27}$$

where ω_0 is the Larmor frequency, ω_1 is the RF field spin frequency, and ω is the RF oscillation frequency. RF pulses typically have very short durations, therefore relaxation during its application can be neglected. The relaxation processes after RF application can still be described by Equations 3.18, 3.24, and 3.25, after the transformation into the RF rotating reference frame where ω_0 is replaced by $\Delta\omega \equiv \omega_0 - \omega$.

3.1.3 Signal detection

In NMR, the precessing components of the transverse magnetisation after RF excitation causes a time varying magnetic flux that, according to Faraday's law, induces an electromotive force (*emf*) that can be detected by a receiver coil. The *emf* induced in the coil is described by:

$$emf = -\frac{d}{dt}\int_{sample} \vec{M}(\vec{r},t) \cdot \vec{\mathcal{B}}(\vec{r})d^3r \tag{3.28}$$

where *emf* is the free induction decay (FID), $\vec{r}$ is the spatial location vector, and $\vec{\mathcal{B}}$ is the magnetic field per unit current produced by the coil at position $\vec{r}$. Typically, the Larmor frequency is significantly larger in magnitude than $1/T_1$ and $1/T_2$; therefore when Equations 3.18 and 3.26 are inserted into 3.28, $e^{-i\omega_0 t}$ is the dominant factor and the observed signal $s(t)$ is proportional to:

$$s(t) \propto \omega_0 \int M_+(\vec{r},t) \cdot \mathcal{B}_+(\vec{r})d^3r \tag{3.29}$$

and can be further simplified to give:

$$s(t) \propto \omega_0 \int e^{-t/T_2(\vec{r})} M_{xy}(\vec{r}, 0) \cdot \mathcal{B}_{xy}(\vec{r}) e^{i(\omega_0 t + \theta_{\mathcal{B}}(\vec{r}) - \phi_0(\vec{r}))} d^3 r \tag{3.30}$$

where ϕ_0 and $\theta_{\mathcal{B}}$ are the initial phases for M_+ and $\mathcal{B}_+$, respectively. Equation 3.30 demonstrates that the dominant signal induced in the receiver coil is related to the rapid oscillations of the transverse magnetisation at Larmor frequency. In practice, the signal is demodulated to remove the rapid oscillations at Larmor frequency by multiplication of both a sinusoid or cosinusoid at Larmor frequency, corresponding to data storage in two (real and imaginary) channels. An effective spin density parameter $\rho(\vec{r})$ that incorporates all proportionality constants and time-independent components can be introduced to describe the simplified demodulated signal:

$$s(t) = \int e^{-t/T_2(\vec{r})} \rho(\vec{r}) e^{-i\phi(\vec{r},t)} d^3 r \tag{3.31}$$

3.2 Magnetic resonance imaging

The development of magnetic resonance imaging (MRI) originated from the seminal work of Lauterbur [154] and Mansfield [155], where magnetic field gradients were used to distinguish NMR signals from different spatial locations. This section provides the theoretical background for the spatial encoding and sampling processes associated with image acquisition in common MR imaging sequences.

3.2.1 Spatial encoding and *k*-space

The objective of MR imaging is to determine the effective spin density $\rho(\vec{r})$ at a spatial location $\vec{r}$ from the measured signal as a function of time. If a spatial magnetic field gradient $G(\vec{r}, t)$ is applied, the total magnetic field becomes dependent on position ($\vec{r}$), and the Larmor equation is given by:

$$\omega(\vec{r}, t) = \gamma B_0 + \gamma G(\vec{r}, t) \cdot \vec{r} \tag{3.32}$$

In the B_0 rotating reference frame the net change in precession frequency is:

$$\omega(\vec{r}, t) = \gamma G(\vec{r}, t) \cdot \vec{r} \tag{3.33}$$

For a gradient duration t, the spatially varying phase (ϕ) accumulated by $G(\vec{r}, t)$ is then given by:

$$\phi(x, t) = \gamma \vec{r} \int_0^t G(\vec{r}, t') dt' \tag{3.34}$$

A spatial frequency vector, $\vec{k}(t)$ can be defined that resides in 'k-space', and has units of inverse distance (typically cm^{-1}):

$$\vec{k}(t) = \frac{\gamma}{2\pi} \int_0^t G(\vec{r}, t')dt' \tag{3.35}$$

Neglecting relaxation effects, the signal from Equation 3.31 is now expressed by:

$$s(\vec{k}) = \int \rho(\vec{r})e^{-i(2\pi\vec{k}\vec{r})}d^3r \tag{3.36}$$

The measured signal is therefore the Fourier transform of the effective spin density $\rho(\vec{r})$, and thus $\rho(\vec{r})$ at position ($\vec{r}$) can be obtained with the inverse Fourier transform:

$$\rho(\vec{r}) = \int s(\vec{k})e^{+i(2\pi\vec{k}\vec{r})}d^3r \tag{3.37}$$

In Equation 3.35, the spatial frequency vector $\vec{k}(t)$ was introduced that describes the trajectory through k-space in the presence of magnetic field gradients. Each location in k-space represents a spatial frequency, and its magnitude denotes how much this spatial frequency is represented in the imaged object. A 2D image is described by k-space with two spatial frequency dimensions (k_x and k_y) (Figure 3.3); while a 3D image corresponds to a 3D k-space with an additional dimension (k_z).
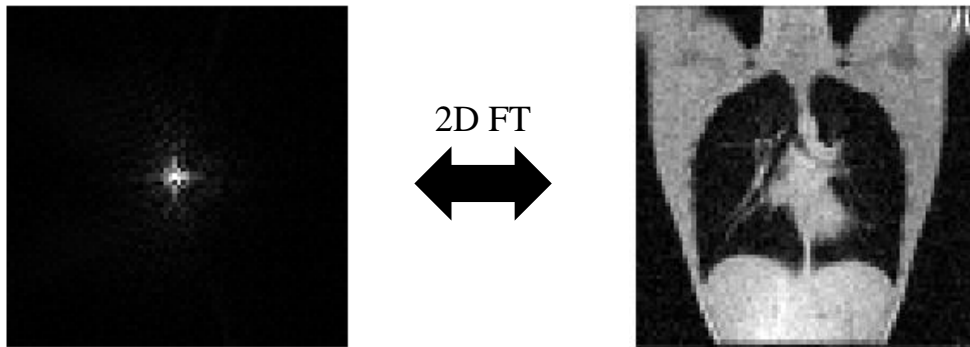
Figure 3.3: Example of 2D k-space (left) and its corresponding image (right) that are related by the 2D Fourier transform (FT). The majority of signal is found in the centre of k-space corresponding to low spatial frequencies.

The application of linear magnetic field gradients on all three axis directions (G_x, G_y, G_z) creates spatial magnetic field variations in the object of interest and results in a controlled change in the frequency or phase of the precessing nuclear spins. This process is termed spatial encoding, and enables the acquisition of the k-space, required for image reconstruction. The different spatial encoding processes for 2D and 3D imaging are discussed in the following sections.

Frequency (read) encoding

Frequency encoding is one method of spatial localisation that assigns a unique Larmor frequency to each spatial location along a gradient direction (conventionally G_x), such that the frequency is linearly related to the spin isochromat location along the gradient direction. The frequency encoding gradient waveform consists of two gradient lobes; a prephasing (dephasing) lobe and a readout gradient lobe. For gradient echo sequences, the two lobes are typically combined with different polarity (G_x in Figure 3.4); while in spin echo sequences, the gradient lobes have the same polarity but are separated by a 180° refocusing pulse.

Figure 3.4: Pulse sequence diagram for frequency encoding on the G_x axis in a gradient echo sequence. Two gradient lobes, the prephasing lobe, and readout lobe, have opposite polarity and are played out after the RF pulse. DAQ corresponds to the position of the data acquisition window. The formation of the gradient echo is shown on the signal axis.
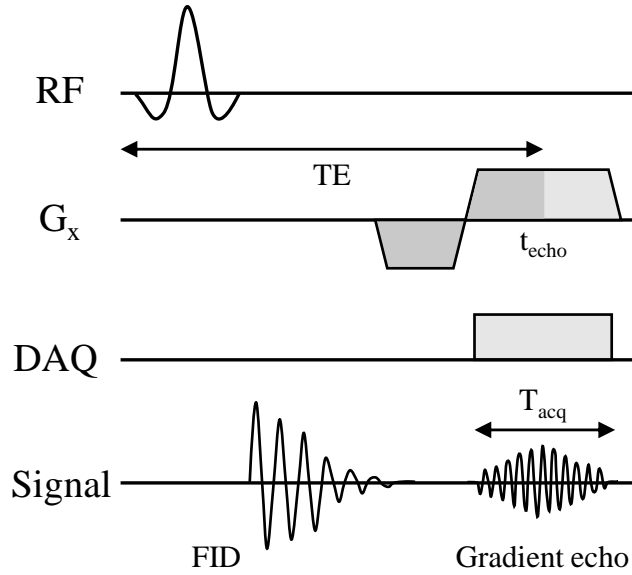
The purpose of the negative prephasing gradient is to dephase spins such that an echo can be formed at the centre of k-space when the positive readout gradient is applied. The readout gradient reverses the accumulated phase to form an echo, such that the peak echo signal (t_{echo}) occurs when the area under the prephasing gradient lobe is cancelled out by the readout (see Figure 3.4), corresponding to the centre of k-space ($k_x = 0$). The duration of data acquisition (T_{acq}) is determined by receiver bandwidth ($\pm BW$) and the number of k-space points along the readout direction (n_x); and can also be described by the sampling or dwell time (Δt) such that:

$$T_{acq} = \frac{n_x}{2BW} = n_x \Delta t \tag{3.38}$$

For a constant readout gradient the spacing in k-space (Δk_x) is given by:

$$\Delta k_x = \frac{\gamma G_x \Delta t}{2\pi} \tag{3.39}$$

and for a given field of view (FOV) (L_x) along the readout direction, the k-space expres-

sion can be described by:

$$\Delta k_x = \frac{1}{n_x \Delta x} = \frac{1}{L_x} \qquad (3.40)$$

The amplitude of the readout gradient lobe (G_x) can therefore be derived by combining Equations 3.38 to 3.40:

$$G_x = \frac{4\pi BW}{\gamma L_x} \qquad (3.41)$$

This relationship implies that for fixed receiver bandwidth, large readout gradient amplitudes are required for smaller FOVs. For a full echo acquisition, t_{echo} is in the centre of the readout gradient; while for partial or fractional echo acquisitions, the readout gradient is applied asymmetrically around t_{echo} to allow fewer points sampled before t_{echo}. These acquisitions can reduce echo time (TE) and exploit redundancies in k-space to synthesise missing k_x data (see Section 3.4).

Phase encoding

The second method for spatial localisation in conventional MR imaging is phase encoding, where linear variations are made to the transverse magnetisation phase in a direction (typically G_y for 2D or G_y and G_z for 3D imaging) that is orthogonal to the frequency encoding direction. Phase encoding is implemented by applying a gradient lobe after the RF pulse (when the magnetisation is in the transverse plane) but before the readout gradient. Phase differences induced by gradients in one direction are permanent, and do not cancel out when the readout gradient is applied. In contrast to frequency encoding where the entire k_x range (corresponding to one line in the k-space) is sampled with one readout gradient, only one phase encoding value can be acquired during one readout. Therefore the acquisitions must be repeated for each desired phase encoding step to fill the required k-space, and this is implemented by varying the area under each phase encoding gradient (see G_y Figure 3.5) for each repetition of the pulse sequence (TR).

To resolve N phase components, N phase encodes are required; typically this is an even number such that phase encoding is symmetric about $k_y = 0$. Assuming sequential phase encoding that starts at the edge of k-space, the location of a specific phase encode is given by:

$$k_y(m) = \left(\frac{N-1}{2} - m\right)\Delta k_y \qquad (3.42)$$

where $m = 0, 1, ..., N-1$, and Δk_y is the phase encoding step size. Similar to Equation 3.40, Δk_y is related by:

$$\Delta k_y = \frac{1}{N\Delta y} = \frac{1}{L_y} \qquad (3.43)$$

Figure 3.5: Pulse sequence diagram for phase encoding on the G_y axis in a gradient echo sequence. Phase encoding gradients are depicted as a stack of different gradient amplitudes representing how each phase encode amplitude corresponds to one k_y line in 2D k-space acquired for each repetition time (TR). Frequency encoding occurs on the G_x axis after phase encoding.
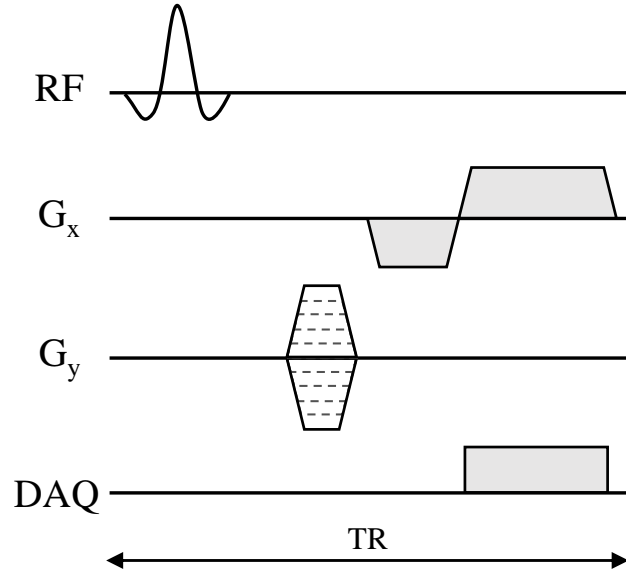
The maximum area of the phase encoding gradient lobe $A_{y,max}$ (when $m = 0$ in Equation 3.42) can be derived from:

$$A_{y,max} = \frac{2\pi}{\gamma}k_{y,max} = \frac{\pi(N-1)}{\gamma L_y} \tag{3.44}$$

In practice, to minimise the TE and TR, phase encoding gradient lobes are designed to be as short as possible. Therefore, $A_{y,max}$ is usually achieved using maximum gradient amplitude and slew rate. For the 2D sequence depicted in Figure 3.5, the full 2D k-space is acquired in $N \times TR$. Phase encoding can also be extended to the G_z axis to enable 3D acquisitions; where the number of required phase encodes to cover 3D k-space is now $N_y \times N_z$. It is possible to avoid the N_z times increase in acquisition time by selectively imaging 2D slices using slice selection gradients, and this is described in the following section.

Slice selection

Slice encoding uses a slice selection gradient in combination with a spatially selective RF pulse to selectively sample an image section or slice. The simplest selective RF pulse is a sinc waveform, that has a rectangular/boxcar frequency profile after the Fourier transform in the spatial domain. Typically slice selection occurs on the z axis, and when the RF pulse is played out concurrently with a constant slice select gradient (G_z), the range of frequencies (bandwidth, Δf) excited can be translated into range of spatial locations (Δz), corresponding to the desired slice thickness (Figure 3.6).

Assuming a RF pulse that is played during the plateau of the constant slice select gradient, the change in Larmor frequency in relation to position along z is described by:

$$f(z) = \frac{\gamma}{2\pi}G_z z \tag{3.45}$$
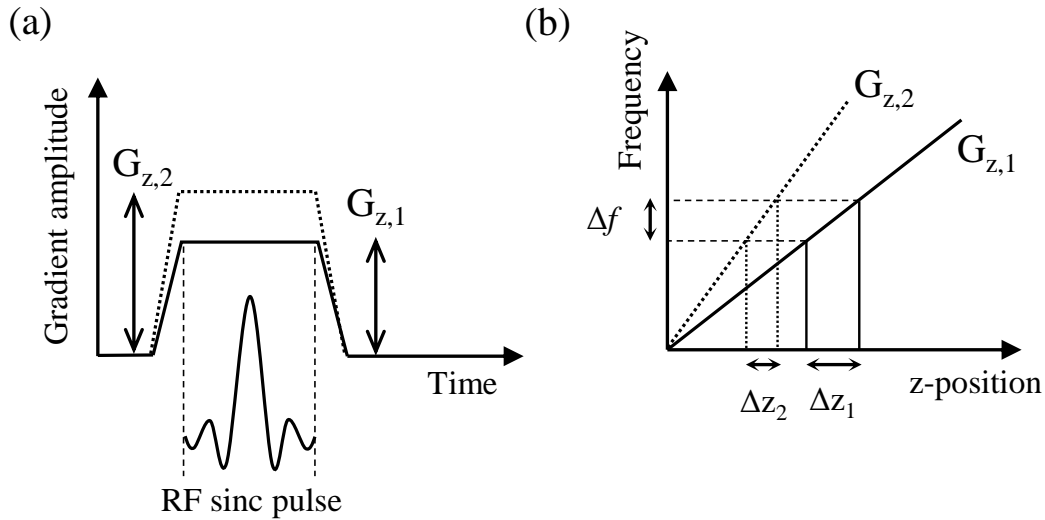
Figure 3.6: Diagram for slice select encoding on the G_z axis. (a) A selective RF sinc pulse is applied concurrently during the plateau of a slice selection gradient ($G_{z,1}$ or $G_{z,2}$). (b) The bandwidth of this RF pulse (Δf) encodes a range of spatial locations (Δz_1 or Δz_2) that form the image slice. For a given RF pulse bandwidth, the amplitude of the slice selection gradient controls the thickness of the image slice.

For a slice located at the gradient iso-centre, the bandwidth (Δf) of RF pulse frequencies and slice select gradient amplitude is related to the spatial range (Δz) by:

$$\Delta z = \frac{2\pi \Delta f}{\gamma G_z} \tag{3.46}$$

Therefore, for a fixed RF pulse bandwidth, a thinner slice can be obtained by using a larger slice select gradient amplitude. If the desired slice is located at an offset from the gradient iso-centre (δz), the frequency of the RF pulse must be offset by a factor δf from the Larmor frequency such that:

$$\delta z = \frac{2\pi \delta f}{\gamma G_z} \tag{3.47}$$

The slice selection gradient causes some phase dispersion (dephasing) across the image slice that leads to signal loss. To compensate for this, a slice rephasing gradient lobe of opposite polarity is typically applied following the slice selection gradient. The area of the slice rephasing is calculated based on the RF pulse (half of the RF pulse width) and corresponds to half the area of the slice selection gradient.

A combination of the frequency, phase and slice selection encoding is used in MR imaging. A 2D sequence utilises slice selection to encode slices of thickness Δz with frequency and phase encoding in the other two dimensions; while a 3D sequence has phase encoding on an additional dimension and can be implemented with or without slice select encoding. The choice of either 2D or 3D acquisition is predominantly dependent on the desired slice resolution, spatial coverage needs, and acquisition time constraints. Equation 3.46 indicates that the

thickness of a slice select 2D image slice can be limited by maximum gradient amplitude and RF bandwidth, therefore 3D acquisitions typically have smaller Δz than 2D acquisitions. However, this comes at the expense of increased acquisition time because the entire FOV of the object needs to be acquired to avoid aliasing. 3D acquisitions also typically involve the excitation of the whole FOV, therefore the measured signal is higher than in 2D, and can avoid slice bleeding effects characterised by imperfect RF pulse excitation profiles.

The signal of an MR acquisition is proportional to the image voxel volume (Δx, Δy, and Δz) and any sequence-dependent relaxation factors (F_{seq}). The source of noise in MR acquisitions is random fluctuations in electrical currents from the MR coil and the conducting tissues of the body. These fluctuations in current generate small magnetic fields and induce a noise voltage in the coil. The amount of inherent noise in an acquisition is proportional to the bandwidth (BW), number of k-space samples (N_x, N_y, and N_z), and the number of signal averages (NSA). The signal to noise ratio (SNR) per voxel of a 2D MR acquisition can therefore be represented by:

$$SNR_{2D} \propto \frac{\Delta x \, \Delta y \, \Delta z \, F_{seq} \, \sqrt{N_x \, N_y \, NSA}}{\sqrt{BW}} \tag{3.48}$$

For 3D acquisitions, the signal has an extra N_z term representing the additional phase encoding:

$$SNR_{3D} \propto \frac{\Delta x \, \Delta y \, \Delta z \, F_{seq} \, \sqrt{N_x \, N_y \, N_z \, NSA}}{\sqrt{BW}} \tag{3.49}$$

and it can be seen that the 3D acquisition SNR is $\sqrt{N_z}$ times larger than the 2D equivalent. However, the SNR per time is the same between 2D and 3D acquisitions, as N_z separate acquisitions are required for 3D.

3.2.2   Discrete sampling

The spatial frequency vector $\vec{k}(t)$ describes a continuous trajectory through k-space that would require an infinite number of samples to fully describe its trajectory. In practice, this is not feasible, and discrete sampling of a finite number of measurements is made at a sampling interval (Δk). Discrete sampling of k-space is achieved through the multiplication of a sampling (comb) function with the continuous signal $s(k)$:

$$s_{acq}(k) = s(k) \cdot comb(k) \tag{3.50}$$

where the comb function is equal to a sum of n Dirac delta functions (δ) evenly spaced by Δk:

$$comb(k) = \Delta k \sum_n \delta(k - n\Delta k) \tag{3.51}$$

The process of discrete sampling is demonstrated in Figure 3.7 where a sinc function is shown in k-space (Fig. 3.7a), and its Fourier transform is a rectangular function (Fig. 3.7d). When k-space is multiplied by a comb function with a sampling interval of Δk (Fig. 3.7b), a discrete sampled version of the sinc function is obtained (Fig. 3.7c). The Fourier transform of the comb function is the comb function; therefore in image space, the resulting discrete sampled rectangular object (Fig. 3.7f) is obtained with the convolution of the Fourier transform of the rectangular function and the comb function (Fig. 3.7e). By definition the Fourier transform operates on continuous functions, therefore a discrete Fourier transform is derived from the Fast Fourier transform (FFT) to reconstruct images acquired from the discrete sampled k-space.
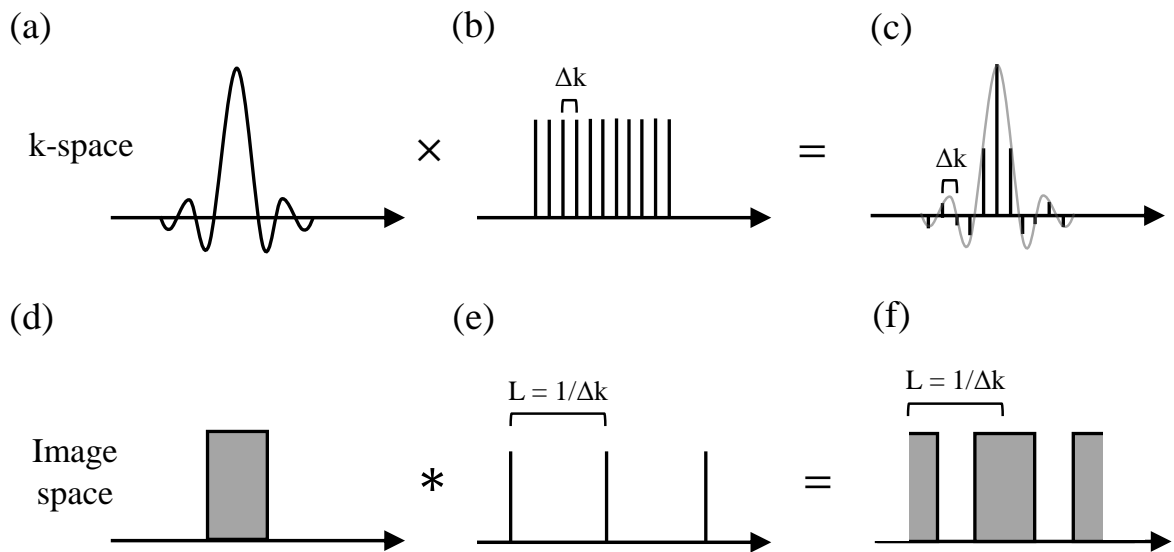
Figure 3.7: Depiction of the process of discrete sampling of a sinc function.

The periodic nature of the comb function indicates that the reconstructed images is also periodic, and the spatial interval of the image (L) is inversely related to the sampling interval or spacing of k-space (Δk):

$$L = \frac{1}{\Delta k} \tag{3.52}$$

Therefore, the size of L denotes the field of view (FOV) of the image and if L is smaller than the object then images of adjacent periods will overlap causing aliasing (Figure 3.8).
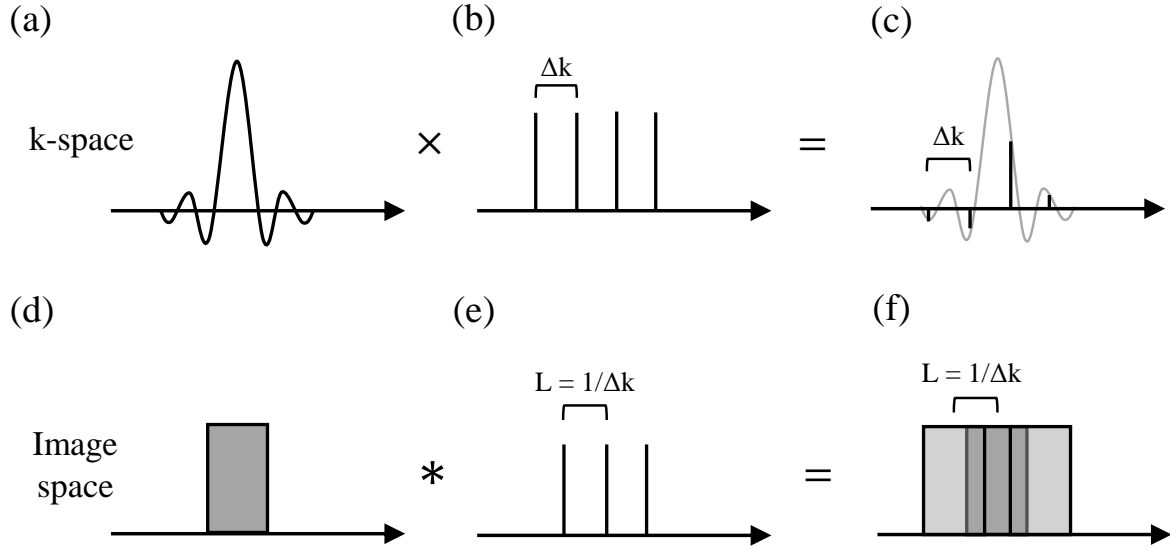
Figure 3.8: Depiction of image aliasing with discrete sampling. Compared to Figure 3.7, the sampling interval Δk is larger corresponding to a smaller FOV (L). L is now smaller than the rectangular object causing overlapping of adjacent periods and aliasing.

The Nyquist criterion states aliasing is avoided when the object size (A) is smaller than L:

$$\Delta k = \frac{1}{L} < \frac{1}{A} \tag{3.53}$$

Nyquist criterion is applicable on all three spatial encoding directions. In the frequency encoding direction, for a constant readout gradient (G_x), Equation 3.39 can be related to the Nyquist criterion by:

$$\Delta k_x = \frac{\gamma G_x \Delta t}{2\pi} = \frac{1}{L_x} < \frac{1}{A_x} \tag{3.54}$$

For a constant G_x, the receiver bandwidth (BW_x) determines the range of precession frequencies and Equation 3.54 can be rewritten as:

$$BW_x = \frac{1}{\Delta t} = \frac{\gamma G_x L_x}{2\pi} > \frac{\gamma G_x A_x}{2\pi} \tag{3.55}$$

BW_x is the full receiver bandwidth (i.e $\pm BW$), and satisfies the Shannon-Nyquist theorem that states if the sampling rate is at least twice the size of the bandwidth there is no information loss. In the phase encoding direction(s), the duration of phase gradient lobe (τ_y) is fixed and the area under the gradient lobe is varied by changing the amplitude (ΔG_y). To satisfy Nyquist criterion:

$$\Delta k_y = \frac{\gamma \Delta G_y \tau_y}{2\pi} = \frac{1}{L_y} < \frac{1}{A_y} \tag{3.56}$$

Equation 3.56 can also be re-arranged to:

$$\Delta G_y = \frac{2\pi}{\gamma \tau_y L_y} < \frac{2\pi}{\gamma \tau_y A_y} \tag{3.57}$$

3.2.3 MR imaging pulse sequences

Cartesian MR imaging sequences can be split into two main branches: gradient echo and spin echo sequences. This section aims to provide a brief introduction to the common MR imaging sequences used in this work.

Gradient echo

Gradient echo sequences are characterised by small flip angles that enable short repetition times (TR) between individual phase encodes. A common gradient echo sequence is the spoiled gradient echo (SPGR) sequence; a typical 2D SPGR pulse sequence timing diagram is shown in Figure 3.9. A slice selection gradient (G_{SS}), applied during the low flip angle RF pulse, is followed by a rewinder gradient. Phase encoding (G_{PE}) occurs on one axis direction, and is then followed by frequency encoding (G_{FE}) on an orthogonal axis direction. Finally, the remaining transverse magnetisation is dephased with the application of a large spoiling gradient such that transverse coherence between acquisitions is removed. Spoiling gradients can be applied on all axis directions, but in practice, spoiling on one axis direction is usually sufficient. The amplitude of the spoiling gradient can be also varied to avoid any remaining coherence, and this is termed gradient spoiling.
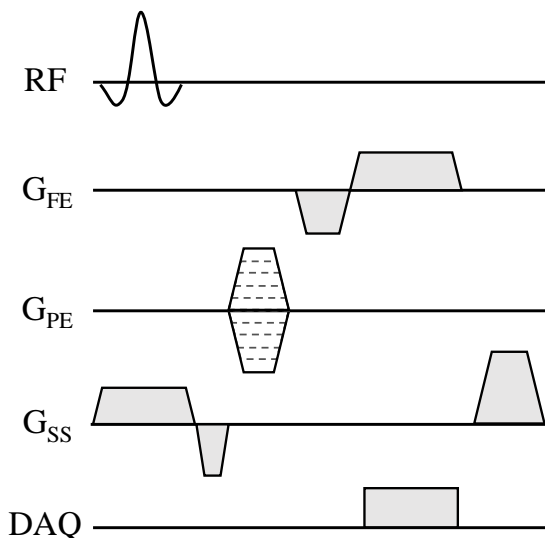
Figure 3.9: 2D spoiled gradient echo (SPGR) pulse sequence diagram. A small flip angle is used to tip the magnetisation into the transverse plane, and a spoiler gradient is employed after frequency encoding to spoil the remaining transverse magnetisation.

The short TR times in gradient echo sequences are usually shorter than T_1, such that the longitudinal magnetisation does not fully recover after TR. This allows, after a few RF pulses, the proportion of longitudinal magnetisation excited to be equivalent to the longitudinal

magnetisation recovered from T_1, and a steady state longitudinal magnetisation is reached. For a SPGR sequence, when the longitudinal and transverse magnetisation is considered, the steady state signal (S_{SPGR}) is given by:

$$S_{SPGR} = \frac{M_0 \sin\theta (1 - e^{-TR/T_1}) e^{-TE/T_2^*}}{1 - \cos\theta e^{-TR/T_1}} \tag{3.58}$$

where the S_{SPGR} is dependent on flip angle (θ) for a fixed TR and T_1. The θ that provides the maximum signal is defined as the Ernst angle (θ_E), and lies between 0° and 90° when TR$<T_1$. θ_E can be calculated by:

$$\theta_E = \arccos(e^{-TR/T_1}) \tag{3.59}$$

An alternative gradient echo based sequence is the balanced steady state free precession (bSSFP) sequence (Figure 3.10), that re-uses or recycles some of the remaining transverse magnetisation instead of spoiling it. In bSSFP all gradients on the three axes are balanced before the next RF pulse, and partial rephasing of the transverse magnetisation occurs leading to steady state of the transverse magnetisation, in conjunction with the longitudinal magnetisation. This approach leads to comparatively higher signal than SPGR sequences due to the more efficient use of the transverse magnetisation. The RF pulse is typically alternated to yield optimal steady state signal at resonance frequency. bSSFP sequences are however very sensitive to magnetic field inhomogeneity, and this manifests in the appearance of banding artefacts. The accumulation of phase from field inhomogeneities is proportional to TR, therefore bSSFP sequences typically have very short TRs to minimise banding artefacts.
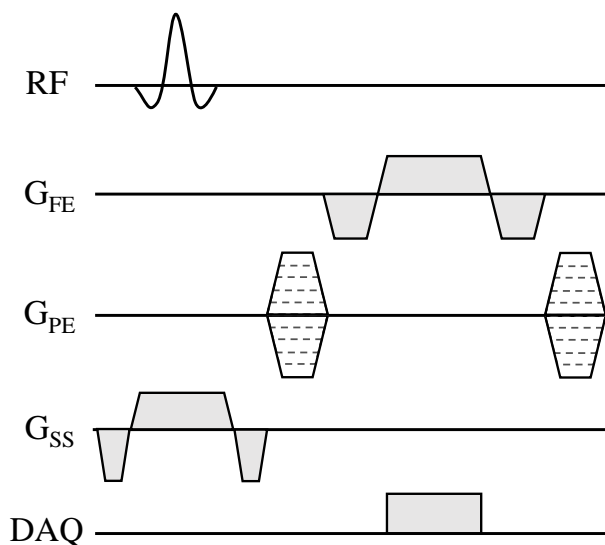
Figure 3.10: 2D balanced steady state free precession (bSSFP) pulse sequence diagram. Gradients on each axis direction are balanced to enable partial rephasing of the transverse magnetisation.

Spin echo

The second main branch of MR imaging sequences are spin echo sequences that use at least two RF pulses, an excitation and a refocusing pulse, to generate a spin echo. Typically, a

90° is used for excitation, and a 180° refocusing pulse is then applied after phase encoding. An example spin echo pulse sequence timing diagram is shown in Figure 3.11. In contrast to the SPGR sequence in Figure 3.9, the prephasing frequency encoding lobe of the spin echo sequence has positive polarity, and is separated from the readout gradient by the 180° refocusing pulse. The echo in spin echo sequences is therefore RF-induced; while in gradient echo it is gradient-induced.
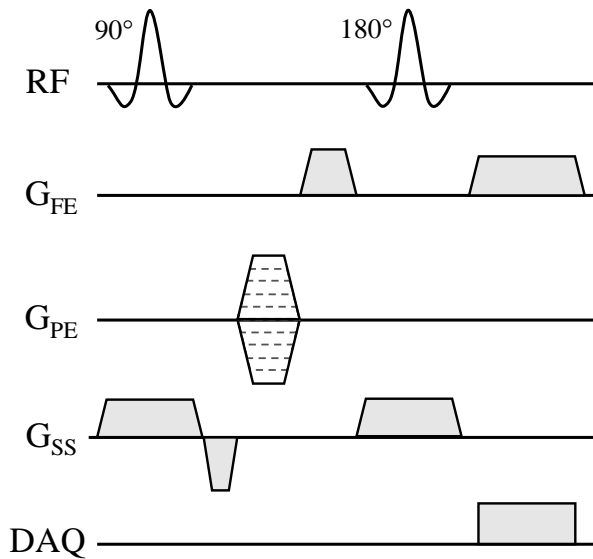
Figure 3.11: 2D spin echo pulse sequence diagram. An additional 180° refocusing pulse is applied before the frequency encoding readout gradient to rephase the spins such that an echo can be formed.

The application of the refocusing pulse has the advantage of reversing spin dephasing from magnetic field inhomogeneities or susceptibility differences, therefore spin echo sequences are T_2-weighted, in contrast, to the T_2^*-weighting of gradient echo sequences. Spin echo sequences also offer the additional advantage of specific contrast weighting through the selection of sequence timing parameters (TE and TR). For a short TE, a short TR will result in T_1-weighting; while a long TR will lead to spin density-weighted images. Finally, a long TE and TR will result in T_2-weighted images. However, the larger flip angles used in spin echo sequences requires more RF power that may not always be achievable due to patient safety concerns or hardware limitations.

3.3   Hyperpolarised gas MRI

In vivo human lung images from inhaled hyperpolarised noble gas isotopes were first demonstrated approximately 20 years ago [2–4]. Through advancements in optical polarisation and MR acquisition techniques, hyperpolarised gas MRI is now a robust imaging technique capable of the functional assessment of various aspects of lung physiology in a range of pulmonary diseases. This section provides an overview of the technical methods and considerations for hyperpolarised gas MR imaging of the lungs.

Helium-3 (^{3}He) and xenon-129 (^{129}Xe) are stable, non-radioactive, noble gas isotopes that have a nuclear spin 1/2 and relatively high gyromagnetic ratios; therefore are sensitive to NMR techniques. The NMR properties of ^{3}He and ^{129}Xe, in comparison to ^{1}H, are summarised in Table 3.1. The T_1 of pure ^{3}He and ^{129}Xe gases are very long (744, and 55 hours at room temperature and atmospheric pressure, respectively) [156]. However, in the presence of paramagnetic oxygen (i.e. when inhaled into the lungs), the T_1 of both gases reduces to tens of seconds. The T_1 of ^{3}He in the lungs is demonstrated to be inversely proportional to the oxygen concentration (Equation 3.65) [121]. The chemically inert nature of ^{3}He alongside its larger gyromagnetic ratio (in relation to ^{129}Xe) provides ^{3}He with inherent sensitivity over ^{129}Xe for probing pulmonary structure and function down to the alveolar length scale.

Table 3.1: Summary of physical properties of ^{3}He and ^{129}Xe, in comparison to ^{1}H.

Properties	**^{1}H**	**^{3}He**	**^{129}Xe**
Isotope abundance (%) [a]	99.99	1.37×10^{-4}	26.44
Nuclear spin, I [a]	1/2	1/2	1/2
Gyromagnetic ratio, γ (MHz/T) [a]	42.58	-32.43	-11.78
Spin density, (10^{19} atoms/cm^3) [b]	6690	2.37	2.37
Chemical shift range, (ppm) [c]	-	~0.8	~250
Self diffusion coefficient, D (cm^2/s) [d,e]	2×10^{-5}	2.05	0.062
Free diffusion coefficient (air), D_0 (cm^2/s) [e]	-	0.86	0.14
Ostwald solubility in water [f]	-	0.0098	0.083
Ostwald solubility in blood [f]	-	0.0083	0.146

[a] From ref [156].

[b] From ref [88], proton density in water.

[c] From ref [157, 158], chemical shift offset from gaseous phase resonance (0 ppm).

[d] From ref [159], self diffusion coefficient of water at 25°C.

[e] From ref [89], assuming gas at 1 atm and 37°C and air mixture of 79% N_2 and 21% O_2.

[f] From ref [160], for gas at 1 atm and 37°C.

However, the rapidly increasing cost and dwindling supply of ^{3}He gas, associated with its very low natural abundance (1.37×10^{-4} %), limits the widespread application in clinical settings. ^{129}Xe, in contrast, has a non-negligible natural abundance (0.087 ppm in the atmosphere [161] of which 26.44% is ^{129}Xe), therefore is seen as the more cost-effective hyperpolarised gas isotope. ^{129}Xe also exhibits solubility in the blood and tissue, and coupled with a large chemical shift range, can be used to probe additional aspects of lung function related to the dissolved environment (i.e. gas exchange) that ^{3}He cannot. Despite the signal disadvantage of ^{129}Xe, related to its approximately three-fold smaller gyromagnetic ratio, recent developments in pulse sequence acquisition and polarisation strategies have demonstrated equivalent structural and functional information can be obtained with both hyperpolarised gases; enabling the transition from ^{3}He to the clinically viable ^{129}Xe for future pulmonary studies.

3.3.1 Spin exchange optical pumping

In Table 3.1, the small spin densities of ^{3}He and ^{129}Xe in relation to ^{1}H in water, permits only very small MR signals in their thermal equilibrium state. However, through optical pumping polarisation techniques, the MR signal can be enhanced or 'hyperpolarised' by a few orders of magnitude. Optical pumping can be classified into two main techniques; spin exchange optical pumping (SEOP) [162], and meta-stability exchange optical pumping (MEOP) [163]. SEOP is currently the more popular technique due to its ability to polarise both ^{3}He and ^{129}Xe, and its reliability in extraction of large volumes of polarised gases for in vivo MRI applications. The following section provides an introduction to the SEOP technique only; for a more detailed summary of SEOP and MEOP, the reader is referred to the reviews by Goodson [164] and Oros and Shah [161].

Laser optical pumping involves utilising circularly polarised light at specific wavelengths to drive the electronic spins of certain atoms into non-Boltzmann energy distributions. In SEOP, the electronic spin polarisation of an alkali metal atom vapour (e.g. rubidium) is transferred to the nuclear spin of noble gas isotopes through collision and spin exchange [162]. This two step process of SEOP is depicted in Figures 3.12 and 3.13. In step one, the spins of unpaired electrons of rubidium (Rb) are polarised by a circularly polarised laser (σ^+) tuned to the wavelength of 794.7 nm. This wavelength corresponds to the D_1 transition resonance of Rb, and drives the electron spins from the ground state sublevel ($5^2S_{1/2}$, $m = -1/2$) to the excited state sublevel ($5^2P_{1/2}$, $m = +1/2$). The electron spins in the excited state sublevels mix and equalise through collisions, and relax to their respective ground state sublevels. This causes a net accumulation of polarised electron spin in the ground state sublevel ($m = +1/2$).
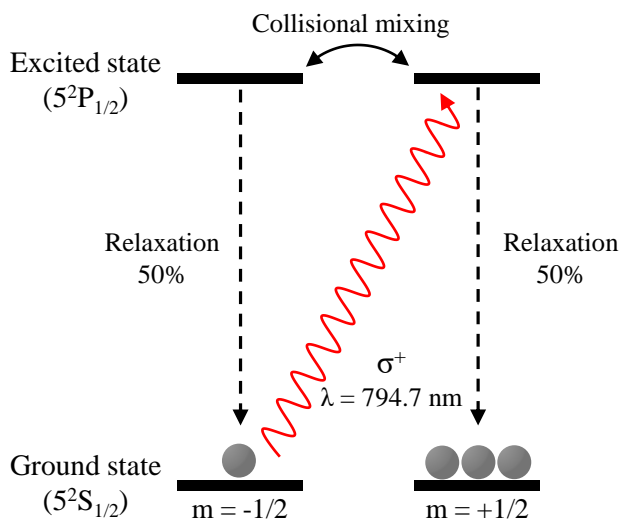
Figure 3.12: Optical pumping process for rubidium (Rb) electron polarisation. Vaporised Rb electrons are transferred from the ground state ($5^2S_{1/2}$) to an excited state ($5^2P_{1/2}$) through the interaction with polarised laser light with a wavelength (λ) of 794.7 nm.

In the second step, the electronic spin polarisation of Rb electrons can be transferred to ^{3}He or ^{129}Xe nuclei by spin exchange through either binary or 3-body collisions. In binary collisions, molecules are bound for 10^{-12} s and dominate Rb-^{3}He spin exchange (Figure 3.13a); while 3-body collisions involve a third molecule (N_2) to form van der Waal molecules

Figure 3.13: Spin exchange process between Rb electrons and noble gas isotopes. (a) Rb-^{3}He spin exchange typically occurs through binary collisions. (b) For the heavier isotope ^{129}Xe, spin exchange can occur through the formation of van der Waal molecules from 3-body collisions between Rb, ^{129}Xe, and N$_2$ molecules.
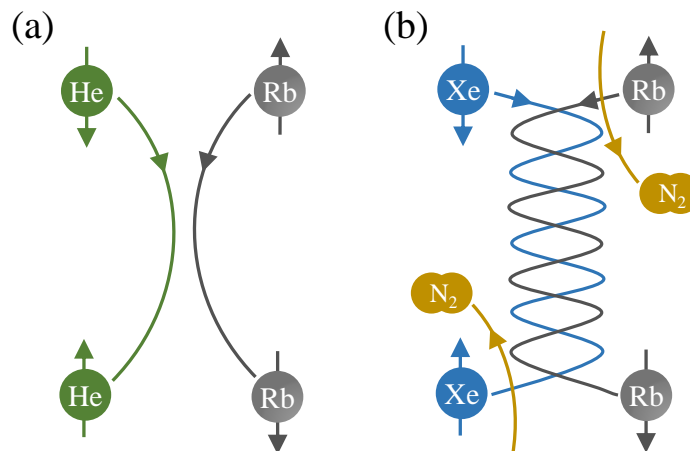
that are bound for a longer time-scale (10^{-8} s), and are typical for Rb-^{129}Xe spin exchange (Figure 3.13b) [162]. The size of the respective electron clouds of ^{3}He and ^{129}Xe directly influences the probability of spin exchange interactions; therefore, SEOP takes longer for ^{3}He and occurs over many hours [165]. While the probability of spin exchange interaction is increased for ^{129}Xe, a corresponding increase in spin destruction probability also occurs. In order to minimise polarisation destruction through Rb-^{129}Xe collisions, gas mixtures of 1–3% ^{129}Xe are balanced with buffer gases (N$_2$ or ^{4}He) for ^{129}Xe SEOP [166, 167]. The polarised ^{129}Xe is subsequently cryogenically separated from the buffer gases with liquid nitrogen. After a required period of time (minutes to hours), the accumulated frozen ^{129}Xe is sublimated and the hyperpolarised ^{129}Xe gas can be administered.

The nuclear polarisation of ^{3}He or ^{129}Xe after a given duration of SEOP (t) can be described by [164]:

$$P(t) = \frac{\rho_{SE}}{\rho_{SE} + \rho_{Loss}} P_{Rb}[1 - e^{-(\rho_{SE}+\rho_{Loss})t}] \qquad (3.60)$$

where P_{Rb} is the electron spin polarisation of Rb, ρ_{SE} is the rate of spin exchange between the ^{3}He or ^{129}Xe nuclei and Rb electrons, and ρ_{Loss} is the rate of noble gas polarisation loss associated with relaxation mechanisms (e.g. wall collisions). Initial applications of SEOP could only produce hyperpolarised gases with low polarisation ($\leq 5\%$) and in small quantities. However, advancements in polarisation technology (e.g. high powered narrow linewidth lasers) have enabled hyperpolarised gases to be produced at the rate and polarisation sufficient for in vivo imaging exams. Prototype commercial ^{3}He polarisers are capable of producing approximately 1L of hyperpolarised ^{3}He per day at polarisation levels ranging from 25–40%; while custom home-built polarisers have demonstrated the feasibility of polarising 3L of ^{3}He per day at 50–60% polarisation [168].

Due to the continuous flow and accumulation process of ^{129}Xe SEOP, the final polarisation of ^{129}Xe after sublimation (P_{Xe}^f) is dependent on the flow rate of the gas mixture in the optical pumping cell (Q_{Xe}), polarisation of ^{129}Xe exiting the cell, and solid state ^{129}Xe T_1

decay [166]. The dose equivalence rate ($DE_{rate} = f P_{Xe}^f Q_{Xe}$) [169] is a recently proposed metric for evaluating polariser performance and provides an expression representing the ^{129}Xe volume production rate of 100% polarised ^{129}Xe from 100% enriched ^{129}Xe ($f = 1$) that is derived from the respective polariser operation parameters (P_{Xe}^f and Q_{Xe}). The majority of polarisers used in ^{129}Xe imaging studies have a DE_{rate} ranging from 100 to 200 ml/h [169]; corresponding to approximately 400 to 800 ml of $P_{Xe}^f \sim$25% per hour. Recent ^{129}Xe polariser development has demonstrated the feasibility of on demand ^{129}Xe production ($DE_{rate} \sim$1000 ml/h; 300 ml of ^{129}Xe at $P_{Xe}^f \sim$30% in 5 mins) for clinical ^{129}Xe MR imaging [170]. All ^{129}Xe imaging acquired in this work used this ^{129}Xe polariser (Figure 3.14) and was operated at the $DE_{rate} \sim$1000 ml/h.
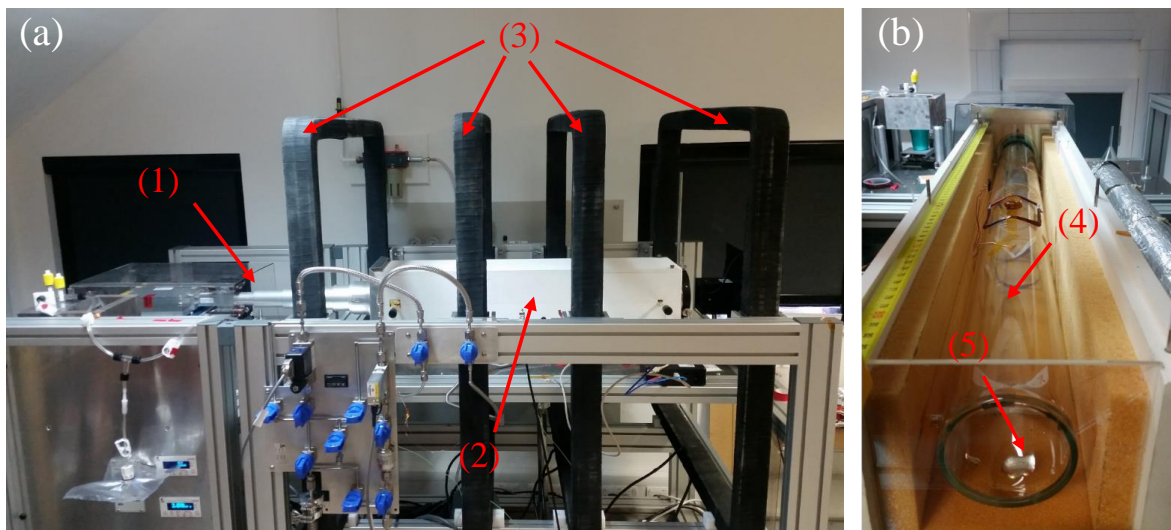
Figure 3.14: (a) Photo of ^{129}Xe spin exchange optical pumping polariser used in this work. (1) Laser diode array (170 W, 794.77 nm wavelength) (BrightLock 200W, QPC, CA, US); (2) temperature-controlled ceramic oven. (3) B_0 coils. (b) Ceramic oven with the lid off. (4) SEOP cell (Volume = 3500 ml, 7.5 cm diameter, 80 cm length); (5) the pool of rubidium is visible at the cell gas entrance. Gas mixture used throughout: 3% Xe, 87% He, 10% N_2.

3.3.2 Considerations for hyperpolarised gas MRI

Hardware considerations

The available ^{3}He or ^{129}Xe polarisation from SEOP is independent of the static magnetic field (B_0) strength and hyperpolarised gas imaging in human lungs has been demonstrated at B_0 ranging from 3 mT [171] to 3 T [172]. The respective T_2^* of ^{3}He and ^{129}Xe is however dependent upon B_0 [119, 120], with shorter T_2^* times observed at higher field strengths as a result of the bulk susceptibility difference between the microscopic air and tissue interfaces within the lungs. This also manifests as increased B_0 inhomogeneity and susceptibility artefacts at higher field strengths [119]. While low field imaging may seem promising, due to less susceptibility artefacts, the majority of conventional clinical (^{1}H)

MR imaging is performed on 1.5 T and 3 T scanners, and as such multi-nuclear imaging is predominantly focused on these field strengths.

MR imaging with hyperpolarised gases requires separate transmit and receive radiofrequency (RF) coils to be tuned to the respective Larmor frequency of the gas. Typical coils used for lung imaging are either vest or birdcage coils; both of which cover the entire chest area of the subject. Hyperpolarised gas MRI is very sensitive to flip angle, therefore, it is desirable for the transmit coil to provide a uniform flip angle across the imaging field of view. Birdcage coils provide more B_1 homogeneity than vest coils [173], but are generally less power efficient and less sensitive for reception. A combination of a birdcage transmit coil with a multi-channel receiver array is a possible compromise that offers increased receive sensitivity and the possibility of parallel imaging (see Section 3.4) for accelerated acquisitions [174].

Pulse sequence considerations

In conventional proton MRI, T_1 is the time constant for the recovery of the longitudinal magnetisation. However, for hyperpolarised gas MRI, T_1 is the 'recovery' to thermal equilibrium polarisation; therefore the time constant is representative of polarisation decay. The short T_1 coupled with patient breath-hold limits further constrains in vivo acquisitions, and requires short hyperpolarised gas MRI pulse sequences. Furthermore, the induced hyperpolarisation is not renewable; as such, pulse sequences are optimised to effectively utilise this finite initial magnetisation (M_0) for high SNR imaging. The most common pulse sequence for hyperpolarised gas MRI is the SPGR sequence (Figure 3.9) with constant low flip angles to slowly deplete the magnetisation. For a series of RF pulses ($n = 1$ to N), a portion of the longitudinal magnetisation (M_z) is consumed with each RF pulse. The M_z for the nth RF pulse with a flip angle (α) is:

$$M_z(n) = M_0(\cos \alpha)^{n-1} \tag{3.61}$$

and the corresponding transverse magnetisation (M_{xy}) decays according to:

$$M_{xy}(n) = M_0(\cos \alpha)^{n-1} \sin \alpha \, \exp[-(n-1)TR/T_1] \tag{3.62}$$

The T_1 decay is assumed to be negligible, because typically the $TR << T_1$ for hyperpolarised gas experiments. For sequential phase encoding, the optimal flip angle (α_{opt}) that maximises the signal at the centre of k-space ($n = N/2$) can be derived from the differentiation of Equation 3.62 and is given by [175]:

$$\alpha_{opt} = \tan^{-1}\left(\frac{1}{\sqrt{N/2 - 1}}\right) \tag{3.63}$$

The decay in magnetisation as a function of RF pulse number imposes a *k*-space filter on the data in the phase encoding direction leading to image blurring or signal attenuation [175]. The specific phase encoding trajectory determines the shape of the *k*-space filter. Figure 3.15 illustrates this with *k*-space filter profiles for sequential and elliptical-centric phase encoding of a 3D SPGR sequence using a constant flip angle (2°). A centric or elliptical-centric encoding order will result in higher SNR at the expense of image blurring and a *k*-space filter that is symmetrical around $N/2$; while sequential encoding results in lower SNR but fine structures in the image are preserved.

Sequential phase-encoding   Elliptical-centric phase-encoding
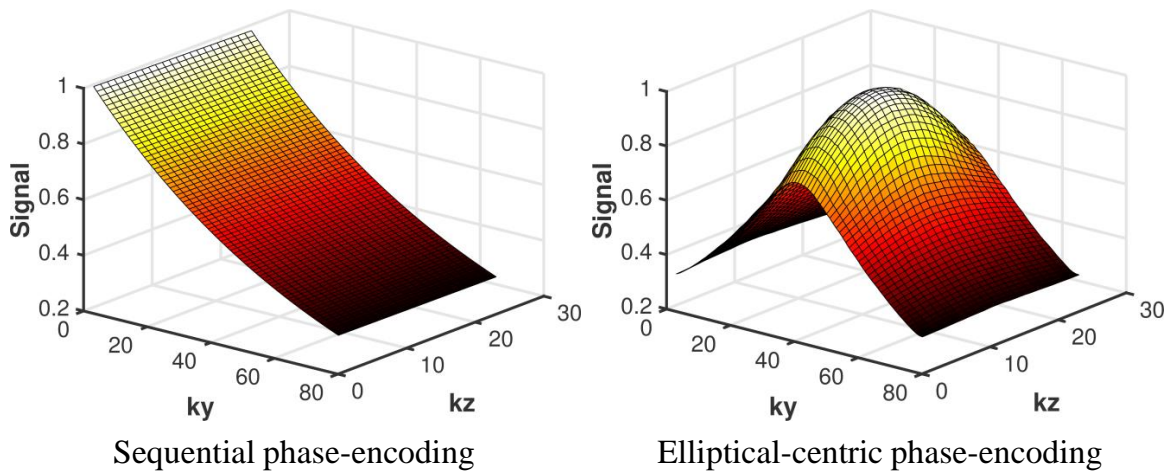
Figure 3.15: *k*-space filter profiles for sequential and elliptical-centric phase encoding of a 3D SPGR sequence ($k_y = 78$, $k_z = 24$) with a constant flip angle of 2°. The flip angle was selected such that ∼30% of the initial magnetisation remains at the end of the acquisition.

The *k*-space filtering effects can be minimised by maintaining a constant M_{xy} through a variable flip angle (VFA) approach by increasing the flip angle for each RF pulse [176]. The flip angle for the *n*th RF pulse can be calculated by:

$$\alpha_n = \tan^{-1}(\frac{1}{\sqrt{N-n}}) \tag{3.64}$$

This VFA approach is in theory the optimum strategy for SPGR sequences, however, RF amplifier limitations may constrain the use of high flip angles ($\alpha_N = 90°$) and a precise flip angle calibration and a homogeneous transmit coil is required to ensure the whole *k*-space is acquired before all available magnetisation is depleted.

In SPGR sequences, the residual transverse magnetisation is spoiled, but sequences such as balanced steady state free precession (bSSFP) allow for the refocusing and recycling of the residual transverse magnetisation. Hyperpolarised gas MR images acquired with bSSFP can use higher flip angles that lead to increased image SNR [177]. However, due to high diffusivity of ^{3}He or ^{129}Xe (in comparison to ^{1}H, see Table 3.1), pulsed gradient diffusion attenuation of the transverse magnetisation can reduce the effective T_2 in bSSFP

imaging. The majority of this diffusion attenuation occurs from the readout gradient and can be derived from Equations 3.75 and 3.78.

3.3.3   Imaging techniques

This section provides an overview of the imaging techniques utilised in hyperpolarised gas MRI to probe lung function and structure. Techniques for imaging the gas-phase will be considered only, and diffusion-weighted imaging with hyperpolarised gases is discussed in Section 3.5.1. For a review of dissolved-phase imaging techniques for hyperpolarised ^{129}Xe, the reader is referred to the following reviews [178, 179].

Static ventilation imaging

The simplest and most common technique for hyperpolarised gas MRI is static ventilation imaging where the distribution of the inhaled gas during breath-hold is used to visualise lung ventilation and homogeneity. Unventilated regions of the lung appear as hyperpolarised gas signal void and directly correspond to regional ventilation abnormalities. High resolution images (4–5 mm^3) of lung ventilation can now be routinely acquired in a single breath-hold using 2D or 3D SPGR or bSSFP sequences. As mentioned previously, bSSFP sequences provide an image SNR advantage over SPGR through the use of higher flip angles [177]. Example ^{3}He bSSFP ventilation images (Figure 3.16) acquired from a range of patients demonstrates differences in ventilation distribution and heterogeneity associated with different pulmonary diseases.

Ventilation distribution can be quantified through either an index or percentage ventilated volume (VV%) or its reciprocal measure – the ventilation defect percentage (VDP); where VV% + VDP = 100% [180]. Structural ^{1}H lung images are typically acquired, in separate- or same-breath [181] acquisitions, in conjunction with ventilation images to provide additional information of the lung cavity volume to aid the calculation of VV% or VDP. These quantitative metrics of lung ventilation demonstrate good same-day and 1-week repeatability [182, 183], and significant correlation with spirometry in normal and smoker volunteers [180], and patients with asthma [184], cystic fibrosis (CF) [185], and chronic obstructive pulmonary disease (COPD) [186]. ^{3}He ventilation MRI has also been used to assess response to treatment [183, 187], and longitudinal studies suggest increased sensitivity, when compared to spirometry, in detecting disease progression [188, 189].

While VV% or VDP are robust metrics of lung ventilation, they do not provide a quantitative measure of lung ventilation heterogeneity. Several analysis techniques have been proposed to quantify regional heterogeneity on a voxel-by-voxel basis including calculation of the coefficient of variation of voxel signal [190, 191] or linear binning [192]. Advancements in imaging and polarising techniques have enabled static ventilation imaging with ^{129}Xe to be acquired with
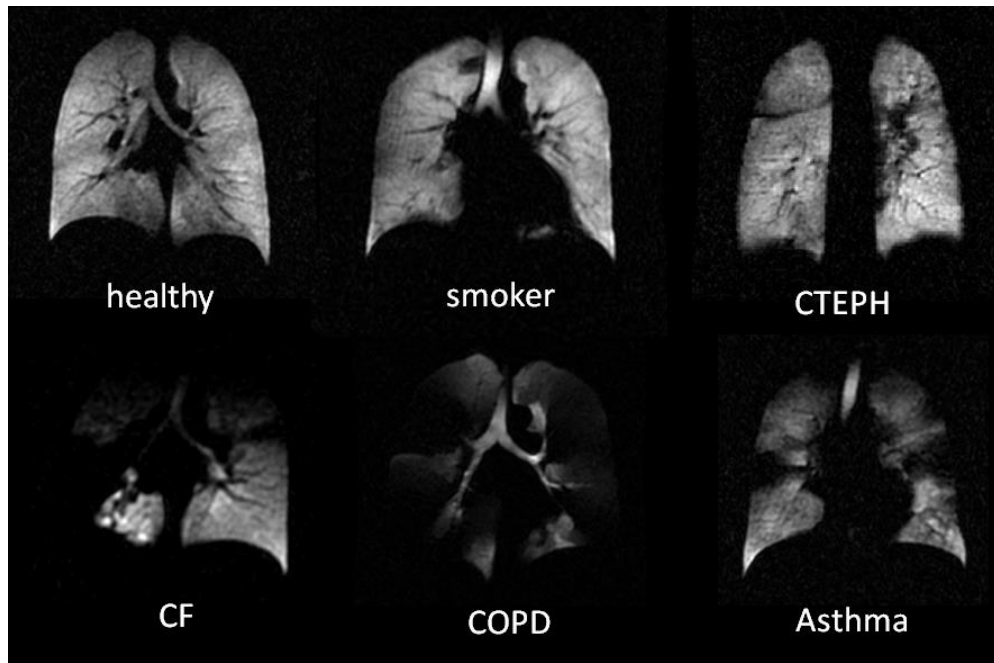
Figure 3.16: Representative ^{3}He ventilation images for a healthy, smoker, chronic thromboembolic pulmonary hypertension (CTEPH), cystic fibrosis (CF), chronic obstructive pulmonary disease (COPD), and asthmatic patient. All images were acquired with a 3D ^{3}He bSSFP sequence [177].

the same diagnostic quality as ^{3}He. Initial comparison studies between the two noble gases suggest that ^{129}Xe may more readily detect ventilation defects (Figure 3.17) due to the lower diffusivity and/or increased density and viscosity of ^{129}Xe gas [117, 191, 193].
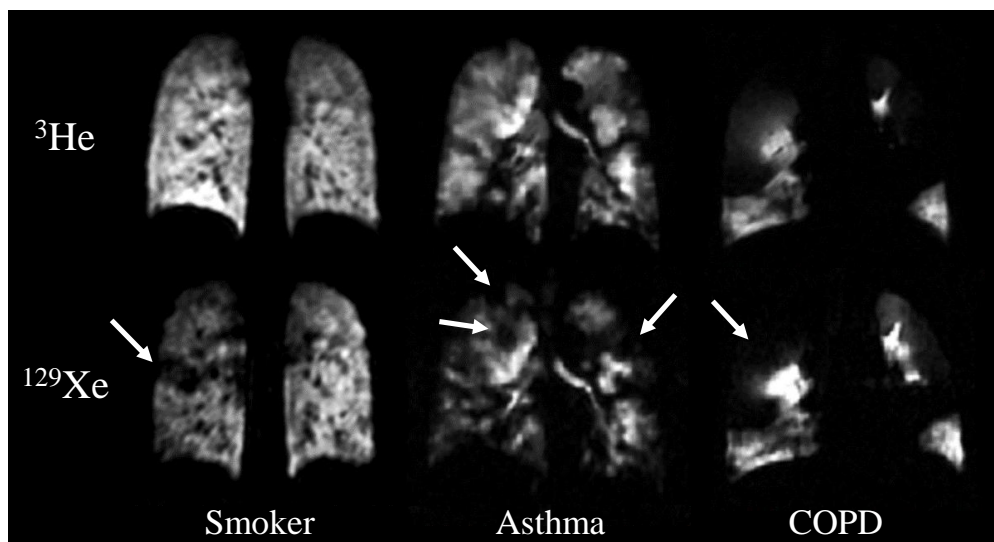
Figure 3.17: Comparison of 3D bSSFP ^{3}He and ^{129}Xe ventilation images from the lungs of a 'healthy' smoker, a patient with asthma, and a patient with COPD. Additional or larger ventilation defects (white arrows) can be observed in the ^{129}Xe ventilation images due to the lower diffusivity and/or increased density and viscosity of ^{129}Xe.

Dynamic imaging

Due to the non-renewable longitudinal magnetisation, there are no signal saturation recovery constraints for hyperpolarised gas MRI. Therefore, images can be acquired with short TRs allowing for the possibility of imaging gas flow dynamics and regional gas ventilation over multiple breaths. Non-Cartesian methods, such as spiral [194] or radial [195] sequences, are typically used to acquire rapid time-resolved images with temporal resolutions as short as 20 ms. These 2D acquisitions have been used to measure gas flow rates in the major airways in patients with COPD [195] and CF [196], but images can be susceptible to radial streaks, susceptibility or motion-induced artefacts. Mapping of gas flow profiles and turbulence in the upper airways is also feasible by combining radial or compressed sensing acquisitions with phase contrast velocity maps [197, 198].

An alternative approach is the imaging of the hyperpolarised gas signal over multiple breaths to derive regional measurements of fractional ventilation, defined as the volume of gas turned over per breath [199]. Regional gas ventilation can be quantified either through wash-in [199] or wash-out [200] dynamics, and more recently, these techniques were combined in a scheme for simultaneous mapping of fractional ventilation, alveolar oxygen tension (pO_2, see below), and apparent diffusion coefficient (ADC, see Section 3.5.1) [201].

Oxygen partial pressure (pO$_2$) mapping

The T_1 of hyperpolarised gases decreases significantly in the presence of oxygen, and this dependence of T_1 with oxygen concentration was demonstrated by Saam et al. [121]. The inverse of the longitudinal decay ($1/T_1$ or Γ_{O_2}) is proportional to the oxygen partial pressure (pO_2) by:

$$\frac{1}{T_1} = \Gamma_{O_2}(t) = \frac{pO_2(t)}{\zeta} \tag{3.65}$$

where ζ is temperature dependent coefficient that was found empirically to be 2.61 bar·s at 37°C. This relationship was subsequently used to derive in vivo estimates of regional pO_2 in pigs and humans with breath-hold experiments [202]. For a single breath-hold, the decrease in longitudinal magnetisation or image signal intensity can be assumed to be related to only RF depletion and $T_1(pO_2)$ effects [202]. This allows the regional pO_2 to be estimated from a time series of images acquired with different image delay times or flip angles, assuming that pO_2 decay in the lungs is linear.

The effects of inter-slice diffusion in 2D slice selective imaging is significant for long image delay times due to the high diffusivity of ^{3}He gas, therefore 3D imaging sequences have been proposed to avoid this possible source of error [203]. A major limitation of this technique is the effect of collateral ventilation observed in emphysematous lungs that provide an additional

source of signal change that is unrelated to oxygen concentrations [204]. pO_2 mapping with ^{129}Xe is feasible, but the quantification of pO_2 is complicated by the solubility properties of ^{129}Xe [205], and the longer T_1 due to dipole-dipole effects [206].

3.4 Sub-Nyquist imaging strategies

Undersampling of *k*-space beyond the Nyquist criterion can shorten the number of required RF excitations and thus acquisition time. However, as demonstrated in Figure 3.8, when the Nyquist criterion is violated, aliasing artefacts manifest in the reconstructed images and different strategies have been proposed to minimise these artefacts. One strategy is the generation of artefacts that are incoherent or less visible through variable density-weighted phase encoding [207, 208] or reduced FOV in dynamic imaging [209, 210]. Another strategy exploits redundancies in *k*-space through parallel imaging [211–213] or partial Fourier reconstructions [214]. The final strategy is exploiting spatial or temporal redundancies through undersampling of the *k-t* space, which contains spatial and temporal information, for dynamic imaging [215–217].

Hyperpolarised gas MRI is limited by both the non-renewable longitudinal magnetisation that is depleted with RF excitations and patient breath-hold limits (∼15s). Therefore, it is a prime candidate for undersampling schemes that can shorten the number of RF excitations and acquisition time. Moreover, the flip angle can be increased with sub-Nyquist sampling such that image SNR is preserved. The focus of this section is to provide a summary of the undersampling techniques that are applicable for hyperpolarised gas MR imaging of the lungs including: partial Fourier reconstructions, parallel imaging, and compressed sensing.

Partial Fourier

In partial Fourier acquisitions, the *k*-space is not sampled symmetrically around its centre; instead *k*-space is asymmetrically sampled with one half of the *k*-space fully-sampled and only a small portion of the other half sampled. A real object can be reconstructed from a partial *k*-space acquisitions because *k*-space exhibits conjugate or Hermitian symmetry, and for 2D *k*-space this can be described by:

$$S(k_x, k_y) = S^*(-k_x, -k_y) \tag{3.66}$$

where S^* is the complex conjugate. This indicates that in theory, a real object can be reconstructed from half of *k*-space. However, in practice, magnetic field inhomogeneities cause phase shifts around $k = 0$ that require correction for accurate reconstruction. Therefore, additional data (typically 5 to 25%) is generally acquired in the incomplete half of *k*-space and used to generate phase correction maps.
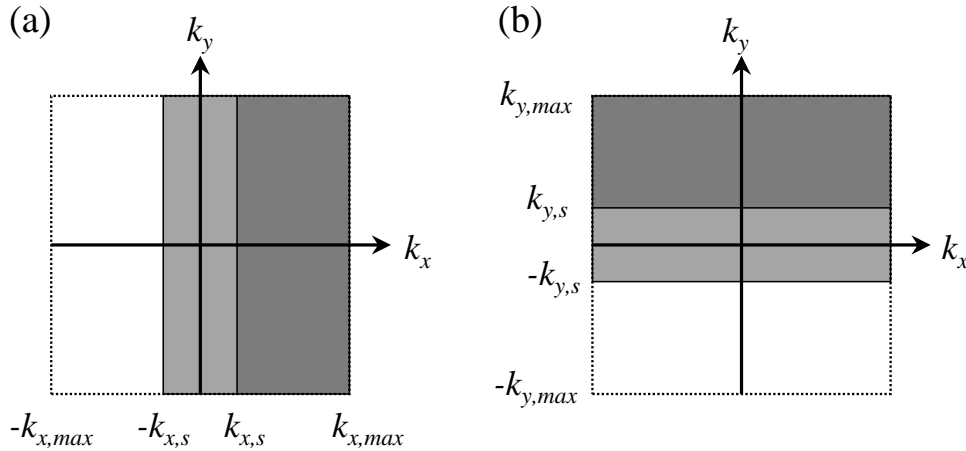
Figure 3.18: Partial Fourier acquisition of 2D k-space. (a) Partial echo acquisition in the k_x direction. k-space is sampled symmetrically ($-k_{x,s}$ to $k_{x,s}$) around the centre of k-space, and then asymmetrically sampled from $k_{x,s}$ to $k_{x,max}$. (b) The equivalent partial acquisition of phase encodes in the k_y direction.

Partial Fourier acquisition is feasible in either the readout direction (k_x), called partial echo, (Figure 3.18a) or the phase encoding direction (k_y) (Figure 3.18b). Both techniques reduce overall acquisition time by either reducing echo time and hence sequence TR or the number of phase encodes at the expense of lower SNR. Partial acquisition in the frequency encoding direction shifts the position of the echo away from the centre of the readout gradient (for full echo), and reduces the time to echo (TE), and the absolute size of readout gradients. Even though from Equation 3.48, acquiring fewer k-space samples theoretically reduces image SNR, the shorter TE can also improve SNR by reducing T_2^* relaxation effects. The simplest method for reconstructing the partially acquired k-space is zero-filling by filling the missing data with zeros. The image can be reconstructed with the standard FFT; however, due to the truncation of k-space, blurring effects and Gibbs artefacts are introduced. Alternative algorithms such as homodyne reconstruction [218] and projection over convex sets (POCS) [219] have been developed for phase correction to accurately reconstruct partial Fourier acquisitions.

Homodyne utilises conjugate symmetry to generate the missing real components of the data, and then corrects the phase of the imaginary components. The undersampled k-space is initially zero-filled and the real component is reconstructed with a homodyne high-pass filter, that doubles the asymmetrically sampled high frequencies ($k_{x,s}$ to $k_{x,max}$ region in Figure 3.18a). A low-pass filter is applied to the symmetrically sampled region of low frequencies ($-k_{x,s}$ to $k_{x,s}$), and a low frequency image is reconstructed. From this image, an estimate of the zero order phase is derived and used to correct the full image. Homodyne reconstruction utilises the phase of a low frequency image, and therefore performs poorly in regions with rapid changes in phase.

Algorithm such as POCS can further improve the estimation of the missing k-space data by iteratively applying phase correction and conjugate symmetry. In the first iteration,

the missing data is zero-filled and phase-corrected in a similar fashion as homodyne. The asymmetric portion of the reconstructed real image component is then used to replace the zero-filled estimate of the missing data. This process is repeated until a stopping criteria is reached such as the number of iterations or the differences between iterations reaches a certain threshold. Iterative algorithms typically converge very quickly, with the majority of the image improvement occurring within the second iteration. Homodyne can be implemented with iterative reconstruction as well, where zero-filling is replaced with the homodyne high pass filtering.

Parallel imaging

The concept of parallel imaging consists of utilising prior knowledge of discrete multiple receiver coil sensitivity profiles to reduce the number of RF pulses required to reconstruct an image. Parallel imaging with hyperpolarised gases is not constrained by the typical SNR trade-off in thermally polarised parallel imaging when the number of RF pulses is reduced because hyperpolarised gas signal can be increased with larger flip angles [220]. Parallel imaging is therefore an attractive option for accelerated hyperpolarised gas lung imaging and high SNR ^{3}He ventilation images have been demonstrated with multiple-channel receiver coils at reduction factors of 2 to 4 [174, 220, 221].

Two common approaches for reconstructing the undersampled k-space are Sensitivity Encoding (SENSE) [212] and Generalized Autocalibrating Partially Parallel Acquisitions (GRAPPA) [213]. Both approaches utilise coil sensitivity profiles to reconstruct the k-space that is undersampled in the phase-encoding direction. In a 2D acquisition, undersampling of phase encodes will correspond to missing lines in 2D k-space. Each acquired k-space line is now separated by an increased Δk spacing that corresponds to the undersampling or reduction factor (R); while the maximum coverage of k-space is fixed to preserve spatial resolution. The increased Δk corresponds to a decreased FOV and aliasing, which is unwrapped with a parallel imaging reconstruction strategy.

In SENSE reconstruction, each receiver coil acquires an undersampled k-space simultaneously, and an aliased image is reconstructed. Each pixel in the aliased image is a superposition of signal from each receiver coil, however the specific contribution of each coil at each spatial location is dependent on the local coil sensitivity. Therefore, the full image can be reconstructed from each aliased image, and this is demonstrated schematically in Figure 3.19. In contrast to SENSE, GRAPPA reconstruction occurs entirely in k-space where the missing k-space lines for each coil are estimated from the weighting factors of each coil. A non-aliased image for each coil can then be reconstructed and combined to form the final image. The weighting factors represent the spatial frequency dependencies of each coil and

is usually calculated from auto-calibration, where the undersampled k-space from each coil has a fully sampled region in the centre of k-space.
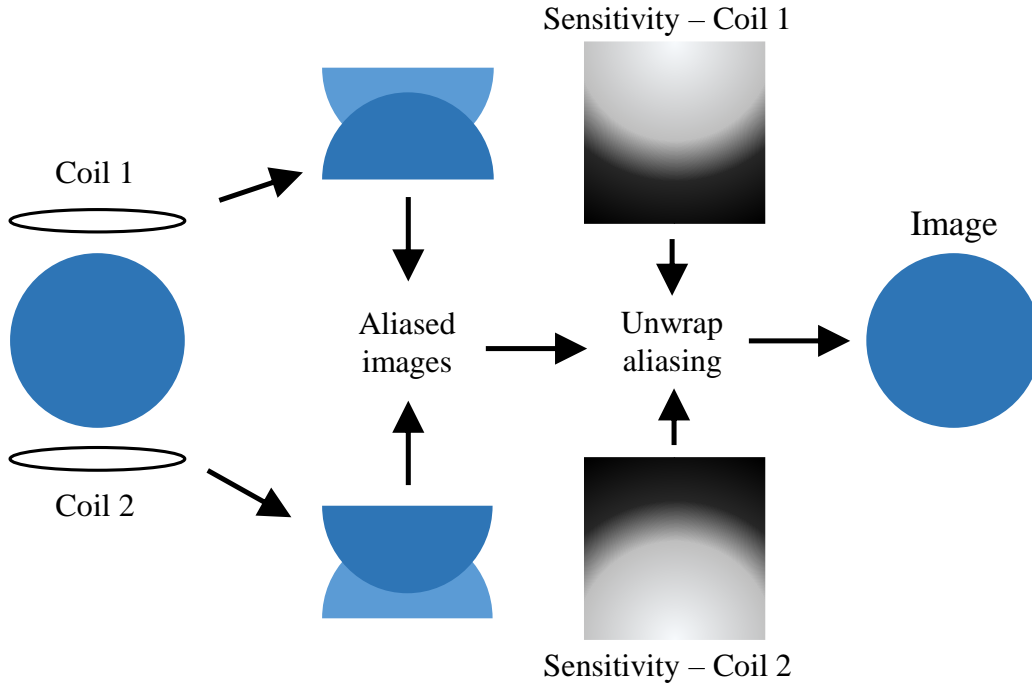
Figure 3.19: Schematic diagram for parallel imaging with SENSE reconstruction. Two receiver coils are used simultaneously to acquire undersampled k-space. The reconstructed undersampled images are aliased, but can be unwrapped with the information of the local spatial sensitivity of each receiver coil.

As for partial Fourier acquisitions, the reduction in k-space sampling leads to SNR reduction. Additionally, a geometry factor g, that is characteristic of the array coil and related to the arrangement of individual coils, leads to sub-optimal SNR. The parallel imaging SNR can be related to a fully sampled equivalent by:

$$SNR_{PI} = \frac{SNR_{full}}{g\sqrt{R}} \tag{3.67}$$

However, as mentioned above, the $\sqrt{R}$ SNR trade-off can be avoided for hyperpolarised gas imaging by increasing the flip angle accordingly.

3.4.1   Compressed sensing

Natural images, including MR images, can be compressed with negligible information loss through compression algorithms such as JPEG or JPEG-2000 [222]. Underpinning these compression algorithms are the sparsifying transformations: discrete cosine transform (DCT) and wavelet transform, respectively. These transformations allow the original image to be compressed by encoding it with a few significant sparse coefficients. With the widespread

success of compression algorithms, the following questions are raised: since natural images are compressible, is it necessary to acquire all the data? If not, is it possible to acquire the significant sparse coefficient information only and accurately reconstruct an image? In 2006, the mathematical framework developed by Candes [223] and Donoho [224] demonstrated that it is feasible to reconstruct an undersampled signal given that the signal is sufficiently sparse or has a sparse representation, and this forms the theory behind compressed sensing (CS) or sparse sampling.

In MRI, CS exploits the sparsity of MR images, in either the image or transformation domains, such that images can be reconstructed from acquired data that does not fulfil the Nyquist sampling criteria [225]. In contrast to parallel imaging, CS does not require the use of multiple-channel RF coils, facilitating translation of the technique across different sites and scanners with transmit and receive coils. Implementation of CS techniques in MRI allows for the reduction of scan acquisition time, and can be used to improve spatial resolution. There are numerous applications for CS in MRI including cardiac perfusion imaging [226], dynamic contrast enhanced MRI [227], angiography [228], functional MRI [229], and hyperpolarised gas lung MRI (see Section 5.1).

Three requirements must be satisfied to ensure good CS image reconstruction: (1) image data must be sparse in either the image domain or a transform domain; (2) k-space must be undersampled randomly with variable-density schemes to ensure that associated artefacts produced during reconstruction are incoherent or noise-like and can be smoothed by the CS algorithm; (3) a non-linear reconstruction method must be used to enforce sparsity and data fidelity. An example of CS implementation is shown in Figure 3.20, where a ^{3}He diffusion-weighted MR image is reconstructed from a three-fold undersampled k-space.

Sparsity

An image is said to be sparse if it can be represented with only a few non-negligible coefficients in either the image or transform domains. Mathematically, an image (x) is considered K-sparse when it can be represented by less than K non-zero coefficients (i.e. the ℓ_0 norm or $\|x\|_0 \leq K$). However, if the image is not naturally sparse, a transform (ψ) can be used to provide a sparse representation (c), and as such, x is still K-sparse given that:

$$x = \psi c, \quad \text{where } \|c\|_0 \leq K \tag{3.68}$$

Numerous sparsifying transformations exist to produce sparse representations of different types of images. MR images, for example, are known to be sparse in the wavelet transform or DCT domains [230]. However, some types of MR images, such as angiograms,
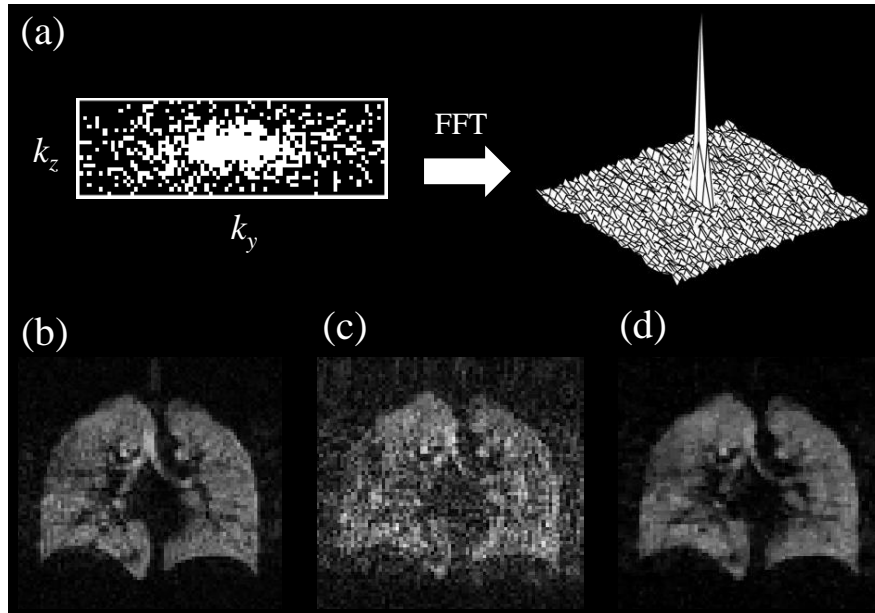
Figure 3.20: Example of compressed sensing with 3D ^{3}He diffusion-weighted MRI. (a) Three-fold variable-density undersampled k-space pattern with undersampling in the k_y and k_z phase-encoding directions (white pixels correspond to phase encodes that are sampled), and with associated point spread function (PSF). (b) Fully-sampled image from a 3D DW-MRI acquisition. (c) Zero-filled reconstruction of the retrospectively undersampled image in (b) using the three-fold undersampling k-space pattern. (d) The CS reconstructed image obtained from the non-linear reconstruction algorithm.

have very few significant pixels with non-zero values, and therefore are naturally sparse or sparse in the image domain.

From the sparse image representation, an approximation image can be reconstructed from a subset of the largest transform coefficients of the original fully-sampled image (Figure 3.21). Numerical experiments have determined that for accurate reconstruction, the number of measurements required should be approximately two to five times that of the number of transform coefficients (K) needed for the image to be K-sparse [225, 231]. For MR images, the percentage of transform coefficients sufficient for diagnostic-quality reconstruction is typically used as a measure of sparsity. This is of course subjective, but from Figure 3.21d, a sufficient quality ^{3}He image can be reconstructed from only the largest 5% of wavelet transform coefficients.

Random sampling

When the k-space is undersampled coherently, spatially coherent artefacts (e.g. aliasing or overlapping) will be generated in the reconstructed images. However, with incoherent or random undersampling, noise-like artefacts will be produced during reconstruction that can be removed through thresholding or smoothing algorithms. While true or uniform random
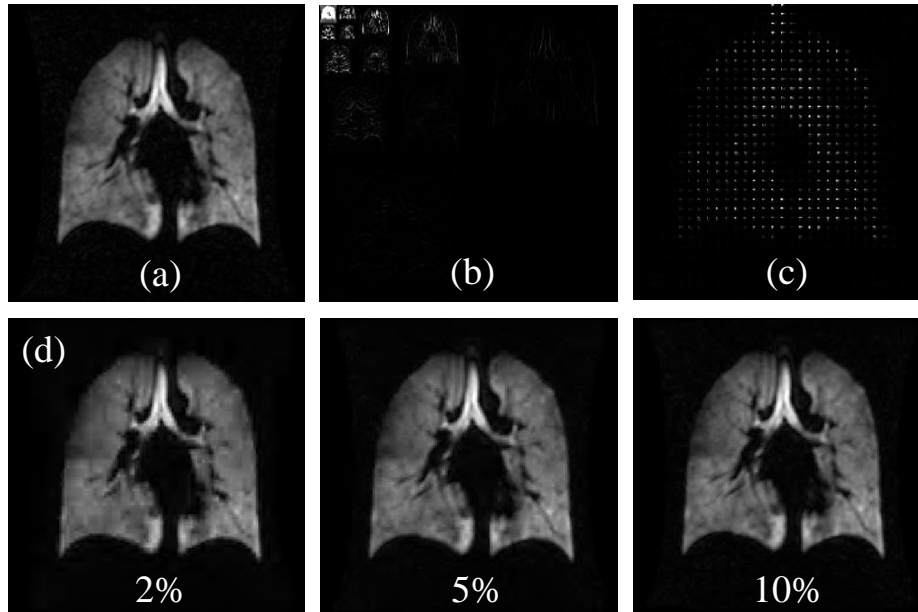
Figure 3.21: (a) 3D ^{3}He bSSFP ventilation image acquired from a healthy volunteer. (b) Wavelet (Daubechies D4) transformation of ^{3}He image. (c) Corresponding transform image with the discrete cosine transform (block size, 8; overlap pixels, 4). (d) Reconstructed ^{3}He image from a subset of the largest 2, 5, and 10% of wavelet transform coefficients.

sampling of *k*-space is preferable, this is hard to implement in practice due to hardware-gradient switching or physiological (peripheral nerve stimulation) limitations. In addition, most of the information of MR images is located in the centre of *k*-space, therefore the density of undersampling should decrease from the centre to the periphery of *k*-space.

For MR imaging, Lustig et al. [225] proposed a pseudo-random variable-density undersampling scheme that mimics the interference pattern of a true random sampling, and this scheme was shown to perform better than uniform density random sampling. The point spread function (PSF) is a good measure of the incoherence, and is defined as:

$$PSF(i,j) = (F_u^* F_u)(i,j) \tag{3.69}$$

where F_u is defined as the Fourier transform of an undersampled subset (u) of *k*-space, and F_u^* is the adjoint operation represented by zero-filling of the undersampled *k*-space followed by the inverse Fourier transform. When the *k*-space is fully-sampled, the PSF is the identity matrix and there are no off-diagonal terms (i.e. $PSF(i,j)|_{i \neq j} = 0$). However, if *k*-space is undersampled, non-zero off-diagonal terms appear in the $PSF(i,j)$ due to interference in the form of energy leakage from the true underlying source pixel to other pixels [230]. Random sampling aims to spread this energy leakage uniformly across the undersampled image, such that the maximum value is small. The incoherence of the $PSF(i,j)$ is thus defined as the

maximum normalised off-diagonal entry or maximum sidelobe-to-peak ratio (SPR):

$$SPR = \max_{i \neq j} \left| \frac{PSF(i,j)}{PSF(i,i)} \right| \tag{3.70}$$

For an image that is sparse in the transform domain through a sparsifying transform (ψ), then a transform point spread function (TPSF) is denoted instead by:

$$TPSF(i,j) = (\psi^* F_u^* F_u \psi)(i,j) \tag{3.71}$$

and the incoherence is measured by the maximum off-diagonal entry in the TPSF. A Monte Carlo algorithm can be used to iteratively generate pseudo-random k-space undersampling patterns, and the PSF is utilised to select the k-space pattern with the maximum incoherence or minimum SPR [225].

Non-linear reconstruction

The final step of CS is the recovery of the sparse image coefficients from a subset of measurements. This can be achieved by using the ℓ_0 norm, which represents the number of non-zero coefficients, to find the sparsest representation that is consistent with the acquired measurements. However, the minimisation of the ℓ_0 norm is a non-convex optimisation problem and can be difficult to solve [232]. The ℓ_1 norm (where $\|x\|_1 = \sum_i |x_i|$) minimisation is the convex alternative and more computationally feasible to solve. The reconstruction is therefore obtained by solving the constrained convex optimisation problem:

$$\begin{aligned} \text{minimise} \quad & \|\psi m\|_1 \\ \text{subject to} \quad & \|F_u m - y\|_2 < \epsilon \end{aligned} \tag{3.72}$$

where m is the reconstructed image, ψ is a sparsifying transformation, F_u is the undersampled Fourier transform, y is the acquired k-space data, and ϵ controls the fidelity of the reconstruction and is usually set below the expected noise level. By minimising the ℓ_1 norm in $\|\psi m\|_1$, sparsity is promoted; while, the ℓ_2 norm (where $\|x\|_2 = \sqrt{\sum_i |x_i|^2}$) in $\|F_u m - y\|_2 < \epsilon$, enforces data consistency. Minimising ℓ_1 norm encourages sparse solutions because many small coefficients will carry larger penalty compared to a few larger coefficients, therefore small coefficients are suppressed. A total variation (TV) penalty term is sometimes included in Equation (3.72) representing the sum of the absolute variations in the image or the ℓ_1 norm of the differences between image pixels. The convex optimisation problem can now be expressed as:

$$\begin{aligned} \text{minimise} \quad & \|\psi m\|_1 + \lambda TV(m) \\ \text{subject to} \quad & \|F_u m - y\|_2 < \epsilon \end{aligned} \tag{3.73}$$

where λ is the penalty weight used for regularisation to ensure that the reconstructed image is sparse in both the transform and finite differences domains. The ℓ_1 minimisation algorithm used in this work is based on the algorithm proposed by Lustig et al. [225] that utilises non-linear conjugate gradients and backtracking line-search. The convex optimisation problem in Equation 3.73 can be expressed as an unconstrained problem:

$$\arg\min_{m}\{\|F_u m - y\|_2^2 + \lambda_1 \|\psi m\|_1 + \lambda_2 \, TV(m)\} \tag{3.74}$$

where λ_1 and λ_2 are penalty weighting parameters that balance data fidelity and artefact reduction. Alternative algorithms have been proposed to recover the sparse signal/image, and these can be classified as iterative or Greedy methods. Examples of iterative/Greedy algorithms include: orthogonal matching pursuit [233], iterative hard thresholding [234], and iterative soft thresholding [235]. These algorithms all adopt an iterative approach to obtain an improved estimate of the sparse signal, and their performance are similar to ℓ_1 minimisation algorithms.

3.5 Diffusion-weighted MR imaging

The application of magnetic field gradients causes an accumulation of spatially varying phase and enables MRI spatial encoding (Section 3.2.1). Magnetic field gradients can also be used to sensitise MR signals to molecular diffusion through random Brownian motion. The first diffusion-weighted sequence, a pulsed gradient spin echo (PGSE) sequence developed by Stejskal and Tanner [236], applies additional bipolar diffusion-weighted gradients lobes to a conventional spin echo sequence. The two gradient lobes have equal area and are separated by the 180° refocusing pulse. A spoiled gradient echo equivalent can be implemented with two diffusion-weighted gradients of opposite polarity (Figure 3.22).

Equation 3.34 describes the phase accumulation in relationship to an applied magnetic field gradient. In random Brownian motion, the spins within a voxel move randomly and accumulate different amounts of phase. Under the assumption of Gaussian phase distribution, the average phase accumulated is zero, and the MR signal is related to the variance of the phase ($<\phi^2>$) by:

$$S = S_0 e^{<\phi^2>} = S_0 e^{-bD} \tag{3.75}$$

where S_0 is the MR signal in the absence of diffusion gradients, and the variance $<\phi^2>$ is equivalent to the product of the b-value (b) and diffusion coefficient (D). The diffusion-weighted MR signal can also be derived from the Bloch equations (Equation 3.16), where an additional term is included to describe the change in transverse magnetisation due to diffusion [237].

$$\frac{d\vec{M}}{dt} = \gamma \vec{M} \times \vec{B} + \frac{1}{T_1}(M_0 - M_z) - \frac{1}{T_2}\vec{M}_{xy} + D\nabla^2 \vec{M} \tag{3.76}$$
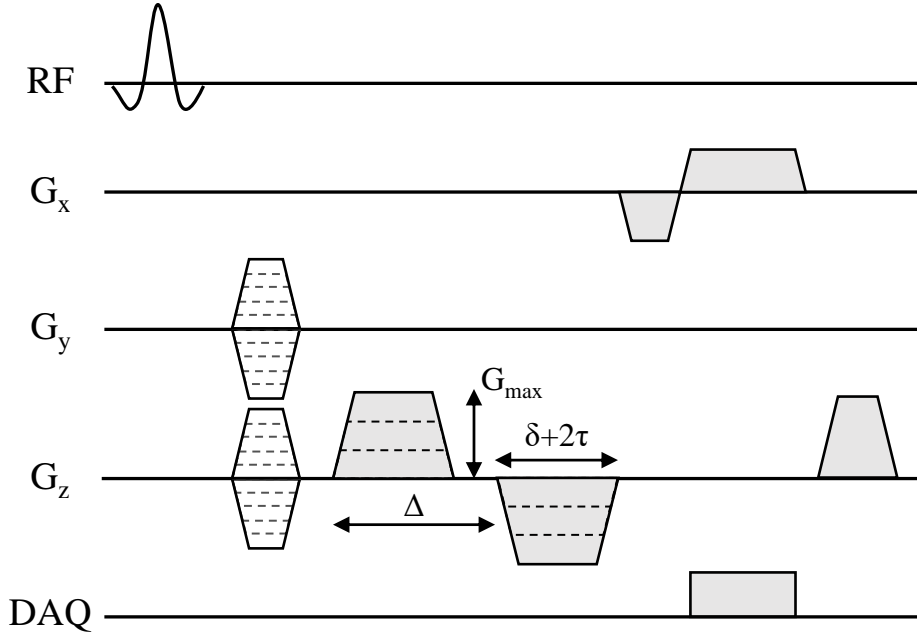
Figure 3.22: A typical hyperpolarised gas diffusion-weighted SPGR pulse sequence, based upon the PGSE sequence. Depicted here is a 3D SPGR sequence with phase encoding on both G_y and G_z, and two bipolar diffusion gradient waveforms on the G_z axis.

The solution for the transverse magnetisation from the Bloch-Torrey equation is given by:

$$\vec{M}_{xy} = M_0 e^{-t/T_2} e^{-bD} \tag{3.77}$$

When the MR signal is measured with and without diffusion-weighted gradients, Equation 3.77 can be used to derive Equation 3.75. The b-value represents all magnetic field gradients that contribute to diffusion-weighted signal attenuation, and is given by:

$$b = (2\pi)^2 \int_0^{TE} \vec{k}(t) \cdot \vec{k}(t) dt = \gamma^2 \int_0^{TE} \left[\int_0^t \vec{G}(t')\ dt' \right]^2 dt \tag{3.78}$$

where the relation between the *k*-space vector and magnetic field gradient is given by Equation 3.35. For the typical trapezoid gradient waveforms used in hyperpolarised gas diffusion-weighted MRI (Figure 3.22), the b-value can be analytically derived from the waveform parameters:

$$b = \gamma^2 G^2 \left[\delta^2 (\Delta - \frac{\delta}{3}) + \tau(\delta^2 - 2\Delta\delta + \Delta\tau - \frac{7}{6}\delta\tau + \frac{8}{15}\tau^2) \right] \tag{3.79}$$

where G is the gradient amplitude (ranging from 0 to G_{max}), Δ is the diffusion time, δ is the gradient plateau time, and τ is the ramp time. The duration of one gradient lobe and time between lobes is defined as the diffusion time (Δ). In practice, the diffusion-weighted sequence is implemented in an interleaving fashion, where each line of *k*-space is repeated for each diffusion-weighting (b-value) before proceeding to the next line. This ensures that each

interleave has the same TE and TR, and that motion artefacts and signal decay associated with the flip angle and T_1 are minimised.

3.5.1 Hyperpolarised gas diffusion-weighted MRI

Diffusion-weighted MRI with hyperpolarised gases and its sensitivity to changes in lung microstructure was introduced in Section 2.2.5. Once inhaled, random Brownian motion causes hyperpolarised gas atom diffusion, and the average distance ($\bar{x}$) an atom can travel in a given direction over a time interval or diffusion time (Δ) is defined by the 1D diffusion equation:

$$\bar{x} = \sqrt{2D\Delta} \tag{3.80}$$

where D is the respective diffusion coefficient of the ^{3}He or ^{129}Xe gas atom, which in the absence of restricting boundaries is the free diffusion coefficient (D_0) diluted in air/N_2 (see Table 3.1). For the typical diffusion times used in hyperpolarised gas MR experiments ($<$10 ms), the gas atoms can travel distances of approximately 1 mm. The alveolar structure ($\sim$0.2 mm in diameter [9]) causes diffusion restriction (Figure 3.23), and under the assumption of Gaussian phase distribution, Equation 3.75 can be described by an apparent diffusion coefficient (ADC):

$$S(b) = S_0 e^{-b \cdot ADC}$$

$$ADC = \frac{\ln(S_0/S(b))}{b} \tag{3.81}$$

The ADC of ^{3}He ($\sim$0.2 cm^2/s [91]) and ^{129}Xe ($\sim$0.035 cm^2/s [113]) is approximately four times smaller than their respective free diffusion coefficients (D_0) in healthy lungs. In diseases such as emphysema, the diffusion restriction is altered by tissue destruction leading to increased diffusion and larger ADC values. The most commonly-used method for hyperpolarised gas diffusion-weighted MRI is a modified SPGR sequence based upon the pulsed gradient spin echo (PGSE) sequence [236]. This sequence (Figure 3.22) is typically implemented with short diffusion times (Δ) because of limitations imposed by T_1 and T_2^* decay.

Healthy Alveoli
^{3}He ADC ~0.2 cm^2/s

Emphysema Alveoli
^{3}He ADC ~0.5 cm^2/s
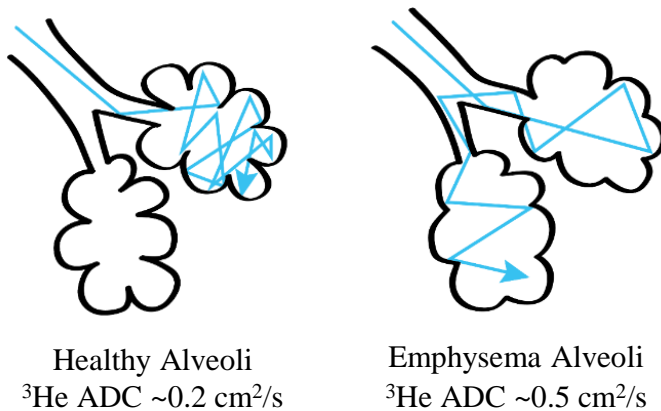
Figure 3.23: In healthy alveoli, the gas atoms are restricted and therefore results in a small ADC ($\sim$0.2 cm^2/s for ^{3}He). While in emphysema, where the alveolar walls are damaged, diffusion is less restricted and larger ADC values ($\sim$0.5 cm^2/s) are obtained.

The relationship between the PGSE diffusion experiment timing parameters and the underlying geometry size determines the hyperpolarised gas diffusion MR signal behaviour. This relationship can be defined through three different length scales (ℓ_S, ℓ_D, ℓ_G) [238, 239]. The underlying size of the confining structure (alveolar diameter) determines the structural length (ℓ_S). ℓ_D corresponds to the 1D theoretical diffusion length (Equation 3.80) for the free diffusion coefficient (D_0). Finally, ℓ_G is the gradient dephasing length, defined as the average length a spin must diffuse before it dephases by 2π radians for a given gradient strength G:

$$\ell_G = (D_0/\gamma G)^{1/3} \tag{3.82}$$

For a given PGSE diffusion experiment, the relative sizes of each length scale determines the specific diffusion regime (free, restricted, and localised) of the experiment. A schematic diagram of these three asymptotic diffusion regimes for ^{3}He diffusion experiments with different gradient amplitudes, and structure sizes is shown in Figure 3.24.
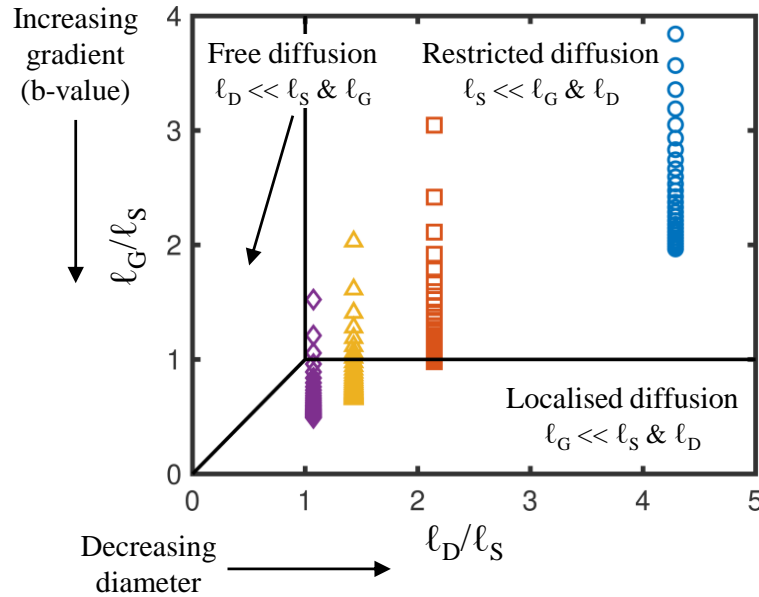
Figure 3.24: Schematic diagram of the three asymptotic diffusion regimes for ^{3}He diffusion experiments with $D_0 = 0.88$ cm^2/s, and $\Delta = 1.6$ ms (as typically used in most ^{3}He ADC experiments). Restricting structure sizes of 0.25 (circles), 0.50 (squares), 0.75 (triangles), and 1.00 (diamonds) mm are shown. Each data point corresponds to a diffusion gradient amplitude ($G = 1$–30 mT/m), with the downward trajectory representing increasing gradient strength and b-value.

The assumption of Gaussian phase distribution that underpins Equation 3.81 is valid for the free and restricted diffusion regimes. In the free diffusion regime ($\ell_D \ll \ell_S, \ell_G$), the derived ADC is constant and equivalent to the D_0. In the restricted regime ($\ell_S \ll \ell_D, \ell_G$), the ADC is constant for all gradient amplitudes, and is determined by the confining geometry size and experimental diffusion time. The final asymptotic regime corresponds to localised diffusion ($\ell_G \ll \ell_D, \ell_S$) [240], where the phase distribution strongly deviates from a Gaussian

distribution and the MR signal is non-uniform. The observed signal becomes spatially dependent where spins further away from the restricting boundaries have dephased more than those within a distance ℓ_G, leading to an edge enhancement effect [241].

3.5.2 Theoretical models of hyperpolarised gas diffusion

The ADC value derived from hyperpolarised gas diffusion experiments, which assumes a Gaussian distribution of phases and mono-exponential decay of MR signal, is an indicator of changes in alveolar size. However, the ADC value is also dependent upon experimental acquisition parameters such as field strength [104], and diffusion sensitising gradient strength, orientation and timings (Figure 3.25) [97, 242, 243] . This dependence indicates that care should be taken when making a direct comparison of ADC results, between different sites, acquired with different diffusion-weighting sequence parameters. The numerous airways with varying sizes and orientations with respect to the diffusion-sensitising gradient contained within one voxel contribute to a non-Gaussian phase dispersion and a non-mono-exponential signal decay [244].
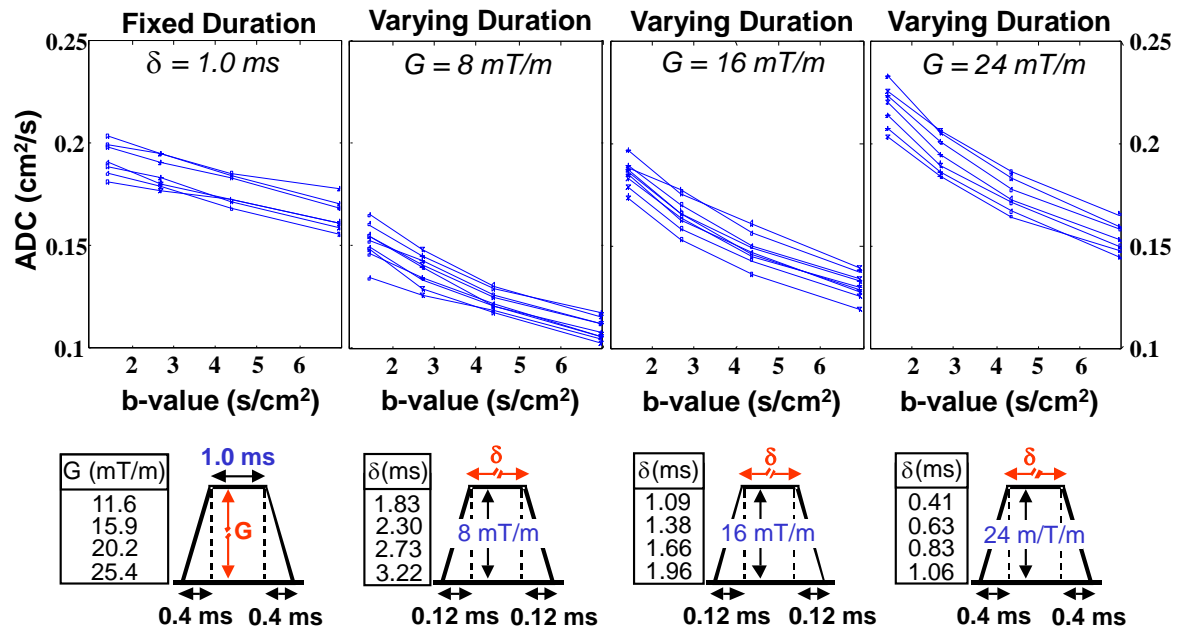
Figure 3.25: The dependence of ADC values on experimental acquisition parameters is demonstrated in a healthy volunteer with ^{3}He diffusion-weighted MRI acquired using a range of different b-values and diffusion gradient durations. For each diffusion-sensitising scheme, ^{3}He ADC data from ten regions-of-interest are plotted for each b-value (b = 1.438, 2.695, 4.377, and 6.932 s/cm^2). The TE and TR for each diffusion interleave was fixed. ADC value is observed to decrease with increasing diffusion time, increasing gradient strength, and increasing b-value. Adapted with permission from Fichele et al. [242]. Copyright Elsevier.

The non-Gaussian effects lead to different apparent diffusion rates, which are not fully compensated by motional averaging for the relatively short diffusion times used in typical ^{3}He or ^{129}Xe diffusion-weighted MR measurements [245]. The heterogeneity of the apparent diffusivity is further enhanced by localised diffusion effects caused by strong gradients at structural edges [239], and effects related to the airway branching [245] and background susceptibility gradients [104]. All of these contributing factors cause difficulties when extracting quantitative information about lung microstructure from in vivo diffusion-weighted MR imaging, and as such there is no direct one-to-one correspondence between measured ADC value and lung morphometry parameters of lung microstructure.

Theoretical models of hyperpolarised gas diffusion have been proposed to extract lung morphometry measurements from the non-Gaussian diffusion MR signal. Much work has been performed in modelling the effect of restricted diffusion of ^{3}He and ^{129}Xe inside geometrical models of lung microstructure that include: cylindrical geometries [5, 128, 136], acinar trees [246], branching structures [242, 247, 248], and alveolar ducts [249]. To date, cylindrical geometrical models [5, 128, 136], stretched exponential models [129], and q-space transforms [130] are the only theoretical models that derive estimates of alveolar length scales from in vivo hyperpolarised gas diffusion measurements, akin to those from obtained from histology. The following sections provide the theoretical background for the cylinder and stretched exponential models that are used in the subsequent experimental chapters.

Cylinder model

Studies into the geometry of the acinus by Haefeli-Bleuer and Weibel, through silicone casts, determined that alveoli surround the acinar airways forming alveolar sleeves, and there is very little variation in the outer and inner acinar airway radii (350 $\pm$ 60 µm and 160 $\pm$ 30 µm, respectively) throughout the acinar airway tree in healthy lungs [11]. The relatively small variation in acinar airway radii is utilised in the cylinder model to characterise acinar airway geometry.

In the cylinder model, the acinar airway is approximated as infinitely long cylinders covered by alveoli according to the Haefeli-Bleuer and Weibel [11] geometry (see Figure 3.26). With the typical diffusion times used in ^{3}He diffusion-weighted MRI experiments (Δ $\sim$1.6 ms), the characteristic 1D free diffusion length (ℓ_1) of ^{3}He atoms is approximately 550 µm (assuming free diffusion of ^{3}He in air is 0.88 cm^2/s). This indicates that during the typical ^{3}He experimental diffusion times, ^{3}He atoms can diffuse out of the alveolus (radius $\sim$150 µm [9]) and into the acinar airway. However, the ℓ_1 is significantly shorter than the length of acinar ducts ($\sim$730 µm) and sacs ($\sim$1000 µm) [11], therefore each cylinder is treated as an individual, non-connected airway and as such branching and interconnectivity effects are considered negligible.
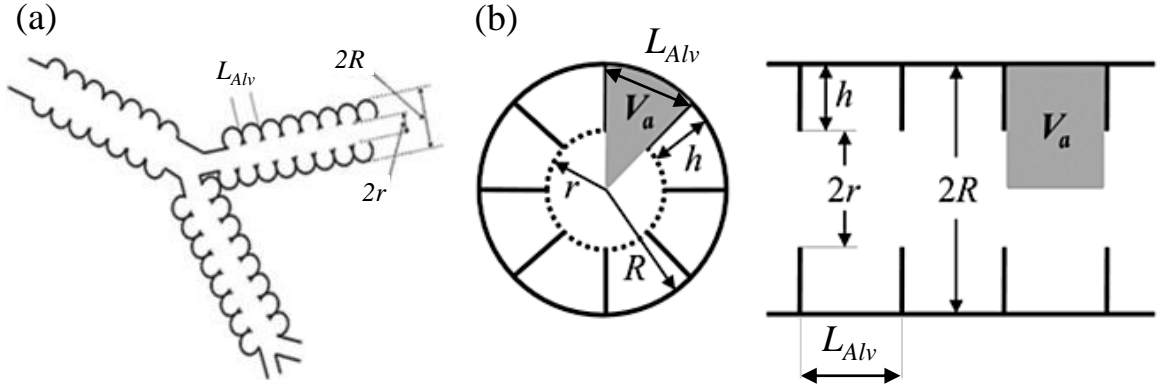
Figure 3.26: (a) Model of acinar airway geometry for the cylinder model based upon the acinar geometry of Haefeli-Bleuer and Weibel [11]. The acinar airway is depicted as cylinders surrounded by an alveolar sleeve, and is defined by two geometrical parameters - outer radii (R), and inner radii (r). (b) Cross-section of the cylinder model geometry. The alveolar sleeve contains eight alveoli, therefore the length or diameter of an alveolus (L_{Alv}) is defined as $2R\sin(\pi/8) = 0.765R$. The depth of the alveolar sleeve (h) is defined as $R - r$, and the alveolar volume (V_a) includes the volume of the alveolus and the alveolar duct. Adapted with permission from Sukstanskii et al. [128] (Copyright Elsevier), and Yablonskiy et al. [250] (Copyright John Wiley and Sons).

From the underlying geometry of the cylinder model, more diffusion restriction exists perpendicular to the airway axis due to the alveolar walls, while less restriction is observed along the airway axis. This anisotropic diffusion was initially characterised by Callaghan et al. [251] as two orthogonal diffusion coefficients, longitudinal D_L and transverse D_T. For a diffusion gradient direction at an arbitrary angle (ϕ) to the airway axis, the ADC can be approximated as:

$$\text{ADC}\,(\phi) = D_L\cos^2\phi + D_T\sin^2\phi \tag{3.83}$$

A typical diffusion-weighted MR imaging voxel is of the order of several millimetres, therefore within each voxel are hundreds of airways with different orientations. Under the assumption of a uniform distribution of cylinders in all orientations within a measured voxel, the total signal attenuation, for given diffusion-weighted b-values, can be obtained by integration over all possible angles [251]:

$$\frac{S(b)}{S_0} = \frac{\int_0^\pi \exp\left[-b(D_L\cos^2\phi + D_T\sin^2\phi)\right]\sin\phi\,d\phi}{\int_0^\pi \sin\phi\,d\phi} \tag{3.84}$$

where S_0 is the diffusion signal in a given voxel in the absence of diffusion-weighting. Integration of Equation 3.84 derives an expression for the non-mono-exponential signal observed in ^{3}He DW-MRI lung experiments as a superposition of mono-exponential signals from

each individual airway [5]:

$$\frac{S(b)}{S_0} = \exp{(-bD_T)}(\frac{\pi}{4\,bD_{AN}})^{1/2} \cdot \Phi[(bD_{AN})^{1/2}]$$

$$(3.85)$$

$$D_{AN} = D_L - D_T, \quad \Phi(x) = \frac{2}{\sqrt{\pi}} \int_0^x e^{-t^2} dt$$

where $\Phi(x)$ is defined as the error function. The anisotropic diffusion coefficients D_L and D_T, derived from the fitting of Equation 3.85, are subsequently related to the cylinder model airway geometrical parameters (R and h) with phenomenological expressions determined through Monte-Carlo simulations. The expressions originally developed by Yablonskiy et al. [5] have subsequently been updated to account for non-Gaussian effects and a more complex geometry that incorporates alveoli [6, 128]. The model implemented in this work was based upon an eight alveolar model [6] (Figure 3.26), where the effective alveolar diameter (L_{Alv}) is equivalent along the airway and across the alveolus, therefore is 1/8 of the chord length of the cylindrical acinar airway:

$$L_{Alv} = 2R\sin(\pi/8) = 0.765R$$

$$(3.86)$$

This enables the cylinder model to be characterised by two geometrical parameters (R and h) that are related to D_L and D_T by the following expressions [6]:

$$D_L = D_{L0}(1 - \beta_L \cdot bD_{L0}); \qquad D_T = D_{T0}(1 + \beta_T \cdot bD_{T0})$$

$$(3.87)$$

$$\frac{D_{L0}}{D_0} = \exp[-2.89 \cdot (h/R)^{1.78}]; \qquad \beta_L = 35.6 \cdot (R/\ell_1)^{1.5} \cdot \exp[-4/\sqrt{h/R}]$$

$$(3.88)$$

$$\frac{D_{T0}}{D_0} = \exp[-0.73 \cdot (\ell_2/R)^{1.4}] \cdot [1 + \exp(-A \cdot (h/R)^2) \cdot u(h/R)]$$

$$u(h/R) = \exp(-5 \cdot (h/R)^2) + 5 \cdot (h/R)^2 - 1$$

$$A = 1.3 + 0.25 \cdot \exp(14 \cdot (R/\ell_2)^2)$$

$$(3.89)$$

Within the physiological range of the cylinder model ($h/R < 0.6$), the β_T parameter is observed to be constant at 0.06. $\ell_1 = \sqrt{(2D_0\Delta)}$ and $\ell_2 = \sqrt{2}\,\ell_1$ are the respective 1D and 2D characteristic free diffusion lengths of ^{3}He in air. The above expressions are valid only for $R = 300$–400 µm, and $\Delta = 1.5$–2 ms; therefore incorporating alveolar parameters ranging from healthy to mild emphysema [252]. After the estimation of R and h, additional parameters, including alveolar volume (V_a) and alveolar surface area (S_a), can be derived based upon the cylindrical airway geometry (Figure 3.26).

$$V_a = \frac{\pi}{8}R^2 L_{Alv}; \qquad S_a = \frac{\pi}{4}R \cdot L_{Alv} + \frac{\pi}{4}h \cdot (2R - h) + 2h \cdot L_{Alv}$$

$$(3.90)$$

The alveolar volume includes both the volume of the alveolar duct and the alveolus. With S_a

and V_a, alveolar number density (N_a) and mean chord length (Lm) can be estimated using the histological relationship between Lm and surface-to-volume ratio [9]. In the calculation of Lm, the thickness of the alveolar wall ($\sim$10 µm), is neglected such that the mean linear intercept is equivalent to the mean chord length.

$$N_a = \frac{1}{V_a}; \qquad Lm = \frac{4V_a}{S_a} \tag{3.91}$$

^{129}Xe Cylinder model

The inherent differences in diffusivity (D_0) and gyromagnetic ratio (γ) of ^{3}He and ^{129}Xe prevents the direct application of the cylinder model phenomenological expressions, derived for ^{3}He in Equations 3.88 and 3.89, for ^{129}Xe diffusion-weighted MRI. In the cylinder model, the anisotropic diffusion coefficients D_L and D_T are dependent upon R/ℓ_1 and bD_0. Therefore, if ^{129}Xe acquisition parameters were scaled to allow for the same R/ℓ_1 and bD_0 as ^{3}He, Equations 3.88 and 3.89 can be applied for ^{129}Xe diffusion-weighted MRI. However, for this to occur, the ^{129}Xe diffusion time would need to be approximately 6$\times$ longer than that for ^{3}He, significantly increasing acquisition time. Therefore, through Monte Carlo simulations, new phenomenological expressions for ^{129}Xe diffusion-weighted MRI were derived by Sukstanskii and Yablonskiy [136], and these expressions are valid for ^{129}Xe $D_0 = 0.14$ cm^2/s, $R = 300$–400 µm, and ^{129}Xe $\Delta = 4$–6 ms, and are as follows:

$$\frac{D_{L0}}{D_0} = \exp[-2.81 \cdot (h/R)^{1.76}]; \qquad \beta_L = 21.2 \cdot (R/\ell_1)^{1.5} \cdot \exp[-3.65/\sqrt{h/R}] \tag{3.92}$$

$$
\begin{aligned}
\frac{D_{T0}}{D_0} &= \exp[-0.74 \cdot (\ell_2/R)^{1.47}] \cdot [1 + u(h/R)] \\
u(h/R) &= c_1(R) \cdot (h/R) + c_2(R) \cdot (h/R)^2 \\
c_1(R) &= 1.13 \cdot (R/\ell_2) - 1.40 \cdot (R/\ell_2)^2 \\
c_2(R) &= 3.55 - 11.27 \cdot (R/\ell_2) + 7.44 \cdot (R/\ell_2)^2
\end{aligned}
\tag{3.93}
$$

$$
\begin{aligned}
\beta_T &= c'_0(R) + c'_1(R) \cdot (1 - h/R) + c'_2(R) \cdot (1 - h/R)^2 \\
c'_0(R) &= 1.89 + 5.82 \cdot (R/\ell_2) + 3.60 \cdot (R/\ell_2)^2 \\
c'_1(R) &= -4.21 + 14.1 \cdot (R/\ell_2) - 9.52 \cdot (R/\ell_2)^2 \\
c'_2(R) &= 2.14 - 7.35 \cdot (R/\ell_2) + 5.03 \cdot (R/\ell_2)^2
\end{aligned}
\tag{3.94}
$$

Stretched exponential model

An alternative theoretical model of hyperpolarised gas diffusion signal behaviour in the
lungs is the mathematical stretched exponential model [129], that does not require any
assumptions about the lung microstructural geometry in order to derive in vivo estimates
of alveolar length scales. Within each ^{3}He or ^{129}Xe MR lung imaging voxel, the diffusion
of gas atoms is restricted by the walls of airways with different sizes and orientations with
respect to the diffusion sensitising gradient leading to different local diffusion regimes. Hence,
the measured macroscopic voxel signal can be represented as the superposition of signals
with different apparent diffusivities (D):

$$\frac{S_b}{S_0} = \int\limits_0^{D_0} p(D)e^{-bD}dD \tag{3.95}$$

where S_0 is the signal when $b = 0$, S_b is the signal corresponding to a non-zero b-value, D_0 is
the free diffusion coefficient of ^{3}He or ^{129}Xe in air or N_2, and $p(D)$ is the probability density
function. A numerical expression of $p(D)$ can be obtained for the non-mono-exponential signal
decay by using a stretched exponential function, that addresses the non-Gaussian nature of
the diffusion MRI signal [140]. The stretched exponential function is defined as follows:

$$\frac{S_b}{S_0} = e^{[-b \cdot DDC]^\alpha} \tag{3.96}$$

where DDC is the distributed diffusivity coefficient term, and α is the heterogeneity index
that describes how much deviation there is from a mono-exponential decay ($\alpha = 1$). The
$p(D)$ can be estimated from stretched exponential function parameters using the approach
developed by Berberan-Santos et al. [253]:

$$p(D) = \tau_0 \frac{B}{D\tau_0^{(1-\alpha/2)/(1-\alpha)}} \cdot \exp\left[-\frac{(1-\alpha)\alpha^{\alpha/(1-\alpha)}}{D\tau_0^{\alpha/(1-\alpha)}}\right] \cdot f(D), \tag{3.97}$$

where τ_0 is $1/DDC$, and $f(D)$ is defined by:

$$f(D) = \begin{cases} 1/[1 + C(D\tau_0)^\delta], & \delta = \alpha(0.5 - \alpha)/(1-\alpha), & \alpha \leq 0.5, \\ 1 + C(D\tau_0)^\delta], & \delta = \alpha(\alpha - 0.5)/(1-\alpha), & \alpha > 0.5, \end{cases} \tag{3.98}$$

The parameters B and C are functions of α, and parameters at specific α values can be
found in Table 1 of Berberan-Santos et al. [253]. For other α values, interpolation can be
used to derive corresponding B and C parameters. The expression for $p(D)$ can subsequently
be related to a probability distribution of diffusion length scales $p(L_D)$ associated with the
different apparent diffusivities (D) through the 1D diffusion equation (i.e. root mean squared
displacements in Equation 3.80). The $p(L_D)$ distributions are a measure of the distribution of
microscopic dimensions of the airways, such as the different diffusion-restricting boundaries,

contained within a given voxel. In Figure 3.27, for the $p(L_D)$ distributions for different alpha (α) values demonstrates a change in distribution profile.
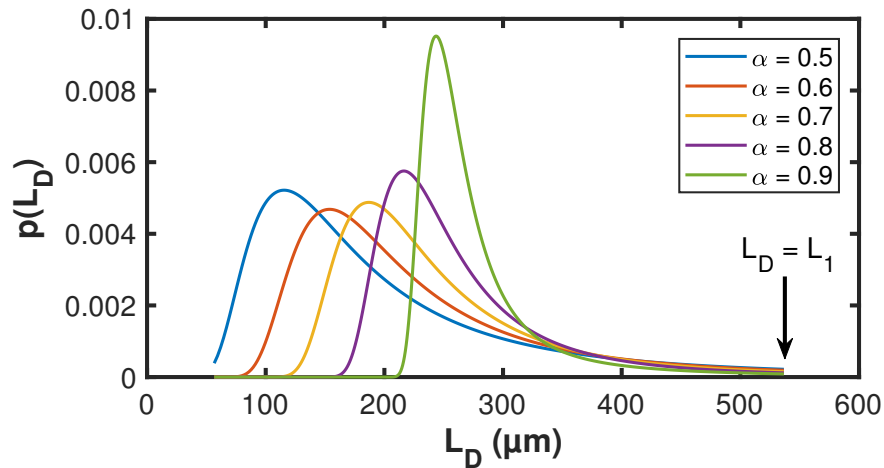
Figure 3.27: Probability distribution of diffusive length scales (L_D) for different alpha (α) values. For a constant DDC value (0.25 cm^2/s), a larger alpha value results in more narrow probability distribution. The $p(L_D)$ distribution is set to zero when $L_D > L_1$ corresponding to the 1D free diffusion length (black arrow).

From the $p(L_D)$ distribution a mean diffusive length scale (Lm_D) can be derived for each voxel by:

$$Lm_D = \sum p(L_D) \cdot L_D \tag{3.99}$$

Lm_D values therefore provide quantitative estimates of the mean acinar airway dimensions within a voxel. The diffusive length scale distributions for the representative healthy and emphysema subjects in Figure 2.13, are shown in Figure 3.28 and correspond to global mean Lm_D values of 208 and 316 µm, respectively. The representative distributions of alveolar diffusive length scales seem to match the distribution of mean intercept length derived from histology (Figure 3.29).
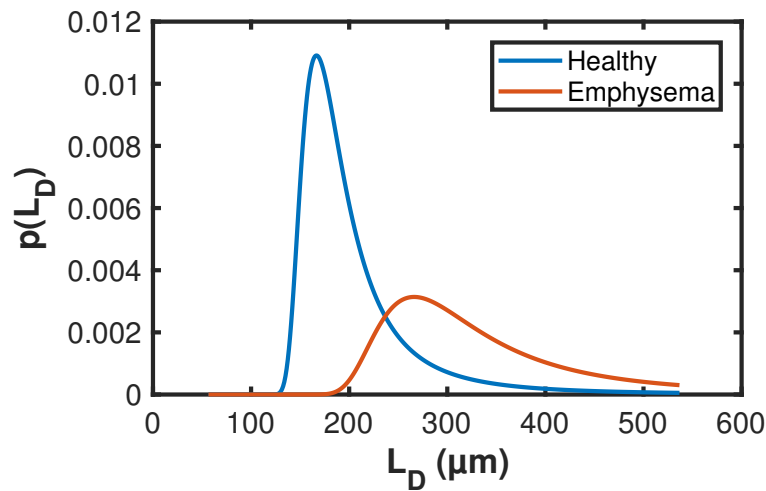
Figure 3.28: Diffusive length scale (L_D) distributions for a representative healthy (global mean DDC = 0.14 cm^2/s, global mean α = 0.83) and emphysema (DDC = 0.45 cm^2/s, α = 0.74) subjects. The smaller α and larger DDC value in the emphysema subject corresponds to a right-shifted and wider distribution of L_D that reflects increased heterogeneity due to emphysematous disease.
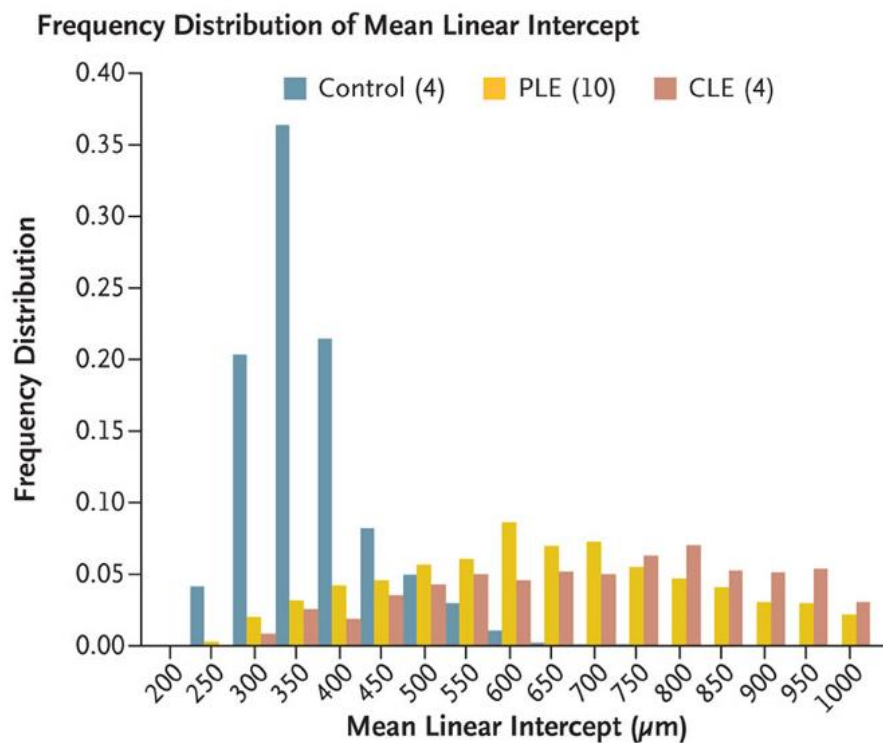
Figure 3.29: Histologically-derived frequency distribution of measurements of mean linear intercept in four control lungs, compared to the frequency distribution in four lungs affected by centrilobular emphysema (CLE) and ten lungs affected by panlobular emphysema (PLE). Reproduced with permission from McDonough et al. [66]. Copyright Massachusetts Medical Society.

Chapter 4

Lobar comparison of lung microstructure with CT and ³He diffusion-weighted MRI

4.1   Introduction

Lung microstructure encompasses the pulmonary acinus, the structural unit of the airways that participates in gas exchange. Changes to this lung microstructure affect the function of the lungs, therefore it is important to measure or model this microstructure to improve our understanding of lung physiology and disease. A range of non-invasive imaging techniques and modalities can be used to measure lung microstructure (see Chapter 2); with each technique and modality offering unique lung structure and function information with different spatial resolutions and volumetric coverage. Reconciling this complementary microstructural information from multi-modality imaging can help improve the understanding of pulmonary disease mechanisms and help develop or validate computational models of lung physiology. In this chapter, the lung microstructure metrics from CT and ³He diffusion-weighted MR imaging were investigated in a cohort of subjects with asthma.

The enlargement of airspaces and destruction of alveolar walls can be detected through changes in CT attenuation values [33], where a change in CT density distribution is indicative of structural changes in the lung tissue due to disease. Areas of gas trapping can be assessed in expiratory CT images, and the amount of gas trapping correlates with asthma severity [254, 255]. Changes to structural dimensions of airway trees segmented from CT images are also indicative of asthma disease severity [256, 257]. Diffusion-weighted MRI (DW-MRI) with hyperpolarised gases is sensitive to changes in lung microstructure through restricted Brownian diffusion [91, 92, 117]. In asthmatic patients, ³He apparent diffusion coefficient

(ADC) value is demonstrated to be elevated (9% increase) in comparison to healthy subjects, and may be representative of localised regions of air-trapping [106].

The lung microstructure information from CT and ^{3}He DW-MRI has been previously compared in emphysema patients, and a significant correlation between CT metrics and ^{3}He ADC was demonstrated [93, 116, 117]. However, these comparisons were global and did not regionally compare the two imaging modalities. More recent comparisons of CT and hyperpolarised gas ^{3}He and ^{129}Xe ADC have demonstrated the potential for regional [114] and voxel-by-voxel comparison [258] of the two imaging modalities. Lung morphometry parameters from ^{3}He models of gas diffusion have also demonstrated significant correlation with both CT emphysema index [131], and mean CT lung density [129]. However, to date, there has been no regional comparison of CT metrics and ^{3}He DW-MRI derived lung morphometry.

The aim of this chapter was therefore to compare the stretched exponential model derived mean diffusive length scale (Lm_D) and CT metrics in a cohort of asthmatic patients on a lobar level. The lung lobes were segmented in both ^{3}He DW-MRI and CT images, allowing for a regional comparison of CT and DW-MRI metrics in each lobar region.

4.2   Methods

Study subjects and image acquisition

29 patients (17 male, 12 female) with moderate to severe asthma (Global Initiative for Asthma (GINA) 2–5) were recruited for high resolution computed tomography (HRCT) imaging and hyperpolarised ^{3}He DW-MRI. This study was performed with national ethics research committee approval. Inclusion criteria were physician diagnosis of asthma, GINA 2–5, and sputum eosinophil count >2%; exclusion criteria included recent lower respiratory tract infection and acute illnesses. The mean $\pm$ standard deviation age for all patients was 53.4 ± 11.6.

Each asthmatic patient was imaged at lung inflation states of function residual capacity (FRC) and total lung capacity (TLC) with HRCT, corresponding to expiratory and inspiratory lung volumes, respectively. CT scanner settings were: Sensation 16 (Siemens, Forchheim, Germany), 120 kV tube voltage, 120 mA tube current, and B30f reconstruction kernel. The HRCT image slice thickness was 1 mm with approximately 600 slices for each patient. Images were reconstructed to an in-plane resolution of approximately 0.86×0.86 mm^2 and an image matrix of 512×512.

^{3}He DW-MRI was acquired for all patients on a 1.5 T GE HDx MRI scanner using 350 ml of hyperpolarised ^{3}He gas ($\sim$25% polarisation) mixed with 650 ml of N$_2$. Patients were instructed to breath 1L of gas mixture from FRC. Five coronal image slices (15 mm thickness and 10 mm spacing) of the lungs were acquired with a 2D spoiled gradient echo (SPGR) imaging sequence

with bipolar diffusion gradients (64×64 matrix, TE/TR = 4.8/9.0 ms, FOV = 38.4×28.8 cm^2, diffusion time (Δ) = 1.6 ms, DW gradient strength = 30 mT/m, ramp = 0.3 ms, plateau = 1.0 ms, flip angle = 5.8° (sinc RF pulse), and bandwidth = ±31.25 kHz). For each image slice, four interleaved acquisitions were obtained corresponding to b-values of 0, 2.4, 4.8, 7.2 s/cm^2.

HRCT and ^{3}He DW-MRI analysis

The major fissures for both inspiratory and expiratory CT volumes were identified using medical image segmentation software (Mimics; Materialise, Leuven, Belgium), and individual lobes were segmented automatically. Due to the difficulty in identifying minor fissures within the right lung of some patients, the right middle and right upper lobes were combined forming a right upper lobar region. This resulted in four lobar regions for regional lung microstructure comparison – left lower (LLL), left upper (LUL), right lower (RLL), and right upper (RUL) regions.

Quantitative CT metrics, including mean lung tissue density, emphysema index, 15th percentile and gas trapping index, were derived for each lobar region (see Figure 2.7). Mean lung tissue density was calculated for both inspiratory (HU$_{\text{insp}}$) and expiratory (HU$_{\text{exp}}$) CT lobar regions from the summation of all voxels within each lobar region. Emphysema index (RA$_{950}$) was defined as the percentage of inspiratory CT voxels that are below -950 HU; while gas trapping index (RA$_{856}$) was the proportion of expiratory CT voxels below -856 HU. Finally, 15th percentile (HU$_{15\%}$) cut off is the inspiratory CT HU value at which 15% of voxels have a lower HU value.

3D Inspiratory CT Slice   **2D ^{3}He DW-MRI Slice**
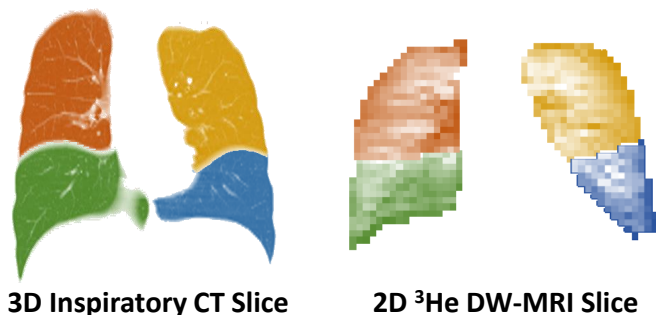
Figure 4.1: Manual segmentation of ^{3}He DW-MRI lobar regions. CT coronal slices were selected to approximately correspond to ^{3}He DW-MRI slices. Lobar regions in the segmented CT were used to guide manual selection of ^{3}He DW-MRI lobar regions.

Due to the relatively low resolution of ^{3}He DW-MRI in comparison to CT, segmentation of the lobar regions on MRI was performed manually (Figure 4.1). To guide the manual segmentation, the axial 3D CT images were reformatted into coronal slices and approximate corresponding CT slices were chosen. Using the CT segmented lobar regions in the chosen corresponding slices as reference, lobar regions of interest (ROI) were manually selected in the DW-MRI. The left and right lungs were first segmented, and to ensure that there was no overlap in manually selected lobar regions, the upper lobar region (LUL and RUL)

was only selected for each lung. The complementary mask region corresponds to respective lower lobar regions (LLL and RLL).

After the segmentation of the four lobar regions from ^{3}He DW-MRI, measures of lung microstructure were calculated for each lobar region. Maps of ADC were generated from the mono-exponential fit (Equation 3.81) of the first two diffusion-weighted interleaves (b = 0 and 2.4 s/cm^2). Maps of distributed diffusivity coefficient (DDC) and alpha were derived from the stretched exponential model fit from all four diffusion-weighted interleaves (Equation 3.96). Finally, mean diffusion length scale estimates (Lm_D) were calculated using Equations 3.97 to 3.99, deriving estimates of alveolar dimension for each voxel.

Lung microstructure measurements from CT imaging and ^{3}He DW-MRI were calculated in each lobar region in a cohort of 29 asthmatic subjects. Correlations between the lung microstructure metrics of the two imaging modalities were determined through statistical analysis using SPSS (IBM Corp. Version 22.0. Armonk, NY: IBM Corp). Repeated measures one-way analysis of variance (ANOVA) with Bonferroni post-hoc adjustment was conducted to compare the lung microstructure metrics within each lobar region. Significance was determined at the adjusted p-value<0.05 level.

4.3   Results

Lobar regions were identified in all asthmatic patients' CT images and manually matched to ^{3}He DW-MRI data. Table 4.1 and Table 4.2 summarises the mean lung microstructure metrics in each lobar region for CT and ^{3}He DW-MRI, respectively. All lobar CT and ^{3}He DW-MRI metrics (except alpha value) were significantly different (P<0.001) across the four lobar regions as determined through repeated measures ANOVA.

Table 4.1: Summary of mean CT metrics from each lobar region from the lungs of a cohort of asthmatic patients.

	Inspiratory CT			Expiratory CT	
	HU_{insp} (HU)	RA_{950} (%)	$HU_{15\%}$ (HU)	HU_{exp} (HU)	RA_{856} (%)
LLL	-791 ± 54	11.3 ± 9.0	-928 ± 32	-670 ± 71	19.7 ± 19.7
LUL	-817 ± 46	14.1 ± 8.5	-939 ± 28	-716 ± 52	25.7 ± 16.6
RLL	-801 ± 48	11.5 ± 7.9	-931 ± 30	-677 ± 67	19.6 ± 19.0
RUL	-821 ± 42	13.5 ± 8.3	-940 ± 25	-735 ± 44	29.8 ± 15.6
Whole	-809 ± 46	12.7 ± 8.2	-935 ± 27	-704 ± 53	24.4 ± 16.6

Table 4.2: Summary of mean ^{3}He DW-MRI metrics from each lobar region from the lungs of a cohort of asthmatic patients.

	^{3}**He diffusion-weighted MRI**			
	ADC (cm^2/s)	DDC (cm^2/s)	Alpha	Lm_D (µm)
LLL	0.207 ± 0.042	0.178 ± 0.048	0.809 ± 0.046	230 ± 22
LUL	0.227 ± 0.039	0.205 ± 0.044	0.814 ± 0.039	245 ± 20
RLL	0.214 ± 0.036	0.187 ± 0.042	0.803 ± 0.040	233 ± 20
RUL	0.225 ± 0.037	0.201 ± 0.042	0.808 ± 0.036	242 ± 19
Whole	0.220 ± 0.037	0.196 ± 0.042	0.809 ± 0.037	239 ± 20

Bonferroni's multiple comparison tests between lobar regions are summarised in Figure 4.2 for selected CT and ^{3}He DW-MRI metrics. A significant difference (adjusted $P<0.05$) between lower and upper lobar regions for all CT metrics was obtained. A statistically significant decrease in HU_{insp}, HU_{exp}, and $HU_{15\%}$ between lower and upper lobar regions was observed; while a significant increase in RA_{950} and RA_{856} was observed. Similarly, a statistically significant (adjusted $P<0.05$) increase in all ^{3}He DW-MRI metrics was observed between the lower and upper lobar regions (apart from RLL and RUL ADC).

CT-based measures were significantly correlated ($P<0.05$) with all ^{3}He DW-MRI lung microstructure measurements for all lobar regions, with the exception of alpha value which was only significantly correlated with RA_{856} for all lobar regions except RLL. Pearson correlation coefficients and significant correlations are summarised in Table 4.3. Generally, expiratory CT-based measurements (HU_{exp} and RA_{856}) exhibited stronger linear correlations with DW-MRI measures of ADC, DDC and Lm_D when compared with inspiratory CT measurements (HU_{insp}, RA_{950}, and $HU_{15\%}$).

The linear correlations suggest that acinar microstructural metrics (ADC, DDC and Lm_D) are strongly related to CT metrics of tissue density in the lungs of patients with asthma. Patients with lower mean tissue density or more severe indices of disease (RA_{950} and RA_{856}) have larger corresponding lung microstructure dimensions. Scatter plots depicting the linear correlation between mean diffusive length scale (Lm_D) and CT metrics are shown in Figures 4.3 to 4.6.
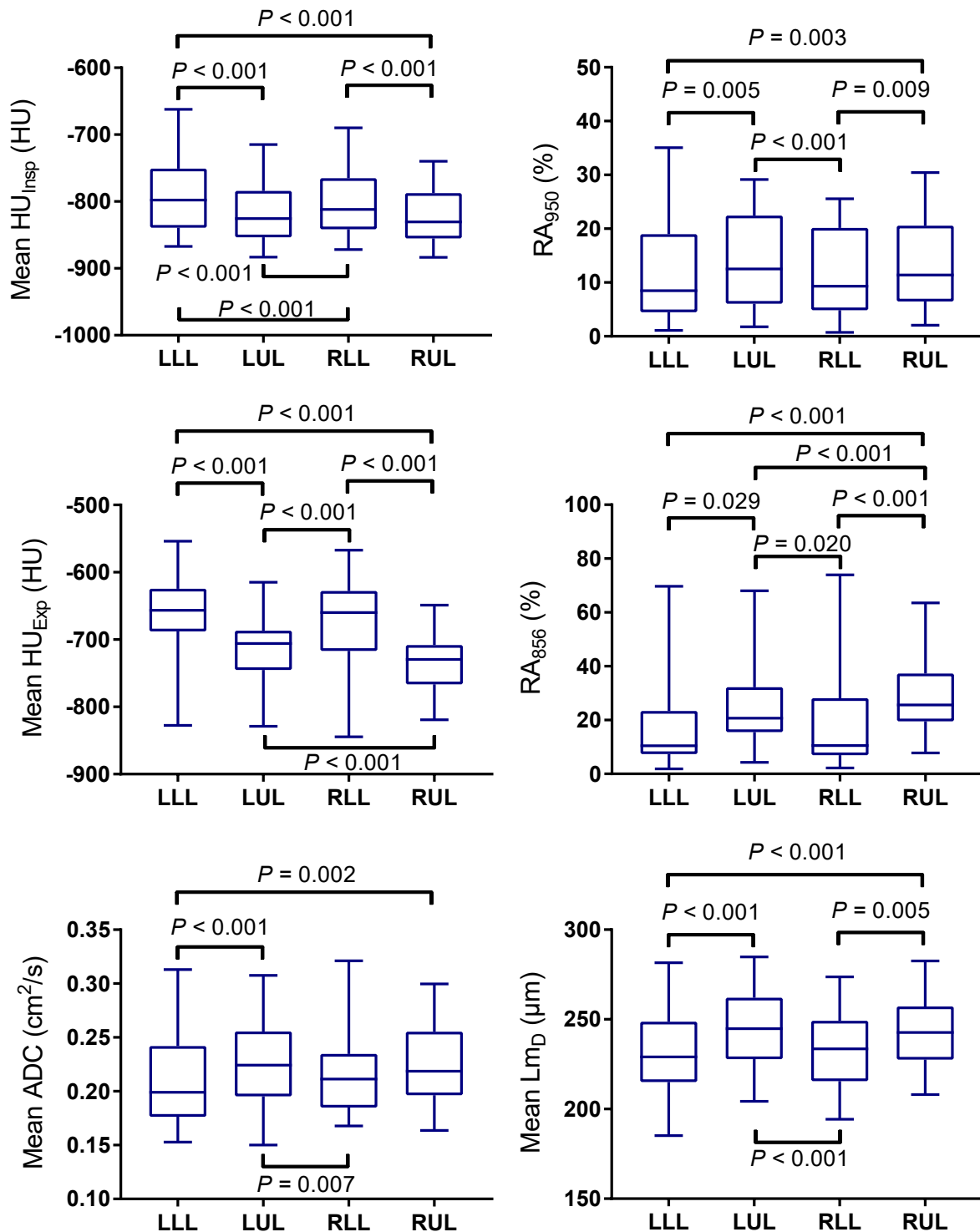
Figure 4.2: Box and whisker plots of CT (HU$_{\text{insp}}$, RA$_{950}$, HU$_{\text{exp}}$, and RA$_{856}$) and ^{3}He DW-MRI (ADC and Lm_D) metrics for each lobar region. Adjusted p-values for each statistically significant lobar comparison are given.

Table 4.3: Summary of correlations between CT and ^{3}He DW-MRI metrics of lung microstructure for each lobar region.

	LLL ADC	LLL DDC	LLL Alpha	LLL Lm_D
LLL HU$_{insp}$	-0.511 **	-0.571 **	0.023	-0.562 **
LLL RA$_{950}$	0.633 ***	0.586 ***	-0.326	0.491 **
LLL HU$_{15\%}$	-0.608 ***	-0.553 **	0.254	-0.492 **
LLL HU$_{exp}$	-0.713 ***	-0.698 ***	0.367	-0.692 ***
LLL RA$_{856}$	0.721 ***	0.691 ***	-0.410 *	0.584 ***
	LUL ADC	**LUL DDC**	**LUL Alpha**	**LUL Lm_D**
LUL HU$_{insp}$	-0.499 **	-0.497 **	0.154	-0.501 **
LUL RA$_{950}$	0.513 **	0.478 **	-0.282	0.424 **
LUL HU$_{15\%}$	-0.564 **	-0.526 **	0.274	-0.489 **
LUL HU$_{exp}$	-0.616 ***	-0.644 ***	0.316	-0.585 ***
LUL RA$_{856}$	0.625 ***	0.638 ***	-0.400 *	0.536 **
	RLL ADC	**RLL DDC**	**RLL Alpha**	**RLL Lm_D**
RLL HU$_{insp}$	-0.552 **	-0.602 ***	0.039	-0.614 ***
RLL RA$_{950}$	0.590 ***	0.559 **	-0.350	0.445 *
RLL HU$_{15\%}$	-0.614 ***	-0.597 ***	0.238	-0.527 **
RLL HU$_{exp}$	-0.647 ***	-0.663 ***	0.350	-0.564 **
RLL RA$_{856}$	0.576 **	0.584 ***	-0.365	0.536 **
	RUL ADC	**RUL DDC**	**RUL Alpha**	**RUL Lm_D**
RUL HU$_{insp}$	-0.605 ***	-0.617 ***	0.168	-0.620 ***
RUL RA$_{950}$	0.659 ***	0.638 ***	-0.233	0.616 ***
RUL HU$_{15\%}$	-0.690 ***	-0.671 ***	0.213	-0.671 ***
RUL HU$_{exp}$	-0.711 ***	-0.712 ***	0.380	-0.649 ***
RUL RA$_{856}$	0.725 ***	0.716 ***	-0.421 *	0.639 ***
	Whole ADC	**Whole DDC**	**Whole Alpha**	**Whole Lm_D**
Whole HU$_{insp}$	-0.589 ***	-0.609 ***	0.168	-0.625 ***
Whole RA$_{950}$	0.643 ***	0.610 ***	-0.233	0.560 ***
Whole HU$_{15\%}$	-0.659 ***	-0.632 ***	0.213	-0.606 ***
Whole HU$_{exp}$	-0.759 ***	-0.764 ***	0.380	-0.708 ***
Whole RA$_{856}$	0.742 ***	0.734 ***	-0.423 *	0.659 ***

* $P<0.05$; ** $P<0.01$; *** $P<0.001$
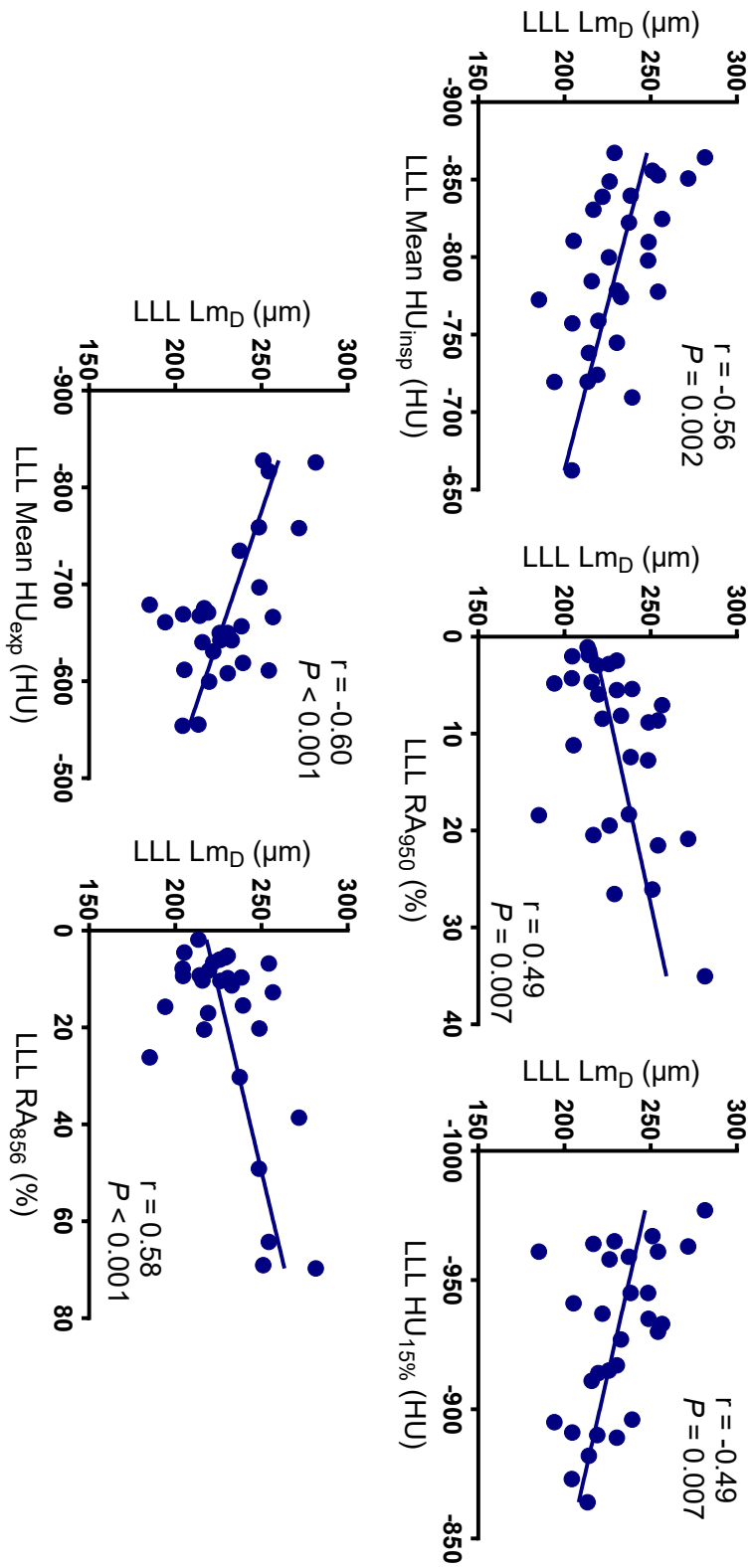
Figure 4.3: Scatter plots depicting the statistically significant correlations between ^{3}He DW-MRI derived estimate of alveolar dimension (Lm_D) and CT-derived metrics for the left lower lobar (LLL) regions. P-values (P) and Pearson's coefficients (r) are shown for each correlation.
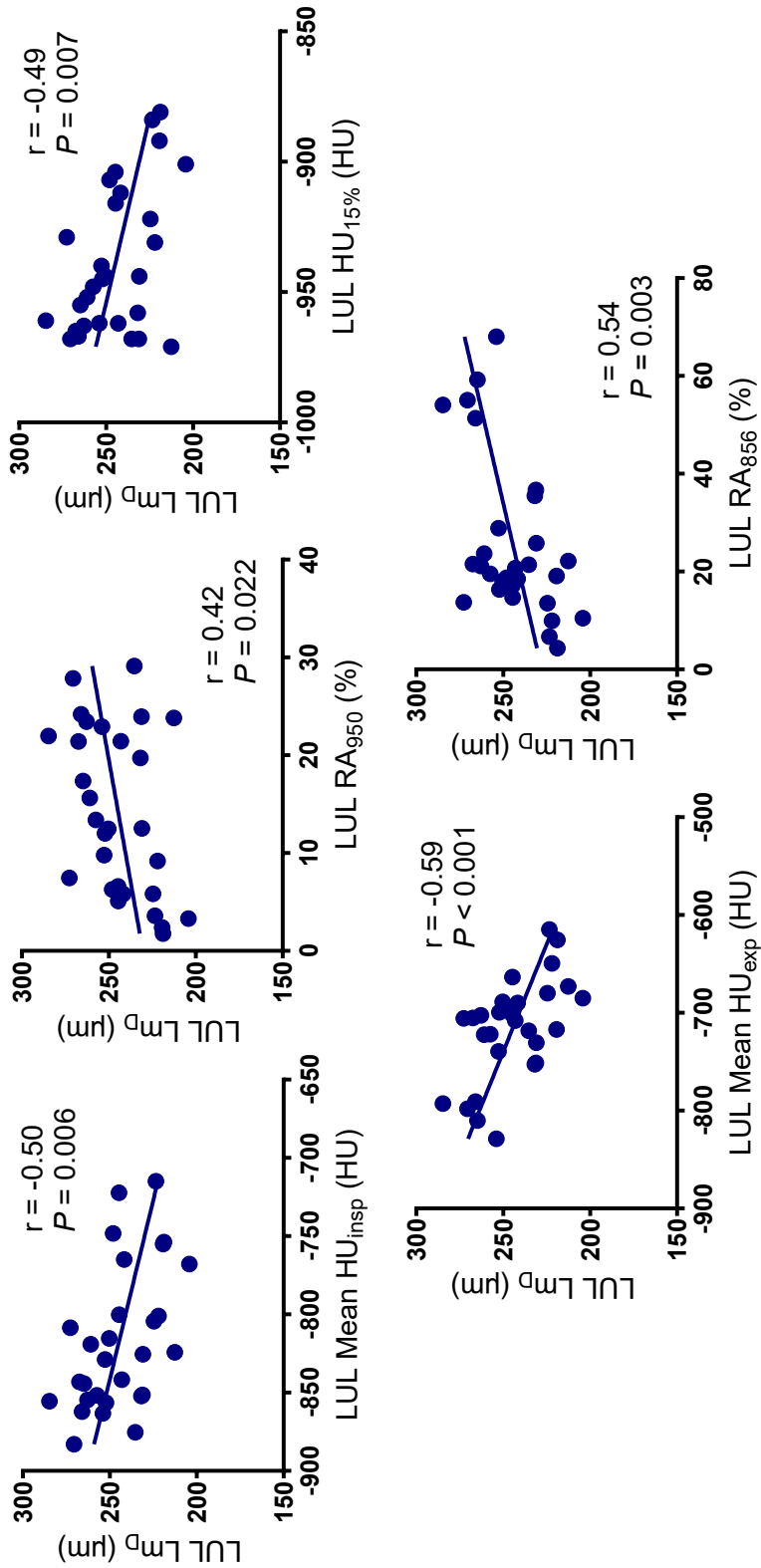
Figure 4.4: Scatter plots depicting the statistically significant correlations between ³He DW-MRI derived estimate of alveolar dimension (Lm_D) and CT-derived metrics for the left upper lobar (LUL) regions. P-values (P) and Pearson's coefficients (r) are shown for each correlation.
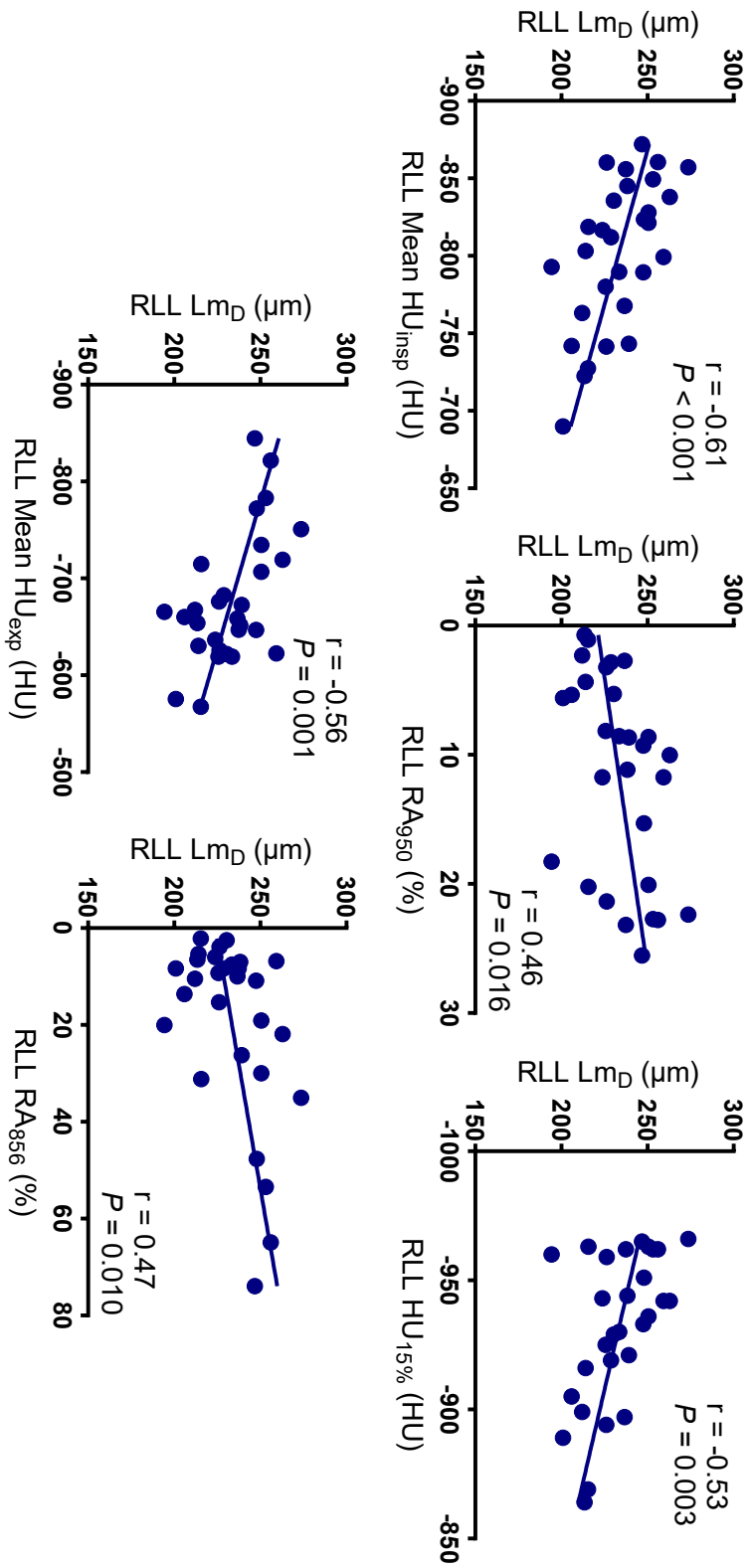
Figure 4.5: Scatter plots depicting the statistically significant correlations between ^{3}He DW-MRI derived estimate of alveolar dimension (Lm_D) and CT-derived metrics for the right lower lobar (RLL) regions. P-values (P) and Pearson's coefficients (r) are shown for each correlation.
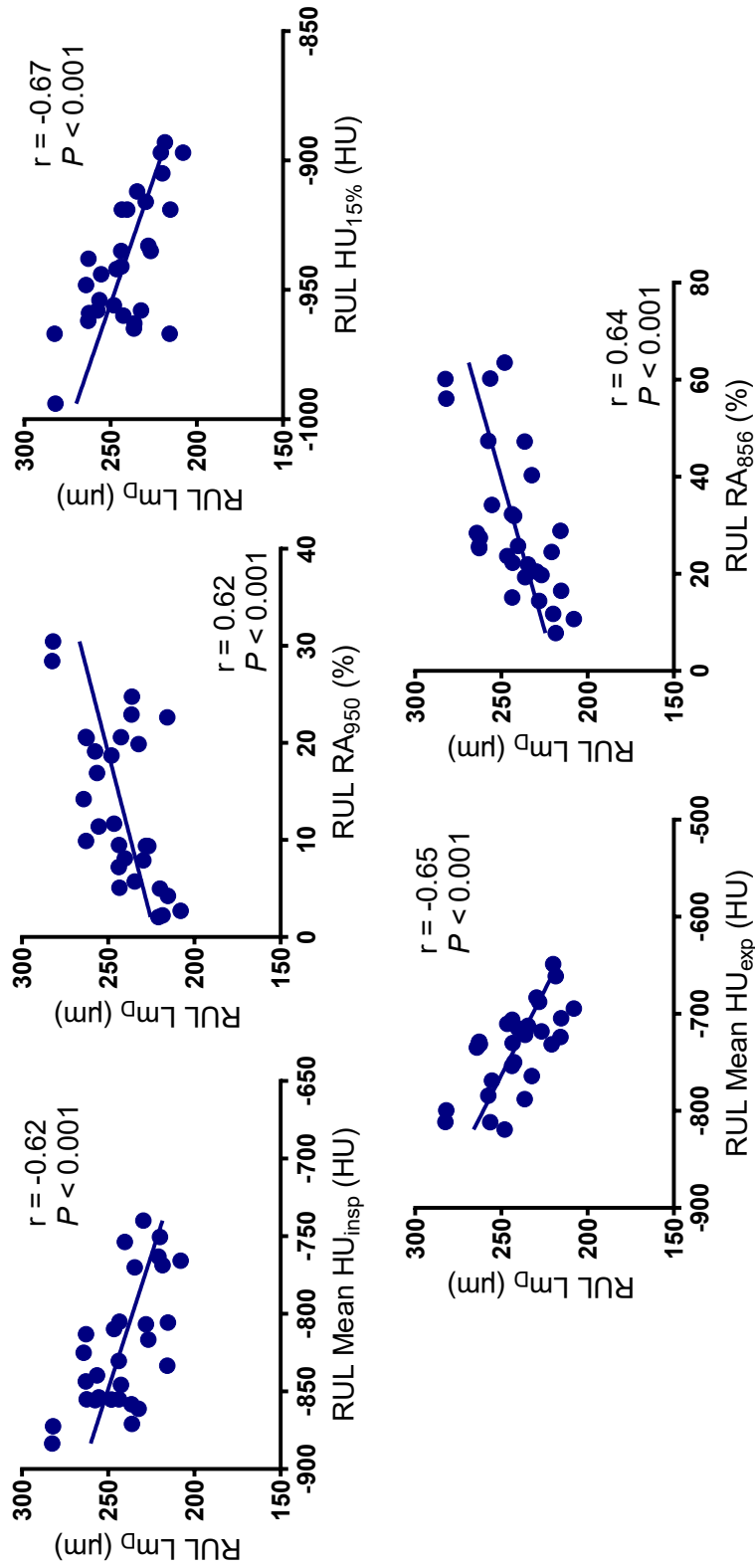
Figure 4.6: Scatter plots depicting the statistically significant correlations between ^{3}He DW-MRI derived estimate of alveolar dimension (Lm_D) and CT-derived metrics for the right upper lobar (RUL) regions. P-values (P) and Pearson's coefficients (r) are shown for each correlation.

4.4 Discussion

This work demonstrates that CT and ^{3}He DW-MRI can be analysed at a lobar level in order to compare regional measures of tissue density and acinar microstructure, respectively. The statistically significant differences between upper and lower lobar microstructural metrics matches the previously observed trend between apex and basal regions with CT [259] and ^{3}He DW-MRI [100, 260]. The average whole lung ADC for the asthmatic cohort (0.22 cm^2/s) is elevated in comparison to the reported values in healthy volunteers (0.16 cm^2/s) that were acquired with the same diffusion time ($\Delta = 1.6$ ms) but different b-value (b = 1.6 s/cm^2) [104]. The b-value used to calculate ADC in this comparison, b = 2.4 s/cm^2, is slightly larger than the more routinely utilised b = 1.6 s/cm^2 for ^{3}He ADC calculation [92, 93, 103, 117]. This discrepancy in b-value is due to an oversight in the DW-MRI protocol, and will lead to smaller estimates of ADC at b = 2.4 s/cm^2 [242]. Wang et al. [106] reported a similar ADC value (0.25 cm^2/s) for asthmatic patients at 1.5 T, and also a slight increase in average ADC value when compared to healthy controls. The smaller ADC values obtained in this asthmatic cohort could be attributed to the longer diffusion time (1.6 ms vs. 1.0 ms) and larger b-value (b = 2.4 vs. 1.6 s/cm^2).

Statistically significant correlations suggest that in lungs with asthma, measurements of lung microstructure from ^{3}He DW-MRI and CT tissue density are inter-related. In a separate study of the same asthmatic cohort [129], the whole lung mean Lm_D was also found to significantly correlate with CT HU$_{exp}$ (P<0.001, r = -0.79). This correlation is similar to the one observed in this analysis (P<0.001, r = -0.71). The slightly lower correlation strength found in this analysis may be a result of fewer asthmatic patients (29 vs. 33) or inter-observer differences in CT and DW-MRI lobar analysis. The correlation between HU$_{exp}$ and Lm_D for individual lobar regions were all smaller than for the entire lung; this could be attributed to errors in lobar segmentations associated with manual selection of lobar regions.

The differences in statistical correlation strength between HU$_{insp}$ and HU$_{exp}$ for all DW-MRI lung microstructure metrics suggests that a smaller lung volume provides stronger correlations between lung alveolar size and mean tissue density. One possible explanation for this trend could be that ^{3}He DW-MRI inflation state (FRC+1L) is closer to FRC (expiratory CT) than TLC (inspiratory CT). An alternative explanation is related to the higher lung tissue density at smaller lung volumes, thus providing better SNR of the parenchyma in the CT image. The improvement in image SNR leads to better contrast between tissue density in healthy and non-healthy regions in the CT images, which could explain the stronger correlations between the lung microstructural measurements of the two imaging modalities. A stronger correlation with expiratory CT volumes was also obtained in other studies comparing CT densitometry and PFTs in emphysema evaluation [49, 50].

Previously reported in vivo comparisons of ^{3}He DW-MRI and CT [93, 116, 117] have predominantly been focused on patients with varying degrees of emphysematous disease. Therefore, in these studies mean ADC value was observed to strongly correlate with RA_{950} and $HU_{15\%}$ (r = 0.9, and -0.9, respectively); while HU_{insp} (r = -0.59 [93]) and RA_{856} (r = 0.67 [116]) exhibited weaker correlations. Nevertheless, in our asthmatic patient cohort, statistically significant correlations between ^{3}He DW-MRI measurements and all CT metrics were observed on a global lung and lobar level. The weaker correlation (r = 0.5 to 0.7) is likely the result of a smaller range of alveolar dimensions and hence range of measurements within this cohort when compared to that observed in patients with emphysema. However, in contrast to the patients with emphysema, the CT metrics with the strongest correlations in the asthmatic cohort were HU_{exp} and RA_{856}. This metric of gas trapping in expiratory CT images is more relevant in asthmatic patients when compared to emphysema metrics (RA_{950} and $HU_{15\%}$). The strong correlation of ^{3}He DW-MRI with gas trapping matches the trend seen in a previous analysis of quantitative CT parameters in a cohort of asthmatic patients, where the percentage proximal airway wall area and gas trapping index (RA_{856}) were the strongest predictor of lung function impairment [261].

A major caveat in this ^{3}He DW-MRI and CT comparison is that only ventilated regions of the lungs receive hyperpolarised gas and have detectable MR signal in ^{3}He DW-MRI. Therefore, diffusion-weighted images of asthmatic patients with ventilation defects have areas of the lung with no signal corresponding to areas of the lung that the ^{3}He gas cannot reach after a single inhalation. However, in CT imaging which utilises X-ray radiation, the entire lung and body cavity is imaged; this means the lung/lobar regions compared are not identical to those in the lung microstructure analysis. Stronger correlations might be obtained if ^{3}He DW-MRI were compared to CT images with excluded unventilated lung regions. This could be achieved through image registration where CT images are registered to ^{3}He DW-MRI using a similar methodology where ^{3}He ventilation images are registered to CT via the registration of a ^{1}H structural scan acquired in the same-breath as the ^{3}He ventilation images [262] (see Figure 9.1).

This lobar analysis was developed and implemented retrospectively after the acquisition of all CT and ^{3}He MR imaging. The goal of the original study was to monitor the effect of a new therapeutic drug treatment over time in a cohort of patients with asthma. Patients were imaged pre-bronchodilator (BD) therapy with ^{3}He DW-MRI but CT imaging was acquired post-BD. This slight oversight in imaging protocol could potentially affect the correlation strength of the multi-modality lung microstructure comparison. In patients with asthma, a significant decrease in ^{3}He or ^{129}Xe ventilated defect percentage (i.e. the percentage of lung volume un-ventilated) has been observed between pre- and post-BD therapy [191, 263]. In COPD patients, Kirby et al. [99] demonstrated no significant difference in whole lung ADC

pre- and post-BD therapy; however, the effects of bronchodilator therapy on ADC or other DW-MRI metrics in asthmatics patients is currently unknown.

A small subset (9 patients) of the asthmatic patient cohort were imaged with ^{3}He DW-MRI both pre- and post-BD therapy. In this sub-cohort analysis, DW-MRI lung microstructure metrics were not significantly different pre- and post-BD; consistent with previous reported results in COPD patients [99]. However, some of the CT and ^{3}He DW-MRI lobar correlations were stronger post-BD therapy. This was predominantly observed between expiratory CT and ^{3}He DW-MRI metrics, and Table 4.4 demonstrates this for correlations between expiratory CT and Lm_D in all lobar regions. The stronger post-BD correlations observed in lower lobar regions and on a whole lung basis, may simply be the result of increased number of DW-MRI voxels becoming ventilated following BD therapy. In COPD patients, a significant change in anterior-posterior (AP) ADC gradient was observed with application of BD therapy [99]. This observation was related to regional reductions in gas trapping and could explain the small regional lobar improvements in correlation of expiratory CT and DW-MRI metrics. Although limited by the size of the cohort, the results suggest that post-BD DW-MRI metrics may correlate better with CT than pre-BD. Further work is required to confirm these preliminary results.

Table 4.4: Effect of bronchodilator therapy on lobar correlations between expiratory CT metrics and ^{3}He mean diffusive length scale (Lm_D).

	Lobar HU_{exp}		Lobar RA_{856}	
	Pre-BD	Post-BD	Pre-BD	Post-BD
LLL Lm_D	-0.831 **	-0.886 **	0.797 *	0.872 **
LUL Lm_D	-0.704 *	-0.621	0.664	0.630
RLL Lm_D	-0.778 *	-0.919 **	0.713 *	0.883 **
RUL Lm_D	-0.717 *	-0.678 *	0.678 *	0.700 *
Whole Lm_D	-0.852 **	-0.859 **	0.785 *	0.828 **

* correlations at a significance level of $P<0.05$

** correlations at a significance level of $P<0.01$

The manual lobar segmentation of the DW-MRI remains the largest source of error in this analysis framework. Due to the limited spatial resolution of the 2D ^{3}He DW-MRI, it was difficult to delineate individual lobar regions from the DW-MRI. The manual MRI segmentation process was guided by visual comparison with approximate corresponding CT coronal image slices, and is inherently prone to observer error. The segmentation process could be improved by the acquisition of 3D ^{3}He DW-MRI data at a smaller voxel resolution that ensures whole lung coverage. This would allow CT lobar segmentations to be registered to the new 3D diffusion images increasing MRI lobar segmentation accuracy, and ultimately allowing a voxel-wise comparison of DW-MRI microstructure metrics with 3D CT. 3D ^{3}He DW-MRI

datasets could also have a higher resolution and subsequently contain more pixels in each lobar region, potentially further improving accuracy of the lung microstructure analysis.

This current analysis of lung microstructure metrics across image modalities is limited to asthmatic patients only. The inclusion of different patient groups and healthy volunteers with CT and ^{3}He MRI measurements of lung microstructure is of interest because each patient group exhibits different changes to the lung microstructure due to disease. For example, in emphysema, the destruction of lung tissue corresponds to decreased tissue density values and larger alveolar size. A wider range of lung microstructure measurements could increase the statistical strength of correlations in the lobar analysis.

4.5 Conclusion

In this chapter, a framework for a lobar comparison of lung microstructure metrics derived from CT and ^{3}He DW-MRI was developed and implemented in a cohort of asthmatic patients. Significant correlations across all microstructure metrics suggests the metrics from the two imaging modalities are inter-related. Expiratory CT-derived metrics were more strongly correlated due to better image SNR and are more applicable to asthmatic patients.

The major limitation of this lobar comparison is the manual segmentation of 2D DW-MRI due to low spatial resolution. The implementation of 3D DW-MRI would open the possibility for image registration of CT and MRI lobar regions. Currently the limitation of 3D DW-MRI is the long scan times associated with multiple b-value acquisitions. Undersampling techniques, such as compressed sensing, could potentially reduce scan time to a single breath-hold, and the feasibility of compressed sensing for 3D multiple b-value ^{3}He and ^{129}Xe DW-MRI is explored in Chapters 5 and 6.

Chapter 5

Whole lung morphometry with 3D multiple b-value ³He diffusion-weighted MRI and compressed sensing

5.1 Introduction

The non-Gaussian phase behaviour of hyperpolarised gases in the lungs was introduced in Section 3.5.2, where the interplay of experimental and microstructural factors causes non mono-exponential signal attenuation with increasing b-value [104, 242, 244]. Various models of gas diffusion in the lungs have been proposed to address the non-Gaussian diffusion-weighted signal behaviour and provide estimates of lung alveolar length scales from the hyperpolarised gas signal [5, 6, 129, 130]. All of these models have a common requirement for the acquisition of multiple b-value DW-MRI data in order to sample the non mono-exponential diffusion signal. The acquisition of multiple b-value DW-MRI in a single breath-hold requires long scan times, and as such multi-slice 2D sequences have been used to date, which do not provide whole lung volumetric coverage for lung morphometry. This limitation was demonstrated in Chapter 4 where the lobar analysis of ³He DW-MRI estimates of lung microstructure was restricted by the lung coverage and low spatial resolution of the 2D multi-slice ³He multiple b-value DW-MRI acquisitions.

In our previous work, 2D ³He DW-MRI sequences permitted acquisition of approximately five slices with four to six b-values in a single breath-hold (∼15s) (see Section 4.2 and [104, 129]). 3D DW-MRI sequences designed with a similar slice thickness (∼10–15 mm) and the same number of b-values would require an acquisition time of almost one minute to obtain

whole lung coverage, which is beyond the limits of a tolerable breath-hold (<18 seconds). Acquisition methods such as radial [195], spiral [194], and parallel radiofrequency (RF) coil encoding [220] have been previously applied to hyperpolarised ^{3}He lung MRI to decrease image acquisition time. However, these techniques require the use of non-Cartesian gradient trajectories or custom-built multi-channel RF coils. Compressed sensing (CS) presents an alternative acceleration technique that can be used to reduce the total scan time to within the limits of a breath-hold by exploiting the sparsity (or compressibility) of lung MR images to acquire a randomly undersampled *k*-space [225] (see Section 3.4.1).

The feasibility of acquisition and reconstruction of hyperpolarised ^{3}He lung MR images with CS was first investigated by retrospectively undersampling and reconstructing 2D and 3D Cartesian fully-sampled ventilation images [264]. Initial results showed that acquisition time could be improved by a factor of two in 2D, and four to five in 3D ^{3}He ventilation images without compromising image quality and information. In the same work, prospective undersampled 2D ^{3}He DW-MRI data acquired with CS demonstrated preservation of spatial resolution and mean ADC values when compared with fully-sampled data. The reduction in acquisition time offered by CS has since enabled 3D isotropic resolution ^{3}He and ^{1}H lung MR images to be acquired in the same breath-hold [265]. Furthermore, the acquisition of ^{1}H structural images as prior knowledge for use in the CS reconstruction was shown to reduce error in the reconstruction of ^{3}He ventilation images [266]. CS techniques have also been implemented to enable high temporal resolution ^{3}He gas flow measurements in the upper airways with phase contrast velocimetry for validation of computational fluid dynamic simulations [198]. Further hyperpolarised ^{3}He studies have incorporated CS to permit acquisition of additional functional or structural data within a single breath-hold, such as 2D multi-interleaved ^{3}He MRI data for mapping of ADC, T_2^* and B_1 [267].

In this chapter, CS was implemented to reduce scan time and facilitate 3D multiple b-value ^{3}He DW-MRI within a single breath-hold. Simulations were first performed to investigate the feasibility of 3D ^{3}He multiple b-value DW-MRI with CS undersampling, and reconstructed images were evaluated to ensure that quantitative microstructural information was preserved. Prospective 3D ^{3}He multiple b-value DW-MRI data was subsequently acquired in five healthy volunteers and one COPD patient. DW-MRI data was used to calculate maps of ADC values and mean diffusive length scale (Lm_D), and these were compared to values obtained from fully-sampled 3D and 2D multiple b-value DW-MRI. Finally, the CS techniques were further applied in a 3D ^{3}He multi-interleaved sequence for the acquisition of whole-lung coverage co-registered ^{3}He ventilation images, and parametric maps of ADC, Lm_D, and T_2^* within a single breath-hold.

Parts of this chapter are based on the following publication: *"Whole Lung Morphometry with 3D Multiple b-Value Hyperpolarized Gas MRI and Compressed Sensing"*. **H.-F. Chan**, N. J. Stewart, J. Parra-Robles, G. J. Collier, J. M. Wild. *Magnetic Resonance in Medicine*,

5.2 Retrospective simulations of CS undersampling in 3D ^{3}He DW-MRI

This section explores the feasibility of using CS for 3D multiple b-value ^{3}He DW-MRI by performing CS simulations on retrospectively undersampled data. All CS simulations and subsequent calculations of mean absolute error (MAE), ADC and Lm_D were implemented in-house using MATLAB (Mathworks, Natick, MA) software. All in vivo MRI experiments were performed under the approval of the UK national research ethics committee.

5.2.1 Methods

Fully-sampled 3D hyperpolarised ^{3}He diffusion-weighted MR images were acquired from the lungs of a healthy male volunteer (30y) in a 22 second breath-hold on a GE HDx 1.5 T MR scanner using a 3D spoiled gradient echo (SPGR) sequence based on that described in [268] with additional diffusion-sensitising gradients (Figure 3.22). A flexible quadrature transmit-receive RF coil (Clinical MR Solutions, Brookfield, WI), tuned to the Larmor frequency of ^{3}He (48.63 MHz) was used. The inhaled gas dose was 300 ml of hyperpolarised ^{3}He ($\sim$25% polarisation), mixed with 700 ml of N$_2$. The lung inflation level at imaging was functional residual capacity plus 1 litre (FRC+1L).

Images were acquired with sequential phase-encoding and the following acquisition parameters: Two diffusion-weighted interleaves (b = 0, 1.6 s/cm^2), 96×78×24 matrix, FOV = 40×32.5×28.8 cm^3, effective slice thickness = 12 mm, TE/TR = 4.2/5.7 ms, diffusion time = 1.6 ms (diffusion-weighted gradient strength = 14.1 mT/m, ramp = 0.3 ms, plateau = 1.0 ms), flip angle = 1.5° (hard RF pulse of 0.24 ms duration), bandwidth = ±31.25 kHz. A constant flip angle was selected, using Equation 3.63, such that $\sim$25% of the initial non-renewable magnetization remained at the end of the acquisition as a result of RF pulse depolarisation.

From the fully-sampled 3D image data, random k-space undersampling patterns were generated in the two orthogonal phase encoding directions (k_y and k_z) for acceleration factors (AF) ranging from 2 to 5. For each AF, eight different probability density functions with polynomial variable density sampling were generated by altering the size of the fully-sampled k-space centre and the variable density polynomial power. A Monte Carlo-based algorithm was then used to determine a k-space undersampling pattern with the maximum incoherence after 10000 iterations for each respective probability density function. The eight different k-space

undersampling patterns for each AF were used to retrospectively undersample the full *k*-space dataset, and corresponding images were reconstructed using the non-linear conjugate gradient descent algorithm with back-tracking line search to solve Equation 3.74 [225]. In this work, no sparsifying transformations were used in the retrospective CS simulations because 3D hyperpolarised ^{3}He lung MR images are naturally sparse and reconstructed data from the simulations were found to be equivalently accurate with and without sparsifying transformations.

In previous applications of CS with hyperpolarised gas MRI, reconstructed images from CS simulations were optimised by minimising the MAE between the original fully-sampled magnitude image (b = 0 for DW-MRI) and the CS-reconstructed magnitude image (MAE_{MAG}) [244, 265]. In contrast, the reconstructions in this work were optimised by minimising the MAE between the fully-sampled ADC maps and the CS-reconstructed equivalent (MAE_{ADC}). For the ultimate goal of quantitative lung microstructural analysis, MAE_{MAG}, MAE_{ADC} and ADC maps were evaluated on a pixel-by-pixel basis within a region of interest (ROI) representing the lungs. MAE_{MAG} was calculated using:

$$\text{MAE}_{\text{MAG}} = \frac{\sum_{i=1}^{N} \sum_{j=1}^{M} |CS(i,j) - FS(i,j)|}{N \times M} \tag{5.1}$$

where CS and FS denote the normalised pixel values in the CS-reconstructed and original fully-sampled images respectively, and $N \times M$ is the total number of pixels in the lung ROI. ADC maps were computed using a pixel-by-pixel mono-exponential fit of signal intensities in the two interleaves of the 3D ^{3}He DW-MRI dataset (Equation 3.81). An asymmetric cut-off of negative (ADC<0), or physically too high (ADC>D_0 = 0.88 cm^2/s) values was applied during the creation of the ADC maps. MAE_{ADC} was calculated via a similar approach to MAE_{MAG}:

$$\text{MAE}_{\text{ADC}} = \frac{\sum_{i=1}^{N} \sum_{j=1}^{M} |CS_{ADC}(i,j) - FS_{ADC}(i,j)|}{N \times M} \tag{5.2}$$

except that CS_{ADC} and FS_{ADC} refer to the calculated ADC pixel values in the CS-reconstructed and the original fully-sampled cases, respectively. Whole lung ADC histograms were generated for each AF, and skewness and full width at half maximum (FWHM) values were derived from each ADC histogram.

5.2.2   Results

CS simulations performed on the fully-sampled two interleaved 3D ^{3}He DW-MRI dataset led to optimal sampling patterns (Figure 5.1a) and penalty weight parameters for each AF. An increase in MAE_{MAG} was observed with increasing AF; however, this error (with a maximum value of 3.8% at AF = 5) did not manifest in the appearance of image artefacts. Reconstructed (b = 0) images for AFs of 2 and 3 showed good preservation of image details when compared to the fully-sampled (AF = 1) image (examples are shown in Figure 5.1b).

At AFs of 4 and 5, a loss in image detail was observed due to increased blurring resulting from heavier undersampling of high frequency *k*-space components.
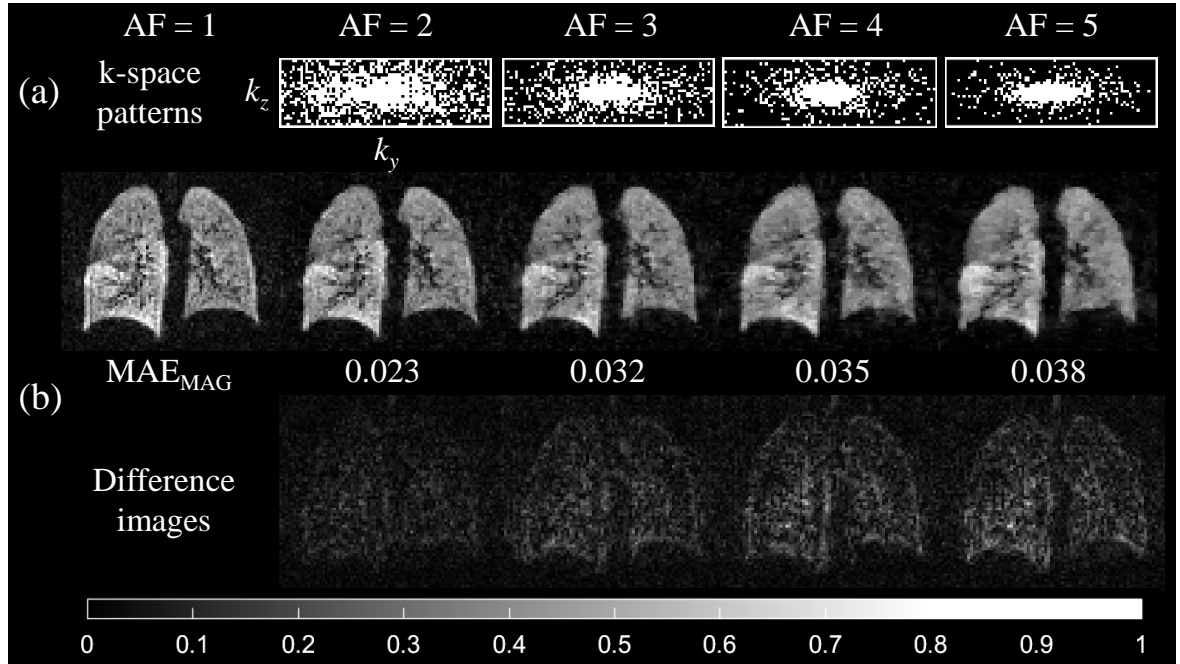
Figure 5.1: Results from 3D ^{3}He CS simulations. (a) The optimal variable-density *k*-space undersampling patterns (78×24 pixels) for each acceleration factor (AF) determined from CS simulations. (b) Example reconstructed magnitude (b = 0) and difference images for each AF, with corresponding MAE$_{\mathrm{MAG}}$ values.

ADC maps were computed for each reconstructed 3D ^{3}He CS dataset and compared to the 3D fully-sampled ADC maps. CS simulation ADC results are summarised in Table 5.1 and Figure 5.2. MAE$_{\mathrm{ADC}}$ exhibited a similar trend to MAE$_{\mathrm{MAG}}$, where increased undersampling resulted in larger error values. The skewness of the whole lung ADC histograms increased with AF; skewness = 1.08 and 2.14 at AF = 1 and AF = 5, respectively. An opposite trend was observed with the FWHM of the histogram, which decreased at higher AFs; FWHM = 0.141 cm^2/s at AF = 1 and 0.118 cm^2/s at AF = 5, respectively. In addition, a slight increase in global ADC values was observed with increasing AF, reflecting the increase in MAE$_{\mathrm{ADC}}$. The maximum difference in global ADC value between CS and fully-sampled acquisitions was 4% at AF = 5. Despite this slight increase in global ADC values, single slice ADC maps and whole lung ADC histograms for each AF (see Figure 5.2) appeared visually similar, indicating good preservation of quantitative lung microstructural information.

5.2.3 Discussion

CS simulations performed on a fully-sampled 3D ^{3}He DW-MRI dataset led to optimal sampling patterns and penalty weight parameters for different acceleration factors (between 2 and 5).

Table 5.1: Summary of global ADC values and whole lung ADC histogram results from 3D ^{3}He CS simulations.

AF	$\mathbf{ADC_{Global}}$ $\mathbf{(cm^2/s)}$	Skewness	FWHM $\mathbf{(cm^2/s)}$
1[a]	0.198 ± 0.085	1.08	0.141
2	0.203 ± 0.094	1.79	0.127
3	0.202 ± 0.091	1.95	0.123
4	0.204 ± 0.093	2.12	0.120
5	0.206 ± 0.094	2.14	0.118

[a] AF = 1 corresponds to the fully-sampled dataset

ADC_{Global} = mean global ADC value

FWHM = full width at half maximum
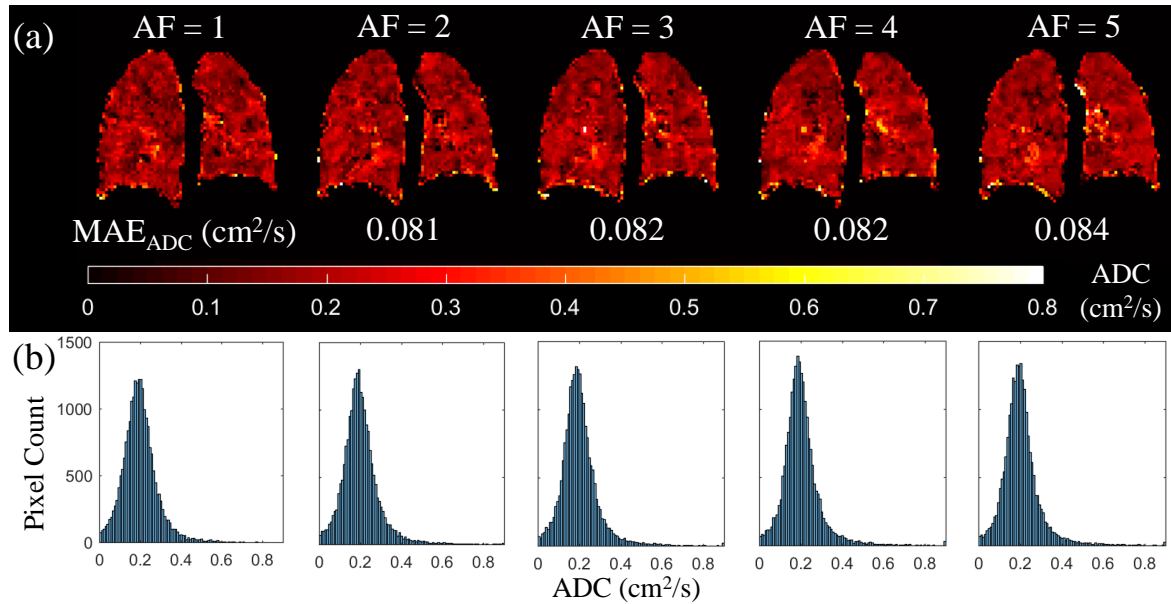
Figure 5.2: ADC results from 3D ^{3}He CS simulations. (a) ADC maps for an example slice at each AF, with corresponding MAE_{ADC} values. (b) Whole lung ADC histograms for each AF.

As expected, MAE_{MAG} increased with AF in CS simulations, which manifested as blurring of image detail due to a reduction in sampling of high frequency k-space components at higher AFs. These blurring effects are an intrinsic result of the variable density k-space sampling patterns used in the CS simulations. The majority of the information in hyperpolarised gas lung images arises from low frequency k-space components, therefore, a probability density function is used to sample the centre of k-space more heavily than the periphery. The increasingly lower sampling density of high frequency components with increasing AF may limit the implementation of high AFs (4 or 5) for 3D ^{3}He lung MRI acquisitions due to the increasing loss of spatial resolution of the reconstructed images at these high AFs. These blurring effects could be mitigated by incorporating prior-knowledge into the CS reconstruction

process to improve reconstruction accuracy [266], and thus improve the preservation of edge details of the 3D CS multiple b-value diffusion-weighted MR lung images. This may permit the use of higher AFs for higher nominal spatial resolutions or the acquisition of additional diffusion interleaves in the same acquisition time.

In this work, a constant flip angle ($\sim2°$) scheme was used that has an associated decrease in signal with each phase encode due to depletion of the non-renewable magnetisation. This results in a k-space filter (Figure 3.15), and in conjunction with random k-space sampling, discontinuities in signal amplitudes may be generated that manifest as ringing image artefacts. The implementation of a variable flip angle scheme, in theory, the optimal scheme for SPGR sequences, could prevent this due to the increasing flip angle per phase encode that maintains a constant transverse magnetisation. However, no ringing artefacts were observed in the reconstructed CS undersampled images, therefore constant flip angles were used for all undersampled DW-MRI acquisitions.

Mean ADC and skewness of the ADC histogram was observed to increase with AF. The slight increase in mean ADC value observed with retrospective undersampling was within the range of healthy lung ADC values (~0.20 cm^2/s) at b = 1.6 s/cm^2 found in previous studies [91, 92, 103]. Increased skew and mean ADC value can be attributed to the increase in mean absolute error (MAE$_{MAG}$ and MAE$_{ADC}$) with increased undersampling. With CS, some information loss is inevitable from the undersampling of k-space, which increases errors and creates a noise-like artefact in the magnitude images.

	AF = 1	AF = 2	AF = 3	AF = 4	AF = 5
Global ADC	0.193	0.193	0.193	0.195	0.195
Skew	0.497	0.340	0.295	0.412	0.212
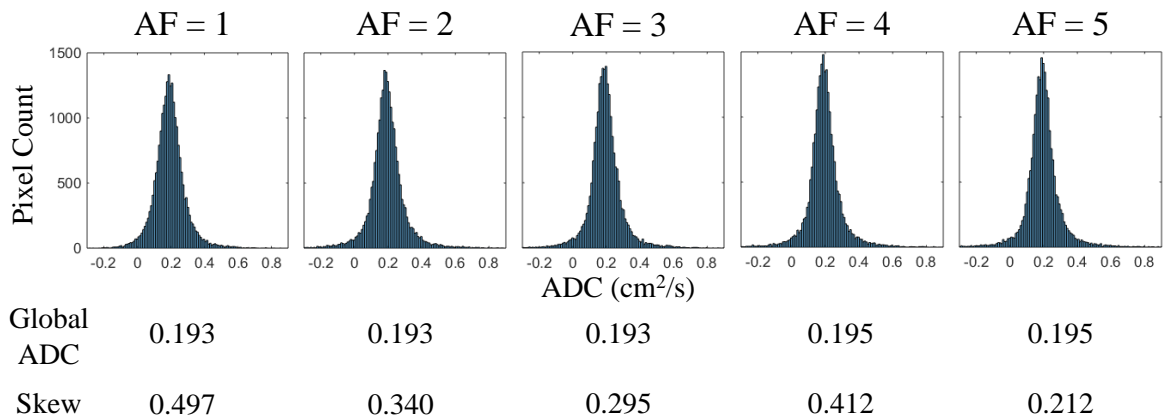
Figure 5.3: Whole lung ADC histograms for each AF without asymmetric ADC cut-off. Less skew and more comparable global mean ADC values are observed with increased undersampling.

The small increase in MAE$_{ADC}$ results in a few physiologically-unrealistic low and high ADC values in some pixels. Examples can be observed at the periphery of the single slice CS undersampled ADC maps in Figure 5.2a. An asymmetric cut-off of negative (ADC<0), or physically too high (ADC>$D_0 = 0.88$ cm^2/s) values was applied during the creation of the ADC maps; however, some of the retained artificially high pixel values will still influence

the mean and skewness of the histogram. If the whole histogram is considered (Figure 5.3) (i.e. no cut-off of lower and higher ADC limits is applied), the change in skewness of the ADC histogram between AFs is much lower and the maximum difference in global ADC value becomes only 1.0%, when compared to the 4.0% difference observed (see Table 5.1) when the asymmetric cut-off is applied.

ADC histograms also appeared narrower at larger AFs due to the smaller FWHM values observed with increased undersampling. This trend can be explained by the properties of CS reconstruction; in that de-noising is used to remove noise artefacts introduced by undersampling [225]. Narrower ADC histograms from increasingly undersampled ^{3}He ADC data were also observed previously [264]. The standard deviation of the global and slice ADC values from reconstructed CS datasets were larger than corresponding fully-sampled values; a trend opposite to that reported by Ajraoui et al. [264]. This difference is likely the result of pixels with high ADC value being introduced from increased MAE$_{ADC}$, causing a larger standard deviation of ADC values. The decrease in FWHM value observed with increased undersampling more accurately reflects the de-noising and smoothing of the CS reconstruction process.
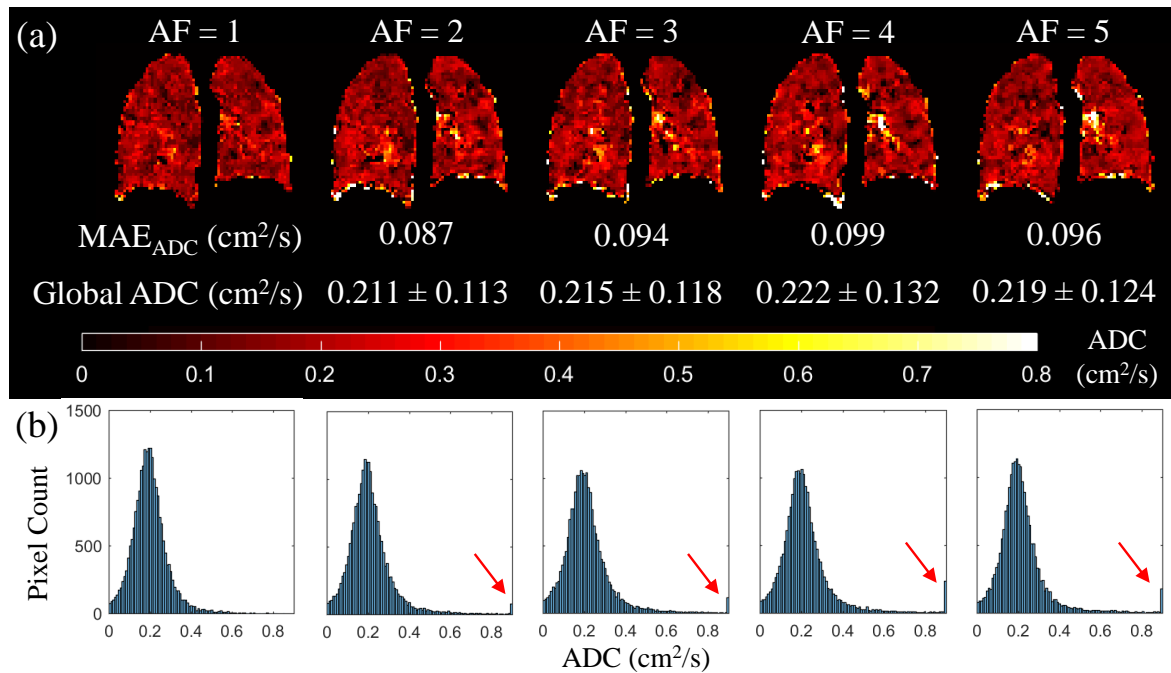
Figure 5.4: MAE$_{MAG}$ optimised ADC results from 3D ^{3}He CS simulations. (a) ADC maps for an example slice at each AF, with corresponding MAE$_{ADC}$ and global ADC values. (b) Corresponding whole lung ADC histograms for each AF.

In this work, CS simulations were optimised by minimising MAE$_{ADC}$, while in previous work, only MAE$_{MAG}$ was minimised for 2D ADC mapping with ^{3}He [264]. Here, the ADC values obtained from simulations optimised with minimum MAE$_{ADC}$ were found to be more comparable with fully-sampled datasets than those using the minimum MAE$_{MAG}$ method. In Figure 5.4a, the representative slice ADC maps optimised with the MAE$_{MAG}$ method

demonstrated an increased number of physiologically-unrealistic high ADC pixels at the lung periphery in comparison to the ADC maps in Figure 5.2a. These high ADC pixels, which can also be observed on the far right (red arrows) of the whole lung ADC histograms in Figure 5.4b, resulted in increased MAE_{ADC} and global ADC values (in comparison to the MAE_{ADC} optimisation method) for the MAE_{MAG} optimised CS-reconstructed images.

The optimal penalty weight parameters (λ_1 and λ_2) for simulations resulting in minimum MAE_{ADC} were also found to be smaller than those resulting from MAE_{MAG} simulations. Considering the non-linear CS reconstruction algorithm in Equation 3.74, this finding indicates that the reconstructed images with minimum MAE_{ADC} have more total variation and less sparsity when compared with images reconstructed with minimum MAE_{MAG}, implying that data consistency was better maintained during the reconstruction process, leading to improved preservation of quantitative lung microstructural information.

5.3   Prospective acquisition of 3D multiple b-value ^{3}He DW-MRI with CS

This section implements the optimised three-fold undersampling *k*-space pattern from Section 5.2 for prospective CS undersampling of 3D multiple b-value ^{3}He DW-MRI to obtain maps of whole lung morphometry in a single breath-hold.

5.3.1   Methods

Prospective CS datasets with four diffusion-weighted interleaves were acquired in five healthy volunteers and one COPD patient (spirometric forced expiratory volume in 1 second, FEV_1 = 31.2% predicted) using the optimal undersampling pattern for AF = 3 (see Figure 5.1a). Three-fold undersampling was chosen because it was the highest AF achievable without introducing extensive image blurring, and allowed a scan time reduction from 45 seconds to 15 seconds, which is a tolerable breath-hold for most clinical subjects. The 3D CS multiple b-value DW-MRI datasets were acquired in a similar fashion to the fully-sampled acquisition in Section 5.2 with an identical ^{3}He dose, FOV, and voxel size. Additional imaging parameters were: 4 diffusion-weighted interleaves (b = 0, 1.6, 4.2, 7.2 s/cm^2), TE/TR = 4.2/6.0 ms, diffusion time = 1.6 ms (maximum diffusion-weighted gradient strength = 30 mT/m, ramp = 0.3 ms, plateau = 1.0 ms), flip angle = 1.9° (hard RF pulse as above). ADC maps were calculated from the first two interleaves, while Lm_D maps were derived from all four interleaves using the stretched exponential model (see Section 3.5.2).

To validate the ADC and Lm_D microstructural measurements derived from prospective 3D CS data, the same five healthy volunteers were imaged with fully-sampled 3D and 2D ^{3}He

DW-MRI using the scan parameters detailed in the Section 5.2 and below, respectively. 3D fully-sampled data was also acquired from the COPD patient, however 2D fully-sampled data was not acquired due to patient overall scan time constraints. The selection of b-values used in all scans was consistent and chosen to ensure that one of the diffusion interleaves corresponded to b = 1.6 s/cm^2; the b-value most commonly used for ^{3}He ADC calculation in the literature to date [92–94, 101–104, 117]. 2D multiple b-value DW-MRI data was acquired with similar FOV and slice thickness as the corresponding 3D datasets. Six slices were acquired with 12 mm thickness and 12 mm gap, using a gas dosage of 300 ml ^{3}He (mixed with 700 ml N$_2$) at a lung inflation state of FRC+1L. Additional imaging parameters were: 4 diffusion-weighted interleaves (b = 0, 1.6, 4.2, 7.2 s/cm^2), 96×72 in-plane matrix, in-plane FOV = 40×30 cm^2, TE/TR = 4.9/10 ms, diffusion time = 1.6 ms (maximum diffusion-weighted gradient strength = 30 mT/m, ramp = 0.3 ms, plateau = 1.0 ms), flip angle = 5° (sinc RF pulse), bandwidth = ±31.25 kHz.

Comparisons of ADC and Lm_D values were made between each corresponding dataset acquired from each subject. ADC values were compared between 3D fully-sampled and 3D CS acquisitions, while Lm_D estimates were compared between 2D fully-sampled and 3D CS acquisitions from corresponding slices. To investigate the agreement between the two sets of measurements, scatter plots and Bland-Altman analysis were used to compare the relative difference in ADC and Lm_D values on a slice-by-slice level.

5.3.2   Results

The four-interleaved 3D ^{3}He DW-MRI CS datasets were reconstructed from the three-fold undersampled (AF=3) *k*-space using the optimal reconstruction parameters determined in Section 5.2. Example 3D whole lung coverage maps of ADC (mean = 0.198 cm^2/s) and Lm_D (mean = 222.8 µm) are shown for a representative healthy subject in Figure 5.5.

A summary of global mean ADC and Lm_D values for all subjects imaged (five healthy volunteers and one COPD patient) is presented in Table 5.2. For every subject, the global mean ADC value derived from the 3D CS acquisition was equal to or higher than the value obtained from the corresponding 3D fully-sampled acquisition. The difference in ADC values between fully-sampled and CS datasets ranged from 0.0% to 5.9% with a mean difference of 3.4%. Global Lm_D values exhibited a similar increase for 3D CS acquisitions and a slightly higher mean difference of 5.1% was calculated. Lm_D values provide an estimate of the alveolar size, (example whole lung Lm_D maps from a healthy subject and the COPD patient are shown in Figure 5.6) demonstrating the clinical potential of this 3D CS multiple b-value DW-MRI sequence to provide volumetric, quantitative microstructural maps.
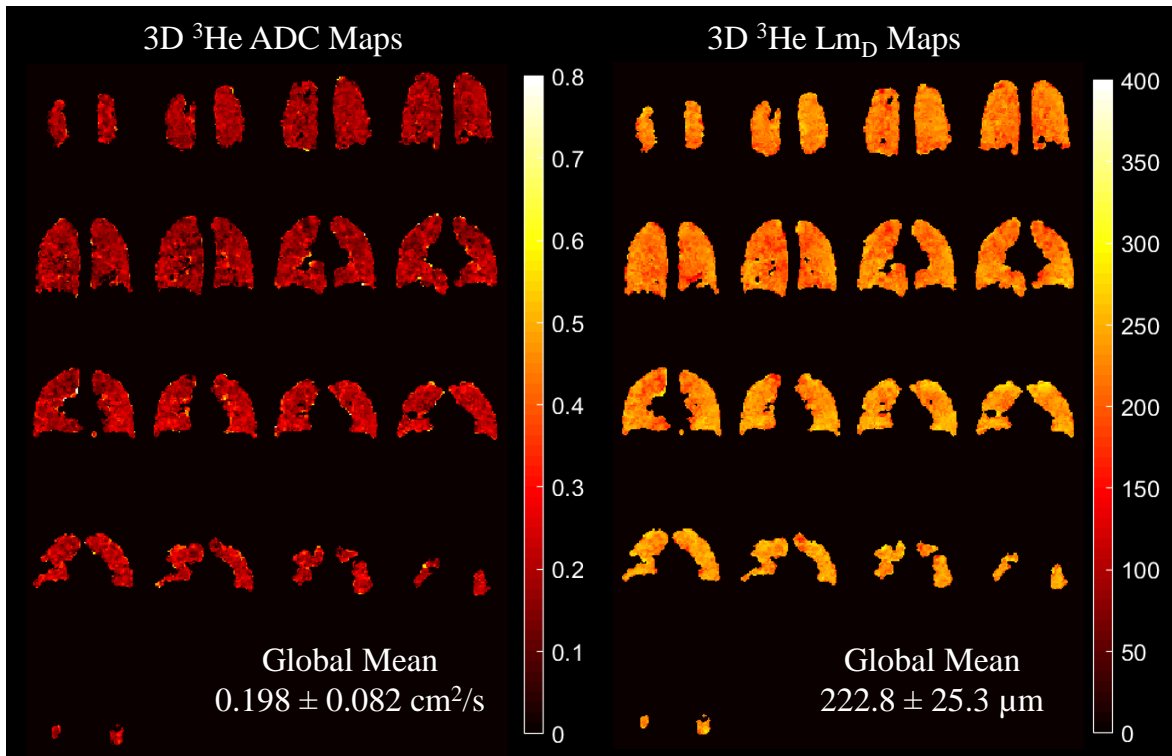
Figure 5.5: 3D ADC and mean diffusive length scale (Lm_D) maps derived from prospective 3D ^{3}He DW-MRI CS acquisition from a healthy volunteer (15 s breath-hold) with three-fold undersampling and four diffusion interleaves.

Table 5.2: Global ADC and Lm_D values calculated from fully-sampled and CS acquisitions for the five healthy volunteers and one COPD patient.

Subject	Imaging Method	Global ADC (cm^2/s)	ADC difference	Global Lm_D (µm)	Lm_D difference
Healthy 1	FS	0.198 ± 0.085	0.0%	208.6 ± 29.8	6.8%
	3D CS	0.198 ± 0.082		222.8 ± 25.3	
Healthy 2	FS	0.163 ± 0.082	4.3%	192.6 ± 27.0	6.0%
	3D CS	0.170 ± 0.077		204.1 ± 23.2	
Healthy 3	FS	0.152 ± 0.083	5.9%	184.5 ± 31.0	8.3%
	3D CS	0.161 ± 0.069		199.8 ± 27.0	
Healthy 4	FS	0.163 ± 0.068	1.8%	197.5 ± 24.2	3.6%
	3D CS	0.166 ± 0.067		204.6 ± 23.6	
Healthy 5	FS	0.169 ± 0.081	5.9%	207.5 ± 24.6	0.7%
	3D CS	0.179 ± 0.078		209.0 ± 29.1	
COPD 1	FS	0.525 ± 0.169	2.7%	_a	-
	3D CS	0.539 ± 0.186		313.6 ± 56.1	

[a] 2D fully-sampled DW-MRI was not acquired from the COPD patient due to overall scan time constraints
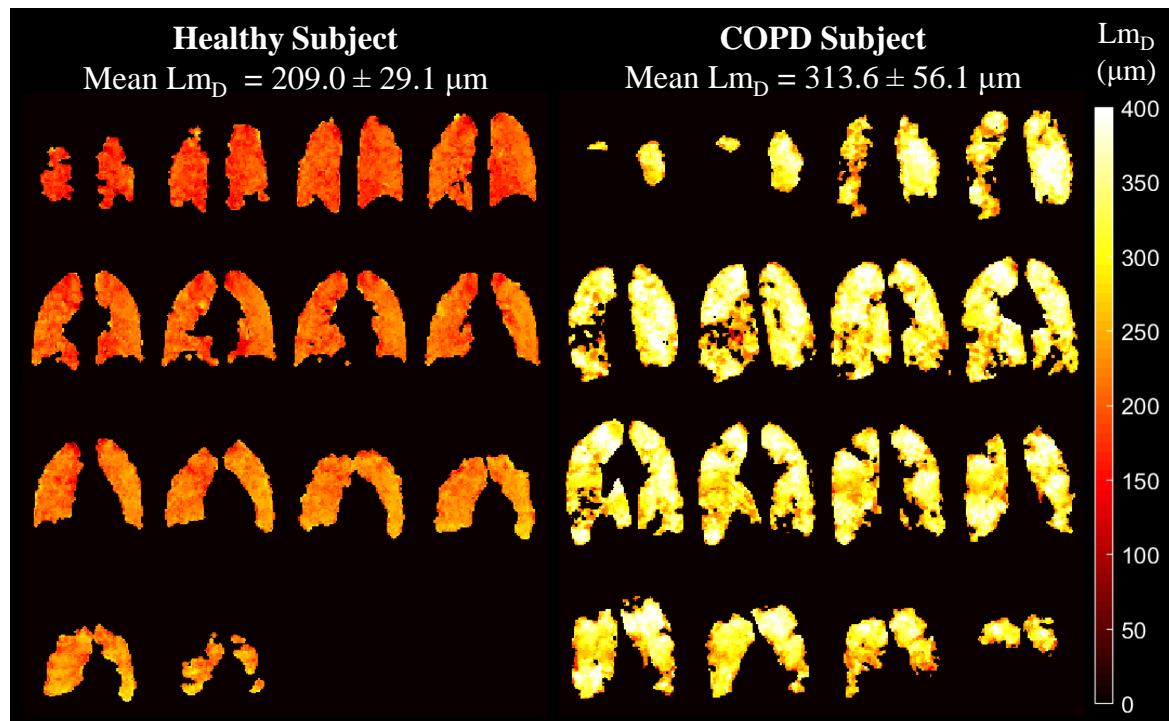
Figure 5.6: Whole lung coverage Lm_D maps calculated from 3D multiple b-value ^{3}He DW-MRI with CS from a healthy (left) and COPD subject (right).

A scatter plot of single slice ADC values calculated from 3D fully-sampled and 3D CS datasets (Figure 5.7a) shows excellent correlation (r = 0.995, $P{<}0.001$). Two clusters of data points can be observed, corresponding to the healthy and COPD patient groups. The agreement between the two measurements was confirmed by Bland-Altman analysis (Figure 5.7b). The mean slice-by-slice ADC % difference between methods was +2.1% (absolute difference of 0.005 cm^2/s), and 95% of the difference was within -9.2% to +13.4% (-0.024 to 0.034 cm^2/s). Similar levels of agreement in the Lm_D value was observed, as illustrated in the equivalent scatter and Bland-Altman plots (see Figure 5.7c and 5.7d). The mean Lm_D % difference of +4.7% (absolute difference of 9.29 µm) was larger than the mean ADC % difference, and 95% of the difference was within -2.1% to +11.4% (-4.65 to 23.23 µm).

5.3.3   Discussion

CS has facilitated the acquisition of 3D multiple b-value diffusion-weighted MR lung images with hyperpolarised ^{3}He in a single breath-hold, for the purpose of diffusion modelling of lung microstructure using a stretched exponential model approach. Prospective three-fold undersampled 3D ^{3}He DW-MRI datasets were acquired in five healthy volunteers and one COPD patient, and quantitative measures of lung microstructure were compared to fully-sampled 2D and 3D DW-MRI datasets.
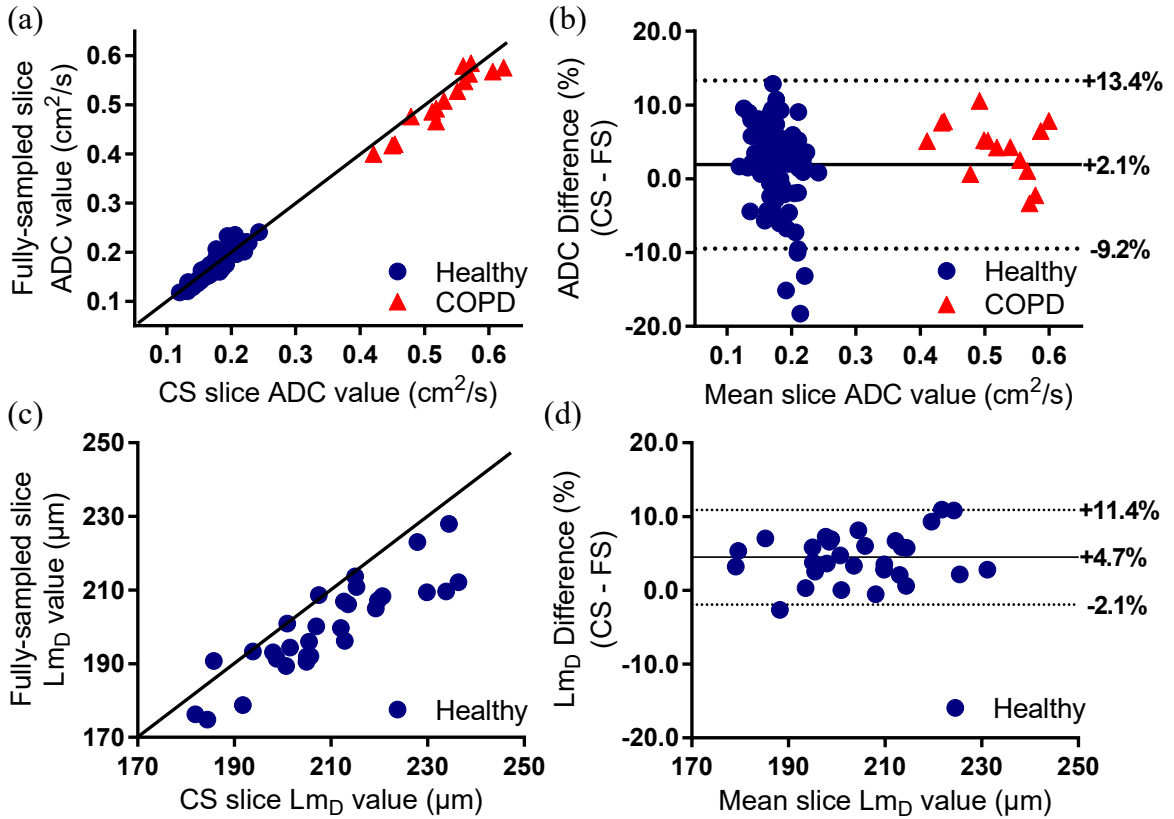
Figure 5.7: (a) Slice-by-slice comparison of mean ADC values between 3D fully-sampled and 3D CS datasets for all five healthy volunteers and one COPD patient. (b) Bland-Altman plot showing the agreement between the two methods. The percentage difference in slice ADC values is plotted against the mean slice ADC values between the two measurements. (c) Equivalent slice-by-slice comparison of mean Lm_D values between 2D fully-sampled and 3D CS datasets for all five healthy volunteers. (d) Equivalent Lm_D Bland-Altman plot showing a similar agreement between the two methods.

A small positive bias in global mean ADC and Lm_D value was observed between 3D CS and fully-sampled 2D and 3D datasets for all subjects (see Table 5.2), which could be attributed to the increase in MAE_{ADC} due to undersampling. These values were however within typical mean standard deviation ranges, and consistent with reported healthy and COPD lung ADC values [91, 92, 103] and similar to mean linear intercept values obtained from human lung histology samples ($\sim$200 µm in healthy, $\sim$400 µm in COPD) [96]. A small positive bias in undersampled ADC and Lm_D values is similar to the trend observed previously in accelerated 2D ^{3}He DW-MRI with parallel imaging [269]. In this feasibility study, GRAPPA reconstructions enabled an effective AF of 1.74, and a similar small positive bias in lung morphometry measurements, derived from the cylinder model, was reported.

The dependency of lung microstructural measurements on SNR has been explored previously [270, 271], and it was determined with Monte Carlo simulations that in low SNR conditions, ADC and cylinder model metrics can be biased leading to low mean values with high

standard deviations. O'Halloran et al. [270] demonstrated that for SNR<15, ADC values are SNR-dependent; while when SNR>15, ADC is independent of SNR for the typical physiological range of ADC values (up to 0.6 cm^2/s). In this work, the SNR for each dataset was computed in the magnitude images (b = 0) by dividing the mean signal of the entire segmented lung region by a background noise region corrected for Rician distribution bias [272]. It should be noted that SNR calculated from CS images present a biased measure of SNR, due to the denoising process associated with CS reconstruction. The average global SNR for 3D CS undersampled and fully-sampled datasets used for ADC validation (see Table 5.2) were 25 and 12, respectively. This indicates that derived ADC values are predominantly SNR independent, and differences between CS and fully-sampled values are likely attributed to the CS reconstruction process.

In a slice-by-slice comparison of fully-sampled and CS-derived ADC and Lm_D values, good agreement was found with values close to the line of unity. In the quantitative comparisons of both ADC and Lm_D, 95% of the difference between fully-sampled and CS datasets was well within the standard deviation range of mean values. In the CS simulations (where there is intrinsically no variability between scans, unlike the prospective acquisitions that are performed in separate breath-holds) a ∼2% ADC mismatch was observed between the fully-sampled and three-fold undersampled CS reconstruction, which was attributed to CS reconstruction error.

Despite the observation of a small positive bias in CS-derived ADC and Lm_D values, the biases are negligible when compared with the large differences in lung microstructure between healthy and COPD subjects; ADC and mean linear intercept length values of emphysema subjects vary depending on disease severity but are typically 2–2.5 times larger than those of healthy subjects [91, 96]. Thus, our results indicate that 3D multiple b-value ^{3}He DW-MRI with CS has the potential to be used clinically to track changes in lung microstructure associated with emphysematous disease. 3D multiple b-value data enables the derivation of Lm_D across the entire lung volume from the stretched exponential model, allowing for volumetric lung microstructural estimates and reformatting of lung morphometry maps in any slice direction. The 3D multiple b-value acquisition strategy proposed here is also fully compatible with alternative diffusion analyses and morphometric models, for instance the cylinder model [5, 128] or q-space transform analysis [130].

One limitation of the slice-by-slice comparison of lung microstructural measurements between fully-sampled and CS datasets was that the lung volume was assumed to be the same for each acquisition. Subjects were instructed to inhale the ^{3}He and N$_2$ gas dosage from FRC to produce a lung volume of FRC+1L. However, this inflation volume may not have been reproduced exactly for each acquisition. A difference in lung inflation level of 6% when compared with 15% of total lung capacity (TLC) has been shown to have a relatively minor effect on global mean ADC values [103]. However, this could also result in mismatched slices

from the fully-sampled and CS datasets that can be additionally affected by the gravitational dependence of lung ventilation. For example, in the supine position, ^{3}He ADC values have been shown to be larger in the anterior regions of the lung when compared to the posterior regions, due to the gravitational compression of lung tissue in the posterior dependent lung [100].

5.4 3D ^{3}He multi-parametric mapping with multi-interleaved sequence and CS

Hyperpolarised ^{3}He gas MRI has been shown to provide quantitative measures of regional lung ventilation [181], and lung microstructure through ADC [91] and lung morphometry parameters [5, 6, 129, 130]. The effective transverse relaxation time (T_2^*) is also sensitive to lung microstructure through changes in microscopic magnetic field inhomogeneity [273]. Equation 3.21 states that T_2^* is the combination of relaxation from spin-spin interactions (T_2) and magnetic field inhomogeneities (T_2'). In hyperpolarised gas MRI, the majority of magnetic field inhomogeneity is due to air-tissue interfaces that cause bulk magnetic susceptibility, and leads to short T_2^* times (^{3}He T_2^* at 1.5 T ∼28 ms [119]). T_2^* is therefore representative of the underlying lung microstructure and has been demonstrated to be sensitive to changes in the air-tissue interface [274], lung inflation [275], and alveolar dimension through gravitational gradients [276].

The acquisition of all these complementary metrics of lung structure and function requires multiple ^{3}He acquisitions, a process that is currently unsustainable due to shortage and expensive cost of ^{3}He gas [110]. Previously, hybrid gradient echo sequences have been developed to allow the acquisition of 2D ^{3}He ADC maps with ventilation images [277] and T_2^* maps [278] in a single breath-hold. Further advances in imaging techniques have allowed single breath-hold acquisition of 2D ^{3}He ventilation, ADC, T_2^*, and B_1 maps at 3 T with CS [267]. This 2D multi-slice acquisition however, did not provide whole lung coverage or multiple b-value data for Lm_D or lung morphometry calculation. The purpose of this section was to investigate the feasibility of implementing a 3D ^{3}He multiple-interleaved sequence with CS for acquisition of whole lung co-registered ^{3}He ventilation images, and parametric maps of ADC, Lm_D, and T_2^* within a single breath-hold.

5.4.1 Methods

A schematic of the 3D multi-interleaved sequence is presented in Figure 5.8. This is based upon the 3D multiple b-value DW-MRI sequence developed in Section 5.3 with an additional interleave at a different echo time to enable the calculation of T_2^* maps from a two-point exponential fit. The first interleave, that has no diffusion-weighting gradients,

was used as ventilation images. ADC maps were computed from the first and second in-
terleaves; while the first four interleaves were used to calculate Lm_D by fitting data with
the stretched exponential model (Section 3.5.2). Lastly, the first and fifth interleaves were
used to compute T_2^* maps as follows:

$$T_2^* = \frac{TE_2 - TE_1}{\ln(S_1/S_2)} \qquad (5.3)$$

where TE_1 and TE_2 are two different echo times with corresponding signal intensities
of S_1 and S_2, respectively.
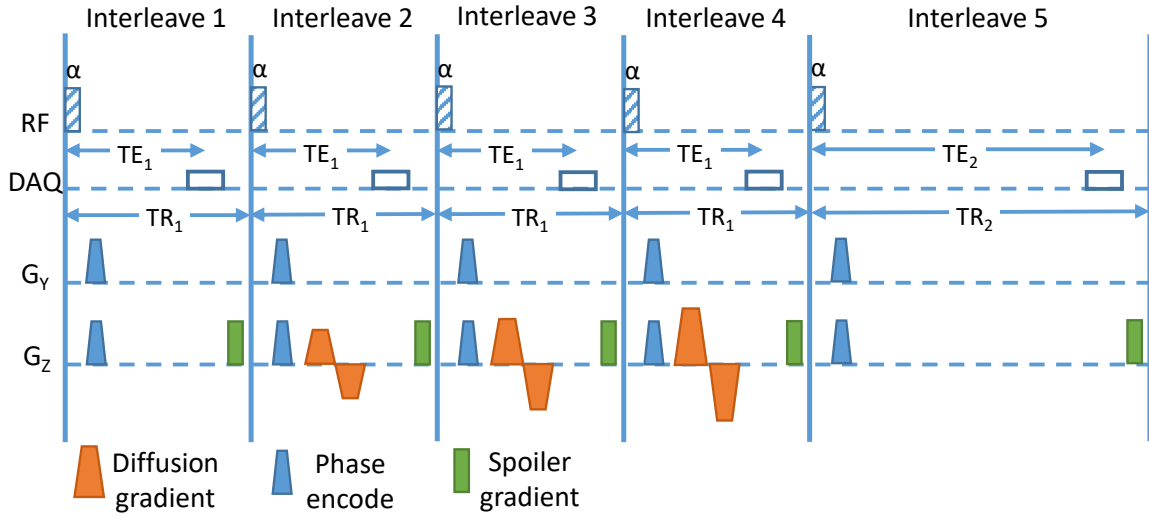
Figure 5.8: 3D multi-interleave sequence schematic. TE_1 and TE_2 are the two echo times
used for T_2^* mapping, with respective repetition times TR_1 and TR_2.

A fully-sampled three-interleaved dataset (interleaves 1, 2 and 5 in Figure 5.8) was acquired
in a healthy volunteer (M, 25y) on a GE HDx 1.5 T MR scanner using 400 ml of ^{3}He ($\sim$25%
polarisation) and 600 ml of N$_2$ at FRC. Imaging parameters were: 3D SPGR, b = 0, 1.6
s/cm^2, 80$\times$66$\times$22 matrix, FOV = 40$\times$32.5$\times$26.4 cm^3, TE$_1$/TR$_1$ = 4.1/5.7 ms, TE$_2$/TR$_2$ =
9.8/11.4 ms, diffusion time = 1.6 ms (diffusion-weighted gradient strength = 14.1 mT/m,
ramp = 0.3 ms, plateau = 1.0 ms) flip angle = 1.4°, bandwidth = $\pm$31.25 kHz. Retrospective
CS undersampling of the fully-sampled dataset was implemented to determine optimal *k*-
space undersampling patterns for AFs between 2 to 5. CS simulations were optimised by
minimising the MAE between retrospectively undersampled and fully-sampled ventilation
images (MAE$_\text{MAG}$), ADC maps (MAE$_\text{ADC}$), and T_2^* maps (MAE$_\text{T2*}$).

The five-interleaved sequence was then implemented with CS in a prospective acquisition
in the same healthy volunteer. Three-fold undersampling was introduced as a compromise
between scan time reduction ($\sim$17 s) and preservation of ADC and T_2^* information. Imaging
parameters were as above, except four b-values (0, 1.6, 4.2, 7.2 s/cm^2), DW gradient strength
= 30.0 mT/m, and flip angle = 1.9° were used. Prospectively acquired CS ADC and T_2^*
maps were compared to corresponding fully-sampled maps calculated from the fully-sampled

dataset. Lm_D maps were compared to those acquired previously in the same volunteer using 2D fully-sampled multiple b-value DW-MRI (see 'Healthy 5' in Table 5.2).

A second set of prospective CS multi-interleaved ^{3}He and 3D ^{1}H anatomical images were acquired in the same breath-hold from the same healthy volunteer to enable the calculation of percentage ventilated volume (VV%) from co-registered ^{3}He and ^{1}H images [181] for comparison with the ^{3}He multi-parametric maps demonstrated in the previous prospective acquisition. Prospective CS imaging parameters were the same, apart from a decrease in effective slice thickness from 12 to 10 mm, and elliptical-centric phase encoding to maximise SNR lost through increased slice resolution. The ^{1}H anatomical scan was acquired at the same voxel size as prospective CS multi-interleaved ^{3}He; additional parameters were: 3D SPGR, TE/TR = 0.5/1.3 ms, bandwidth = ±83.3 kHz, and flip angle = 5°.

VV% was calculated using a custom-built semi-automated image segmentation workflow [279]. Briefly, ^{3}He and ^{1}H images were filtered using a bilateral filter, and then clustered using a spatial fuzzy C-means algorithm to create binary masks. VV% was subsequently calculated from the respective binary masks by dividing the ^{3}He ventilated volume (VV) by the ^{1}H total lung volume (TLV):

$$VV\% = \frac{VV}{TLV} \times 100\% \tag{5.4}$$

5.4.2 Results

Optimal k-space undersampling patterns and penalty weight parameters for each AF were established from retrospective CS simulations. Table 5.3 summarises the CS simulation results for each retrospective CS dataset reconstructed from optimal undersampling patterns. The MAE_{MAG} value, the MAE between fully-sampled and reconstructed ventilation images (b = 0), increased for each AF; however, ventilation images showed good qualitative preservation of main spatial details and no additional artefacts were observed at high AFs (Figure 5.9a). Reconstructed ADC maps exhibited a similar trend; the global mean ADC value slightly increased with increasing MAE_{ADC}, and ADC maps appeared visually similar indicating a good preservation of lung microstructural information (Figure 5.9b). The comparatively large MAE_{T2*} values observed with increasing AF are reflected in decreased global T_2^* values (up to 30% smaller at AF=5) and increased homogeneity of reconstructed T_2^* maps (Figure 5.9c).

The prospective CS five-interleaved dataset has enabled whole lung coverage, 3D co-registered ^{3}He ventilation images, parametric maps of ADC, Lm_D, and T_2^* to be acquired in a single breath-hold. Prospective CS-derived global mean ADC (0.172 ± 0.069 cm^2/s) and Lm_D (210.7 ± 28.6 µm) values were 0.6% and 1.7% larger than the corresponding 3D and 2D fully-sampled equivalent values (0.171 ± 0.070 cm^2/s and 207.2 ± 24.6 µm, respectively). The global mean T_2^* value for the prospective CS dataset (21.3 ± 19.5 ms) was 11.3% smaller

Table 5.3: Summary of 3D ^{3}He multi-interleaved sequence CS simulations.

AF	MAE$_{\text{MAG}}$	Global ADC (cm^2/s)	MAE$_{\text{ADC}}$ (cm^2/s)	Global T_2^* (ms)	MAE$_{\text{T2*}}$ (ms)
1	-	0.171 ± 0.070	-	24.0 ± 20.2	-
2	0.018	0.172 ± 0.076	0.048	20.7 ± 18.5	12.7
3	0.024	0.173 ± 0.077	0.053	18.7 ± 16.9	13.7
4	0.029	0.173 ± 0.074	0.056	17.9 ± 16.6	14.1
5	0.034	0.173 ± 0.072	0.056	16.8 ± 15.4	14.1
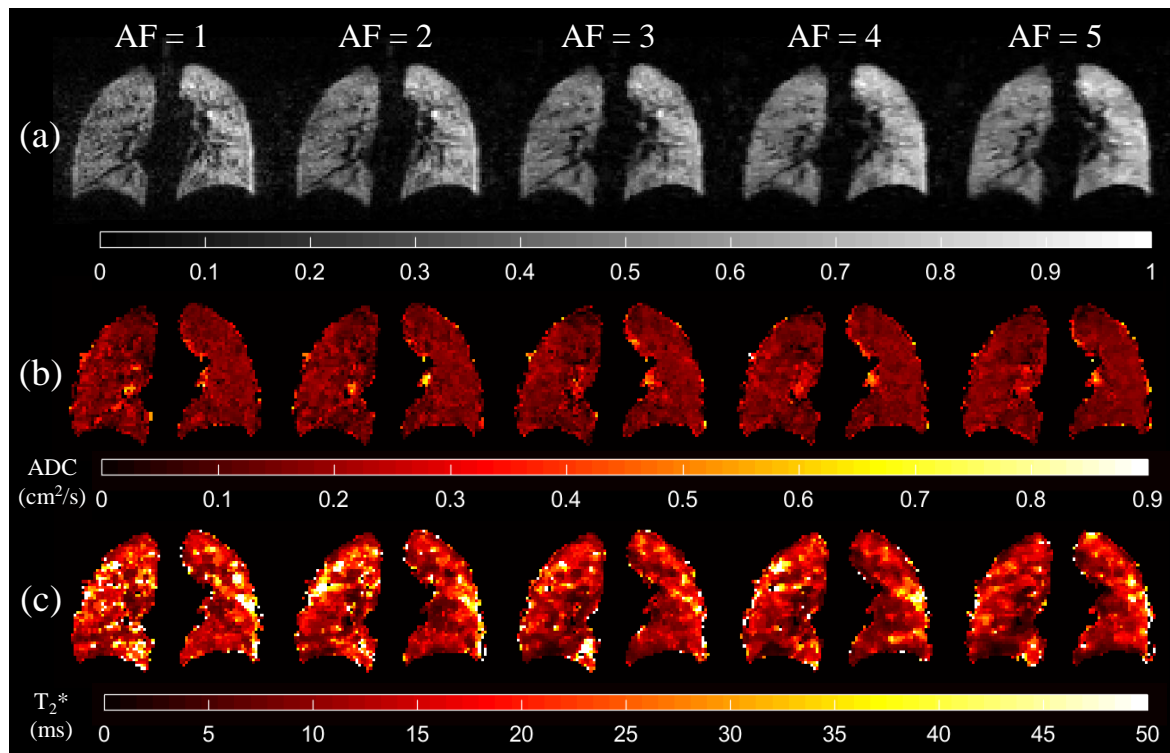
Figure 5.9: Example lung slice ^{3}He ventilation images, ADC maps and T_2^* maps for each acceleration factor obtained from CS simulations.

than the fully-sampled mean value (24.0 ± 20.2 ms); however, the CS value was 13.9% larger than the simulated AF=3, T_2^* value.

The combined ^{3}He prospective CS and ^{1}H anatomical scan was acquired in a single 22 second breath-hold. Maps of ventilated volume, ADC, Lm_D, and T_2^* were calculated and shown in Figure 5.10. Global ADC and Lm_D were comparable to values obtained in the same volunteer previously. In contrast, global T_2^* (16.1 ± 12.5 ms) was notably smaller than previous prospective CS acquisition, and 32.9% smaller than the fully-sampled T_2^* value. Semi-automated segmentation of ^{3}He ventilation (b = 0) and ^{1}H images derived a global 90.7% VV% for the healthy volunteer.
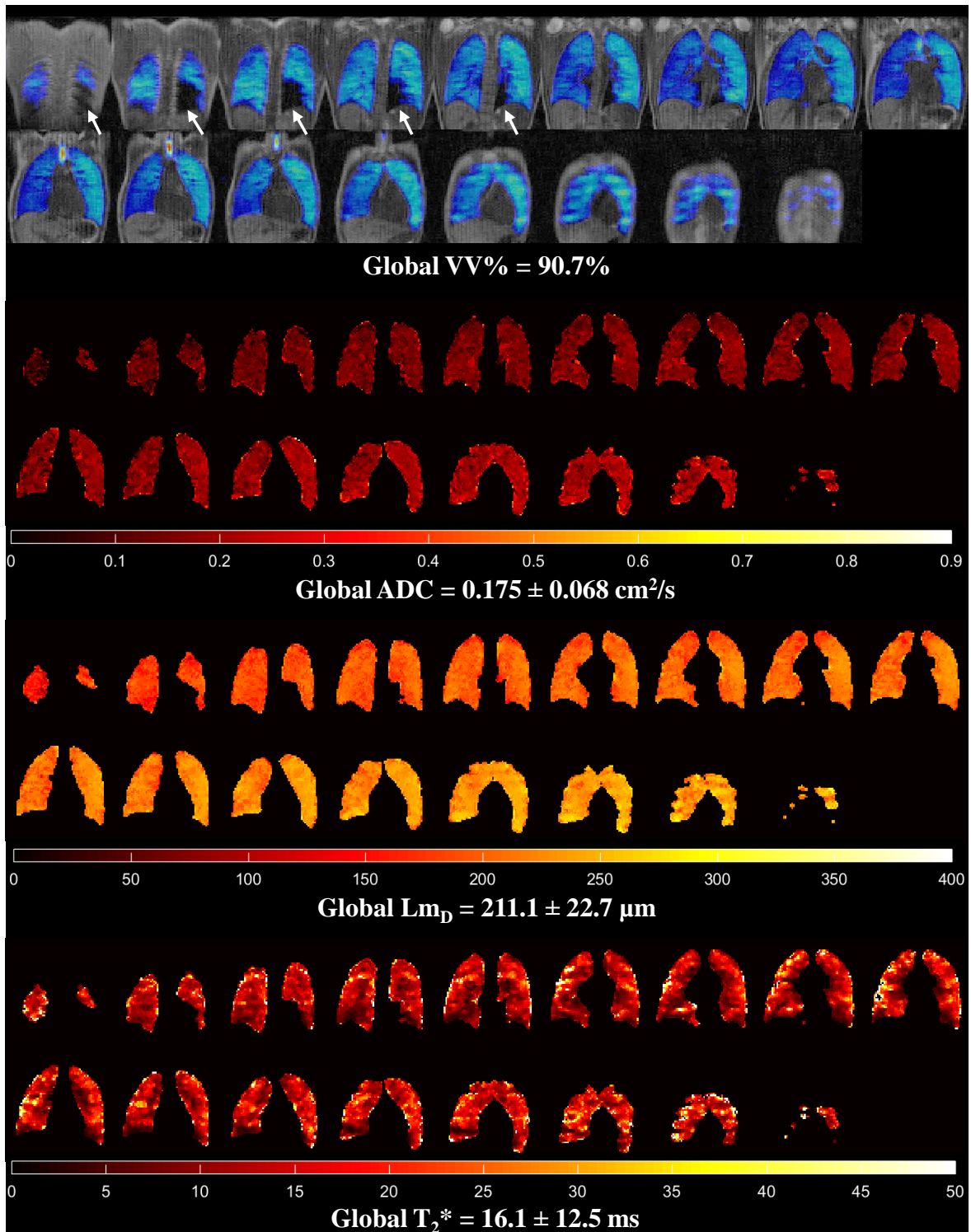
Figure 5.10: Maps of percentage ventilated volume (VV%), ADC, Lm_D, and T_2^* for a healthy volunteer imaged with prospective CS ^{3}He multi-interleaved sequence and ^{1}H anatomical scan in a single breath-hold.

5.4.3   Discussion

Global mean ADC and T_2^* values from the fully-sampled three-interleaved dataset were consistent with reported values for healthy lungs at b = 1.6 s/cm^2 [92] and 1.5 T [119]. Increases in MAE$_{MAG}$, MAE$_{ADC}$ and global ADC value with increased undersampling matched the results observed in previous 3D ^{3}He DW-MRI CS simulations (Section 5.2). MAE$_{T2*}$ value also increased with AF, corresponding to a decrease in global T_2^* values that may be attributed to the smoothing process associated with CS reconstruction [267]. The small positive bias in prospective CS-derived ADC and Lm_D values is consistent with previous observations in CS-derived microstructure measurements. The prospective CS acquired T_2^* value was considerably smaller than the fully-sampled T_2^* value; this was in agreement with the T_2^* CS simulations.

The choice of ΔTE for the multi-interleaved sequence was 5.7 ms, which was significantly shorter than the ΔTE = 13 ms used previously for T_2^* estimation at 1.5 T [119]. This ΔTE was chosen to minimise acquisition time and maximise image SNR, whilst attempting to sample the T_2^* signal decay to reliably calculate T_2^*. For validation, a multi-slice two interleaved fully-sampled dataset with a ΔTE of 13 ms and a 3D fully-sampled three-interleaved dataset with ΔTE = 10.7 ms were acquired in the same healthy subject. The voxel size for the validation datasets were identical to the 3D multi-interleaved sequence. Global T_2^* estimates for the fully-sampled ΔTE = 13 ms, and ΔTE = 10.7 ms datasets were 23.7 ± 17.6 ms and 23.7 ± 18.4 ms respectively; consistent with the fully-sampled T_2^* value obtained for ΔTE = 5.7 ms (24.0 ± 20.2 ms).

Table 5.4: Summary of mean % biases between CS simulation undersampled (AF) and fully-sampled signal intensities for each interleave of the fully-sampled three-interleaved dataset. The mean bias in the ratio signal intensities used to derive ADC and T_2^* values are shown as well.

	Mean % bias in signal intensity (undersampled (AF) – fully-sampled)				
AF	**Interleave 1** (TE$_1$ = 4.1 ms) (b = 0)	**Interleave 2** (TE$_1$ = 4.1 ms) (b = 1.6 s/cm^2)	**Interleave 3** (TE$_2$ = 9.8 ms) (b = 0)	**ADC signal ratio** (Int 1/Int 2)	T_2^* **signal ratio** (Int 1/Int 3)
2	-5.7	-5.5	-12.0	-0.2	6.3
3	-7.7	-7.6	-17.7	-0.1	10.0
4	-9.6	-9.4	-22.8	-0.2	13.4
5	-11.3	-11.3	-26.9	0.0	16.1

To investigate if the observed smaller CS-derived T_2^* values are related to CS reconstruction, the signal intensities of each interleave in the fully-sampled three-interleaved dataset were compared to the corresponding signal intensities of the CS-simulated datasets in Table 5.3. The mean % bias in signal intensity between undersampled and fully-sampled datasets for

each interleave is summarised in Table 5.4. For all three interleaves, an increase in mean %
bias was observed with increasing AF that is reflective of the increase in MAE$_{\text{MAG}}$ value (see
Table 5.3). However, even in the presence of increased bias in each individual interleave with
undersampling, the mean bias of the signal intensity ratio used to calculate ADC (between b
= 0 and b = 1.6 s/cm^2/s interleaves) was almost zero and did not increase with AF (Table
5.4). Bland-Altman plots of this ADC ratio of signal intensities for every pixel of each AF
(Figure 5.11) confirms this trend, and a small spread of ADC ratio bias is observed. The
absence of change in the ratio of ADC signal intensities, according to Equation 3.81, will
therefore result in a preservation of ADC values, as observed in Table 5.3.
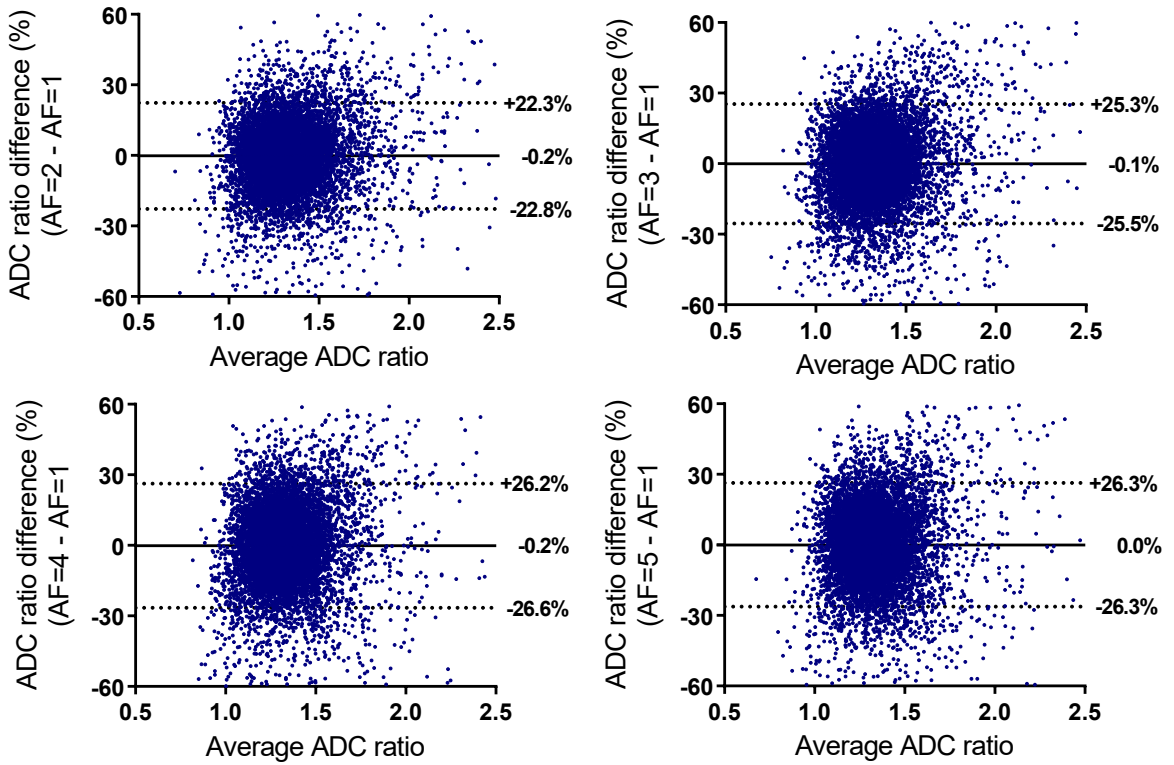
Figure 5.11: Bland-Altman plots of mean bias for each pixel between undersampled (AF)
and fully-sampled (AF=1) ratios of signal intensities of b = 0 and b = 1.6 s/cm^2 interleaves,
used to derive ADC values. Mean % bias and 95% confidence intervals are given for each
plot.

In contrast, a larger increase in mean % bias was obtained for the longer TE (9.8 ms)
interleave in comparison to the other two interleaves with TE = 4.1 ms, and this translates
to the observed increase in mean bias of the signal ratio used to derive T_2^* (between TE$_1$
= 4.1 and TE$_2$ = 9.8 ms) with increased undersampling. Corresponding Bland-Altman
plots of this T_2^* ratio of signal intensities (Figure 5.12) demonstrates this increase in mean
bias, and a larger spread of biases was obtained with T_2^* signal ratio when compared to
ADC ratio biases in Figure 5.11. According to Equation 5.3, an increase in the ratio of
signal intensities will correspond to smaller T_2^* values, and this is in agreement with the
observed decreased global T_2^* value in Table 5.3. The larger error obtained for the longer

TE interleave may be related to the inherently lower SNR of this interleave due to T_2^* decay, and the CS reconstruction error of hyperpolarised gas MR images has been demonstrated to be SNR-dependent [264]. This error manifests in a decrease of T_2^* value, and suggests that heavy undersampling with CS may not be suitable for T_2^* mapping.
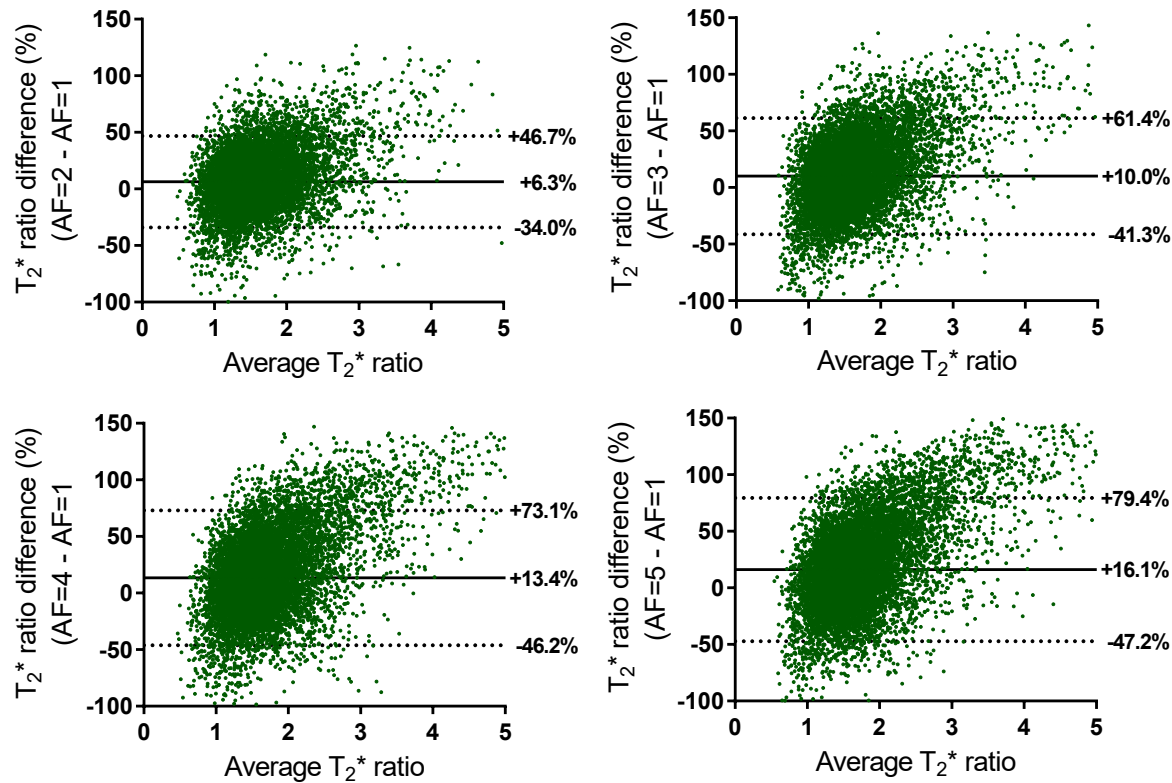
Figure 5.12: Bland-Altman plots of mean bias for each pixel between undersampled (AF) and fully-sampled (AF=1) ratios of signal intensities of TE = 4.1 and TE = 9.8 ms interleaves, used to derive T_2^* values. Mean % bias and 95% confidence intervals are given for each plot.

With the addition of a ^{1}H anatomical scan, VV%, ADC, Lm_D, and T_2^* were derived from a single ^{3}He scan of 22 seconds. The VV% for the healthy volunteer was 90.7% and is lower than the reported VV% for healthy volunteers (96%) [117]. The smaller than expected VV% in this volunteer is likely a result of the un-ventilated region of the left lower lobe, possibly due to partial lung obstruction observed in the first five slices (white arrows) in Figure 5.10. The volunteer had normal spirometry and was referred for CT that found no evidence of any structural changes. The difference in mean T_2^* between the two prospective CS scans is likely associated with the implemented phase encoding trajectories. Elliptical-centric phase encoding increases image blurring when compared to sequential encoding due to the RF depolarisation k-space filter that originates from the centre of k-space [175]. Whilst this maximises SNR, the introduced image blurring will correspond to less image heterogeneity and decreased T_2^* values. SNR is crucial for accurate CS reconstruction of ^{3}He images [264], and preservation of T_2^* has been shown to be SNR-dependent [267]. However, the prospective CS T_2^* results indicate that

SNR increase achieved through a different k-space filter will have a negative effect on T_2^*, and as such subsequent prospective acquisition should consider sequential phase encoding.

A positive gravitational gradient (posterior to anterior) was observed for both mean slice ADC (Figure 5.13a) and T_2^* (Figure 5.13b) values in fully-sampled and CS acquisitions. The gravitational gradients are also demonstrated in prospective CS reconstructed axial maps of ADC and T_2^*, respectively. The smaller ADC and T_2^* obtained in posterior slices are probably related to the gravitational compression of parenchymal tissue in the supine posture corresponding to decreased alveolar dimensions and thus causes an increase in bulk susceptibility and microscopic field inhomogeneity [276]. In Figure 5.13b, the dip in mean slice T_2^* value around 30 to 60 mm can be observed in the right lung of the respective axial T_2^* map, and appears to correspond to a region with a large number of blood vessels and subsequently increased localised field inhomogeneity.
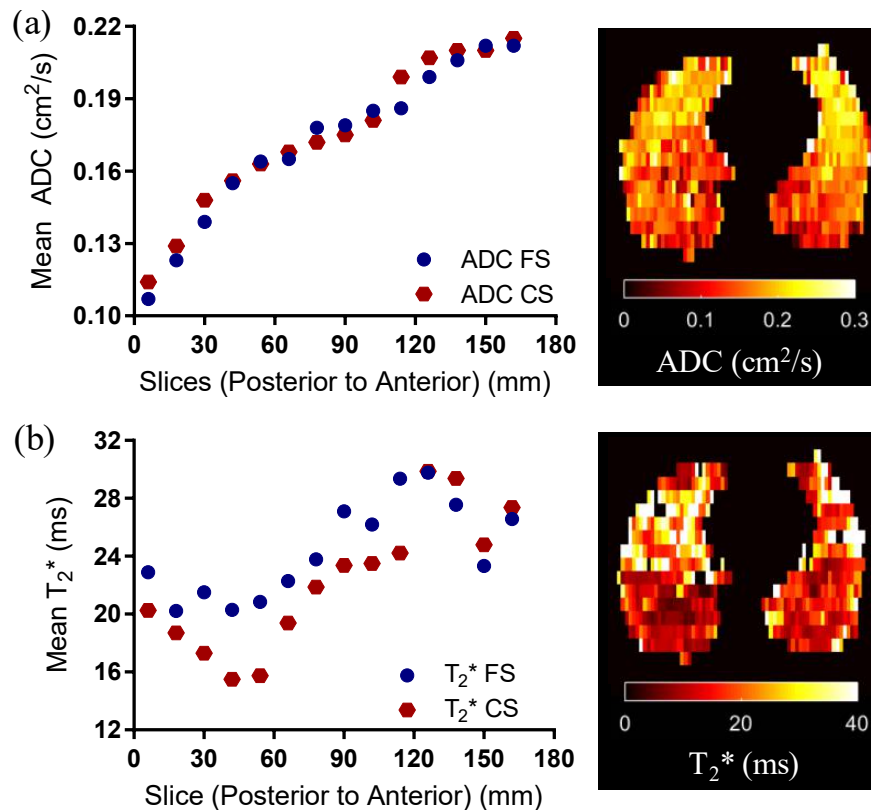
Figure 5.13: Mean slice ADC and T_2^* results for healthy volunteer. (a) A positive gravitational gradient in mean slice ADC value is observed from the posterior to anterior lung in both fully-sampled (FS) and CS prospective acquisitions. Corresponding CS reconstructed axial ADC map demonstrates this gravitational trend. (b) A similar positive gravitational trend is observed with mean slice T_2^* value, and in the reconstructed axial T_2^* map.

A statistically significant correlation between ADC and T_2^* in both fully-sampled and CS acquisitions (r=0.66, P=0.011, and r=0.78, P=0.001, respectively) supports the gravitational trends observed and suggests the measurements are related. Previously, the gravitational gradient in T_2^*, and ADC and T_2^* correlation was only observed in fully-sampled acquisitions [267, 276].

The T_2^* of hyperpolarised gases in the lungs has been demonstrated to be affected by diffusion dephasing from imaging gradients [177]. Therefore, due to the contribution of diffusion in the effective T_2^*, it stands to reason that ADC and T_2^* are significantly correlated.

In this work, ventilation images are obtained from the b = 0 diffusion interleave, and therefore have a longer, less optimal minimum TE. Previously at 3 T, a shorter TE interleave was acquired before the longer TE diffusion-weighted interleaves, and this enabled higher SNR ^{3}He ventilation images to be obtained [267]. In theory, this implementation could be applied to 1.5 T; however, the comparatively smaller ΔTE in this implementation may be insufficient due to the longer T_2^* of ^{3}He observed at 1.5 T ($\sim$28 ms [119]) when compared to 3 T ($\sim$14 ms [119]). Further work is required to investigate this, but this implementation could be promising and may allow diagnostic quality hyperpolarised gas ventilation images to be acquired in the same-breath as diffusion-weighted imaging. This sequence could potentially reduce the number of required scans, and therefore cost and duration, of hyperpolarised gas MRI sessions.

5.5 Conclusions

In this chapter, compressed sensing has been implemented for the acquisition of 3D multiple b-value diffusion-weighted MR lung images with hyperpolarised ^{3}He in a single breath-hold for quantitative whole lung microstructural assessment and multi-parametric mapping. The feasibility of 3D ^{3}He DW-MRI with CS was investigated with retrospective undersampling. Simulation results optimised by $\mathrm{MAE_{ADC}}$ demonstrated good preservation of spatial resolution and quantitative lung microstructure information.

Prospective 3D multiple b-value ^{3}He DW-MRI CS datasets were acquired in five healthy volunteers and one COPD patient using an optimised three-fold undersampled k-space pattern, and CS-derived ADC and Lm_D results were validated against fully-sampled 3D and 2D ^{3}He DW-MRI. Good agreement between prospective CS and fully-sampled datasets was found, with a mean difference of +3.4% and +5.1% in global mean ADC and Lm_D values, respectively. These results confirm that CS acquisition of undersampled 3D ^{3}He MRI datasets with multiple b-values for whole lung morphometry is ready for use in clinical lung imaging studies.

Finally, 3D multi-parametric mapping with a CS undersampled multi-interleaved sequence was demonstrated. Prospective CS multi-interleaved ^{3}He data enabled the simultaneous acquisition of co-registered ^{3}He ventilation, ADC, Lm_D, and T_2^* maps in a single breath-hold. This sequence has the potential to reduce the number of ^{3}He scans required in hyperpolarised gas lung imaging studies. However, the results from a healthy volunteer indicate that CS reconstruction does not preserve T_2^* value to the same extent as DW-MRI metrics, and suggests that CS may not be suitable for T_2^* mapping of ^{3}He in lungs.

Chapter 6

Whole lung morphometry with 3D ^{129}Xe diffusion-weighted MRI and compressed sensing

6.1 Introduction

Chapter 5 demonstrated the feasibility of whole lung morphometry mapping in a single breath-hold, for quantitative regional assessment of lung microstructure, with 3D multiple b-value ^{3}He DW-MRI and compressed sensing (CS). With the limited availability of ^{3}He gas [110], ^{129}Xe provides a cost-effective alternative for pulmonary MRI, and with advancements in polarisation levels [167, 170], recent studies have shown that comparable lung ventilation and microstructural information can be obtained using both nuclei [116–118, 191, 193].

However, DW-MRI with ^{129}Xe is inherently more challenging due to the lower diffusivity and lower gyromagnetic ratio of ^{129}Xe when compared to ^{3}He, resulting in longer diffusion gradient times, low bandwidth readouts, longer sequence TR and lower image SNR. Theoretical gas diffusion models have been proposed for interpreting the ^{129}Xe DW-MRI signal from multiple b-value acquisitions [136], and estimates of alveolar length scales have been derived from healthy subjects, and COPD patients [137–139]. Due to the associated long scan times, the multiple b-value interleaves in previous studies were acquired using non-contiguous and relatively thick 2D slices without whole lung coverage – and in some cases, with separate breath-holds. Furthermore, to our knowledge, no direct comparison of alveolar length scales derived from the application of theoretical diffusion models of ^{3}He and ^{129}Xe diffusion-weighted MRI in vivo has yet been presented.

CS is an acceleration technique that has the potential to reduce the acquisition time of 3D multiple b-value ^{129}Xe DW-MRI to a single tolerable breath-hold. Previous ℓ_1-norm

minimisation and sparse sampling strategies for ^{3}He CS reconstruction, developed by our group [198, 264, 266, 267], should be readily transferable to ^{129}Xe due to inherent similarities between acquisition techniques, and the spatial similarity and sparsity of the lung images. The feasibility of CS with ^{129}Xe was first demonstrated for the acquisition of respiratory-gated ^{129}Xe lung MR images of mice [280]. Recently, the feasibility of in vivo ^{129}Xe MRI with CS was demonstrated, and facilitated the acquisition of co-registered 3D ^{129}Xe ventilation and ^{1}H structural images in a single breath-hold [281]. However, to date, the viability of ^{129}Xe DW-MRI with CS for single breath whole lung acquisitions has not been explored.

In this chapter, the feasibility of acquiring 3D multiple b-value ^{129}Xe DW-MRI data with CS was first assessed through retrospective undersampling simulations. Prospective CS was used to acquire multiple b-value ^{129}Xe diffusion-weighted MR images in a single breath-hold, and 3D morphometry maps of mean diffusive length scale (Lm_D) were generated using the stretched exponential model (SEM). Results were compared against equivalent 3D ^{3}He Lm_D morphometry maps acquired with CS, and an optimal ^{129}Xe diffusion time of Δ=8.5 ms was derived empirically. Prospective acquisitions with the empirically-optimised ^{129}Xe diffusion time were then benchmarked against ^{3}He equivalent measurements in healthy volunteers, ex-smokers, and COPD patients with both SEM-derived Lm_D and cylinder model (CM)-derived mean chord length (Lm) measurements.

This chapter is based on the following publication: *"3D Diffusion-Weighted ^{129}Xe MRI for Whole Lung Morphometry"*. **H.-F. Chan**, N. J. Stewart, G. Norquay, G. J. Collier, J. M. Wild. *Magnetic Resonance in Medicine*, doi:10.1002/mrm.26960, 2017. Author contribution statement: study design, HFC, NJS, GJC, JMW; acquisition of data, HFC, NJS, GN, GJC; analysis of data, HFC, GJC, JMW; preparation of manuscript, HFC, NJS, GN, GJC, JMW.

6.2   3D ^{129}Xe DW-MRI with CS

The feasibility of CS undersampling for 3D multiple b-value ^{129}Xe DW-MRI was investigated in this section. Retrospective undersampling of fully-sampled 3D ^{129}Xe DW-MRI data were performed to optimise k-space undersampling patterns. Prospective CS datasets from four healthy volunteers were acquired with the reported ^{129}Xe diffusion time of 5 ms [136] and Lm_D results were compared against equivalent ^{3}He measurements.

6.2.1   Methods

A fully-sampled 3D ^{129}Xe DW-MRI dataset was acquired from a healthy male volunteer (HV1) on a 1.5 T (GE HDx) MR scanner using a flexible quadrature transmit-receive vest coil (Clinical MR Solutions, Brookfield, WI) which was tuned to the Larmor frequency of

^{129}Xe at 1.5 T (17.66 MHz). Imaging was performed at a lung volume of functional residual capacity plus 1L following inhalation of a dose of 800 ml enriched ^{129}Xe (86% ^{129}Xe, ~30% polarisation [167, 170]) balanced with 200 ml of N_2. Image acquisition parameters were: 3D SPGR sequence; 2× interleaves (b = 0, 12 s/cm^2); elliptical-centric phase encoding; in-plane resolution 64×52 (6.25 mm pixel dimension); 18 effective coronal slices (15 mm slice thickness); FOV = 40×32.5×27 cm^3; TE/TR = 11.2/14.4 ms; diffusion time (Δ) = 5 ms (diffusion gradient strength = 22.7 mT/m, ramp time = 0.3 ms, plateau time = 3 ms, gap between lobes = 1.4 ms); flip angle = 2.2°; and bandwidth = ±6.97 kHz.

A ^{129}Xe diffusion time of $\Delta = 5$ ms was first chosen as it corresponds to the diffusion time originally proposed by Sukstanskii and Yablonskiy for ^{129}Xe lung morphometry with the CM [136]. This diffusion time was derived theoretically such that acinar airway geometrical parameters from the CM would be the same with both ^{129}Xe and ^{3}He [136], and these values have been subsequently used in 2D ^{129}Xe DW-MRI experimental studies at University of Virginia and Robarts Research Institute sites [137–139]. Retrospective CS simulations of the fully-sampled dataset with acceleration factors (AF) between 2 – 5 were implemented using the methodology described in Section 5.2. The Wilcoxon signed-rank test was employed to assess differences between fully-sampled and retrospectively reconstructed ADC maps for each AF on a pixel-by-pixel basis.

The optimum *k*-space sampling pattern for three-fold (AF=3) undersampling was chosen based on the simulation results and used for prospective acquisition of 3D ^{129}Xe multiple b-value DW-MRI data from four healthy volunteers (HV1 – HV4). Prospective data was then acquired with an inhaled gas mixture of 750 ml ^{129}Xe and 250 ml N_2, with imaging parameters as for the fully-sampled acquisition apart from the following: four interleaves (b = 0, 12, 20, 30 s/cm^2); TE/TR = 11.7/15.0 ms; $\Delta = 5$ ms (maximum diffusion gradient strength = 31.9 mT/m, ramp time = 0.3 ms, plateau time = 3.5 ms, gap = 0.9 ms); and flip angle = 2.7°. The AF of 3 reduces the scan time from 57 s to a tolerable 19 s breath-hold. ^{129}Xe Lm_D maps were calculated using the SEM (see Section 3.5.2), and results were compared to Lm_D maps derived from the same volunteers' lungs using 3D ^{3}He DW-MRI as described in Section 5.3. ^{3}He Lm_D with $\Delta = 1.6$ ms was chosen for comparison because healthy and COPD Lm_D values derived at this diffusion time have been demonstrated to be comparable to histologically-derived healthy and COPD mean linear intercept values [6, 96].

6.2.2 Results

A range of *k*-space undersampling patterns with different variable density weighting functions were generated for each AF, and optimal sampling patterns were determined from the CS simulations. Retrospectively reconstructed datasets from each optimal sampling pattern showed a small increase in mean absolute error (MAE) of normalised signal intensity value for

the b = 0 data (from 2.27% at AF = 2 to 4.25% with AF = 5); however, a good preservation of image details was still observed with increased undersampling (Figure 6.1). Whole lung mean ADC histogram and single slice ADC maps generated from the reconstructed CS datasets also showed a good preservation of quantitative information and low MAE of ADC (MAE$_{ADC}$) (Figure 6.2). Wilcoxon signed-rank tests for each AF indicated no significant differences between CS-reconstructed and fully-sampled ADC maps on a pixel-by-pixel basis, confirming preservation of quantitative information and indicating that CS is suitable for 3D ^{129}Xe multiple b-value DW-MRI.
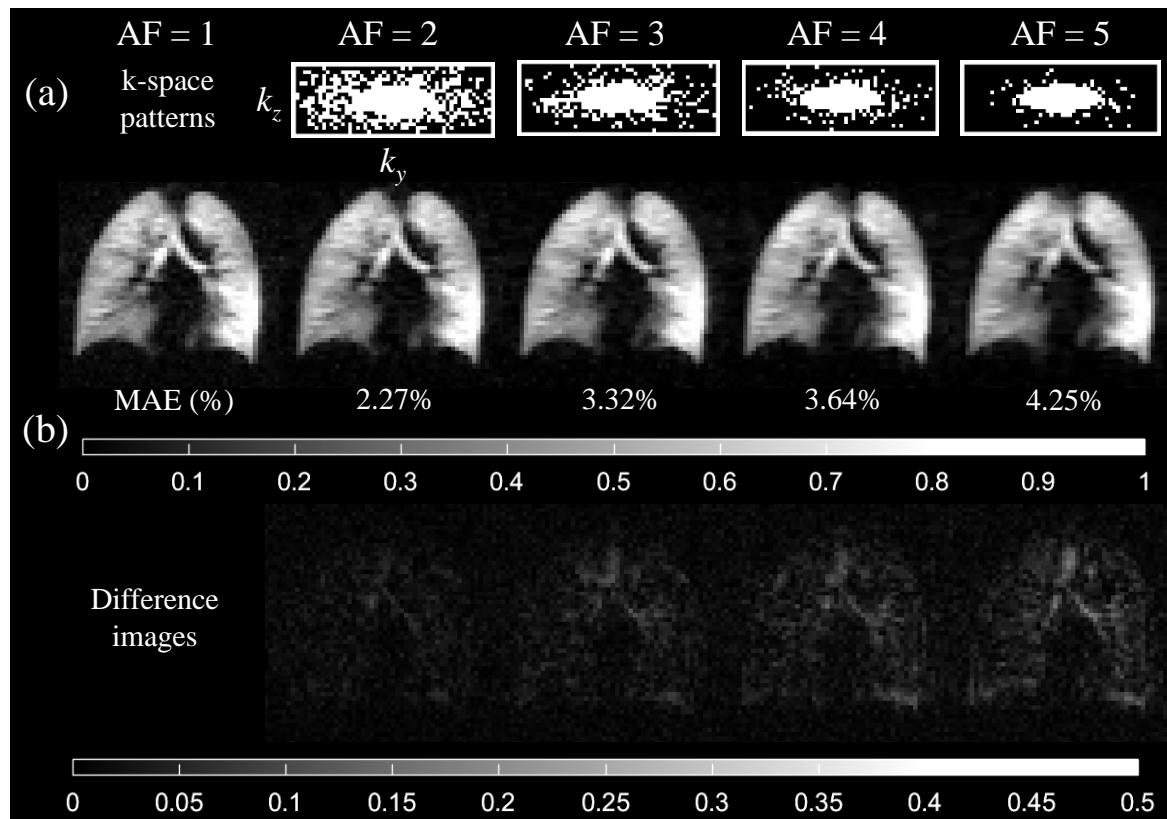
Figure 6.1: CS simulation results for 3D ^{129}Xe DW-MRI. (a) Optimal *k*-space undersampling patterns (52×18 pixels) for each acceleration factor (AF). (b) Example reconstructed magnitude (b = 0) and difference images for each AF, with corresponding MAE values.

Prospective 3D ^{129}Xe multiple b-value DW-MRI were then acquired in four healthy volunteers with AF = 3 and ^{129}Xe Δ = 5 ms, and the resulting ADC and Lm_D maps were compared with previously calculated lung microstructural maps acquired using 3D ^{3}He multiple b-value DW-MRI. The prospective CS whole lung mean ^{129}Xe ADC value for volunteer HV1 (0.0329 cm^2/s) was very similar (+1.2% difference) to the fully-sampled mean ADC value (0.0325 cm^2/s) that was obtained from CS simulations. Example ^{129}Xe and ^{3}He Lm_D maps from comparative slices in HV1 are shown in Figure 6.3 and a summary of mean ADC and Lm_D values for each volunteer is provided in Table 6.1. At ^{129}Xe Δ = 5 ms, mean ^{129}Xe Lm_D values for all subjects were ∼50 μm (∼25%) smaller than the corresponding mean ^{3}He values.
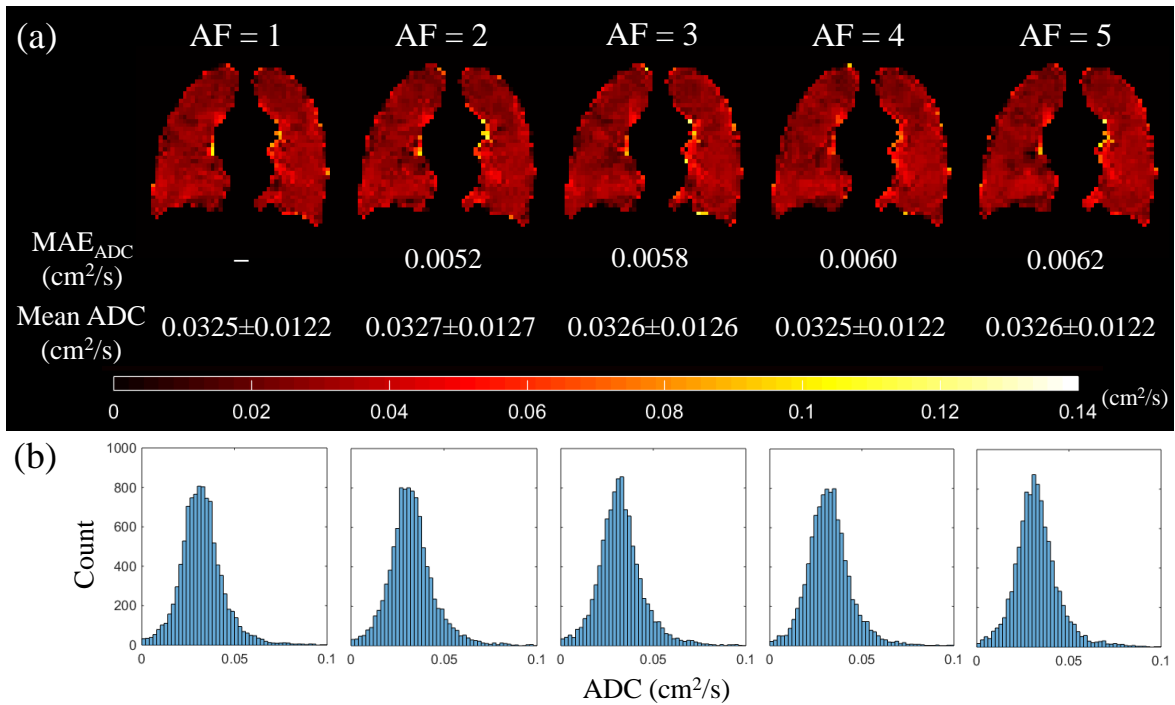
Figure 6.2: ADC results for 3D ^{129}Xe DW-MRI CS simulations. (a) Single slice ADC maps with the MAE_{ADC}, and mean global ADC values for each AF. (b) Corresponding whole lung ADC histograms for each AF.

Table 6.1: Summary of global mean ADC and Lm_D values for four healthy volunteers derived from prospective 3D multiple b-value ^{129}Xe and ^{3}He DW-MRI with CS.

Subject	^{129}Xe ADC (cm²/s) ($\Delta = 5$ ms)	^{129}Xe Lm_D (µm) ($\Delta = 5$ ms)	^{3}He ADC (cm²/s) ($\Delta = 1.6$ ms)	^{3}He Lm_D (µm) ($\Delta = 1.6$ ms)
HV1	0.033 ± 0.012	161 ± 23	0.182 ± 0.085	208 ± 30
HV2	0.039 ± 0.012	176 ± 20	0.196 ± 0.077	223 ± 24
HV3	0.030 ± 0.011	157 ± 19	0.166 ± 0.068	205 ± 23
HV4	0.030 ± 0.011	156 ± 18	0.169 ± 0.065	210 ± 20

6.2.3 Discussion

CS has enabled the acquisition of 3D multiple b-value ^{129}Xe DW-MRI in a single breath-hold for the generation of whole lung maps of alveolar diffusion length scale with a voxel size of $6.25 \times 6.25 \times 15$ mm³. Retrospectively undersampled ^{129}Xe datasets, reconstructed with CS sampling patterns (optimised through simulations), demonstrated good preservation of image details and microstructural information with increased undersampling. MAE and MAE_{ADC} values from ^{129}Xe CS simulations were similar to those reported with ^{3}He (Section 5.2).

The presence of image blurring in the fully-sampled ^{129}Xe images (AF=1 in Figure 6.1) is likely the result of elliptical-centric phase encode ordering used with ^{129}Xe in contrast to the
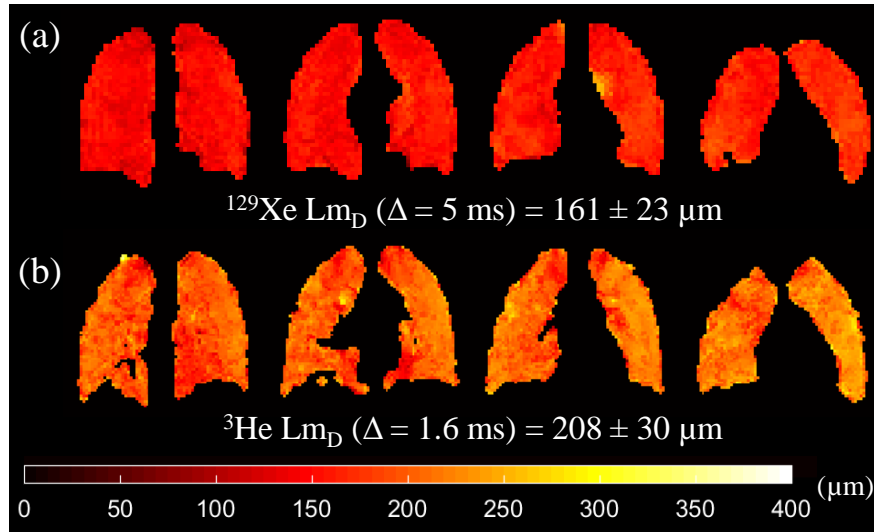
Figure 6.3: Prospective CS results for a healthy volunteer (HV1). (a) Example ^{129}Xe Lm_D maps derived from 3D multiple b-value ^{129}Xe DW-MRI. (b) Example ^{3}He Lm_D maps in comparative slices demonstrate a mismatch in Lm_D values between the two nuclei.

sequential encoding used previously with ^{3}He. Elliptical-centric phase encoding maximises SNR at the consequence of increased image blurring with an RF depolarisation k-space filter that originates from the centre of k-space (Figure 3.15) [175]. The full width at half maximum (FWHM) values of retrospectively undersampled ^{129}Xe ADC histograms decreased with AF; this trend matches the results of ^{3}He CS simulations (Section 5.2) and demonstrates decreased spatial heterogeneity associated with the de-noising reconstruction process of CS. However, this loss of spatial heterogeneity did not result in a statistically significant difference between fully-sampled ADC and undersampled CS ADC maps.

Prospective three-fold undersampled 3D multiple b-value ^{129}Xe DW-MRI were acquired in four healthy volunteers at $\Delta = 5$ ms. The difference of $+1.2\%$ between CS (0.0329 cm^2/s) and fully-sampled mean ^{129}Xe ADC (0.0325 cm^2/s) for one volunteer (HV1) is similar to the small differences previously reported between fully-sampled and CS undersampled 2D and 3D ^{3}He ADC values (see [264] and Table 5.2). The whole lung mean ^{129}Xe ADC values for all four healthy volunteers ($\sim$0.033 cm^2/s) was also consistent with previously reported healthy subject ADC values acquired with b = 12 s/cm^2 at 1.5 T [113]. The observed mean Lm_D mismatch of approximately 50 µm ($\sim$25%) between ^{3}He and ^{129}Xe suggests that the ^{129}Xe diffusion time of $\Delta = 5$ ms, previously proposed for in vivo lung morphometry with the CM [136], is not applicable for ^{129}Xe lung alveolar length scale measurements derived from the SEM and other diffusion times need to be explored.

6.3 Empirical optimisation of ^{129}Xe diffusion time

^{129}Xe Lm_D values, calculated from prospective 3D ^{129}Xe multiple b-value with $\Delta = 5$ ms, were approximately 50 µm smaller than ^{3}He Lm_D values acquired in the same four healthy volunteers. In this section, an optimal ^{129}Xe diffusion time was derived empirically from a single volunteer to obtain comparable ^{129}Xe and ^{3}He Lm_D values. The empirically-optimised ^{129}Xe diffusion time was subsequently validated with both SEM-derived Lm_D and CM-derived Lm in a cohort of subjects with a varying range of alveolar sizes expected due to age and smoking-related emphysema.

6.3.1 Methods

The observed difference in SEM-derived Lm_D values suggests that the optimal diffusion time of $\Delta = 5$ ms proposed in the cylinder model for ^{129}Xe [136] is not suitable for the SEM. With the aim of obtaining best agreement between ^{129}Xe and ^{3}He lung morphometry results, rather than simply implementing the ^{129}Xe $\Delta = 5$ ms, HV1 was imaged at additional ^{129}Xe diffusion times ($\Delta = 5$, 7, 8 and 10 ms). ^{129}Xe $\Delta = 10$ ms was chosen specifically as it corresponds to the same 1D characteristic free diffusion length ($\sqrt{2D_0\Delta} = 530$ µm) as experienced in the reference ^{3}He experiment (assuming $D_0^{\text{Xe-air}} = 0.14$ cm^2/s, $D_0^{\text{He-air}} = 0.88$ cm^2/s, and $\Delta_{\text{He}} = 1.6$ ms). Each additional ^{129}Xe DW-MRI scan was acquired with an identical gas mixture and b-values as per the previous prospective CS acquisitions at ^{129}Xe $\Delta = 5$ ms (Section 6.2), and Lm_D maps were calculated from each dataset.

The resulting empirically-optimised diffusion time (^{129}Xe $\Delta = 8.5$ ms – see Results 6.3.2) was then benchmarked against ^{3}He equivalent measurements for lung morphometry mapping over different ranges of acinar length scales that are experienced with smoking-related emphysema. Five healthy volunteers (31.0 ± 3.1 years), six ex-smokers (51.3 ± 2.7 years, 20.3 ± 10.8 pack years), and two COPD patients (63.0 ± 1.4 years, GOLD II-IV) were recruited for this preliminary study. Subject demographics and pulmonary function test (PFT) data for each subject are summarised in Table 6.2. All in vivo MRI experiments were performed under the approval of the UK national research ethics committee and the local NHS research office.

Each subject was imaged with 3D multiple b-value ^{129}Xe DW-MRI, using 750 ml of ^{129}Xe and the following imaging parameters: TE/TR = 14.0/17.3 ms; maximum DW gradient strength = 32.6 mT/m; $\Delta = 8.5$ ms; ramp time = 0.3 ms; plateau time = 2.3 ms; gap = 5.6 ms; and flip angle = 3.1°. Utilising a ^{129}Xe $\Delta = 8.5$ ms, the duration of three-fold undersampled CS scans was consequently increased by 3 s due to the associated increased diffusion time. Therefore, four-fold undersampling (AF = 4) was now implemented in the subsequent prospective CS acquisitions to further reduce the scan time and keep the breath-hold within 16 s. This value is similar to the 15 s acquisition for ^{3}He, and was chosen to demonstrate the clinical-viability

Table 6.2: Subject demographics and pulmonary function test data for five healthy volunteers (HV), six ex-smokers (ES), and two COPD patients in the ^{129}Xe and ^{3}He comparison cohort.

Subject	Age (Sex)	FEV$_1$ (% pred)	FEV$_1$/FVC (%)	TLC (% pred)	RV (% pred)	T$_{LCO}$ (% pred)	Pack Years
HV1	26 (M)	102.9	81.2	105.6	107.0	–	–
HV2	31 (M)	102.0	82.8	100.3	85.0	–	–
HV3	34 (M)	77.0	88.0	91.7	107.2	–	–
HV4	31 (M)	105.0	87.0	91.6	70.7	–	–
HV5	33 (M)	85.1	76.0	84.0	74.1	–	–
Mean HV	**31.0**	**94.4**	**83.0**	**94.6**	**88.8**	–	–
ES1	47 (F)	86.7	68.8	108.4	105.3	93.0	30.0
ES2	51 (M)	95.2	69.2	106.7	100.9	97.2	30.0
ES3	53 (F)	90.1	59.7	130.0	139.2	99.2	4.1
ES4	55 (M)	107.7	67.5	132.0	127.0	86.5	10.0
ES5	52 (F)	90.9	71.0	101.9	106.6	89.3	25.0
ES6	50 (M)	111.6	96.1	109.0	89.4	98.4	22.5
Mean ES	**51.3**	**97.0**	**72.1**	**114.7**	**111.4**	**93.9**	**20.3**
COPD1	62 (F)	39.6	36.5	–	–	37.4	–
COPD2	64 (F)	69.7	50.0	–	–	61.0	–
Mean COPD	**63.0**	**54.7**	**43.3**	–	–	**49.2**	–

of this sequence. To verify that good agreement in Lm_D values was obtained between three- and four-fold undersampling, all five healthy volunteers were imaged with an additional AF = 3, ^{129}Xe CS acquisition at $\Delta = 8.5$ ms, and a slice-by-slice comparison of mean Lm_D values was performed. 3D ^{3}He DW-MRI was acquired on the same-day session for all subjects (except for HV1 – HV3, where ^{3}He data was acquired approximately 1 year previously), with the experimental parameters previously described in Section 5.3. ^{129}Xe and ^{3}He Lm_D maps were derived and compared for each subject.

Finally, the applicability of ^{129}Xe $\Delta = 8.5$ ms to the CM derivations of lung morphometry parameters was assessed. The ^{129}Xe-based CM phenomenological expressions are optimised for ^{129}Xe $\Delta = 5$ ms; however, if the same 1D theoretical free diffusion length is probed with both nuclei (i.e. $\Delta_{He} = 1.6$ ms and $\Delta_{Xe} = 10$ ms), the original ^{3}He-based phenomenological expressions should in theory be applicable for derivation of ^{129}Xe lung morphometry parameters [136]. Initial CM analysis of ^{129}Xe DW-MRI data, with the ^{3}He-based CM expressions, in healthy subjects at ^{129}Xe $\Delta = 8.5$ ms and ^{129}Xe $\Delta = 10$ ms, suggested that, as with

the SEM, more consistent ^{129}Xe lung morphometry results were obtained with ^{129}Xe $\Delta =$ 8.5 ms (see Discussion 6.3.3). The 3D multiple b-value ^{129}Xe DW-MRI data at ^{129}Xe $\Delta =$ 8.5 ms was therefore analysed using the ^{3}He-based CM phenomenological expressions [6], and the ^{129}Xe mean chord length (Lm) was hence derived and compared to the ^{3}He-derived Lm for each subject in the preliminary study.

6.3.2 Results

A strong positive linear correlation (r = 0.998, P<0.001) was established between ^{129}Xe Lm_D and ^{129}Xe diffusion times, and at $\Delta =$ 8.5 ms, the ^{129}Xe Lm_D value best matched the volunteer's ^{3}He Lm_D value (Figure 6.4a). In contrast to Lm_D, mean ^{129}Xe ADC decreased with increasing diffusion time; a 12.5% decrease in mean ^{129}Xe ADC was observed from $\Delta =$ 5 to 10 ms. The relationship between ^{129}Xe ADC and diffusion time was however non-linear, and best fitted a logarithmic function (R^2 = 0.961) (Figure 6.4b).
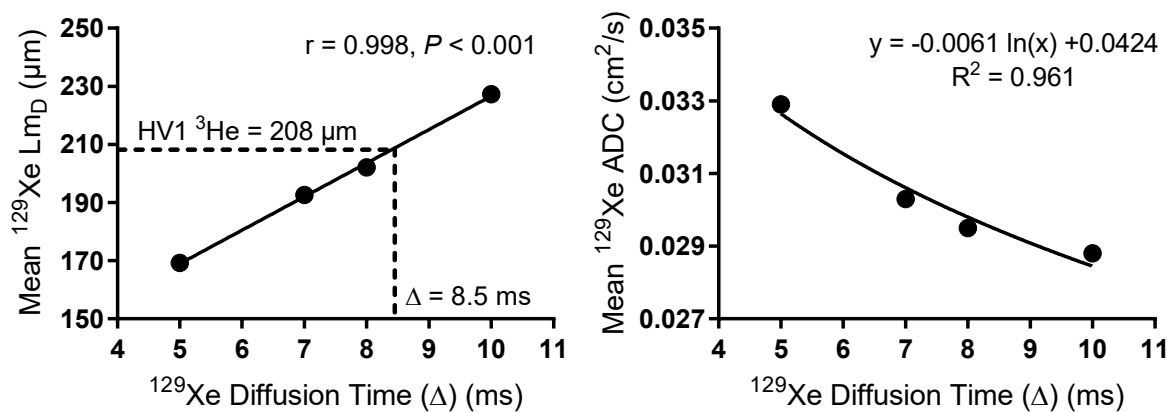
Figure 6.4: Global mean ^{129}Xe Lm_D and ADC results at different ^{129}Xe diffusion times for one healthy volunteer. A strong linear dependence between ^{129}Xe diffusion time and mean ^{129}Xe Lm_D value was observed (left). At ^{129}Xe $\Delta =$ 8.5 ms, the ^{129}Xe Lm_D matches the volunteer's corresponding ^{3}He Lm_D value. Mean ^{129}Xe ADC decreases with increasing diffusion time in a non-linear logarithmic relationship (right).

Bland-Altman analysis of mean slice ^{129}Xe Lm_D values acquired with AF = 3 and AF = 4 in the five healthy volunteers confirmed a mean bias of +1.5% (+2.9 µm) for AF = 4 with a 95% confidence interval of -6.9% to +10.0% (-13.4 to 19.3 µm) (Figure 6.5). A summary of whole lung mean ^{129}Xe and ^{3}He Lm_D values, and corresponding ^{129}Xe and ^{3}He Lm values for each subject are shown in Table 6.3. An improved matching of mean ^{129}Xe and ^{3}He Lm_D was obtained with the empirically-optimised diffusion time, and this is visible in the example Lm_D maps from three representative subjects (Figure 6.6). A difference in Lm_D of less than 7% was observed in all subjects, with a mean difference (^{129}Xe – ^{3}He) in all subjects of -2.2%.

Figure 6.7a shows a very strong correlation (r = 0.987, P<0.001) between individual lung ^{3}He and ^{129}Xe mean Lm_D values in all subjects. Lm_D values fall around the line of equality, and

Table 6.3: Summary of ^{129}Xe whole lung SEM-derived Lm_D and CM-derived Lm values for five healthy volunteers, six ex-smokers, and two COPD patients acquired with AF = 4 and ^{129}Xe Δ = 8.5 ms, and their corresponding ^{3}He mean lung morphometry values (AF = 3, ^{3}He Δ = 1.6 ms) (see Chapter 5).

Subject	Stretched Exponential Model			Cylinder Model [a]		
	^{129}Xe Lm_D (µm)	^{3}He Lm_D (µm)	Lm_D (% Diff)	^{129}Xe Lm (µm)	^{3}He Lm (µm)	Lm (% Diff)
HV1	205	208	-1.4	183	183	0.0
HV2	218	224	-2.7	222	210	+5.6
HV3	206	205	+0.5	196	171	+12.5
HV4	200	210	-4.8	173	178	-3.1
HV5	192	205	-6.3	164	170	-3.6
Mean HV	**204**	**210**	**-2.9**	**188**	**182**	**+2.3**
ES1	232	234	-0.9	259	222	+14.3
ES2	230	234	-1.7	254	240	+5.3
ES3	234	236	-0.8	266	250	+6.0
ES4	245	246	-0.4	326	335	-2.7
ES5	221	231	-4.3	222	226	-2.1
ES6	217	215	+0.9	217	201	+7.2
Mean ES	**230**	**233**	**-1.2**	**257**	**246**	**+4.7**
COPD1	317	323	-1.9	639	671	-5.0
COPD2	251	263	-4.6	318	381	-19.8
Mean COPD	**284**	**293**	**-3.2**	**478**	**526**	**-12.4**
Overall Mean	–	–	**-2.2**	–	–	**+1.1**

[a] Both ^{3}He and ^{129}Xe data was analysed with ^{3}He-based cylinder model expressions [6].

this good agreement was confirmed by Bland-Altman analysis (Figure 6.7b) of individual lung Lm_D values, where a mean bias of -2.1% (-4.8 µm) for ^{129}Xe mean Lm_D, with a 95% confidence interval of -6.7 to 2.5% (-14.8 to 5.2 µm), was observed. The corresponding mean difference in ^{129}Xe and ^{3}He CM Lm values was +1.1% (Table 6.3); demonstrating a similar level of agreement in CM-derived Lm at ^{129}Xe Δ = 8.5 ms as seen for the SEM-derived Lm_D. ^{3}He and ^{129}Xe CM single lung Lm values were also strongly correlated (r = 0.980, $P<0.001$) (Figure 6.7c), and Bland-Altman analysis of mean single lung Lm values indicated a mean bias of +2.3% in ^{129}Xe Lm values with a 95% confidence interval of -15.2 to 19.9% (Figure 6.7d).
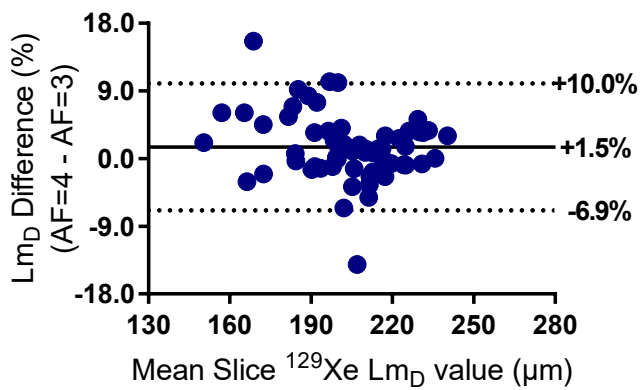
Figure 6.5: Bland-Altman analysis of AF = 3 and AF = 4 mean slice Lm_D values. The percentage difference between the two AFs is plotted against the mean slice Lm_D value for all five healthy volunteers. The solid line represents the mean percentage difference, and the two dotted line indicate the 95% limits of agreement.
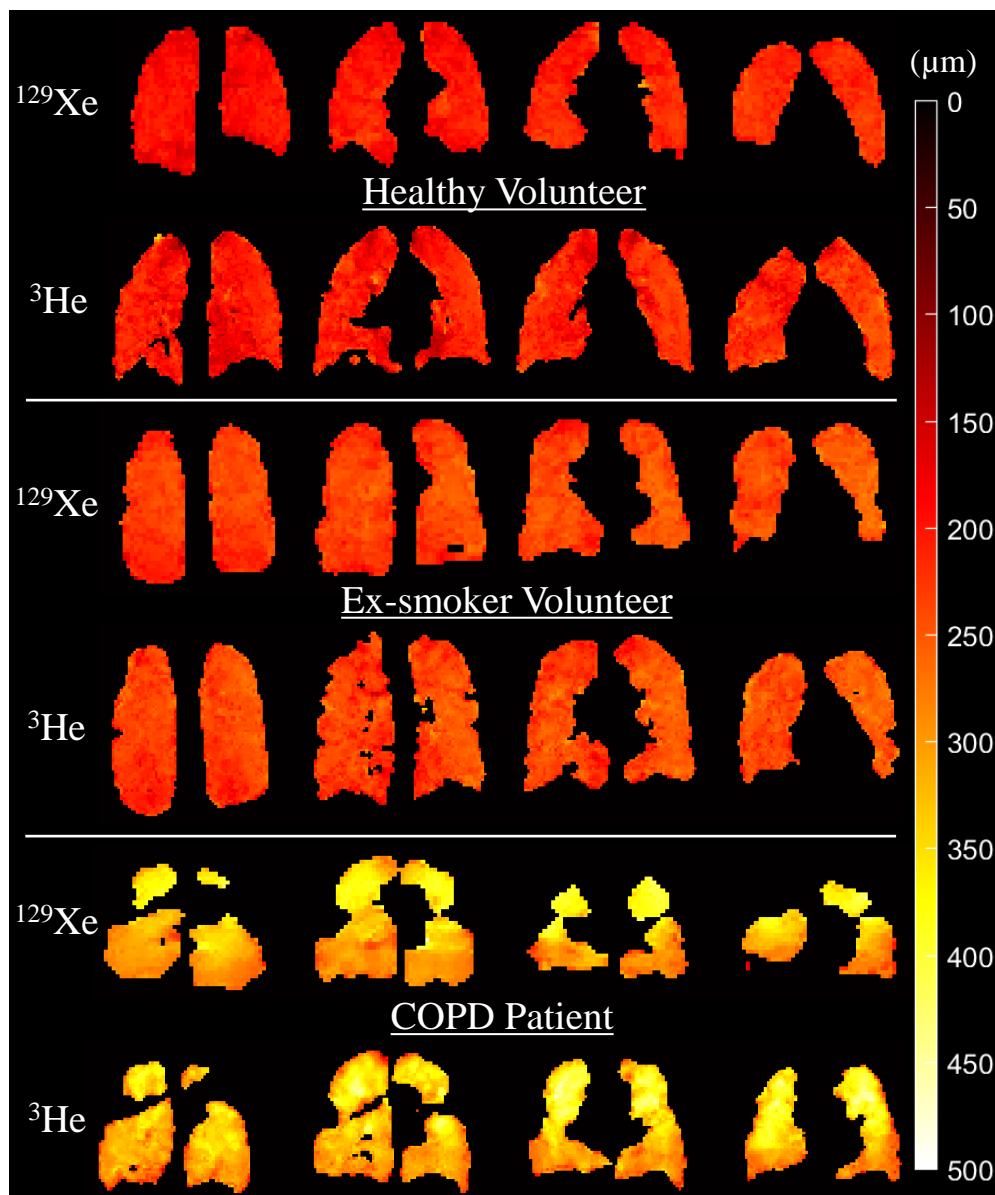
Figure 6.6: Comparison of ^{129}Xe and ^{3}He example slice Lm_D maps for a representative healthy, ex-smoker and COPD subject. ^{129}Xe Lm_D maps derived using 3D multiple b-value ^{129}Xe DW-MRI at an empirically-optimised diffusion time $\Delta = 8.5$ ms demonstrate good visual agreement with ^{3}He Lm_D maps.

Stretched Exponential Model

Cylinder Model
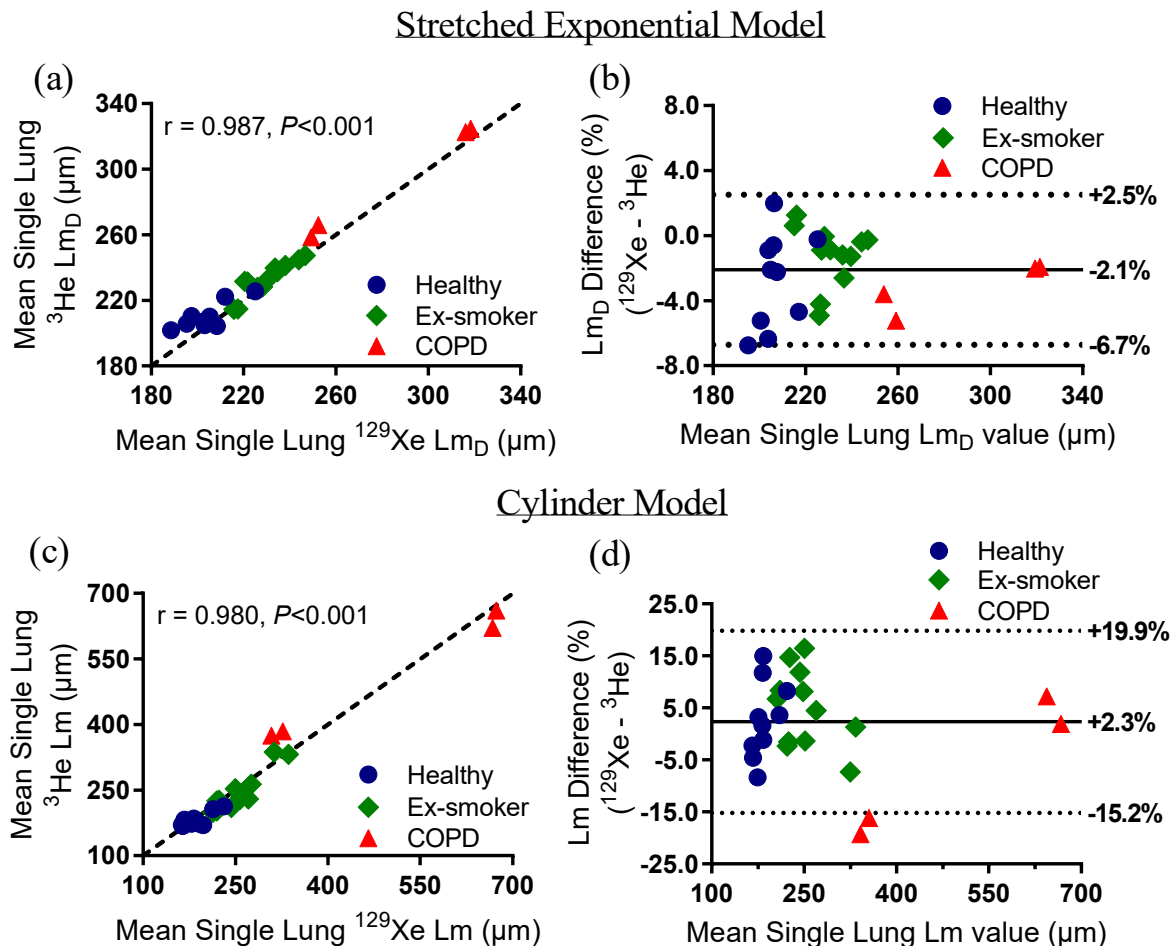
Figure 6.7: (a) Comparison of ^{129}Xe and ^{3}He mean single (left and right) lung Lm_D values derived from the stretched exponential model for all subjects. Dotted line represents the line of equality. (b) Bland-Altman analysis of mean single lung Lm_D values. The percentage difference (^{129}Xe $-^3$He) between the two nuclei is plotted against the mean single lung Lm_D value of the two nuclei for all subjects. The solid line represents the mean percentage difference, and the two dotted lines indicate the 95% limits of agreement. (c) Comparison of ^{129}Xe and ^{3}He mean single lung Lm values derived from the cylinder model for all subjects. Both ^{129}Xe and ^{3}He data were analysed with the ^{3}He-based cylinder model. (d) Corresponding Bland-Altman analysis of mean single lung Lm values.

6.3.3   Discussion

Mean ^{129}Xe ADC values (at b = 12 s/cm^2) decreased non-linearly with increasing diffusion time, a trend observed previously in ^{3}He ADC measurements [97, 242]. The logarithmic relationship observed between ^{129}Xe ADC and diffusion time also matches the trend observed for ^{3}He ADC [97]. We believe this to be the first demonstration of non-Gaussian diffusion with in vivo ^{129}Xe diffusion-weighted MRI. The SEM-derived Lm_D values exhibited a strong positive linear dependence with diffusion time over the range of 5 – 10 ms. The dependence of Lm_D upon diffusion time reflects the changes in the theoretical characteristic free diffusion

lengths probed in each experiment. At ^{129}Xe $\Delta = 10$ ms, corresponding to the characteristic free diffusion length of ^{129}Xe ($\sqrt{2D_0\Delta} = 530$ µm) which is identical to the free diffusion length of ^{3}He in air for the diffusion time used in Chapter 5 ($\Delta_{\text{He}} = 1.6$ ms), a mismatch of Lm_D values was still observed in the data from the three healthy volunteers (see Figure 6.9).

This mismatch suggests that even at the same characteristic free diffusion length there may be inherent differences in the specific diffusion dephasing regime of the respective gases in the lung alveoli which makes this assumption of Gaussian relation between diffusion length and diffusion time inexact. The differences in diffusion dephasing regime stems from intrinsic properties (i.e. gyromagnetic ratio, and diffusivity) of each gas, and thus leads to different mechanisms which contribute to non-Gaussian diffusion signal behaviours which are not accounted for in the calculation of characteristic free diffusion length. For example, differences in the diffusional dephasing regime due to microscopic background susceptibility gradients may exist between ^{129}Xe and ^{3}He at the same field strength due to the smaller gyromagnetic ratio of ^{129}Xe. These effects would manifest themselves in a similar way to the effects of background susceptibility gradients observed at different B_0 field strengths on ^{3}He ADC values [104].

The intrinsic difference in the two gases may also go towards explaining the different diffusion signal decays observed between the two nuclei with increasing b-value (see Figure 6.8), where a more pronounced non-mono-exponential signal decay was observed with ^{3}He than with ^{129}Xe. The SEM corrects for this non-Gaussian behaviour by incorporating a heterogeneity index parameter (α) that determines the extent of the deviation of the signal decay from a mono-exponential decay. A tendency towards a more mono-exponential signal decay (i.e. $\alpha \rightarrow 1$) with ^{129}Xe will result in larger estimates of Lm_D, for the same DDC value (Figure 3.27). The mismatch in α value observed in Figure 6.8 therefore may explain the discrepancy between ^{3}He and ^{129}Xe Lm_D values even when the same theoretical diffusion length is probed. However, more analysis is required to confirm this observation. A similar mismatch in α value is also observed in example ^{3}He (Figure 7.1) and ^{129}Xe (Figure 7.5) α maps in Chapter 7.

The decision to further accelerate with four-fold undersampling was motivated by the need to reduce the breath-hold duration for ^{129}Xe diffusion times that exceed 5 ms. Good agreement in Lm_D values (mean bias of $+1.5\%$, 95% confidence interval of -6.9% to +10.0%) was obtained with three- and four-fold undersampling, in all five healthy volunteers. This slight increase in mean slice Lm_D values obtained with AF = 4 is likely the result of CS reconstruction error associated with increased undersampling. In addition, the broad 95% confidence interval range could also be explained in part by inexact co-registration of image slices due to slight changes in subject position between the AF = 3 and AF = 4 scan sessions. However, the small increase in Lm_D justifies the implementation of AF = 4 in prospective acquisitions with ^{129}Xe $\Delta = 8.5$ ms. The reduction of scan time to within 16 s is more tolerable for a wider range of subjects, therefore AF = 4 was utilised in all subsequent 3D multiple b-value ^{129}Xe DW-MRI acquisitions.
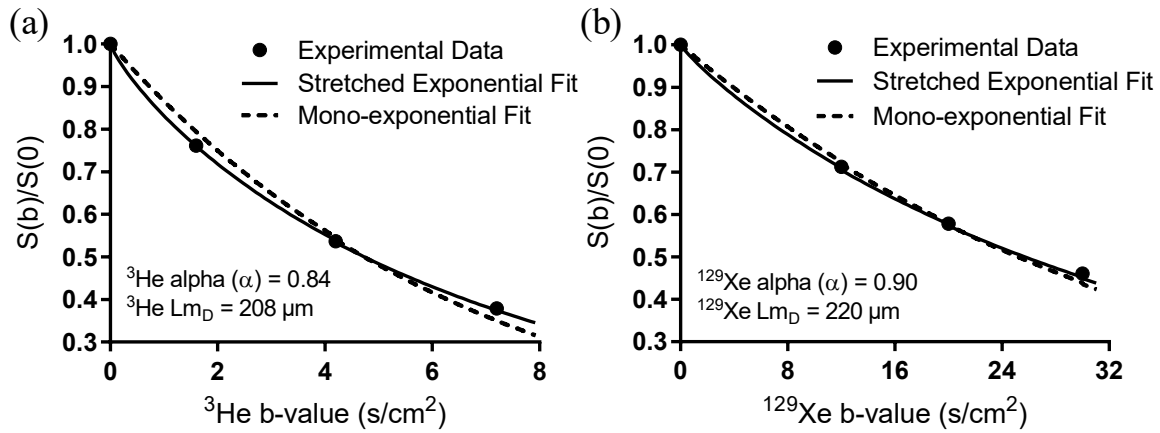
Figure 6.8: Comparison of ^{3}He ($\Delta = 1.6$ ms) and ^{129}Xe ($\Delta = 10$ ms) mean diffusion signal decay for a healthy volunteer (HV1). (a) The stretched exponential fit (solid line) of the mean ^{3}He diffusion signal decay deviates from the mono-exponential fit (dotted line) with an alpha value (α) = 0.84. (b) The mean ^{129}Xe diffusion signal decay ($\Delta = 10$ ms) is more similar to the mono-exponential decay corresponding to a larger α value (0.90) and subsequently a larger Lm_D value even when the same 1D theoretical diffusion length is probed with ^{3}He and ^{129}Xe.

Utilising the empirically-optimised ^{129}Xe diffusion time, ^{129}Xe-derived Lm_D values demonstrated improved agreement with ^{3}He Lm_D at ^{129}Xe $\Delta = 8.5$ ms than with ^{129}Xe $\Delta = 5$ ms. The mean difference between whole lung mean ^{129}Xe and ^{3}He Lm_D values across all subjects was -2.2%, and the mean bias in individual lung ^{129}Xe Lm_D was -2.1%. The diffusion time ^{129}Xe $\Delta = 8.5$ ms was derived from preliminary data and subsequently this small bias may suggest that a different optimal diffusion time (slightly longer than $\Delta = 8.5$ ms) may bring the bias towards 0%.

When the ^{129}Xe $\Delta = 8.5$ ms Lm_D result for HV1 was considered alongside the results from other diffusion times (^{129}Xe $\Delta = 5, 7, 8, 10$ ms, see Figure 6.4), a ^{129}Xe $\Delta = 9.1$ ms was found to match HV1's ^{3}He Lm_D value (Figure 6.9). Additionally, when the previous ^{129}Xe $\Delta = 5$ and 8.5 ms Lm_D results for HV2 and HV3 were considered in conjunction with an additional acquisition at ^{129}Xe $\Delta = 10$ ms, a similar optimal diffusion time of around 9 ms was obtained as well (Figure 6.9). Nevertheless, the obtained bias of -2.1% at ^{129}Xe $\Delta = 8.5$ ms is equivalent to the same-day reproducibility error (2.1%) of Lm values calculated from multiple b-value ^{3}He DW-MRI using the cylinder model [282]. Therefore, we conclude that comparable lung morphometry maps can be obtained with ^{129}Xe at $\Delta = 8.5$ ms.

One of the limitations of this study is that the ^{129}Xe diffusion time was optimised based upon the Lm_D results from healthy volunteers only. In subjects with emphysematous changes to alveolar length scales, a different relationship between ^{129}Xe Lm_D and diffusion time may well exist. However, the strong agreement between ^{129}Xe and ^{3}He Lm_D results from the subsequent prospective acquisitions in healthy normals, ex-smokers and COPD patients
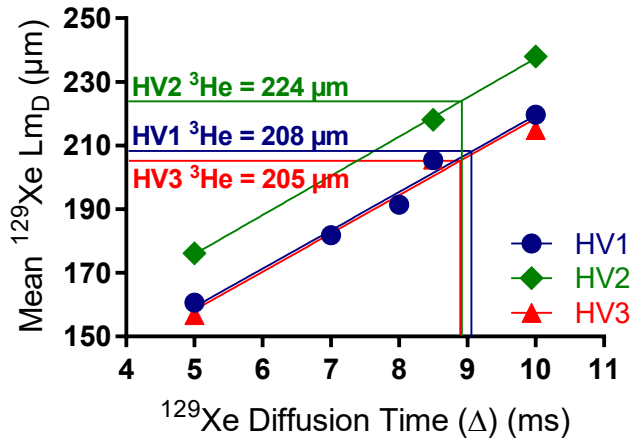
Figure 6.9: Mean ^{129}Xe Lm_D results at different ^{129}Xe diffusion times for three healthy volunteers. With the addition of the ^{129}Xe $\Delta = 8.5$ ms Lm_D result for HV1, a ^{129}Xe $\Delta = 9.1$ ms corresponded to HV1's ^{3}He Lm_D value. A strong linear correlation in ^{129}Xe diffusion time and mean Lm_D value was still observed (r = 0.98, *P*=0.015). In the other two healthy volunteers (HV2 and HV3), ^{3}He and ^{129}Xe Lm_D values match at a similar ^{129}Xe diffusion time ($\sim$9 ms).

suggests to us that ^{129}Xe $\Delta = 8.5 – 9$ ms is valid across a range of alveolar sizes subject to age and smoking-related emphysema. The empirically-optimised ^{129}Xe $\Delta = 8.5$ ms used in this work is however significantly longer than the diffusion time proposed for ^{129}Xe CM lung morphometry ($\Delta = 5$ ms [136]). The associated increase in acquisition time, was compensated by implementation of increased CS undersampling (discussed above). The longer diffusion time also corresponds to a longer echo time and subsequent increased T_2^* decay and lower image SNR. However, the increase in echo time from $\Delta = 5$ ms (TE = 11.7 ms) to 8.5 ms (TE = 14.0) only results in a $\sim$10% increase in T_2^* decay (for ^{129}Xe T_2^* at 1.5 T = 25 ms [120]), and high SNR images were still obtained with the longer echo time.

The mean ^{129}Xe ADC was observed to decrease with increasing diffusion time in Figure 6.4b. Therefore, with the implementation of the new empirically-optimised ^{129}Xe diffusion time, a reduction in mean ^{129}Xe ADC values across all acinar length scales is expected. In this preliminary study cohort, four out of five healthy volunteers were previously imaged with 3D ^{129}Xe DW-MRI at $\Delta = 5$ ms in conjunction with the acquisition at ^{129}Xe $\Delta = 8.5$ ms. The ^{129}Xe ADC at $\Delta = 5$ ms was on average 10% larger than the $\Delta = 8.5$ ms equivalent. This has implications when directly comparing ^{129}Xe ADC results at this new empirically-optimised diffusion time with previously reported results in different patient groups. Despite this reduction in mean ^{129}Xe ADC, a strong linear correlation (r = 0.967, *P*<0.001) between whole lung mean ^{3}He and ^{129}Xe ADC in the preliminary study cohort was observed (Figure 6.10). The linear regression fit ($y = 0.150x + 0.003$) is comparable to the linear fit between 2D ^{3}He and ^{129}Xe ADC ($\Delta = 5$ ms) in similar patient groups ($y = 0.143x + 0.011$) [118]. The mismatch in regression fits further illustrates the difference in ^{129}Xe ADC resulting from the different ^{129}Xe diffusion times.

Cylinder model implementation of optimal ^{129}Xe diffusion time

The empirically-optimised ^{129}Xe $\Delta = 8.5$ ms used in this work is different to the $\Delta = 5$ ms implemented in other ^{129}Xe lung morphometry studies at different centres [136–139]. In

Figure 6.10: Comparison between whole lung mean ^{3}He and ^{129}Xe ($\Delta = 8.5$ ms) ADC in all preliminary study subjects. A significant linear correlation (r = 0.967, P<0.001) was obtained ($y = 0.150x + 0.003$).
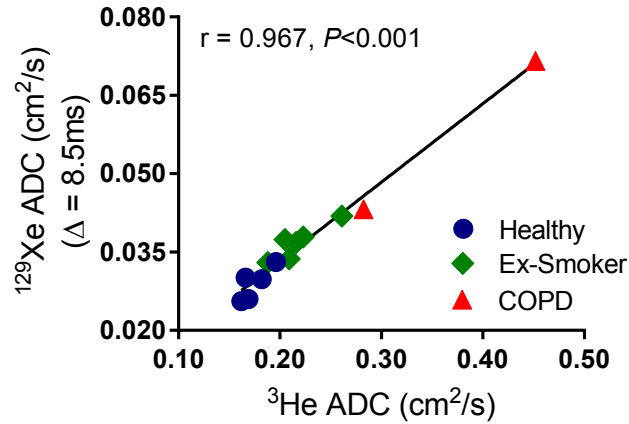
Sukstanskii and Yablonskiy [136], ^{129}Xe $\Delta = 5$ ms was chosen and ^{3}He-based CM phenomenological expressions for acinar airway geometrical parameters were re-calibrated for ^{129}Xe such that lung morphometry results would theoretically match those obtained with ^{3}He. These expressions were implemented in previous studies at 3 T, and lung morphometry metrics derived from applying the cylinder model to ^{129}Xe were demonstrated to be similar to those with ^{3}He, albeit without a direct comparison between the two nuclei in the same subjects' lungs [137–139]. However, it was noted that if the same theoretical free diffusion length is probed with both nuclei (i.e. $\Delta_{\text{He}} = 1.6$ ms and $\Delta_{\text{Xe}} = 10$ ms), the ^{3}He-based phenomenological expressions can be applied to derive ^{129}Xe lung morphometry parameters [136].

In a small subset of the preliminary study cohort (HV1–HV4), the assumption that (like the SEM) the CM will give more comparable lung morphometry results at ^{129}Xe $\Delta = 8.5$ ms than with ^{129}Xe $\Delta = 10$ ms was explored. The four healthy volunteers with 3D ^{129}Xe DW-MRI at ^{129}Xe $\Delta = 5$, 8.5 and 10 ms, and 3D ^{3}He DW-MRI were used to investigate this hypothesis. The ^{3}He-based CM phenomenological expressions [6] (Method 1) were used to analyse the ^{3}He, ^{129}Xe $\Delta = 8.5$ ms, and ^{129}Xe $\Delta = 10$ ms acquisitions, and to derive mean chord length (Lm); while the ^{129}Xe equivalent phenomenological expressions [136] (Method 2) were implemented for the analysis of the ^{129}Xe $\Delta = 5$ ms, and ^{129}Xe $\Delta = 8.5$ ms datasets. The mean Lm value from each ^{129}Xe dataset was subsequently compared against the ^{3}He Lm value, and a summary of the percentage differences in Lm are found in Table 6.4.

The mean ^{3}He-based Lm value for the healthy volunteers (186 µm) was consistent with reported CM-derived Lm values in healthy adults [133]. The ^{129}Xe Lm results derived from the ^{129}Xe $\Delta = 5$ ms data with Method 2 (^{129}Xe CM) (mean difference = +1.4%) were the most comparable with ^{3}He Lm derived with Method 1 (^{3}He CM). This was expected due to the re-calibration of ^{3}He phenomenological expressions for ^{129}Xe at $\Delta = 5$ ms. The results from the implementation of ^{129}Xe $\Delta = 8.5$ ms with Method 1 (mean difference = +4.3%) were similar to those from ^{129}Xe $\Delta = 5$ ms with Method 2. The 4.3% difference was heavily skewed by one subject (HV3), and if excluded, a mean difference of +1.0% is obtained, comparable to that observed with ^{129}Xe $\Delta = 5$ ms (Method 2). It is important

Table 6.4: A summary of the percentage difference in derived *Lm* value between mean ^{129}Xe *Lm*, acquired at different diffusion times and analysed with either ^{3}He- (Method 1) or ^{129}Xe-based (Method 2) cylinder model parameters, and ^{3}He-derived *Lm* in four healthy volunteers.

Subject	^{3}**He *Lm* (μm)** $(\Delta = 1.6$ ms) (Method 1)	**Difference (^{129}Xe − ^{3}He) in *Lm* (%)**			
		^{129}**Xe *Lm*** $(\Delta = 5$ ms) (Method 2)	^{129}**Xe *Lm*** $(\Delta = 8.5$ ms) (Method 2)	^{129}**Xe *Lm*** $(\Delta = 8.5$ ms) (Method 1)	^{129}**Xe *Lm*** $(\Delta = 10$ ms) (Method 1)
HV1	183	+1.6	+5.6	0.0	+9.2
HV2	210	+5.4	+11.3	+5.9	+21.8
HV3	171	+1.5	+19.9	+14.3	+11.2
HV4	178	-2.8	+2.6	-3.0	+3.6
Mean	**186**	**+1.4**	**+9.8**	**+4.3**	**+11.5**

Method 1 = ^{3}He-based cylinder model [6]

Method 2 = ^{129}Xe-based cylinder model [136]

to draw attention to the larger mean difference (+11.5%) obtained with ^{129}Xe $\Delta = 10$ ms when compared with ^{129}Xe $\Delta = 8.5$ ms, with Method 1 used for both diffusion times. This matches the trend seen previously with the SEM and supports the implementation of the ^{3}He-based CM (Method 1) with ^{129}Xe $\Delta = 8.5$ ms acquisitions.

To further investigate whether the empirically-optimised diffusion time of $\Delta = 8.5$ ms is also applicable for the cylinder model derivation of mean chord length (*Lm*), the ^{3}He and ^{129}Xe DW-MRI data for each subject in the preliminary study was analysed using the ^{3}He-based cylinder model expressions [6]. The mean ^{3}He *Lm* values for healthy volunteers (∼180 μm), ex-smokers (∼250 μm), and COPD patients (∼500 μm) were consistent with previously reported ^{3}He *Lm* values [6, 131, 133]. A range of *Lm* and *Lm_D* values, for both ^{3}He and ^{129}Xe, were obtained for the healthy volunteers in Table 6.3, and this could be related to the role of height, age, and/or FRC lung volume on alveolar airspace size. The mean ^{129}Xe *Lm* for ex-smokers (with ^{129}Xe $\Delta = 8.5$ ms) are also in agreement with previous ^{129}Xe *Lm* values reported at 3 T obtained with ^{129}Xe $\Delta = 5$ ms [138, 139]. The ^{129}Xe *Lm* for the GOLD II COPD subject (318 μm) is also comparable to the ^{129}Xe *Lm* (∼350 μm) reported in COPD patients (GOLD I–III) [138, 139].

When ^{129}Xe *Lm* from the ^{129}Xe $\Delta = 8.5$ ms data was evaluated with ^{3}He-based CM (Method 1), an overall mean difference of +1.1% (see Table 6.3) was obtained between ^{129}Xe and ^{3}He *Lm* values. This good agreement was confirmed when comparing ^{3}He and ^{129}Xe cylinder model single lung *Lm* values (Figure 6.7c). Bland-Altman analysis of mean individual lung *Lm* values indicated a mean bias of +2.3% in ^{129}Xe *Lm* values with a 95% confidence interval of -15.2 to 19.9% (Figure 6.7d). The small biases for *Lm* are of a similar magnitude as that

observed for the SEM Lm_D on an individual lung and global level, and therefore suggests that ^{129}Xe lung morphometry results obtained with $\Delta = 8.5$ ms are comparable to ^{3}He results analysed with both the cylinder and stretched exponential models.

6.4 Conclusions

With limited availability of ^{3}He, there is a strong motivation to evaluate functional and structural information that can be derived from the readily available and cheaper ^{129}Xe gas isotope. Compressed sensing has facilitated acquisition of single-breath 3D multiple b-value ^{129}Xe DW-MRI for whole lung morphometry mapping. SEM-derived Lm_D results demonstrated a linear dependence with diffusion time, and the best agreement between ^{129}Xe and ^{3}He Lm_D results was obtained with an empirically-optimised ^{129}Xe $\Delta = 8.5$ ms. Prospective CS acquisitions were used to validate ^{129}Xe $\Delta = 8.5$ ms in healthy volunteers, ex-smokers, and COPD patients, and a strong agreement (mean Lm_D bias of -2.2%) in ^{3}He and ^{129}Xe Lm_D values was obtained. A similar level of agreement (mean Lm bias of +1.1%) was obtained with CM-derived Lm, indicating that ^{129}Xe DW-MRI acquired with ^{129}Xe $\Delta = 8.5$ ms is a viable alternative to ^{3}He for 3D whole lung morphometry assessment with both cylinder and stretched exponential models.

Further validation of this empirically-optimised ^{129}Xe $\Delta = 8.5$ ms will involve DW-MRI acquisitions and finite element diffusion simulations in either in-vitro phantoms with known geometries or ex vivo lungs. These acquisitions and simulations in different sized phantoms or lungs with both ^{3}He and ^{129}Xe, and analysed with both theoretical gas diffusion models, can be used determine if ^{129}Xe $\Delta = 8.5$ ms is valid across a range of different length scales. The B_0 dependence of DW-MRI metrics has been previously demonstrated with ^{3}He [104]. However, the effect of B_0 on ^{129}Xe-derived lung morphometry metrics and ^{129}Xe diffusion time dependence at a different B_0 is currently unknown and requires further investigation.

Chapter 7

Comparison of in vivo lung morphometry models with 3D ^{3}He and ^{129}Xe diffusion-weighted MRI

7.1 Introduction

The diffusion-weighted signal of hyperpolarised noble gases in the lungs demonstrates non-Gaussian phase behaviour that leads to a non-mono-exponential signal attenuation with increasing b-value. Different hyperpolarised gas diffusion models have been proposed to account for the non-Gaussian diffusion-weighted signal behaviour and provide estimates of lung alveolar length scales from the hyperpolarised gas signal. These models include: geometrical models [5, 128, 242, 246, 248, 249], q-space analysis [130], and stretched exponential model [129]. To date, the cylinder geometrical model (CM), and the stretched exponential model (SEM) are the only gas diffusion models to provide in vivo measurements of acinar length scale on a voxel-by-voxel basis, and have been utilised to study changes in lung microstructure in a range of different pulmonary diseases (see Section 2.2.5).

Currently the relationship between estimates of alveolar dimension from these two in vivo diffusion models is relatively unknown. Ouriadov et al. [283] derived estimates of mean chord length (Lm) and mean diffusive length scale (Lm_D) in older never smokers, ex-smokers, and COPD patients with ^{3}He DW-MRI at 3 T. A linear correlation between Lm and Lm_D was obtained suggesting the lung morphometry parameters are related but not equivalent. However, in this analysis the SEM-derived Lm_D was incorrectly implemented (see Discussion in Section 7.4), potentially affecting the observed correlation.

This chapter aims to reproduce the in vivo SEM and CM comparison with ^{3}He at 1.5 T and expand the analysis to ^{129}Xe DW-MRI to further demonstrate the clinical viability of ^{129}Xe MRI. 3D multiple b-value ^{3}He and ^{129}Xe DW-MRI was acquired in a range of patients representing a range of different acinar length scales. The two theoretical gas diffusion models, SEM and CM, were used to evaluate each dataset and derive in vivo lung morphometry parameters. For each ^{3}He and ^{129}Xe dataset, the CM-derived mean chord length (Lm), and mean alveolar diameter (L_{Alv}) were compared to the SEM-derived mean diffusive length scale (Lm_D).

7.2   Methods

In this retrospective analysis, 3D multiple b-value ^{3}He and ^{129}Xe DW-MRI from different pulmonary patient groups (healthy normals, ex-smokers, idiopathic pulmonary fibrosis (IPF), and COPD) representing a range of acinar length scales were acquired on a 1.5 T GE HDx scanner in 51 and 31 subjects, respectively. ^{3}He and ^{129}Xe DW-MRI was acquired with compressed sensing according to the scan parameters in Sections 5.3 and 6.3, and relevant acquisition parameters are summarised in Table 7.1. Lung regions of interest were manually segmented from each subjects' reconstructed DW-MRI dataset, and the multiple b-value diffusion signal decay was fitted to the two lung morphometry models on a voxel-by-voxel basis. One-way analysis of variance (ANOVA) with Tukey post-hoc multiple comparison adjustment was conducted to compare lung morphometry metrics across the different patient groups.

Table 7.1: Scan parameters for 3D multiple b-value ^{3}He and ^{129}Xe DW-MRI acquisitions.

	3D ^{3}He DW-MRI	3D ^{129}Xe DW-MRI
Gas dose (ml)	250	550
b-values (s/cm^2)	[0, 1.6, 4.2, 7.2]	[0, 12, 20, 30]
Voxel size (mm^3)	4.17×4.17×12	6.25×6.25×15
Diffusion time (ms)	1.6	8.5
Scan time (s)	15 (3×CS)	16 (4×CS)

Stretched Exponential Model

The multiple b-value diffusion signal decay was fitted to the stretched exponential function (Equation 3.96) to obtain a distributed diffusivity coefficient (DDC) and heterogeneity index value (α). A probability distribution of diffusivity $p(D)$ within each ^{3}He and ^{129}Xe image voxel was then derived using DDC and α (Equations 3.97 and 3.98). This probability distribution of diffusivity represents all the possible diffusivities, ranging from 0 to the respective free diffusion coefficient of each gas in air ($D_0^{\text{He-air}} = 0.88$ cm2/s, and $D_0^{\text{Xe-air}}$

$= 0.14$ cm^2/s), that may be found within each voxel due to the diffusion restriction of the complex acinar airway structure. A probability distribution of diffusive length scales $p(L_D)$ can then be derived from the transformation of $p(D)$ using root-mean-square diffusion displacements (Equation 3.80) relating diffusivity and diffusion time to length scale. The respective diffusion times of the two gases ($\Delta_{\text{He}} = 1.6$ ms, and $\Delta_{\text{Xe}} = 8.5$ ms, respectively) were empirically optimised (see Section 6.3) to enable comparable mean diffusive length scale (Lm_D) measurements with both ^{3}He and ^{129}Xe.

Cylinder Model

For the cylinder model, the diffusion signal decay from the ^{3}He and ^{129}Xe data was fitted to the Equation 3.85 to derive the anisotropic diffusion coefficients (D_L and D_T). The ^{3}He D_L and D_T were related to the cylindrical model geometrical parameters (R and h) through the phenomenological expressions in Equations 3.87 – 3.89. Acinar airway radii (R) and alveolar sleeve depth (h) were then used to derive the ^{3}He mean chord length (Lm), and mean alveolar diameter (L_{Alv}). L_{Alv} is defined as chord length of one alveolus in the CM cylindrical airway geometry and is equivalent to $2R\sin(\pi/8)$ (see Figure 3.26). Lm is derived from the volume to surface area ratio ($4V/S$) as used in histological measurements of lung morphometry [9]. The volume and surface area of a single alveolar unit was calculated from R, h, and L_{Alv} with the expressions in Equation 3.90.

The ^{129}Xe-based R and h were related to ^{129}Xe D_L and D_T coefficients using the same phenomenological expressions as for the ^{3}He data. The implementation of ^{3}He-based expressions for ^{129}Xe DW-MRI is in contrast to the ^{129}Xe-based phenomenological expressions (Equations 3.92 – 3.94) proposed for the cylinder model. The ^{129}Xe expressions are optimised for a ^{129}Xe $\Delta = 5$ ms; however, with the derivation of an empirically-optimised ^{129}Xe $\Delta = 8.5$ ms, it was concluded that comparable ^{3}He and ^{129}Xe CM Lm can be obtained at this diffusion time (see Section 6.3.3).

7.3 Results

7.3.1 ^{3}He lung morphometry comparison

Maps of lung morphometry parameters were generated for each ^{3}He dataset, and a summary of mean ^{3}He DW-MRI metrics for each patient group is provided in Table 7.2. A statistically significant ($P<0.001$) difference in mean global value across the patient groups was obtained via ANOVA for each ^{3}He DW-MRI metric. Mean ADC, DDC, Lm_D, R, L_{Alv}, and Lm was significantly increased ($P<0.05$) between all patient groups, except between healthy and ex-smoker patients. In contrast, mean α and h was significantly decreased ($P<0.05$)

between all groups, except between healthy and ex-smoker patients. Example maps of lung morphometry indices from the SEM (Figure 7.1) and CM (Figure 7.2) illustrate this difference in lung microstructure between each patient group.

Table 7.2: Summary of mean global ^{3}He diffusion-weighted metrics derived from the cylinder and stretched exponential models in healthy normals, ex-smokers, IPF, and COPD patients.

		^{3}**He Lung Morphometry Metrics**			
		Healthy	**Ex-smoker**	**IPF**	**COPD**
No. of subjects		15	6	18	12
Age		26.4 ± 10.5	51.3 ± 2.7	70.8 ± 5.3	62.1 ± 7.9
ADC (cm^2/s)		0.18 ± 0.07	0.22 ± 0.08	0.33 ± 0.13	0.47 ± 0.15
SEM metrics	DDC (cm^2/s)	0.14 ± 0.05	0.18 ± 0.05	0.30 ± 0.14	0.47 ± 0.20
	Alpha (α)	0.84 ± 0.16	0.82 ± 0.16	0.77 ± 0.17	0.73 ± 0.17
	Lm_D (µm)	212 ± 24	233 ± 25	272 ± 34	312 ± 43
CM metrics	R (µm)	275 ± 65	296 ± 61	351 ± 57	408 ± 67
	h (µm)	129 ± 78	105 ± 77	56 ± 69	25 ± 48
	L_{Alv} (µm)	210 ± 50	227 ± 47	268 ± 44	312 ± 51
	Lm (µm)	186 ± 50	246 ± 89	448 ± 183	656 ± 228

A statistically significant correlation ($P<0.001$) between ^{3}He Lm_D and Lm was observed. Three different curve regression fits (linear, exponential, and power) were performed, and all three fits had similar R-square values (Table 7.3). For each regression fit, Lm was the dependent variable (β_0), and Lm_D was set as the independent variable (β_1). The power model had the largest R^2 (0.960) and is presented in Figure 7.3a. The parameters Lm_D and L_{Alv} (from the CM) were also significantly correlated ($P<0.001$) in a linear relationship (Figure 7.3b). A similar linear regression fit, with L_{Alv} as the dependent variable β_0, derived $\beta_1 = 1$, suggesting excellent agreement between the two parameters. Bland-Altman analysis confirmed this agreement with a mean bias in Lm_D value of $+1.0\%$ and a 95% confidence interval of -3.2% to 5.1% (Figure 7.4).

Table 7.3: Summary of regression fit model parameters for ^{3}He Lm_D and Lm, and Lm_D and L_{Alv} comparisons.

Regression Fit	^{3}**He Lm Estimate**			^{3}**He L_{Alv} Estimate**		
	R^2	β_0 **(Lm)**	β_1 **(Lm_D)**	**R^2**	β_0 **(L_{Alv})**	β_1 **(Lm_D)**
Linear	0.956	-802.3	4.63	0.981	-2.96	1.00
Exponential	0.942	16.1	0.012	–	–	–
Power	0.960	9.1E-06	3.15	–	–	–
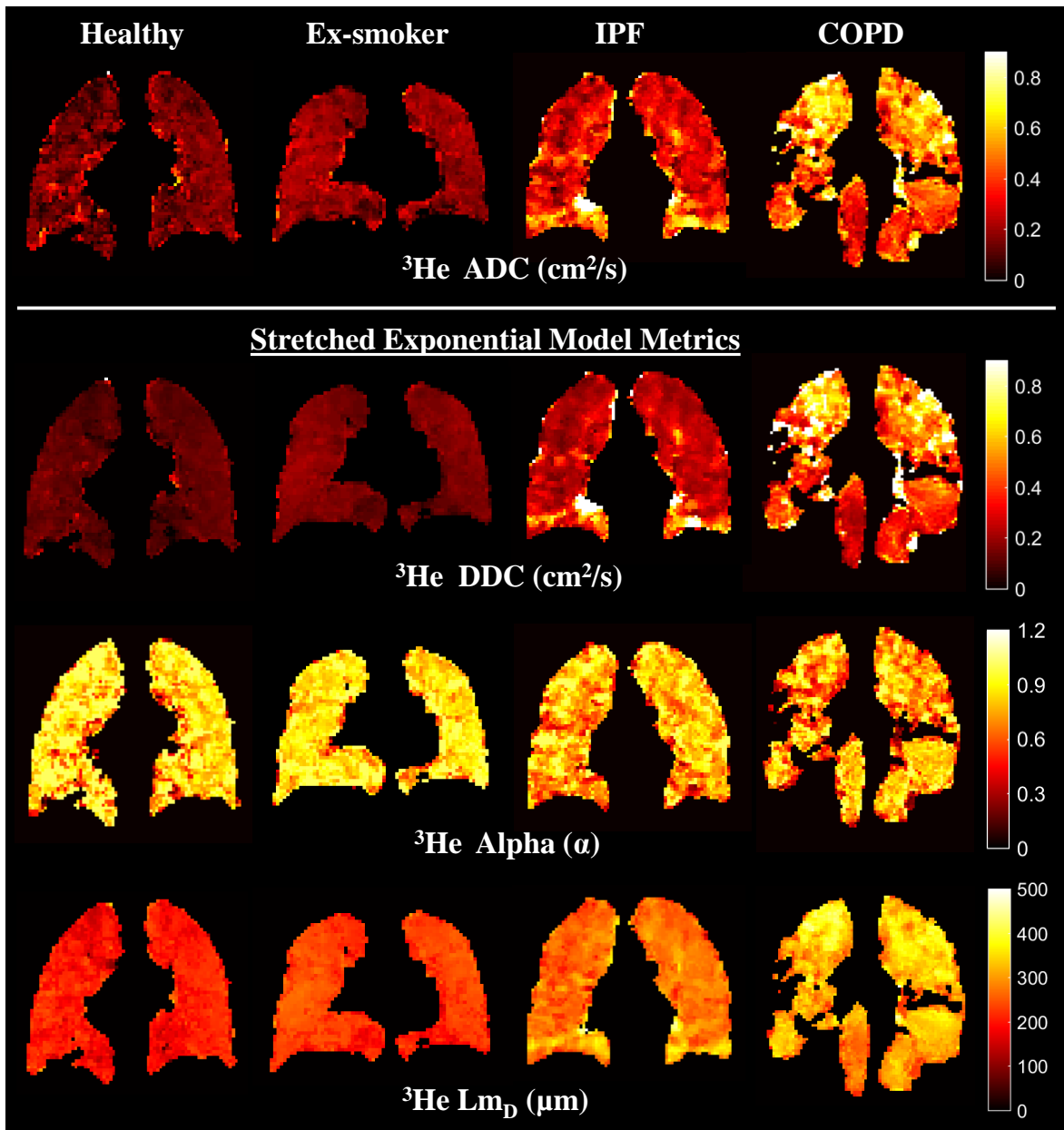
Figure 7.1: Representative ^{3}He maps of ADC, and SEM-derived metrics of DDC, alpha (α), and mean diffusive length scale (Lm_D) for a healthy, ex-smoker, IPF, and COPD subject.

Figure 7.2: Representative ^{3}He maps of CM-derived metrics of acinar airway radius (R), alveolar sleeve depth (h), mean chord length (Lm), and mean alveolar diameter (L_{Alv}) for a healthy, ex-smoker, IPF, and COPD subject.

Figure 7.3: (a) Global ^{3}He Lm_D and Lm for all subjects are strongly correlated ($P<0.001$) in a power relationship. (b) Lung morphometry parameters Lm_D and L_{Alv} are strongly correlated ($P<0.001$) in a linear relationship, demonstrating excellent agreement between the two parameters.

Figure 7.4: Bland-Altman analysis of mean global ^{3}He Lm_D and L_{Alv} values. A mean bias of 1.0% towards Lm_D values is obtained with a 95% confidence interval between -3.2% and 5.1%.

7.3.2 ^{129}Xe lung morphometry comparison

The equivalent ^{129}Xe lung morphometry parameters are summarised in Table 7.4. Similar to the ^{3}He lung morphometry parameters, all ^{129}Xe metrics (except for α value) were significantly different ($P<0.001$), via ANOVA, across the patient groups. The ^{129}Xe α value for all subject groups was also larger than the ^{3}He α value in the healthy subject group, and this could be attributed to the more mono-exponential signal decay (i.e. larger α values) observed with ^{129}Xe when compared to ^{3}He DW-MRI (see Section 6.3.3). A statistically significant increase ($P<0.05$) for ADC, DDC, Lm_D, R, Lm, and L_{Alv} value, and a significant decrease for h, was obtained only between healthy vs. IPF, healthy vs. COPD, and ex-smoker vs. COPD patient groups. Example ^{129}Xe lung morphometry maps from the SEM and CM for each patient group are shown in Figure 7.5 and 7.6.

Table 7.4: Summary of mean global ^{129}Xe diffusion-weighted metrics derived from the cylinder and stretched exponential models in healthy normals, ex-smokers, IPF, and COPD patients.

		^{129}Xe Lung Morphometry Metrics			
		Healthy	**Ex-smoker**	**IPF**	**COPD**
No. of subjects		7	6	8	10
Age		29.4 ± 4.0	51.3 ± 2.7	69.9 ± 4.3	60.9 ± 4.8
ADC (cm^2/s)		0.030 ± 0.009	0.037 ± 0.009	0.046 ± 0.011	0.051 ± 0.013
SEM metrics	DDC (cm^2/s)	0.025 ± 0.007	0.033 ± 0.007	0.042 ± 0.010	0.049 ± 0.014
	Alpha (α)	0.86 ± 0.15	0.86 ± 0.15	0.86 ± 0.12	0.86 ± 0.12
	Lm_D (µm)	205 ± 23	230 ± 22	257 ± 24	270 ± 29
CM metrics	R (µm)	273 ± 79	306 ± 66	346 ± 56	364 ± 59
	h (µm)	132 ± 88	111 ± 85	85 ± 78	76 ± 75
	L_{Alv} (µm)	209 ± 61	234 ± 51	264 ± 43	279 ± 45
	Lm (µm)	187 ± 62	257 ± 96	365 ± 157	422 ± 174

A statistically significant correlation ($P<0.001$) between ^{129}Xe Lm_D and Lm was obtained. The same three curve regression fits (linear, exponential, and power) were performed, and as for ^{3}He, all three fit curves had similar R^2 values (Table 7.5). ^{129}Xe Lm_D and Lm can be described by a power model with R^2 = 0.971 and is presented in Figure 7.7a. The ^{129}Xe parameters Lm_D and L_{Alv} were also significantly correlated ($P<0.001$) in a linear relationship (Figure 7.7b), and the $\beta_1 = 1.05$ suggests excellent agreement. This was confirmed with Bland-Altman analysis, and a mean bias in Lm_D value of -2.6% and a 95% confidence interval of -7.9% to 2.7% was obtained (Figure 7.8).

Table 7.5: Summary of regression fit model parameters for ^{129}Xe Lm_D and Lm, and Lm_D and L_{Alv} comparisons.

| Regression Fit	^{129}Xe Lm Estimate			^{129}Xe L_{Alv} Estimate		
	R^2	β_0 (Lm)	β_1 (Lm_D)	**R^2**	β_0 (L_{Alv})	β_1 (Lm_D)
Linear	0.953	-644	3.96	0.965	-4.51	1.05
Exponential	0.964	17.3	0.012	–	–	–
Power	0.971	3.3E-05	2.92	–	–	–
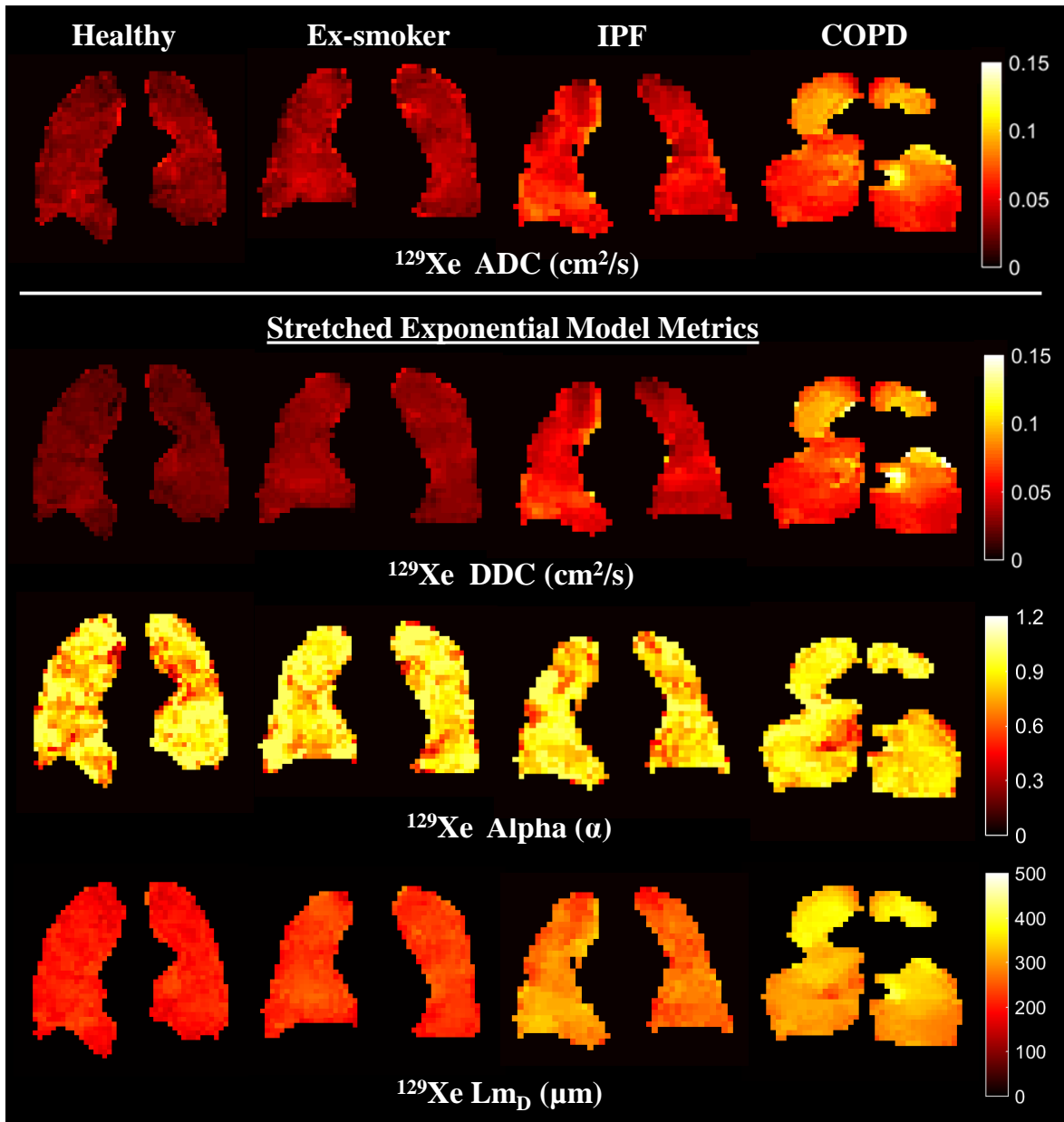
Figure 7.5: Representative ^{129}Xe maps of ADC, and SEM-derived metrics of DDC, alpha (α), and mean diffusive length scale (Lm_D) for a healthy, ex-smoker, IPF, and COPD subject.
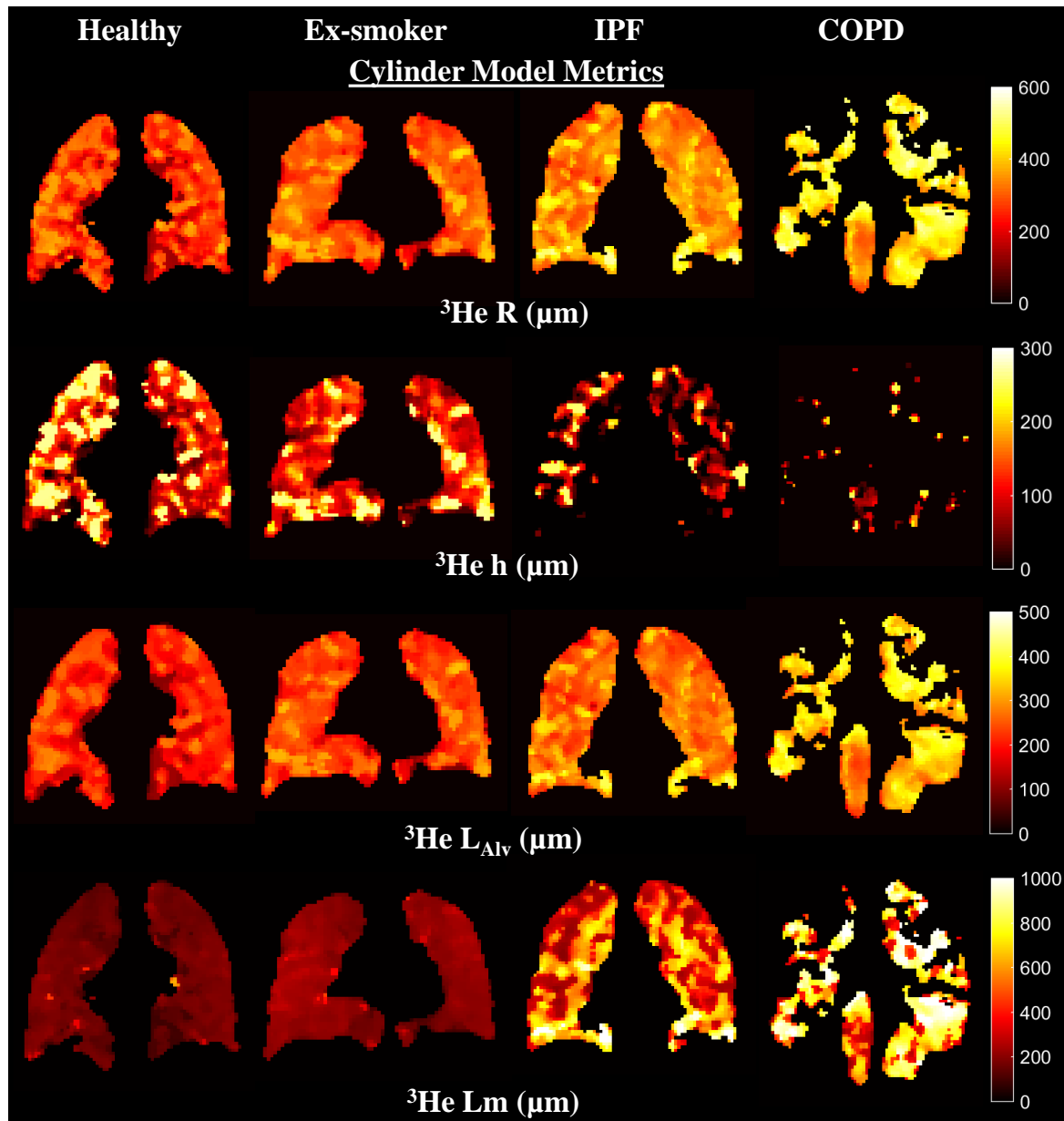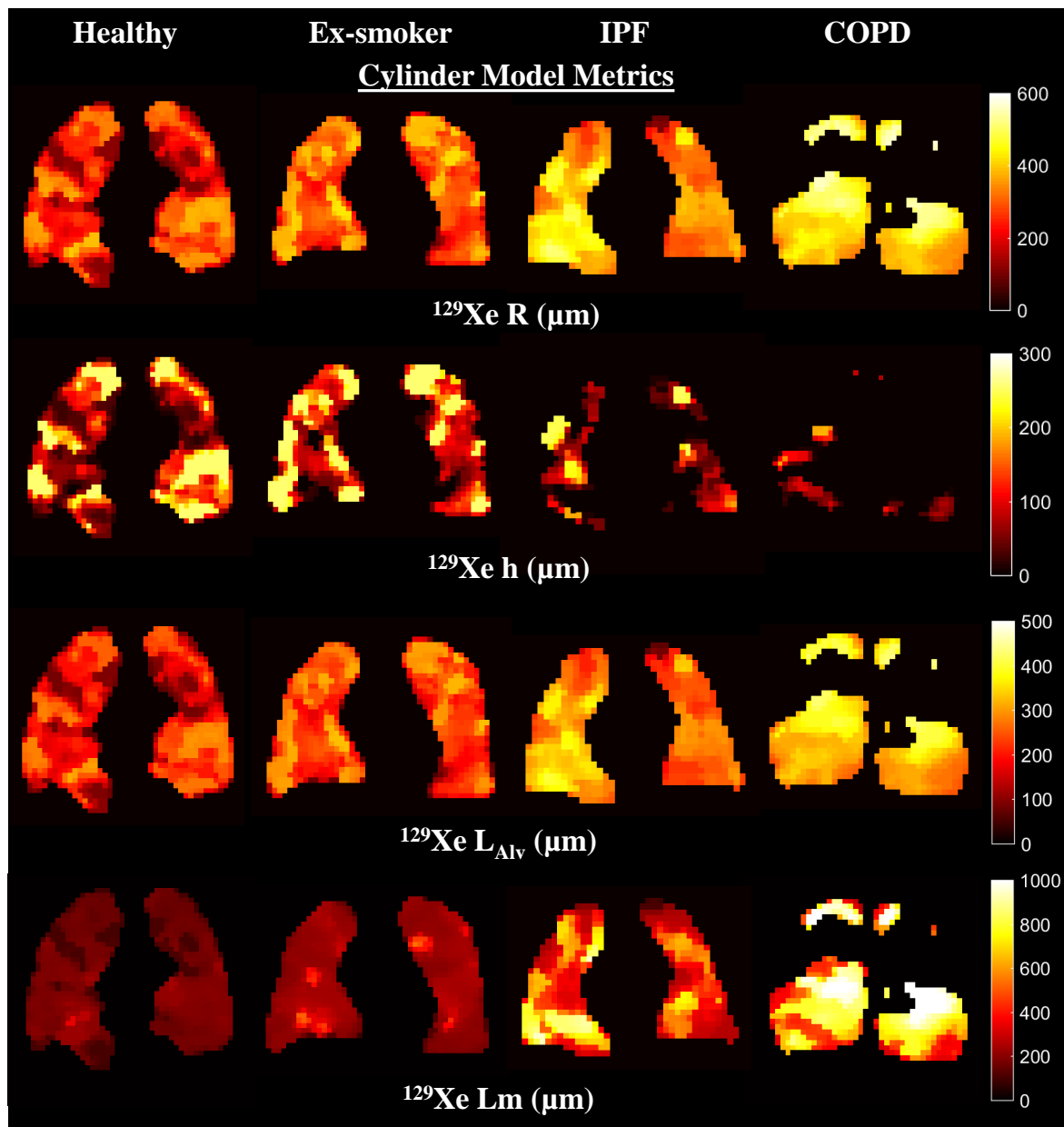
Figure 7.6: Representative ^{129}Xe maps of CM-derived metrics of acinar airway radius (R), alveolar sleeve depth (h), mean chord length (Lm), and mean alveolar diameter (L_{Alv}) for a healthy, ex-smoker, IPF, and COPD subject.
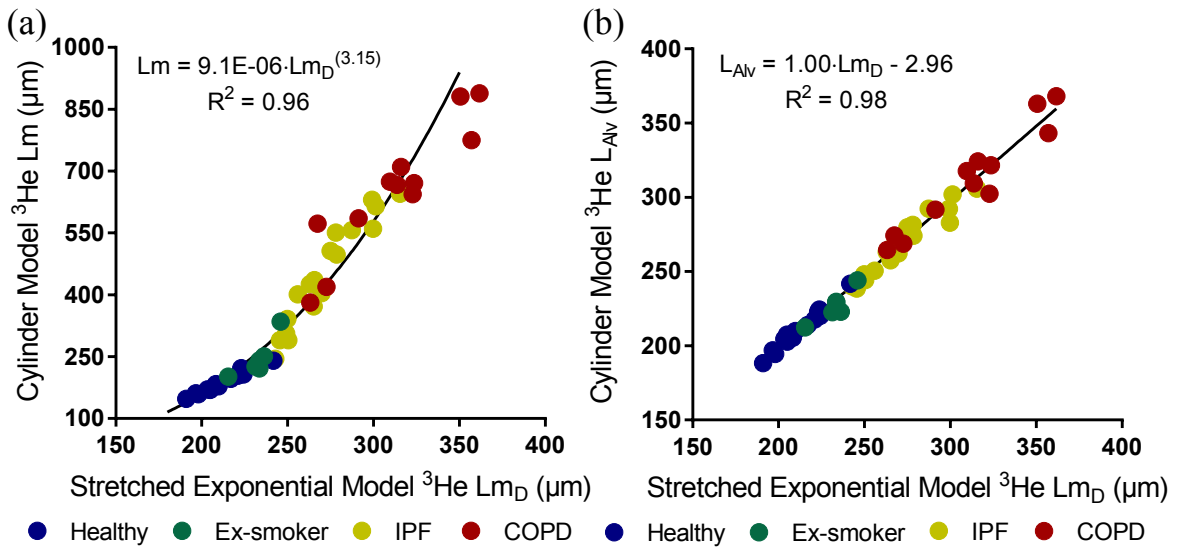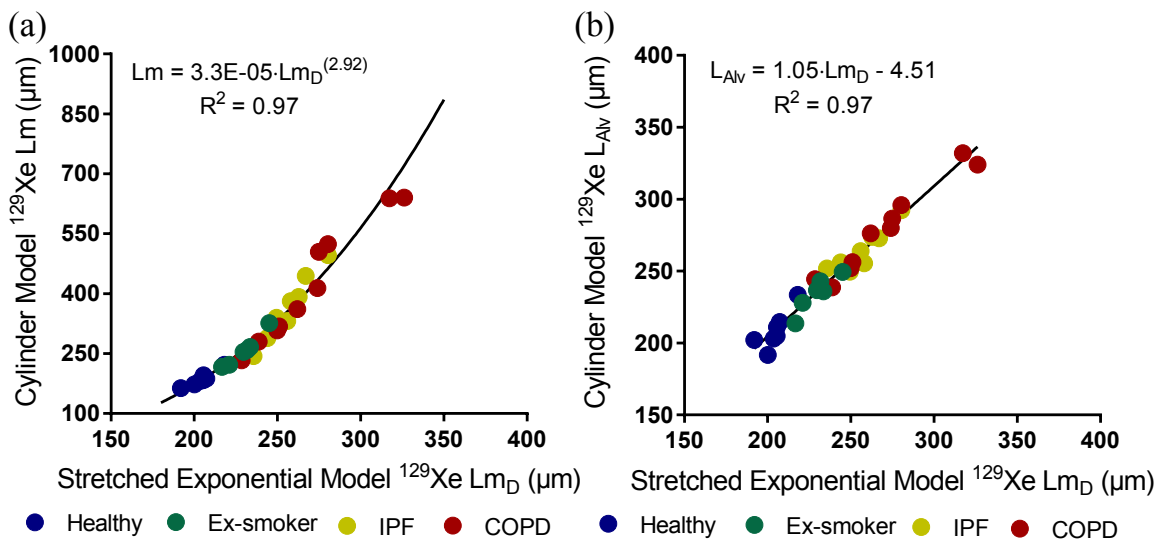
Figure 7.7: (a) Global ^{129}Xe Lm_D and Lm for all subjects are strongly correlated ($P<0.001$) in a power relationship. (b) Lung morphometry parameters Lm_D and L_{Alv} are strongly correlated ($P<0.001$) in a linear relationship and demonstrate excellent agreement between the two parameters.
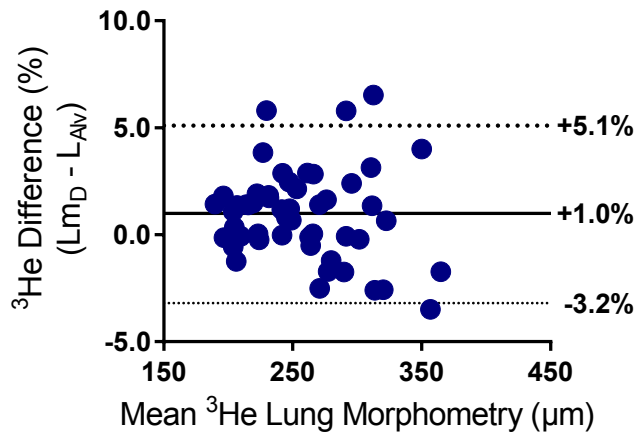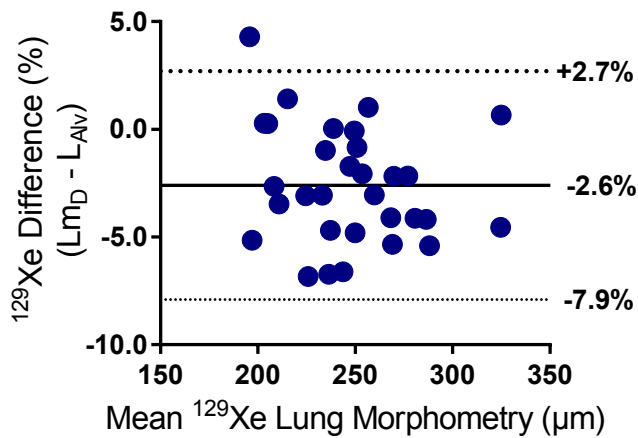

Figure 7.8: Bland-Altman analysis of mean global ^{129}Xe Lm_D and L_{Alv} values. A mean bias of -2.6% towards Lm_D values is obtained with a 95% confidence interval between -7.9% and 2.7%.

7.4 Discussion

7.4.1 Comparison of Lm_D with Lm and L_{Alv}

In this comparison of ^{3}He and ^{129}Xe hyperpolarised gas diffusion lung morphometry models, significant differences ($P<0.001$) between patient groups was observed. Lung morphometry parameters were significantly increased (ADC, DDC, Lm_D, R, L_{Alv}, and Lm) or decreased (α and h) ($P<0.05$) between healthy subjects and IPF and COPD patients. These significant differences reflect the respective changes to acinar microstructure mainly related to fibrosis in IPF patients, and emphysema for ex-smokers and COPD patients. Mean ^{3}He cylinder model-derived parameters of R, h and Lm (Table 7.2) are comparable to the values reported

in the literature for healthy ($R = 304$ µm, $h = 154$ µm, $Lm = 186$ µm) [133], ex-smokers ($R = 304$, $h = 130$, $Lm = 220$) [131], and COPD patients ($R = 450$, $Lm = 450$) [283]. Mean ^{3}He SEM metrics for healthy and COPD subjects also match previously reported DDC (healthy = 0.14 cm^2/s, COPD = 0.39 cm^2/s), α (healthy = 0.86, COPD = 0.69), and Lm_D (healthy = 210 µm, COPD = 293 µm) values (from [141], and Table 6.3). Ex-smoker SEM metrics were also comparable to reported values (DDC = 0.21 cm^2/s, α = 0.81) [283].

To our knowledge, in vivo DW-MRI metrics of patients with IPF have not been reported before. This is the focus of Section 8.2, where multiple b-value DW-MRI was used to assess changes in lung microstructure at baseline and after 6 months in a cohort of patients with IPF. The IPF patients in this comparison are part of this cohort, therefore the ADC and SEM metrics are identical to those presented in Table 8.2. However, CM microstructure metrics for this IPF cohort are not reported in Section 8.2. Lung morphometry metrics for IPF patients from both the SEM and CM appear to lie between the ranges of metrics from the ex-smokers and COPD patient groups. Mean ^{129}Xe DW-MRI metrics of lung morphometry were comparable to the ^{3}He across all subject groups. This was expected because ^{129}Xe DW-MRI was acquired at ^{129}Xe $\Delta = 8.5$ ms, which represents a ^{129}Xe diffusion time that was empirically-tuned such that equivalent lung morphometry parameters (Lm_D and Lm) were derived from both ^{3}He and ^{129}Xe DW-MRI (see Section 6.3).

The R^2 values for the three different regression curve fits of the ^{3}He and ^{129}Xe comparison of Lm and Lm_D were very similar. The linear regression fit R^2 (0.956) was very similar to the power regression model (0.960); however, the power relationship matched the ^{3}He and ^{129}Xe data best. To date, the only previous comparison between the CM and SEM models of gas diffusion was made at 3 T with 2D ^{3}He multiple b-value DW-MRI [283]. In this previous comparison, a statistically significant linear trend was observed between Lm_D and Lm parameters (Figure 7.9).

Figure 7.9: The linear correlation (blue line) between ^{3}He Lm_D and Lm morphometry parameters for the previous 3 T analysis of Ouriadov et al. [283] is compared against the power relationship (orange curve) observed in the comparison at 1.5 T performed here. The dotted line corresponds to the 1D free diffusion length of ^{3}He (530 µm) for the acquisition parameters in Table 7.1.
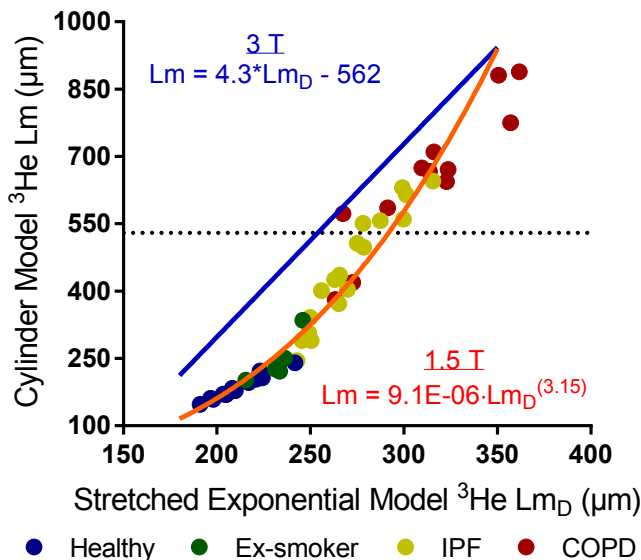
The first contributing factor to this observed difference in lung morphometry parameter relationships is the discrepancy in the derivation of Lm_D between the two studies. In Ouriadov et al. [283], Lm_D was calculated, using the 1D theoretical diffusion length equation (see Equation 3.99), from a mean diffusivity value ($\bar{D}$) obtained from a probability distribution of diffusivities $p(D)$:

$$\bar{D} = \sum p(D) \cdot D$$
$$Lm_D = \sqrt{2\Delta\bar{D}} \tag{7.1}$$

While in our comparison, Lm_D is the mean diffusive length scale derived from a probability distribution of length scales, $p(L_D)$, obtained by transforming $p(D)$ using the 1D theoretical diffusion length equation, and can be summarised as follows:

$$p(L_D) = p(\sqrt{2\Delta D})$$
$$Lm_D = \sum p(L_D) \cdot \sqrt{2\Delta D} \tag{7.2}$$

The order in which the non-linear transformation in the 1D diffusion equation is applied in the derivation of Lm_D will correspond to slightly different Lm_D values, and this is demonstrated graphically in Figure 7.10.
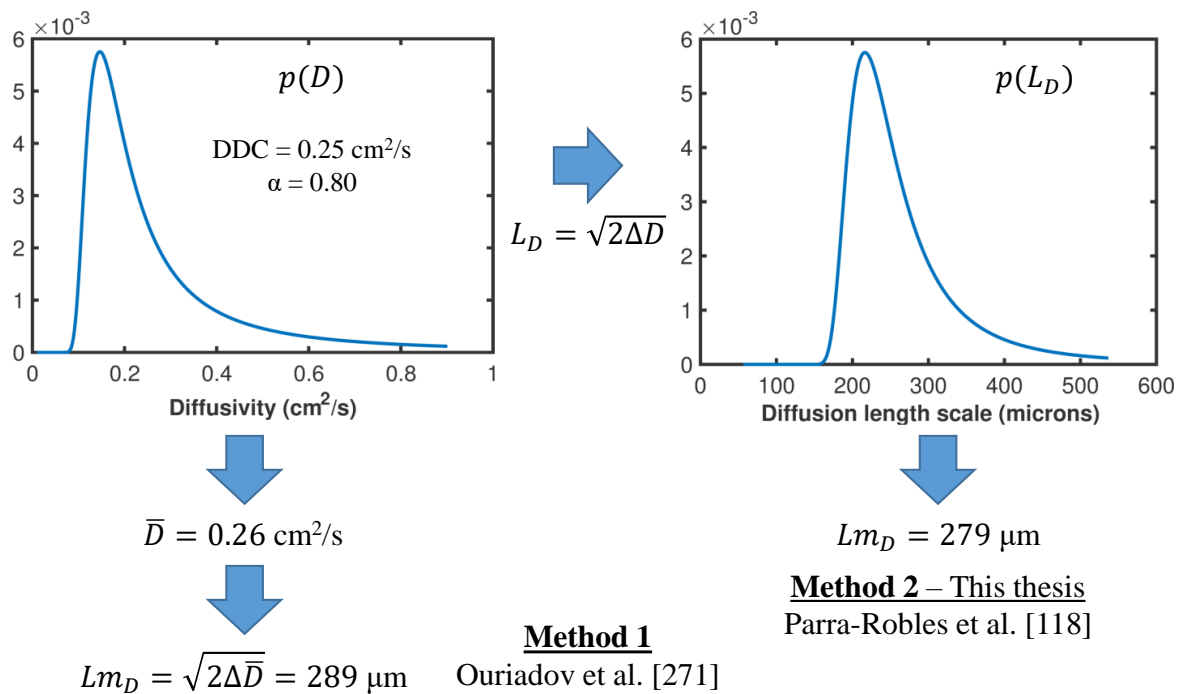
Figure 7.10: The difference in Lm_D derivation between Ouriadov et al. [283] (Method 1), and in this thesis based on Parra-Robles et al. [129] (Method 2). Method 1 will derive larger Lm_D values than Method 2 for the same DDC and α value due to the non-linear transformation occurring at the end of the Lm_D derivation, rather than at the start in Method 2.

A second factor is the different subject cohorts; for example, the healthy cohort in the 3 T comparison were older never-smokers (mean age = 69), while the cohort in this comparison at 1.5 T were considerably younger (mean age = 26). In Figure 7.9, the inclusion of young healthy volunteers with smaller alveolar dimensions contributes significantly to the non-linear power relationship observed at 1.5 T. If healthy subjects were excluded, a linear correlation with a gradient of 5.0 is obtained that is similar to the one observed at 3 T by Ouriadov et al. [283]. The last factor that could contribute to the different lung morphometry relationships is the difference in magnetic field strength. Susceptibility gradients are induced at the tissue and air interfaces within the acinar airspace, and these background field gradients are field strength dependent and have been shown to affect ADC and theoretical gas diffusion model parameters with ^{3}He at 1.5 T vs. 3 T [104]. Measurements of cylinder model Lm at 3 T in healthy volunteers were up to 17% larger than the equivalent measurements at 1.5 T [104], and this could in part explain the larger ^{3}He Lm values observed at 3 T.

The power relationship between Lm and Lm_D, observed in Figure 7.3a and 7.7a, suggests that even though the two lung morphometry parameters are significantly related, they are not equivalent measures of alveolar dimension. The linear correlation and linear regression parameters (Figures 7.3b and 7.7b) between Lm_D and L_{Alv} for both ^{3}He and ^{129}Xe indicates excellent agreement between the two lung morphometry parameters. Bland-Altman comparison of mean Lm_D and L_{Alv} values (Figures 7.4 and 7.8) confirmed this excellent agreement with a mean bias of 1.0% (95% difference range of -3.2% and 5.1%) and -2.6% (95% difference range of -7.9% and 2.7%) obtained for ^{3}He and ^{129}Xe, respectively.

In the representative patient ^{3}He and ^{129}Xe L_{Alv} maps (shown in Figure 7.2 and 7.6), regions of elevated L_{Alv} appear to qualitatively match those observed in the corresponding Lm_D maps (Figure 7.1 and 7.5). This regional matching is further demonstrated by pixel-by-pixel analysis of Lm_D and L_{Alv} in a healthy volunteer and a COPD patient (Figure 7.11). A statistically significant correlation between the two morphometry parameters was observed in both subjects ($P<0.001$); however, linear regression fits resulted in R^2 of 0.71 and 0.13 for the COPD patient and the healthy volunteer, respectively. The comparatively small R^2 for the healthy volunteer can be attributed to the small range of Lm_D and L_{Alv} values associated with healthy lung microstructure. In contrast, the COPD patient has a larger range of microstructural values resulting in a wider range of data point distribution and a better resultant linear fit. The linear regression equations for both representative subjects (see Figure 7.11) were similar to the regression equation obtained for global ^{3}He Lm_D and L_{Alv} (Figure 7.3b) in all subjects.

The pixel-by-pixel analysis of Lm_D and Lm in the same representative healthy volunteer and COPD patient (Figure 7.12) yielded a similar statistically significant correlation ($P<0.001$) between the lung morphometry parameters. Non-linear regression fits with a power model determined an R^2 value of 0.34 and 0.56 for the healthy and COPD subject, respectively. The β_1
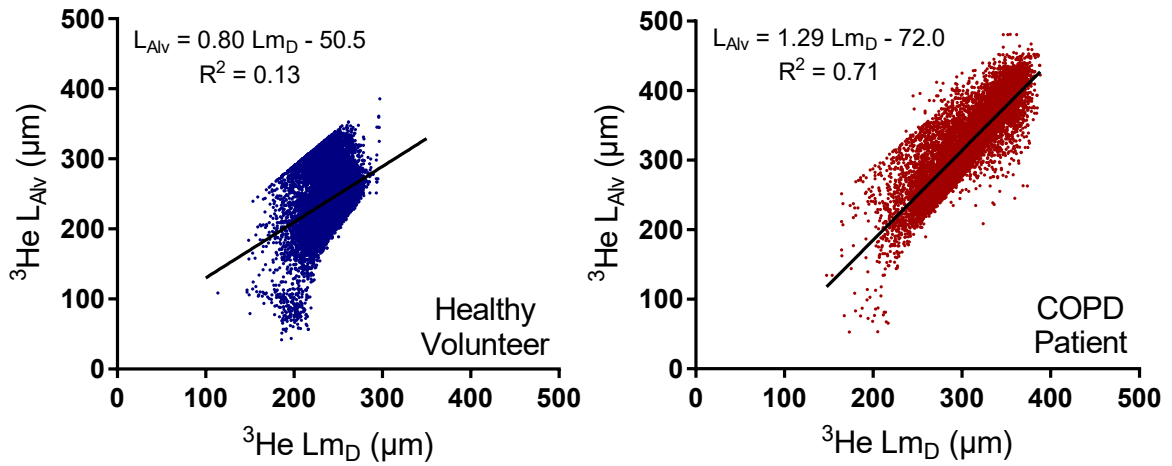
Figure 7.11: Pixel-by-pixel comparison of ^{3}He Lm_D and L_{Alv} values in a representative healthy volunteer and a COPD patient. A statistically significant correlation was obtained in both subjects ($P<0.001$) with a linear regression fit of $R^2 = 0.13$ and $R^2 = 0.71$ for the healthy volunteer and the COPD patient, respectively.

coefficient for both subjects was smaller than the corresponding value ($\beta_1 = 3.15$, Table 7.3) obtained on a global level in all subjects. A difference in this coefficient is expected due to different subject groups considered, but the pixel-by-pixel results in Figure 7.12 appear to demonstrate a similar power relationship between Lm_D and Lm as that observed in Figure 7.3a.
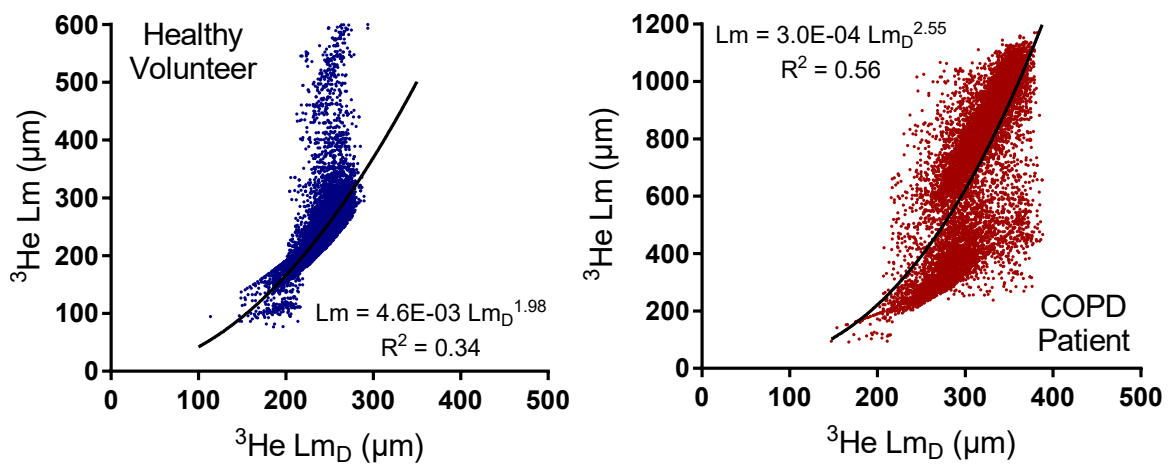
Figure 7.12: Pixel-by-pixel comparison of ^{3}He Lm_D and Lm values in a representative healthy volunteer and a COPD patient. A statistically significant correlation was obtained in both subjects ($P<0.001$) with a non-linear power model regression fit of $R^2 = 0.34$ and $R^2 = 0.56$ for the healthy volunteer and the COPD patient, respectively.

7.4.2   SEM and CM differences and limitations

The in vivo results suggest that mean diffusive length scale (Lm_D) from the SEM is more analogous to the mean alveolar diameter (L_{Alv}) than the mean chord length (Lm) from the CM. Due to the differences in how each parameter is calculated, the portion of the acinar airway geometry that is represented by each parameter is slightly different, and this may go towards explaining the two distinct relationships of Lm_D between Lm and L_{Alv}. In the SEM, where no assumptions of acinar airway geometry are made, Lm_D is directly reflective of the apparent distance ^{3}He or ^{129}Xe gas atoms diffuse within the acinar airspace. The maximum Lm_D is defined by the theoretical free diffusion length of the DW-MRI experiments ($\sim$500 µm) which is dependent upon the experimental diffusion time and respective free diffusion coefficient of the gas. According to histological measurements of lung morphometry, the mean alveolar diameter in healthy adult lungs is approximately 200 to 250 µm [9, 12, 284], and the mean alveolar duct diameter ranges from 200 to 600 µm [9]. Therefore, in these experiments, gas atoms are predominantly restricted by the alveolar geometry and as such Lm_D is reflective of alveolar dimensions.

In contrast, the CM-derived mean chord length (Lm) is calculated through an inferred relationship between the volume and surface area of a single alveolus unit (Equation 3.91). It is important to note that mean chord length is not a measurement of alveolar size, but rather a measurement of the acinar airspace that includes the alveolus and alveolar ducts [17]. This is apparent in the calculation of V_a (Equation 3.90) in the cylinder model (Figure 3.26) which includes both alveolus and alveolar duct volumes. The inclusion of the alveolar duct volume could in theory allow the calculation of Lm values that exceed the theoretical free diffusion length of the gas alone.

This could explain why in predominantly healthy subjects where the gas atoms can diffuse out of the alveoli and into the alveolar duct, there is a reasonable matching of Lm_D and Lm values. However, in patients with more advanced disease where alveolar walls are destroyed, the gas atoms diffuse more freely between enlarged alveoli and alveolar ducts. While a Lm measurement can still be derived, it may exceed the theoretical free diffusion length (see data points above dotted line in Figure 7.9). These conditions can cause a large mismatch in Lm_D and Lm values when large microstructural changes occur, and is demonstrated in the IPF and COPD patients in Figures 7.3a and 7.7a. With increasingly advanced disease the Lm_D will plateau towards the theoretical free diffusion length, while the Lm value will theoretically continue to increase, and this accounts for the power relationship obtained in the in vivo comparisons.

In the latest iteration of the cylinder model, the cylinder duct is surrounded by an alveolar sleeve containing eight alveolus units (Figure 3.26) [6]. The number of alveoli was chosen such

that the chord length or diameter of an alveolus unit (L_{Alv}) would empirically match the alveolar diameter obtained from histological measurements. The L_{Alv} values demonstrated excellent agreement with Lm_D values with both ^{3}He and ^{129}Xe, indicating that the two parameters may be equivalent. Previous studies of in vivo lung morphometry with the cylinder model did not report L_{Alv} values, but L_{Alv} can be retrospectively calculated from the published acinar airway radii (R) values ($L_{Alv} = 0.765R$). The retrospectively calculated ^{3}He L_{Alv} in healthy ($\sim$230 µm [133]), ex-smokers ($\sim$250 µm [131]), and COPD ($\sim$340 µm [283]) patients are similar to those for ^{3}He and ^{129}Xe derived in this in vivo comparison (see Table 7.2 and 7.4).

The cylinder model has a specific prescribed physiological range of operation, such as $h/R < 0.6$ and $R = 300$ to 400 µm, where the phenomenological expressions relating the anisotropic diffusion coefficients and alveolar duct dimensions are considered valid (see Section 3.5.2). In this work, an upper limit of $R = 700$ µm and $r = 600$ µm was prescribed. DW-MRI voxels that exceed this limit were excluded from the cylinder model morphometry maps and represent regions where alveolar duct dimensions are no longer within the physiological range stipulated for the cylinder model [6, 128]. Within the theoretical boundaries of the cylinder model, anisotropic diffusion in a cylindrical acinar airway geometry can be assumed. However, in lungs with significant destruction of the alveolar wall due to advanced lung disease, the diffusion in the enlarged acinar airspace is more isotropic and can no longer be described by anisotropic restricted diffusion.
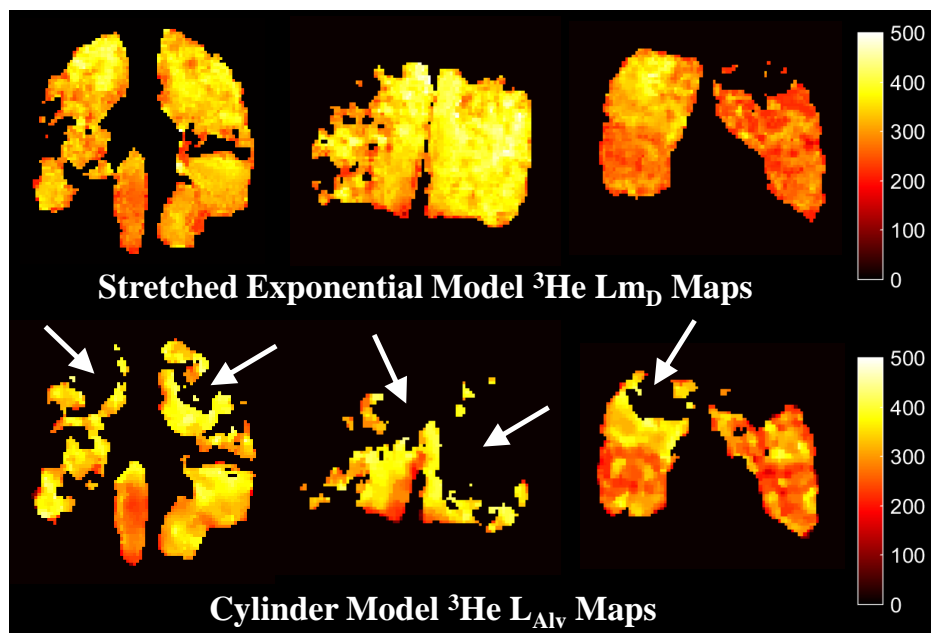
Figure 7.13: Representative Lm_D and L_{Alv} maps for three COPD patients. In the cylinder model derived L_{Alv} maps regions of missing voxels (white arrows) indicate areas where the physiological range of the cylinder model is exceeded. These corresponding regions exist in the stretched exponential model Lm_D maps and also coincide with large Lm_D value areas.

These 'missing' voxel areas can be observed in the COPD L_{Alv} maps from three patients in Figure 7.13, and it is important to emphasise that they are not associated with unventilated lung regions. In contrast, the corresponding regions exist in the Lm_D maps because the stretched exponential model has no underlying geometrical assumptions and can fit the diffusion signal in voxels containing advanced emphysema or those corresponding to conducting airways that show free and/or localised diffusion behaviour. This limitation of the cylinder model suggests that the two gas diffusion models have different operational ranges of length scale estimation accuracy, perhaps due to inherent differences in their geometrical and mathematical assumptions.

Even though the stretched exponential model appears to derive estimates of diffusive length scale across all ranges of acinar structural length scales (up to the theoretical free diffusion length), we emphasise that it has not been directly validated against histology or in phantoms with known geometries. Validating the Lm_D value would increase the clinical potential of this diffusion model in longitudinal monitoring of lung microstructural changes with hyperpolarised gas DW-MRI. Currently, Lm_D results are either qualitatively compared to lung morphometry measurements derived from histology in similar subject populations or validated against cylinder model measurements from the same diffusion data. However, the results in Section 6.3 demonstrate that the SEM-derived Lm_D is dependent upon experimental diffusion time. Therefore, it is possible that the ^{3}He, and subsequently the ^{129}Xe, diffusion time will need to be tuned such that derived Lm_D results match those in the validation geometry.

7.5   Conclusions

This chapter presents the first in vivo comparison of stretched exponential model and cylinder model lung morphometry parameters with both ^{3}He and ^{129}Xe DW-MRI at 1.5 T. The morphometry parameters from the two diffusion models are related where mean chord length (Lm) and mean diffusive length scale (Lm_D) are related by a non-linear power relationship; while Lm_D and mean alveolar diameter (L_{Alv}) demonstrate excellent linear agreement. The two distinct relationships are thought to be representative of the different parts of the acinar airway geometry that are measured with each lung morphometry parameter. Future work will focus on the validation of the stretched exponential model with in vitro experiments using phantoms of simple and realistic acinar geometries and finite element simulations (see Section 9.2 for more details).

Chapter 8

Clinical and physiological investigations of lung microstructure with ^{3}He and ^{129}Xe diffusion-weighted MRI

In Chapters 5 and 6, 3D multiple b-value ^{3}He and ^{129}Xe DW-MRI with compressed sensing acquisition strategies were developed to enable whole lung mapping of ADC and lung morphometry metrics. The clinical evaluation of these methods in several different lung MRI research studies are now summarised.

- In Section 8.1, children with mild cystic fibrosis (CF) lung disease are imaged with 2D multiple b-value ^{3}He DW-MRI to investigate if changes in lung microstructure can be detected in early CF lung disease.

- In Section 8.2, both 3D ^{3}He and ^{129}Xe DW-MRI are used for the assessment of acinar microstructural changes in a cohort of idiopathic pulmonary fibrosis (IPF) patients. The reproducibility of these DW-MRI metrics in patients with IPF and correlations with current clinical measures of IPF disease are also explored.

- Finally, in Section 8.3, 3D ^{3}He and ^{129}Xe DW-MRI are used to investigate changes in acinar dimensions with lung inflation in healthy volunteers.

8.1   Hyperpolarised ^{3}He diffusion-weighted MRI in children with mild cystic fibrosis

8.1.1   Introduction

Cystic fibrosis (CF) is the most common genetic disorder in the Caucasian population [285], and is caused by a mutation in the gene that encodes the CF transmembrane conductance regulator. Advancements in treatment for CF have greatly improved the survival rate in the modern era, however, lung disease is still the primary cause of mortality in the CF population [285]. Measuring early lung disease is crucial in maintaining long-term lung health. In CF, early lung disease is typically characterised by small airways obstruction and increased lung ventilation heterogeneity (Figure 8.1). The current clinical standard in assessing lung disease severity in CF is forced expiratory volume in 1 second (FEV$_1$), but FEV$_1$ has been demonstrated to be insensitive to early changes in lung disease [286].
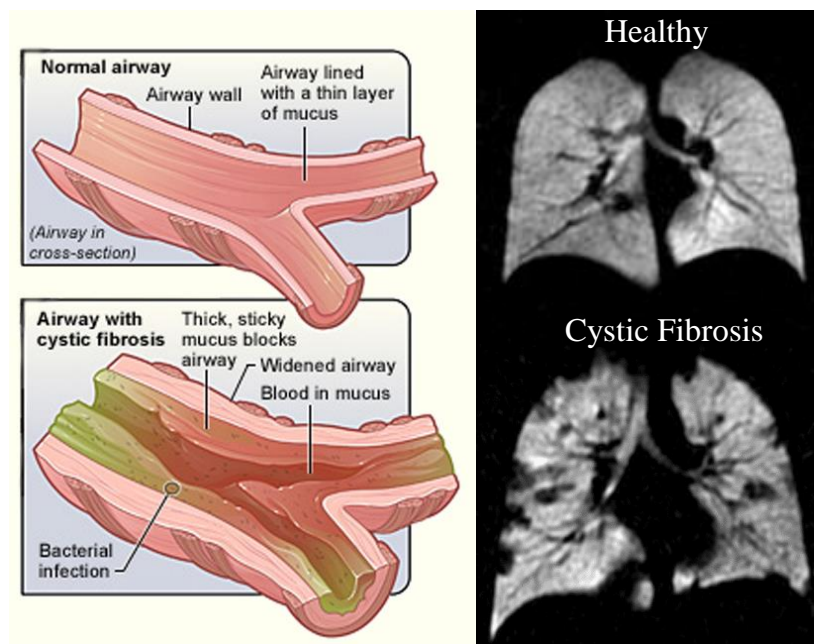
Figure 8.1: Cross-section of normal and cystic fibrosis (CF) airways (left) with corresponding ^{3}He ventilation images (right). In early CF, mucus causes obstruction in the small airways that result in the ventilation defect areas observed in the corresponding ^{3}He ventilation image. Adapted with permission from the National Heart, Lung, and Blood Institute; National Institutes of Health; U.S. Department of Health and Human Services.

Hyperpolarised ^{3}He ventilation MR imaging has been demonstrated to be sensitive to changes in lung ventilation heterogeneity in both children with mild CF disease [286, 287], and in adult CF patients [185, 288]. The global metrics, ventilation defect percentage (VDP) and coefficient of variation (CV) determined from ventilation MRI are highly repeatable in CF patients [185, 289], and were found to be more sensitive than FEV$_1$, lung clearance index

(LCI), and CT in detecting abnormalities in early CF [286]. ^{3}He ventilation MR imaging is also more sensitive than FEV$_1$ in detecting longitudinal changes in CF disease [132, 189], and has subsequently been used to assess the efficacy of CF treatments such as chest physiotherapy [183], inhaled bronchodilators [290], and gene-specific mucolytic drugs (e.g. Ivacaftor) [291]. More recently, ventilation MR imaging with hyperpolarised ^{129}Xe in CF has demonstrated similar sensitivity to changes in ventilation heterogeneity as ^{3}He [292, 293].

However, to date, little is known as to whether changes in acinar lung microstructure accompany this early CF lung disease process. Hyperpolarised gas diffusion-weighted MRI has been shown to be sensitive to changes in lung microstructure at the acinar level [91, 113]. The aim of this study was to investigate if the observed changes in ventilation heterogeneity are related to changes in lung microstructure in children with mild CF disease. ^{3}He DW-MRI metrics were compared in the same mild CF children and age-matched healthy controls cohorts of Marshall et al. [286], and microstructural metrics were also reassessed after a 2-year interval in the same group of CF children.

8.1.2 Methods

This cross-sectional and longitudinal observational study was approved by the Leeds East Research and Ethics committee. Parents/guardians signed informed consent and paediatric subjects provided assent. All subjects (6–16 years old) underwent lung function and MRI assessments during the same visit. 19 children with CF, that were clinically stable and with normal spirometry (FEV$_1$ z-score>-1.96), and 10 age-matched healthy controls were recruited for this study. 14 of the children with CF returned for a 2-year follow-up visit.

All ^{3}He ventilation and diffusion-weighted MRI scans were performed on a 1.5 T GE HDx scanner. The ^{3}He ventilation imaging parameters for this study can be found in the supplementary material of Marshall et al. [286]. A 2D SPGR multiple b-value diffusion-weighted sequence was used for ^{3}He DW-MRI with the following imaging parameters: five diffusion-weighted interleaves (b = 0, 1.6, 3.2, 4.8, 6.4 s/cm^2), 64×48 in-plane matrix, in-plane FOV = 35×26.25 cm^2, slices = 5, slice thickness = 15 mm, slice gap = 10 mm, TE/TR = 4.8/8 ms, diffusion time = 1.6 ms (maximum diffusion-weighted gradient strength = 28.3 mT/m, ramp = 0.3 ms, plateau = 1.0 ms), flip angle = 4.8° (sinc RF pulse), bandwidth = ±31.25 kHz. The ^{3}He dose (∼25% polarisation) was scaled according to subjects' height (Equation 8.1) (between 150 to 250 ml ^{3}He, and was mixed with N$_2$ in a 1:1 ratio), and the total gas volume was inhaled from functional residual capacity (FRC).

Apparent diffusion coefficient (ADC) and estimates of alveolar diffusive length scale (Lm_D), derived from the stretched exponential model (see Section 3.5.2), were calculated voxel-wise, and a global mean value was obtained for each subject. In the baseline study, quantitative lung microstructural metrics derived from DW-MRI, and previously-calculated VDP and

FEV_1 scores [286] were compared between healthy controls and children with mild CF. Phase III slope indices (S_{cond} and S_{acin}) [294] derived from multiple breath inert gas washout with SF_6 (performed in both the sitting and supine postures) were also compared between healthy controls and children with mild CF. For the longitudinal study, ADC, Lm_D, and previously calculated VDP, and FEV_1 [189] metrics for the children with mild CF were reassessed after 2-years, and compared to the metrics derived at baseline. An anterior to posterior (A-P) ADC gradient was also derived for each DW-MRI dataset from the mean ADC value of each image slice. This ADC gradient was compared between baseline and 2-year follow-up visits in the children with mild CF.

All statistical analysis was performed using GraphPad Prism (San Diego, USA). To test for significant differences between the quantitative metrics for healthy control and CF patient groups, a 2-tailed t-test was performed; for significant differences baseline and 2-year follow up quantitative metrics, a paired 2-tailed t-test was implemented. Significance level was set at $P<0.05$.

8.1.3   Results

Table 8.1: Summary of global mean ($\pm$ standard deviation) lung microstructural and functional metrics for healthy controls and children with CF in the baseline comparison, and also for CF patients at baseline and 2-year follow-up visits.

	Baseline Study		Longitudinal Study	
	Healthy Controls	Mild CF	Baseline	2-year Follow-up
No. of subjects	10	19	14	14
Age	11.3 ± 2.8	10.9 ± 2.5	10.3 ± 2.3	12.1 ± 2.3
ADC (cm^2/s)	0.158 ± 0.016	0.161 ± 0.014	0.158 ± 0.014	0.158 ± 0.017
Lm_D (µm)	204 ± 15	207 ± 10	205 ± 10	204 ± 12
FEV_1 z-score	0.00 ± 1.02	-0.30 ± 0.85	-0.12 ± 0.80	-0.26 ± 0.66
VDP (%)	1.53 ± 0.24	4.34 ± 2.00	4.86 ± 1.76	11.11 ± 5.37
S_{cond} sitting	0.01 ± 0.01	0.05 ± 0.02	0.05 ± 0.03	0.06 ± 0.03
S_{cond} supine	0.02 ± 0.01	0.05 ± 0.02	0.05 ± 0.02	0.07 ± 0.03
S_{acin} sitting	0.11 ± 0.04	0.13 ± 0.07	0.13 ± 0.08	0.13 ± 0.08
S_{acin} supine	0.08 ± 0.03	0.12 ± 0.08	0.12 ± 0.09	0.13 ± 0.10
ADC gradient (A-P) (cm/s)	–	–	-0.0004 ± 0.0012	-0.0008 ± 0.0013

A summary of all DW-MRI lung microstructure and lung function metrics for both the baseline comparison and longitudinal study can be found in Table 8.1. The global mean ADC value for both healthy control and children with mild CF was $\sim$0.160 cm^2/s; while the mean Lm_D value for the children in this study was $\sim$205 µm. No significant difference in mean ADC, Lm_D, and FEV$_1$ z-score was observed between healthy controls and children with CF (Figure 8.2). However, in comparison, VDP was significantly elevated ($P<0.001$) in the CF group. The presence of ventilation heterogeneity in the form of unventilated lung regions in children with mild CF are demonstrated in Figure 8.3; however, even though similar unventilated regions are observed in the corresponding ADC and Lm_D maps, this did not translate to changes in DW-MRI metrics of lung microstructure in ventilated lung regions. A summary of the phase III slope indices derived from multiple breath inert gas washout can be found in Table 8.1. Sitting and supine S$_{cond}$ parameters were significantly different ($P<0.001$) between healthy controls and CF patients. In contrast, sitting and supine S$_{acin}$ parameters were not significantly different between the healthy controls and CF patients.
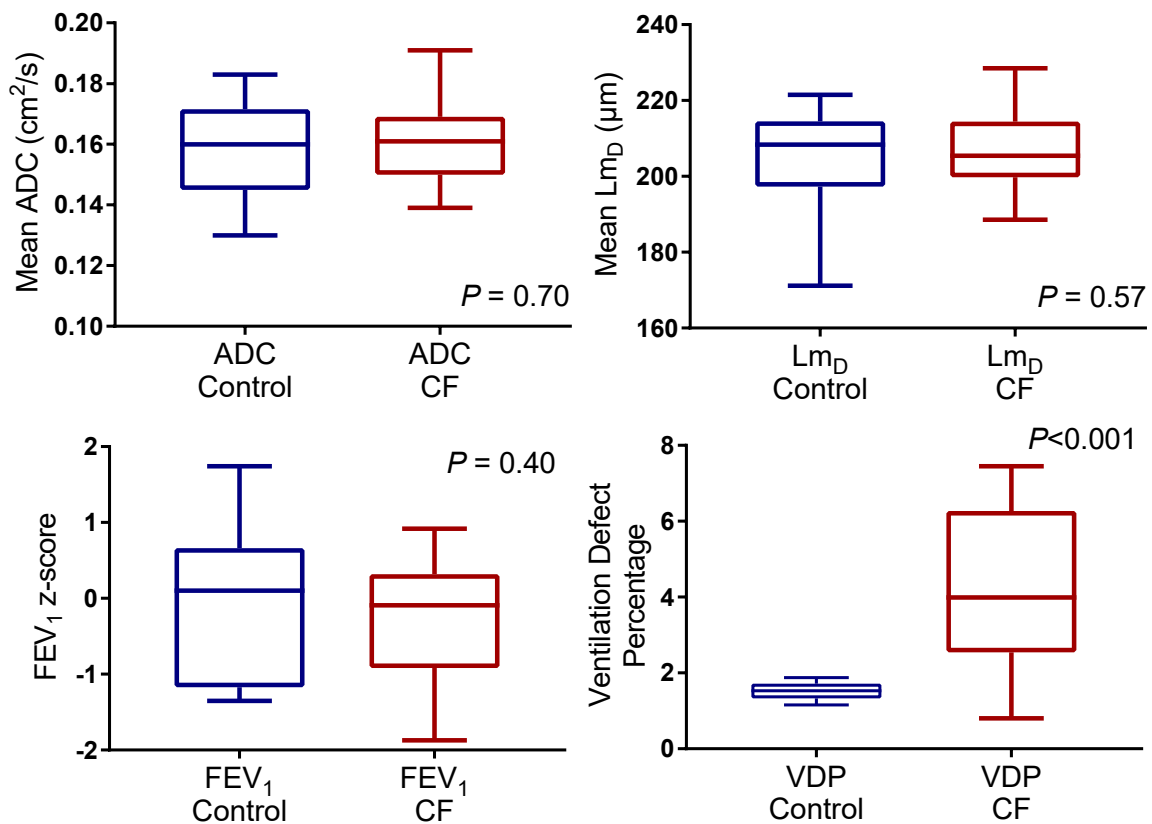
Figure 8.2: Box and whisker plots comparing lung microstructure (ADC and Lm_D) and lung function (FEV$_1$ and VDP) metrics between children with mild CF and age-matched healthy controls.
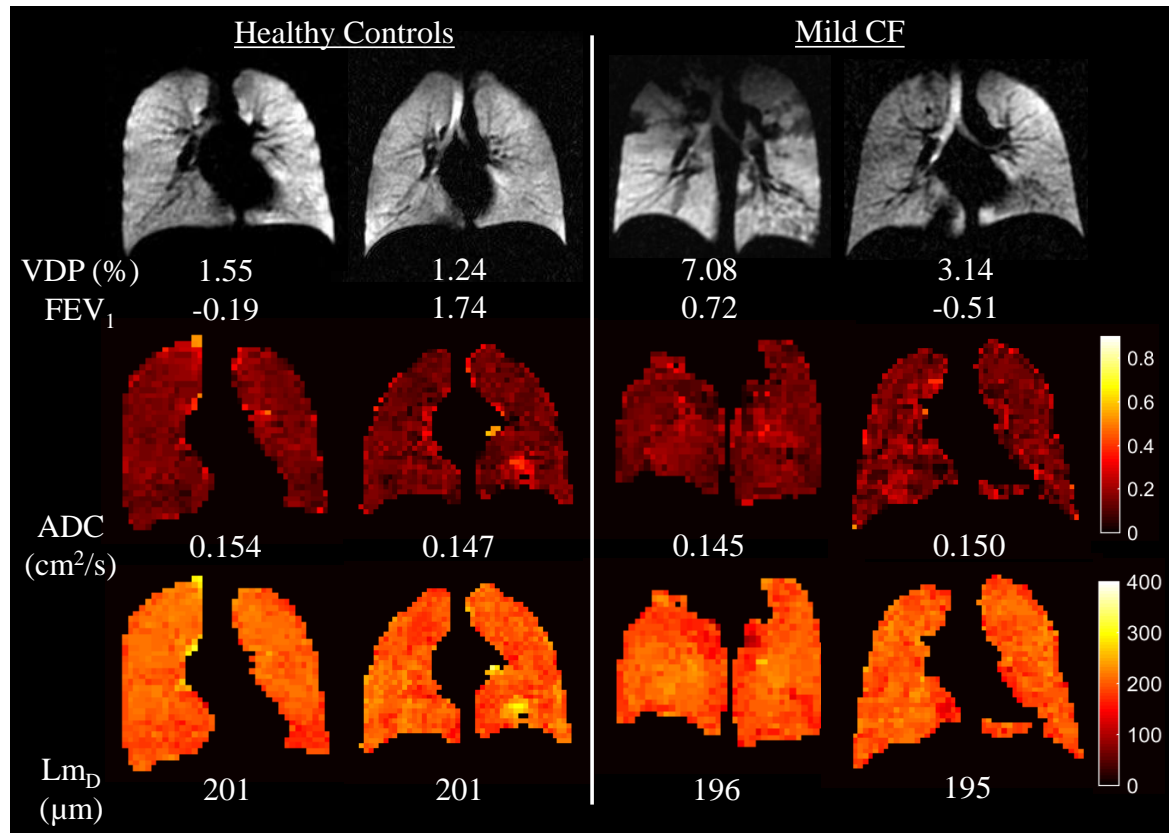
Figure 8.3: Comparative ^{3}He ventilation images, and ADC and Lm_D maps for two representative healthy control and mild CF children. Unventilated lung regions can be observed in the mild CF ventilation images, but this ventilation heterogeneity did not correspond to elevated ADC and Lm_D values.

In the longitudinal study, after 2 years, the children with mild CF did not show a significant change in ADC, Lm_D, and FEV_1 z-score; while a statistically significant increase in VDP was observed (P=0.002) (Figure 8.4). In Figure 8.7, representative static ventilation images and maps of ADC and Lm_D at baseline and after 2-years are presented for the same patients. The presence of new unventilated regions indicated increased ventilation heterogeneity and progression of CF lung disease. However, this disease progression was not associated with changes in lung microstructure. An increase in anterior to posterior (A-P) ADC gradient was observed after 2-years (see example in Figure 8.5), albeit not statistically significant (P=0.29) (Figure 8.6).

8.1.4 Discussion

The mean ADC value for both healthy age-matched subjects and children with mild CF ($\sim$0.160 cm^2/s) matches the value reported for healthy subjects (0.158 cm^2/s) of this age range ($\sim$11 years) at 1.5 T and with b = 1.6 s/cm^2 [101]. There are currently no reported Lm_D values for paediatric subjects; however, the Lm_D parameter is similar to the mean
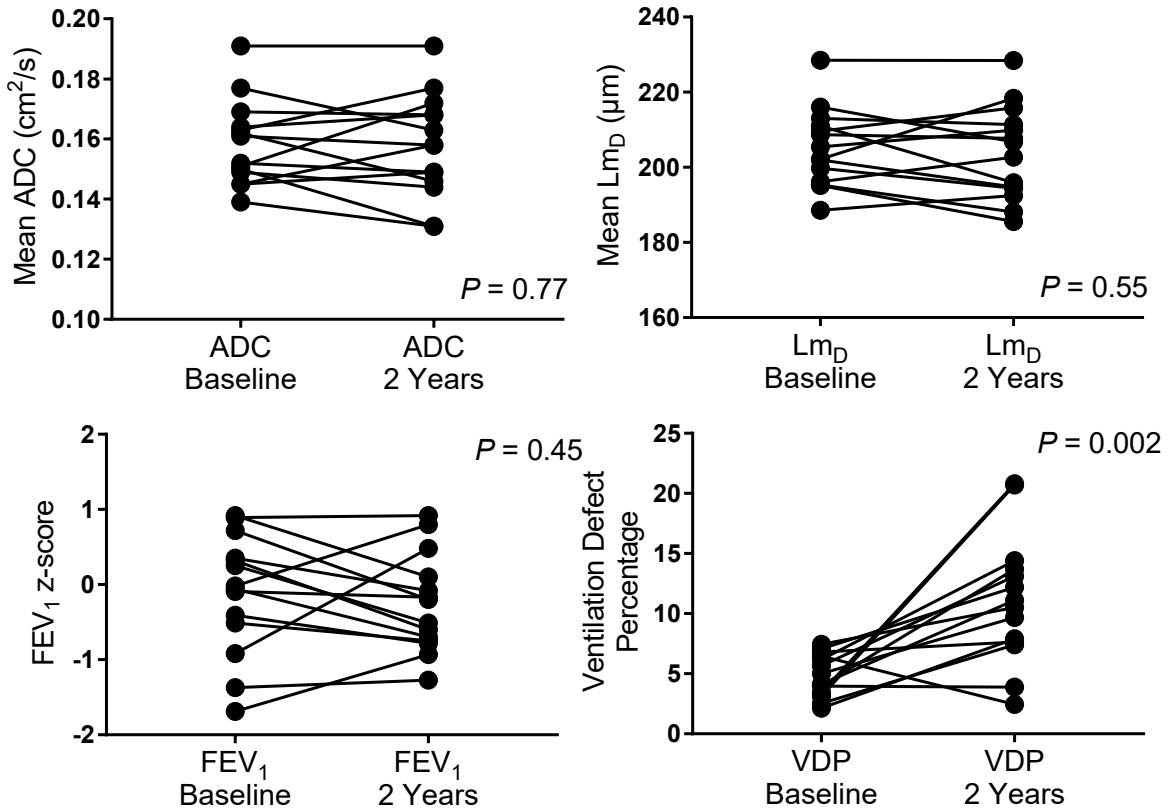
Figure 8.4: Box and whisker plots comparing lung microstructure (ADC and Lm_D) and lung function (FEV$_1$ and VDP) metrics between mild CF children at baseline and 2-year follow-up visits.
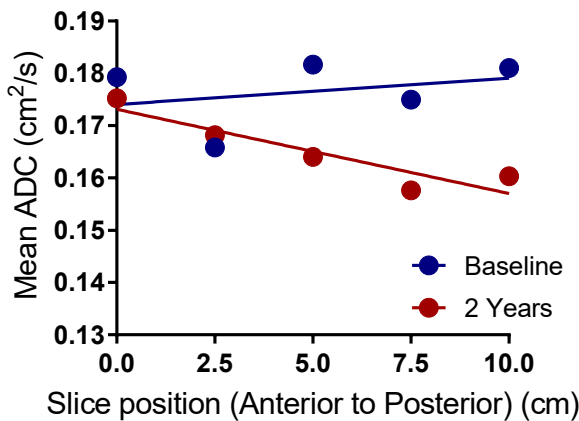
Figure 8.5: Mean slice ADC values from anterior to posterior for a representative CF patient at baseline and after 2-years. An increase in the gravitational ADC gradient (baseline = 0.0005 cm/s; 2-years = -0.0016 cm/s) is observed.

linear intercept length obtained from histological lung samples. The mean Lm_D value ($\sim$205 µm) was comparable to the average intercept distance obtained from explanted paediatric lungs, with no history of respiratory disease, of a similar age ($\sim$215 µm) [295].

A significant increase in VDP, and subsequently in ventilation heterogeneity, was observed for mild CF children when compared to the healthy controls, and after 2-years in the mild CF children. However, no significant difference in ADC and Lm_D was observed; indicating that no lung microstructural changes at the acinar level accompany the increase in ventilation
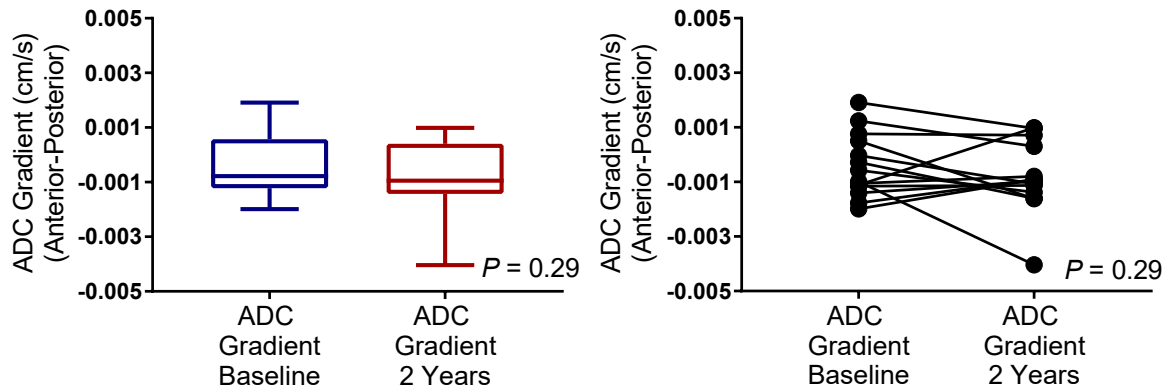
Figure 8.6: Comparison of ADC gradient in the anterior to posterior (A-P) gravitational direction at baseline and after 2-years. The absolute value of the ADC gradient increased in 9 of the 14 CF subjects. However, this was not statistically significant (P=0.29).
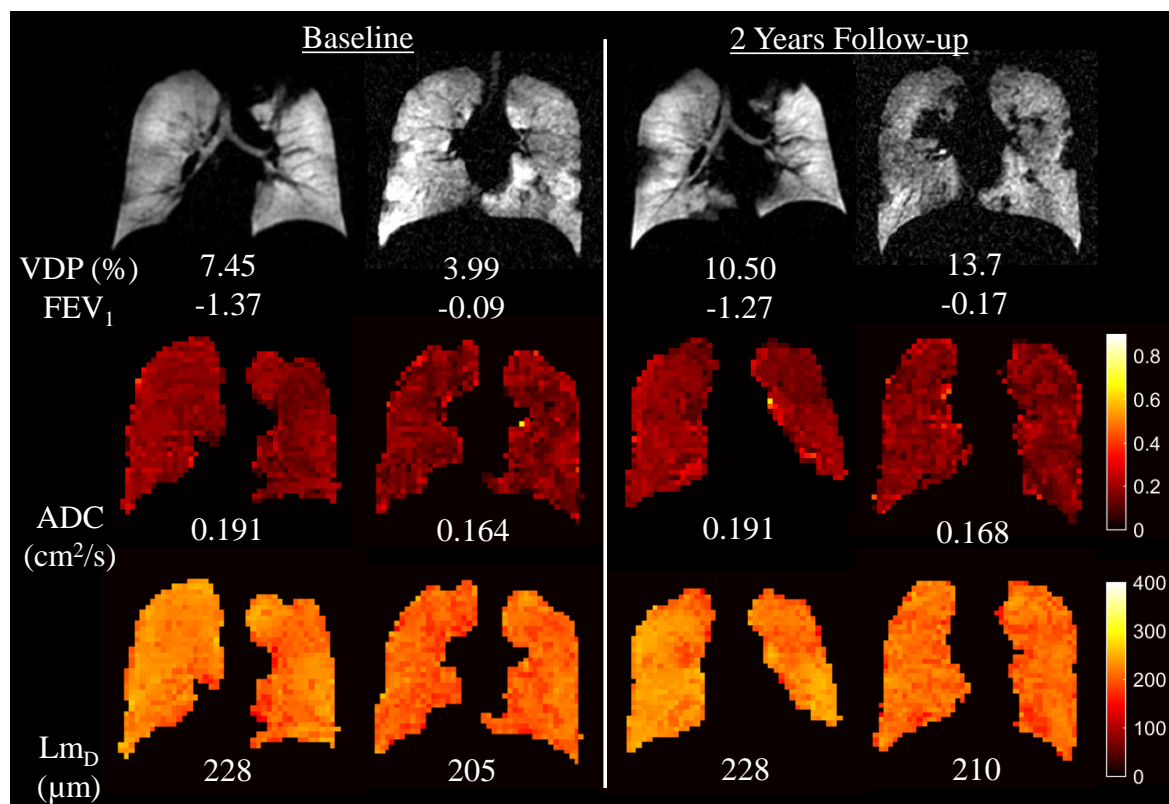
Figure 8.7: Comparative ^{3}He ventilation images, and ADC and Lm_D maps for two mild CF children at baseline and after 2-years. Increased ventilation heterogeneity after 2-years did not result in elevated ADC and Lm_D values.

heterogeneity in early CF lung disease. This trend is expected as CF pathophysiology predominantly starts to affect the small conducting airways rather than acinar regions associated with early lung disease in emphysema. The ^{3}He DW-MRI acquisition in this work was tuned to be sensitive to changes on the acinar length scale by using a ^{3}He diffusion time (Δ) of 1.6 ms, which corresponds to a characteristic 1D free diffusion length ($\sim$530

µm) that allows ^{3}He atoms to diffuse out of the alveoli and into the alveolar duct but not beyond the length of the alveolar duct ($\sim$730 µm [11]). Therefore, the small conducting airways where obstruction occurs through mucous plugging are not probed for the diffusion times used in this ^{3}He DW-MRI sequence.

However, one important limitation of hyperpolarised gas DW-MRI is the absence of lung microstructure metrics in areas of non-ventilated lung, because these regions represent areas of the lung not probed by the ^{3}He gas atoms. There is a possibility that the acinar microstructure in these obstructed regions may undergo change through the CF disease progress, and cannot be measured with hyperpolarised gas DW-MRI. However, in a recent morphometric analysis of explanted lungs from CF patients with micro-CT, no significant difference in mean linear intercept length was determined between lung sample cores of healthy controls and CF patients ($FEV_1 = 24\%$ predicted); while a significant decrease in terminal bronchiole diameter and cross-sectional area was observed in CF [69]. These results from advanced CF patients with micro-CT are in agreement with those obtained in mild CF patients with ^{3}He DW-MRI metrics of lung microstructure, and demonstrates that in mild and advanced CF, changes occur in the conducting airways but not in the alveoli.

Comparison with S_{cond} and S_{acin}

Phase III slopes calculated from multiple breath inert gas washout are used to derive indices (S_{cond} and S_{acin}) that are related to the different contributions of conducting and acinar airways to the observed gas mixing process [296]. S_{cond} represents the convective gas mixing in the conducting airways; while S_{acin} is the interaction between diffusion and convection gas mixing in the acinar zone. These two indices have been shown to be elevated, when compared to healthy normals, in diseases such as COPD [297] and CF [298]. A statistically significant difference in the S_{cond} observed between healthy controls and mild CF patients reflects the increase in ventilation heterogeneity associated with mild CF lung disease. In a previous comparison of children with CF and healthy children, S_{acin} was significantly elevated in CF [298]; a similar increase in mean S_{acin} was observed in this comparison, albeit not statistically significant. The slight differences in the paediatric populations between the two studies could explain this small discrepancy in the S_{acin} parameter.

^{3}He DW-MRI metrics of ADC and Lm_D were not significantly correlated with either sitting or supine S_{acin}, a measure of acinar ventilation heterogeneity. The simplest explanation is that the paediatric patients in this study have very mild/early CF lung disease, it could be possible that in older CF patients that have more advanced CF lung disease a correlation between DW-MRI metrics and S_{acin} could be observed. In Horsley et al. [298] it was demonstrated that S_{acin} correlates strongly with the lung clearance index (LCI) in adult CF patients. However,

it is likely that even in more advanced CF patients, no correlation would be observed due to the inherent differences between the two parameters.

Hyperpolarised gas DW-MRI metrics are a measure of acinar microstructure; in contrast, S_{acin} is a measurement of ventilation heterogeneity in regions of the lung peripheral to diffusion-convection front which is located in the pulmonary acinus [296]. The S_{acin} incorporates the acinar airways; while for the short diffusion times used for ^{3}He DW-MRI, gas atom diffusion restriction occurs predominantly within the alveoli. A previous study of asthmatic subjects with long scale ^{3}He DW-MRI illustrates this difference where a stronger correlation between ADC and S_{acin} was obtained with ^{3}He diffusion times of 1 s when compared to 13 ms [299]. At these comparatively longer diffusion times, ^{3}He gas atoms can diffuse out of the acinar airways, and therefore appear to be more strongly correlated to S_{acin} than at shorter diffusion times.

Longitudinal changes in gravitational ADC gradient

A trend towards increased anterior to posterior (A-P) ADC gradient was observed after 2-years in the children with mild CF. It is unclear what the increase in mean A-P ADC gradient corresponds to; it is possible that this trend is associated with an increase in disease severity between visits. However, one possible explanation for the change in gravitational gradient is a difference in the imaging lung inflation state between the two visits. Changes in lung inflation states have been demonstrated to affect the gravitational gradient of ^{3}He ADC values (see Section 8.3), and this gradient is observed to disappear at TLC [105].

In this study, to account for differences in lung volume across the age range of the paediatric CF cohort, ^{3}He doses were scaled according to the subject's predicted FRC volume. An empirical equation was derived, from the relationship between FRC volume and height in a subset of the CF cohort, to estimate FRC volume from the height of a CF patient. The ^{3}He dose regimen was subsequently calculated from the estimated FRC volume as follows:

$$^3\text{He dose (L)} = \frac{104.5 \times \text{FRC} + 51.3}{1000} \tag{8.1}$$

The final inhaled bag volume consisted of equal parts ^{3}He and N_2 gas. However, as demonstrated in Figure 8.8, the rate that FRC increases with lung growth after 2-years was around half of the rate of TLC increase. Therefore, DW-MRI at baseline was likely acquired at an inflation state that was closer to TLC than the imaging performed after 2-years, resulting in the observed increase in A-P ADC gradient (see Figure 8.6).

To our knowledge, the only other previous study of CF with ^{3}He DW-MRI was a study of adult CF subjects scanned at baseline and after 1 week [300]. This study found a statistically significant decrease in both whole lung ADC, and a decrease in anterior to posterior difference in ADC (ΔAP) at re-scan after 1 week. The ΔAP metric is different to the A-P ADC gradient
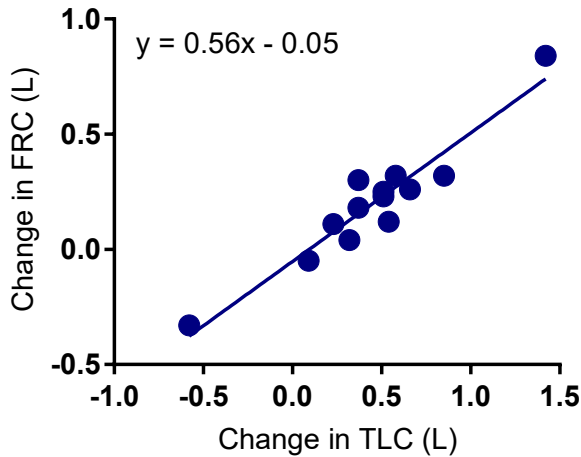
Figure 8.8: Plot of the changes in TLC and FRC, measured by body plethysmography, of the mild CF subjects between baseline and 2-year follow-up visits. The changes in FRC and TLC were linearly correlated (P<0.001, R^2=0.91), and TLC changes at a faster rate than FRC.

as it only represents the difference in ADC value between the most peripheral anterior and posterior slices. It was hypothesised that these short-term changes to ADC are indicative of the movement of mucus plugs and gas trapping regions. The large time-scale differences between the adult CF and children with mild CF studies may explain the difference in ADC results between the respective studies. In Kirby et al. [300], the 1 week follow-up scan represents short-term changes to the lung in adult CF patients; while in contrast, 2 year follow-up scans are more likely to reflect longitudinal changes related to long term CF disease progression or lung volume changes with growth. However, the differences observed between baseline and 1 week re-scan mean ADC value was very small (0.01 cm^2/s) and could also be explained by inter-scan variability of ADC values or differences in lung inflation volumes between scans. The morphometric results by Boon et al. [69] appear to support this hypothesis by demonstrating no difference in mean linear intercept length between healthy controls and end-stage CF patients.

8.1.5 Conclusion

This is the first study to compare hyperpolarised gas ^{3}He DW-MRI metrics in children with mild CF and age-matched healthy controls. No significant difference in ADC and Lm_D metrics was observed between the two groups, despite an increase in ventilation defect percentage in mild CF. After 2 years, where a statistically significant increase in ventilation heterogeneity through ventilation defect percentage was detected, no difference in DW-MRI metrics was still observed in the mild CF patients. These results indicate that in early CF lung disease, acinar microstructural changes do not accompany increased ventilation heterogeneity.

8.2   Assessment of acinar airway microstructure in idiopathic pulmonary fibrosis with hyperpolarised ^{3}He and ^{129}Xe diffusion-weighted MRI

8.2.1   Introduction

Idiopathic pulmonary fibrosis (IPF) is a rapidly progressive and usually fatal disease of older age, characterised by lung fibrosis extending from basal and peripheral lung tissue [301]. Heterogeneous changes to the lung due to fibrosis are observed on both the macro- and micro-scale, as seen in Figure 8.9. On the macro-scale of CT imaging, fibrotic regions are characterised by high CT density attenuation; while in micro-CT images of these fibrotic regions, microscopic changes to the alveolar microstructure (resulting in cyst formation and honeycombing) are observed in addition to interstitial thickening. In spite of recently available therapies which slow the rate of disease progression [302, 303], the current measures of IPF disease severity are insensitive and non-specific, prompting searches for novel clinical markers of disease in order to assist with phenotyping, prognostication and the development of new therapies [45, 304].
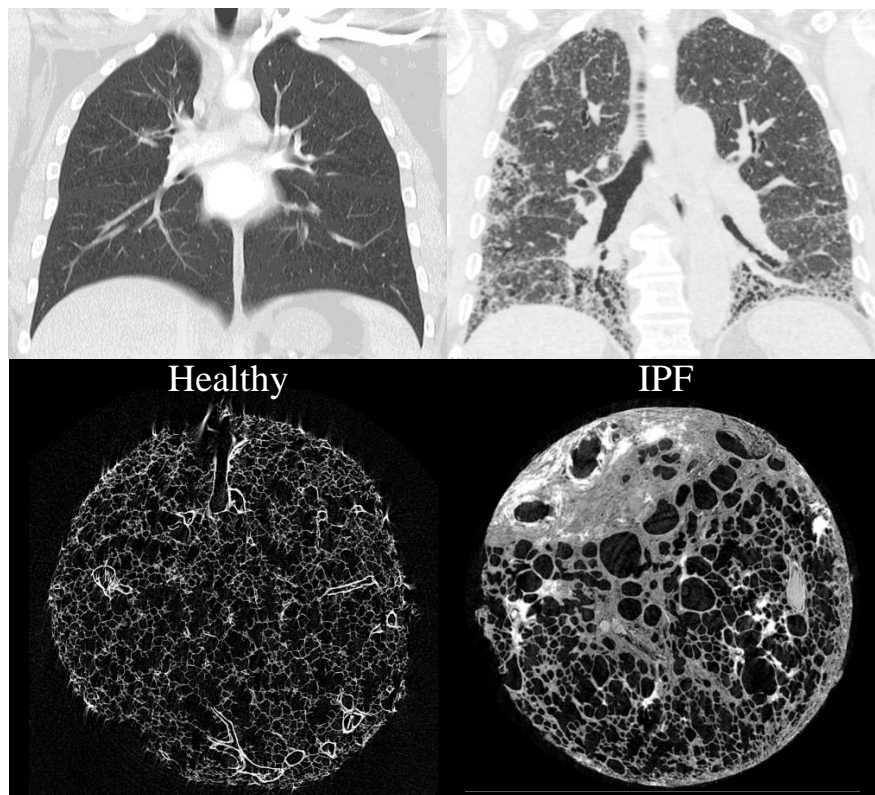
Figure 8.9: Representative CT (top) and micro-CT (bottom) images of a healthy subject and IPF patient. Lung fibrosis can be observed in the basal and peripheral lung regions of the IPF CT image. In the micro-CT image, the fibrosis results in microscopic changes to alveolar microstructure. Healthy CT image reproduced courtesy of Dr. Andrew Dixon, Radiopaedia.org.

MRI with inhaled hyperpolarised noble gases (^{3}He or ^{129}Xe) has enabled in vivo functional and structural imaging of the lungs. In addition, ^{129}Xe is soluble in the lung tissue and red blood cells, allowing for the opportunity to quantitatively assess pulmonary gas exchange through the distinct spectroscopic chemical shift of ^{129}Xe associated with each dissolved phase environment [157]. This physical property of xenon is of particular interest in diseases such as IPF that are characterised by gas exchange impairment. One spectroscopic technique is ^{129}Xe chemical shift saturation recovery (CSSR) which can be used to estimate interstitial septal thickness (ST), and has been demonstrated to be elevated in patients with interstitial lung disease including IPF [305, 306]. An alternative technique is high resolution spectroscopy of the dissolved ^{129}Xe spectra to derive a ratio (RBC/TP) of dissolved xenon in the red blood cell (RBC) and in the tissue plasma/barrier (TP). This RBC/TP ratio has been shown to be diminished in IPF patients, resulting from gas exchange impairment [307]. Recently, the development of a 3D radial, 1-point Dixon sequence has enabled the image acquisition of both dissolved phases of ^{129}Xe in the lungs, which allows for regional analysis of RBC/TP ratio in IPF [308, 309].

Diffusion-weighted MRI (DW-MRI) with hyperpolarised gases provides non-invasive and quantitative assessment of microstructural acinar changes that are comparable to lung histology (see Section 2.2.5). Interest in this field has mainly been focused on demonstrating acinar airway enlargement in emphysema, and to our knowledge, no in vivo studies of IPF patients with DW-MRI exist. Previous DW-MRI studies of patients with IPF have been restricted to the imaging of explanted lungs [108, 115], where in some cases IPF lungs were used as control specimens in comparisons against COPD lungs. However, in these studies, ADC results in IPF patient lungs, with both ^{3}He and ^{129}Xe, appear to demonstrate an increase in ADC when compared to healthy normals. This contrasts with findings from studies with ^{3}He ADC from rats instilled with bleomycin [310], a commonly utilised animal model for IPF.

The aim of this work was therefore to investigate whether lungs of patients affected by IPF demonstrate increased DW-MRI metrics of ADC and Lm_D, representative of acinar airway enlargement and damage, using in vivo measurements of hyperpolarised ^{3}He and ^{129}Xe DW-MRI. In addition, the reproducibility of these microstructural imaging indices is assessed with a future view to their prognostic sensitivity and their correlation with existing clinical measures of IPF disease severity.

8.2.2 Methods

In a prospective study with ethics approval from Liverpool Central NHS Research Ethics Committee, 20 participants with IPF underwent DW-MRI with hyperpolarised ^{3}He gas. 10 participants underwent a second identical scan on the same day for baseline reproducibility assessment; while 14 of the 20 participants returned after six months for a follow-up ^{3}He DW-MRI scan. ^{3}He gas was polarised under regulatory licence, and 250 ml of ^{3}He was

mixed with nitrogen (N$_2$) to make up a total inhaled dose of 1L. Participants were coached to achieve functional residual capacity (FRC) and practised inhaling 1L of room air prior to imaging. Images were acquired during a 15 second breath-hold manoeuvre following inhalation of the gas mix from FRC.

All imaging was performed on a 1.5 T clinical MRI scanner (GE HDx), using a quadrature vest design chest radiofrequency coil (Clinical MR Solutions, Brookfield, Wisconsin) tuned to the ^{3}He Larmor frequency (48.63 MHz). A 3D multiple b-value spoiled gradient echo sequence with compressed sensing was used to acquire 3D ^{3}He DW-MRI as previously described in Section 5.3. Relevant diffusion-weighted imaging parameters include: voxel size = 4.17×4.17×12 mm^3, b = [0, 1.6, 4.2, 7.2] s/cm^2, diffusion time = 1.6 ms, DW gradient strength = 30 mT/m, ramp = 0.3 ms, and plateau = 1.0 ms. Pulmonary function tests (PFTs) were performed on the same day, including spirometry to measure forced vital capacity (FVC) and single-breath carbon monoxide gas transfer/coefficient (T$_{LCO}$ and K$_{CO}$). Percent predicted values were calculated in accordance with usual clinical practice. High-resolution computed tomography (HRCT) of the thorax was performed as close as practically possible to the baseline MR imaging session (mean 55.7 ± 61.7 days).

Undersampled images were reconstructed using in-house MATLAB code with the optimal parameters determined from previous CS simulations (see Section 5.2). ^{3}He DW-MRI metrics of lung microstructure were calculated for each imaging voxel; ^{3}He ADC from a mono-exponential fit of the first two diffusion-weighted interleaves (b = 0, 1.6 s/cm^2), and ^{3}He Lm_D from a stretched exponential function fit (see Section 3.5.2) of all four diffusion-weighted interleaves. ADC and Lm_D histograms encompassing all image voxels within the lung cavity were analysed for mean, skewness, and kurtosis in each subject.

Each baseline ^{3}He DW-MRI dataset was analysed by two different observers using the same MATLAB code (HFC and NW) to assess inter-observer reproducibility using two-way mixed effects model intraclass correlations coefficient. Same day reproducibility was assessed using one-way random effects model intraclass correlations coefficient. Non-parametric analysis (Spearman's rho) determined strength of correlation between PFTs and imaging metrics. Two tailed p-values<0.05 determined statistical significance. The DW-MRI metrics for the 6-month follow-up datasets were compared to baseline metrics with Wilcoxon matched-pairs signed rank test to determine any statistical difference between the DW-MRI metrics in a given subject.

Table 8.2: Summary of ^{3}He diffusion-weighting metrics from baseline, same-day baseline repeat, and 6 month follow-up scans for each participant in the prospective IPF cohort. Values are given as mean ($\pm$ standard deviation).

Subject	Age (Sex)	Baseline		Baseline (Same-day Repeat)		6 Months Follow-up	
		ADC (cm²/s)	Lm_D (µm)	ADC (cm²/s)	Lm_D (µm)	ADC (cm²/s)	Lm_D (µm)
IPF01	77 (F)	0.306 ± 0.119	263 ± 31	0.318 ± 0.100	275 ± 28	0.326 ± 0.097	283 ± 27
IPF02	74 (M)	0.363 ± 0.162	279 ± 43	0.371 ± 0.173	274 ± 42	–	–
IPF03	71 (M)	0.243 ± 0.084	246 ± 27	0.259 ± 0.092	250 ± 27	0.241 ± 0.090	244 ± 27
IPF04	77 (M)	0.275 ± 0.120	250 ± 33	0.283 ± 0.119	252 ± 34	0.288 ± 0.097	264 ± 28
IPF05	70 (M)	0.306 ± 0.119	266 ± 32	0.308 ± 0.124	267 ± 32	0.300 ± 0.112	268 ± 31
IPF06	71 (M)	0.358 ± 0.131	278 ± 33	0.327 ± 0.119	270 ± 30	0.356 ± 0.119	286 ± 30
IPF07	68 (M)	0.334 ± 0.125	275 ± 36	0.318 ± 0.121	269 ± 36	0.316 ± 0.107	273 ± 33
IPF08	70 (M)	0.293 ± 0.116	265 ± 27	0.292 ± 0.118	264 ± 27	0.297 ± 0.105	272 ± 28
IPF09	67 (F)	0.257 ± 0.102	249 ± 28	–	–	0.270 ± 0.095	258 ± 26
IPF10	75 (M)	0.482 ± 0.193	316 ± 52	–	–	–	–
IPF11	72 (F)	0.248 ± 0.084	250 ± 26	0.245 ± 0.075	250 ± 25	0.234 ± 0.067	249 ± 24
IPF12	61 (M)	0.317 ± 0.148	256 ± 33	0.365 ± 0.156	280 ± 38	0.372 ± 0.153	295 ± 42
IPF13	61 (M)	0.439 ± 0.183	299 ± 47	0.419 ± 0.186	292 ± 48	0.423 ± 0.175	301 ± 47
IPF14	73 (M)	0.412 ± 0.153	301 ± 36	–	–	0.396 ± 0.142	303 ± 35
IPF15	80 (M)	0.431 ± 0.193	300 ± 51	–	–	–	–
IPF16	73 (M)	0.293 ± 0.092	270 ± 27	–	–	–	–
IPF17	63 (M)	0.349 ± 0.114	287 ± 32	–	–	0.359 ± 0.097	295 ± 29
IPF18	72 (M)	0.222 ± 0.065	243 ± 22	–	–	0.224 ± 0.062	245 ± 22
IPF19	71 (M)	0.382 ± 0.141	300 ± 40	–	–	–	–
IPF20	76 (M)	0.336 ± 0.119	284 ± 35	–	–	–	–

8.2.3   Results

Baseline DW-MRI Results and Reproducibility

Mean ADC and Lm_D values for each IPF patient scanned at baseline and after 6 months are summarised in Table 8.2. The mean age for this IPF cohort was 71.1 years old, and the mean ^{3}He ADC and Lm_D at baseline, was 0.332 cm^2/s and 274 µm, respectively. Regions of relatively high ADC and Lm_D values appear qualitatively related to fibrotic changes on accompanying HRCT imaging slices (Figure 8.10). A representative ADC map from a coronal slice is shown alongside ADC histograms for two patients with varying disease severity in Figure 8.11.
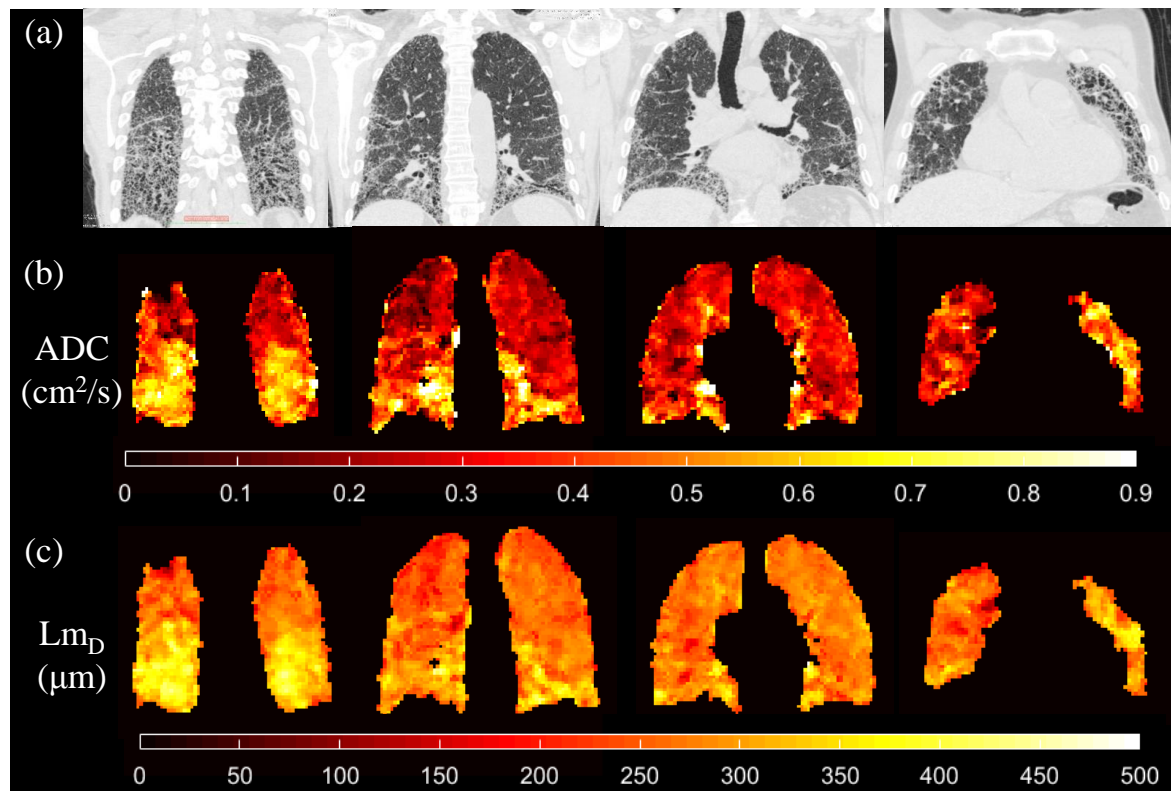
Figure 8.10: Representative IPF patient. (a) Coronal HRCT slices demonstrating fibrotic regions of the lung. Corresponding ^{3}He ADC (b) and Lm_D (c) maps where areas of elevated values are qualitatively related to the fibrotic regions observed with CT.

^{3}He DW-MRI histogram metrics were compared to FVC, T_{LCO}, and K_{CO} metrics from pulmonary function tests (Table 8.3). Both % predicted K_{CO} and T_{LCO} were significantly correlated ($P<0.05$) with mean ADC (r = -0.479 and r = -0.473, respectively) and Lm_D (r = -0.467 and r = -0.463, respectively) (Figure 8.12). ADC histogram kurtosis and Lm_D skewness were also significantly correlated with % predicted K_{CO}. FVC (% predicted) was however not significantly correlated with any of the ^{3}He DW-MRI metrics (except for Lm_D histogram skewness).
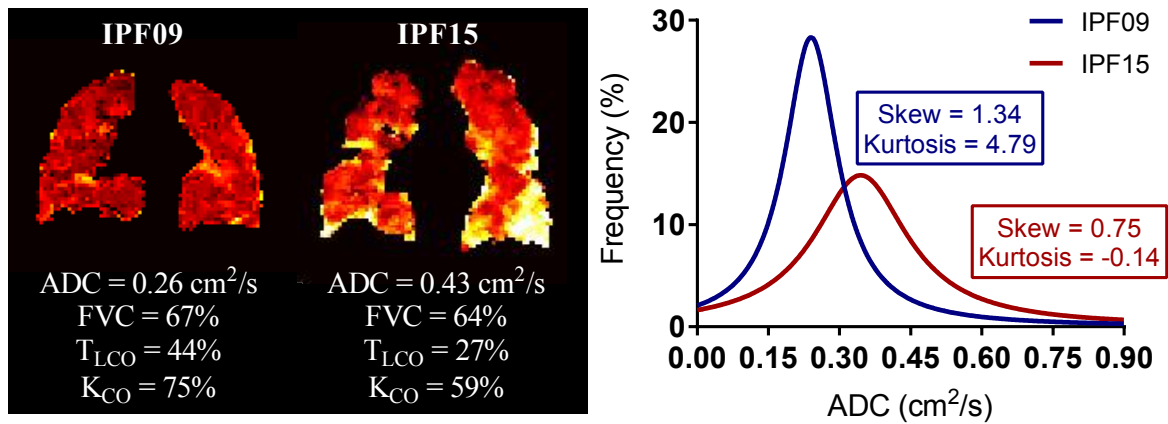
Figure 8.11: Two representative IPF patients (IPF09 and IPF15) with different disease severity. The ADC map of IPF15 demonstrates more elevated ADC regions than IPF09. This corresponds to increased mean ADC, and a decrease in ADC histogram metrics of skewness and kurtosis.

Table 8.3: Summary of correlations between ^{3}He DW-MRI histogram metrics and pulmonary function test metrics of FVC and carbon monoxide gas transfer in IPF patients.

	FVC (% Pred)	K_{CO} (% Pred)	T_{LCO} (% Pred)
Mean ADC	-0.165	-0.479 *	-0.473 *
ADC Skewness	-0.417	0.403	0.066
ADC Kurtosis	0.074	0.471 *	0.415
Mean Lm_D	-0.150	-0.467 *	-0.463 *
Lm_D Skewness	-0.522 *	-0.638 **	-0.355
Lm_D Kurtosis	-0.414	-0.316	-0.126

* correlations at a significance level of $P<0.05$

** correlations at a significance level of $P<0.01$

Intraclass correlation coefficients (ICC) for both ADC and Lm_D histogram metrics can be found in Table 8.4. Same day intra-subject DW-MRI scan metrics were highly reproducible, including mean ADC (ICC = 0.924), mean Lm_D (0.804), histogram skewness (ADC = 0.776, Lm_D = 0.965) and kurtosis (ADC = 0.825, Lm_D = 0.876). Bland-Altman analysis of mean ADC and Lm_D values between the two baseline DW-MRI scans resulted in negligible bias of -0.9% and +0.6%, respectively (Figure 8.13). Strong inter-observer agreement was also obtained for all DW-MRI metrics; ICC for all DW-MRI metrics were all larger than the intra-subject equivalent (except for Lm_D skewness). Bland-Altman comparison of mean ADC and Lm_D values between the two observers resulted in a similar small bias, -1.1% and +0.9%, respectively, as the intra-subject comparison (Figure 8.14).
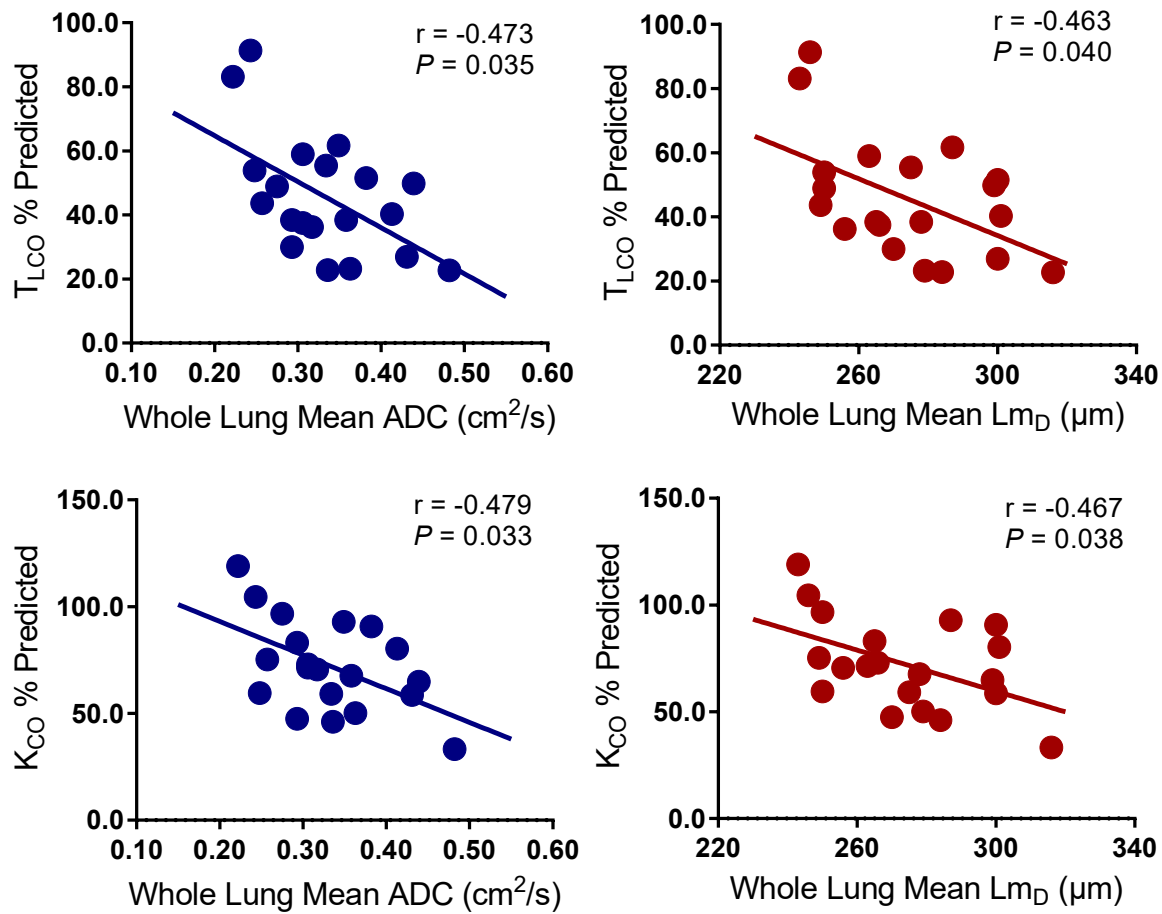
Figure 8.12: Scatter plots of mean ADC and Lm_D with % predicted T_{LCO} and K_{CO} demonstrating significant linear correlation between the metrics.
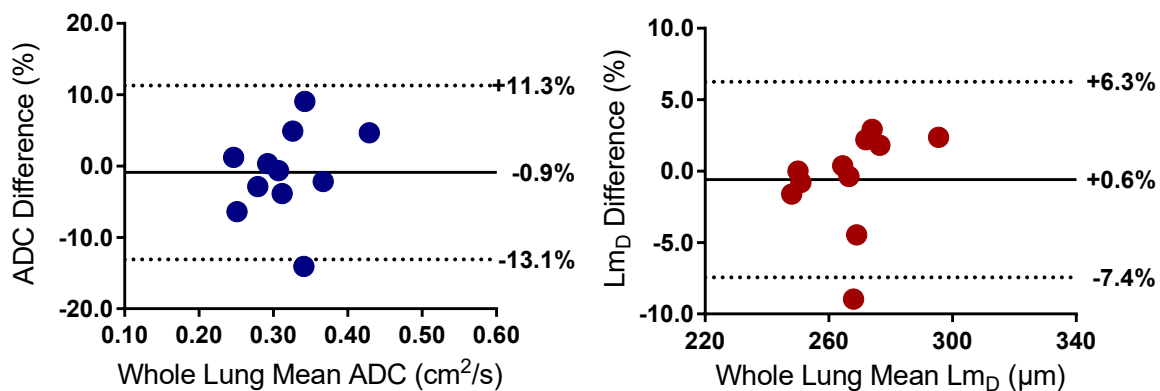
Figure 8.13: Bland-Altman comparison of whole lung mean ADC and Lm_D values for 11 baseline and same-day repeat DW-MRI scans. A small mean ADC and Lm_D bias is obtained indicating intra-subject DW-MRI metrics are highly reproducible.
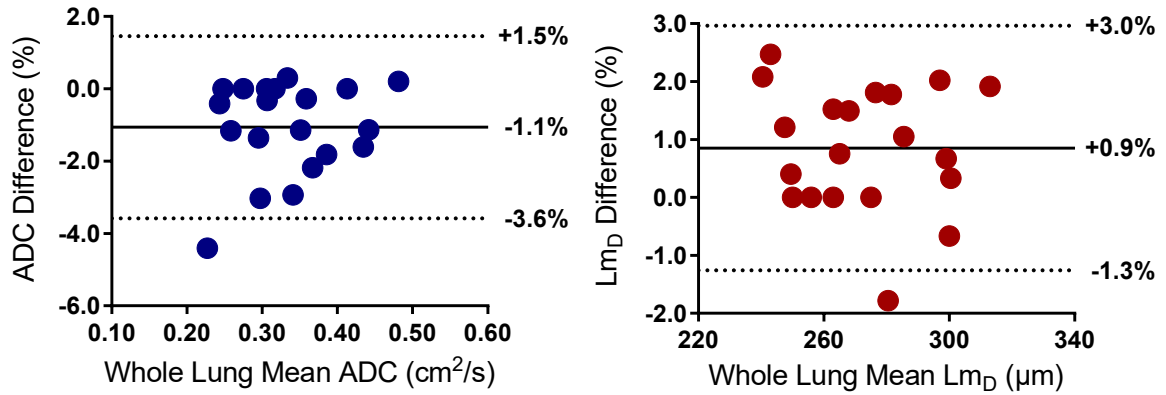
Figure 8.14: Bland-Altman comparison of whole lung mean ADC and Lm_D values between two independent observers. A small mean ADC and Lm_D bias is obtained indicating a good agreement of DW-MRI metrics measured by different observers.

Table 8.4: Mean ^{3}He DW-MRI histogram metrics and intraclass correlation coefficients (ICC) for the intra-subject and inter-observer reproducibility comparisons. Intra-subject reproducibility was assessed between the two same-day baseline scans; while inter-observer reproducibility was determined between two observers using the first baseline scan.

	Intra-subject Reproducibility (n = 11)			Inter-observer Reproducibility (n = 20)		
	Baseline Scan 1	Baseline Scan 2	ICC	Observer 1	Observer 2	ICC
Mean ADC (cm^2/s)	0.317	0.319	0.924	0.332	0.336	0.997
ADC Skewness	1.042	0.946	0.776	0.992	1.007	0.858
ADC Kurtosis	2.978	2.482	0.825	2.736	2.446	0.976
Mean Lm_D (µm)	266.0	267.6	0.804	273.8	271.6	0.992
Lm_D Skewness	-0.012	0.049	0.965	0.081	0.047	0.948
Lm_D Kurtosis	0.918	1.047	0.876	0.974	1.020	0.895

Longitudinal DW-MRI Results

After 6 months, 14 participants from the IPF cohort returned for a follow-up DW-MRI scan. The majority of ADC and Lm_D histogram metrics were not significantly different between baseline and after 6 months (Wilcoxon rank test $P>0.05$), apart from a significant increase in mean Lm_D ($P=0.003$) and Lm_D kurtosis ($P=0.035$) (Figure 8.15). A significant decrease in FVC ($P=0.005$) was also observed, but there was no significant difference in either T_{LCO} and

K_{CO}. Figure 8.16 demonstrates the increase in lung microstructural metrics in a representative IPF patient. An increase in regions with elevated ADC and Lm_D can be observed after 6 months in the basal and peripheral regions of the coronal DW-MRI maps.
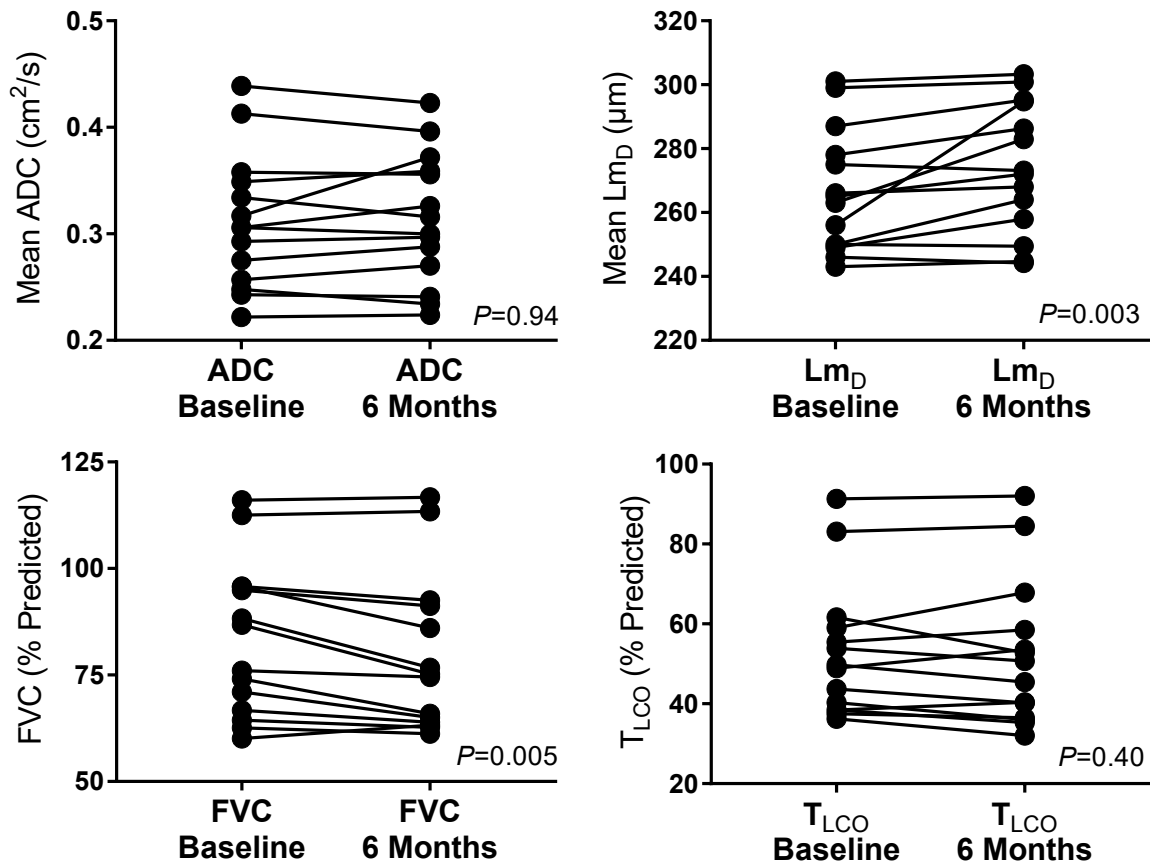
Figure 8.15: Plots of ADC, Lm_D, FVC, and T_{LCO} at baseline and after 6 months for the IPF cohort. A statistically significant difference was observed for mean Lm_D and FVC.

8.2.4   Discussion

Baseline DW-MRI results and reproducibility

Hyperpolarised ^{3}He ADC and Lm_D is elevated in the lungs of patients with IPF when measured with DW-MRI, reflecting increased Brownian gas diffusion in the acinar length scale airways. The mean ADC for the IPF cohort (0.33 cm^2/s, age = 71) is higher than what has been demonstrated in healthy subject cohorts, even accounting for the apparent increase in ADC with advancing age (0.26 cm^2/s, age = 71 at 1.5 T [102], and 0.22 cm^2/s, age = 67 at 3 T [116]). The elevated ADC in IPF matches the results obtained in explanted lungs with fibrosis [108]. The increase in ADC in IPF is however in contrast to the decrease in ADC observed in rats induced with bleomycin as an animal model of IPF [310]. This disagreement may highlight the differences between IPF and drug-induced interstitial lung disease models. Mean Lm_D (274 µm) for the cohort is also elevated when compared to values
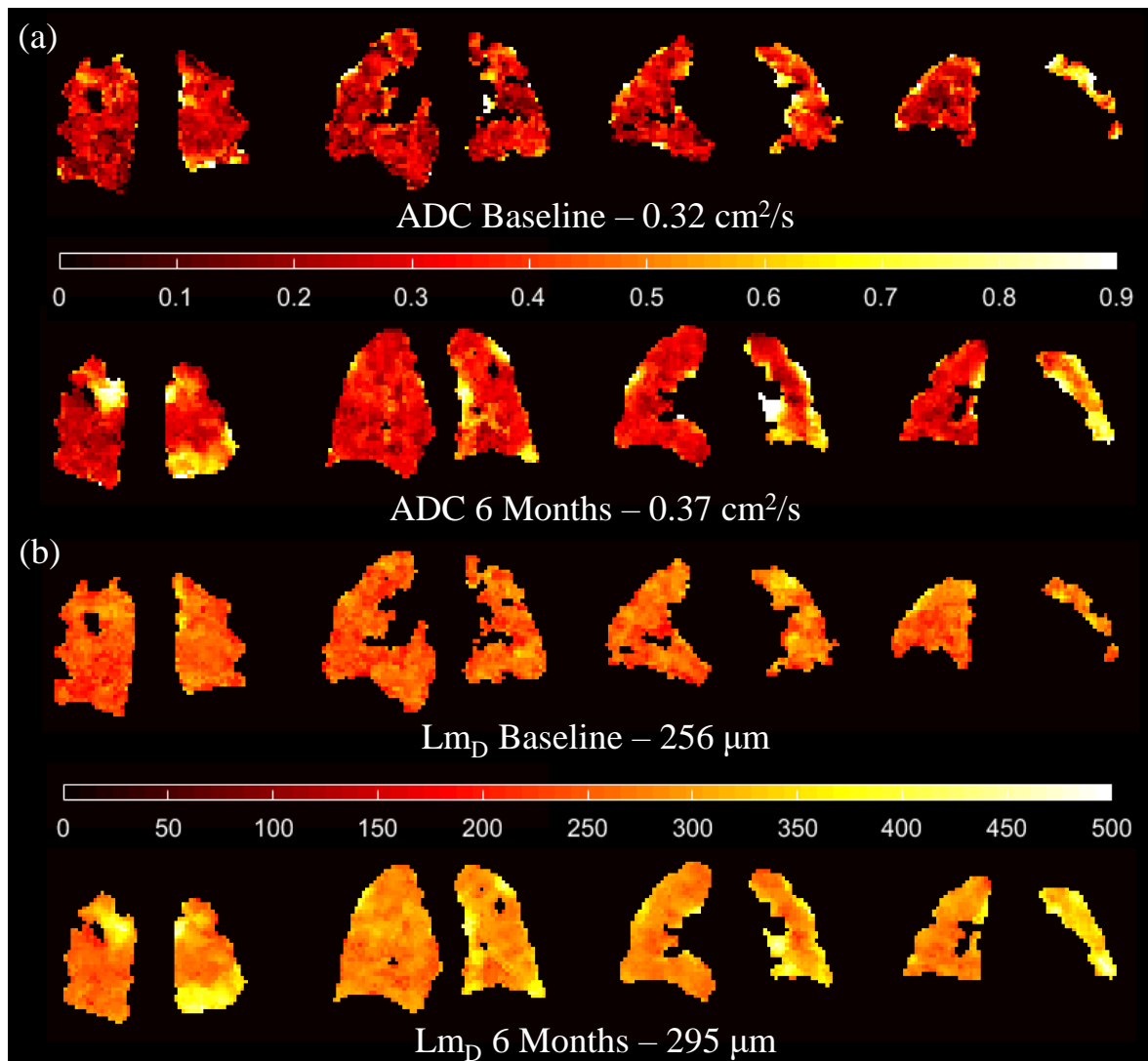
Figure 8.16: Baseline and 6 month follow-up DW-MRI results for IPF12. Selected ADC (a) and Lm_D (b) maps after 6 months demonstrate an increase in mean ADC and Lm_D, and new regions of elevated DW-MRI metrics in the basal and peripheral regions of the lung.

obtained previously in younger (210 µm in Table 6.3) and older healthy subjects (190 µm at 3 T [283]). Elevated ADC and Lm_D reflects loss of acinar integrity due to microstructural changes related to fibrosis. This is qualitatively substantiated by the increase in ADC and Lm_D evident in peripheral and basal regions on the reconstructed MR images, congruous with the expected distribution of disease from CT.

^{3}He DW-MRI metrics demonstrated excellent same day intra-subject and inter-observer reproducibility. The same-day variability for whole lung mean ADC (0.9%) and Lm_D (0.6%) in IPF are smaller than those reported for ADC ($\sim$5%) and lung morphometry (2.1%) parameters in healthy volunteers and patients [282, 311], and are also smaller than the same-day variability of FVC (5%) and D_{LCO}/T_{LCO} (7%) [312]. The improved same-day reproducibility observed in this cohort could be associated with the 3D ^{3}He DW-MRI sequence used that ensures the DW-MRI metrics are acquired across the entire lung volume in each

scan making slice-by-slice comparison easier, which was not possible in 2D selective multi-slice DW-MRI sequences used in previous reproducibility studies. The mean bias of ADC (1.1%) and Lm_D (0.9%) in the inter-observer comparison was comparable to the intra-subject bias; however, the smaller 95% difference range for inter-observer metrics (Figure 8.14) and larger intraclass correlation coefficients indicates ADC and Lm_D are more reproducible between observers than across multiple scans. This was expected and demonstrates that the DW-MRI segmentation and analysis workflow is robust and highly reproducible.

A wide range of mean ADC and Lm_D values were obtained for this IPF cohort in Table 8.2, suggesting a range of disease severity. The whole lung ADC and Lm_D histogram peak shifts to the right in patients with higher mean value, corresponding to decreased skewness and kurtosis, and this reflects the increased heterogeneity in lung microstructure at the acinar length scale. Presumably, this occurs as healthy lung tissue succumbs to fibrotic change. These changes are highly visible on coronal imaging slices and whole lung ADC histogram in Figure 8.11.

In addition, mean ADC and Lm_D significantly correlates with carbon monoxide gas transfer K_{CO} and T_{LCO}, suggesting that the elevated DW-MRI metrics accompany deteriorating alveolar gas transfer associated with the concomitant loss of alveolar surface area. Slightly stronger correlations were obtained with K_{CO} when compared to T_{LCO}, and this may be related to the differences between the two gas transfer metrics. K_{CO} is normalised for alveolar volume (V_A) and is an index of gas exchange efficiency; while T_{LCO} is the gas exchange potential of the lung derived from both K_{CO} and V_A. K_{CO} may therefore be more comparable metric to DW-MRI metrics because both techniques are measured in the areas of the lung that are ventilated (i.e. where tracer or hyperpolarised gas can enter).

For the whole histogram metrics, only ADC kurtosis and Lm_D skewness were correlated with K_{CO}, and no histogram metrics were significantly correlated with T_{LCO}. This suggests that mean ADC and Lm_D values may be a better marker for IPF disease progression. The intraclass correlation coefficients (ICC) in Table 8.4 appear to support this – with larger ICCs observed in mean ADC and Lm_D than other histogram metrics. This could be related to the sensitivity of histogram metrics to the noise thresholding in the DW-MRI segmentation process. The standard deviation of ADC and Lm_D values appear more dependent on the chosen noise threshold than mean values.

The elevated ADC and Lm_D fibrotic regions are visually similar to those found in emphysematous lungs, as seen in Figure 8.17, where emphysematous and fibrotic regions were observed in the same IPF patient. Even though the disease processes of IPF and emphysema are different, both appear to be characterised by an increase in acinar airspace size corresponding to increased ADC or Lm_D values. In emphysema, destruction and loss of elasticity of the alveoli leads to enlarged alveolar airspaces; however, in IPF, thickening of the alveoli wall by fibrotic scarring causes tethering and traction bronchiectasis which in turn leads to increased alveolar dimensions. Qualitatively, emphysematous regions appear to have higher ADC and Lm_D
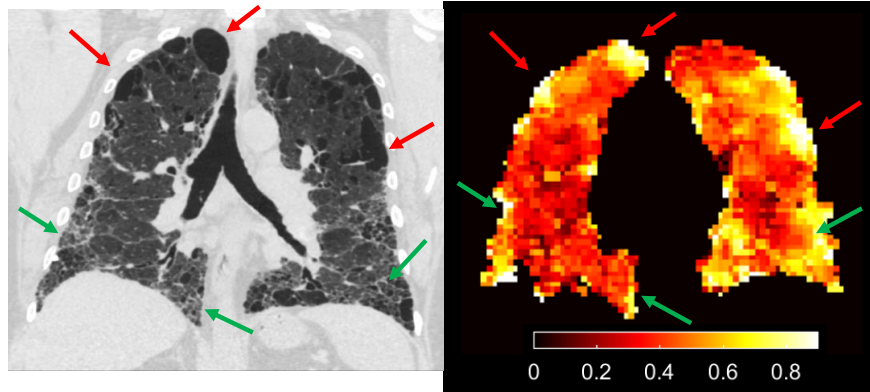
Figure 8.17: CT slice from an IPF patient (IPF10) with regions of bullous emphysema (red arrows) in the upper lobes and fibrotic regions (green arrows) in the lower lobes. In the corresponding ADC map, these emphysematous and fibrotic regions both result in elevated ADC values.

values than fibrotic regions (see mean values for COPD patients in Chapters 5 and 6); a trend that was previously observed in explanted lungs with emphysema and IPF [108]. Interestingly, patients with combined pulmonary fibrosis and emphysema (CPFE) have shown a preservation of FVC [313], due to the confounding effect of the two disease processes, and as such may not demonstrate decline in FVC, a predictor of mortality, with disease progression [314].

Longitudinal changes in DW-MRI results

A significant decrease in FVC ($\sim$4%) was observed in this IPF cohort after 6 months. Even though this decline was less than the validated endpoint for disease progression in IPF (a $\geq$10% FVC decline) [314], it suggests some progression of IPF disease. Mean ADC was not significantly different after 6 months; however, mean Lm_D was significantly elevated by 8 µm. This discrepancy could be related to the mono-exponential fit used to derive ADC, in contrast to the multiple b-value stretched exponential fit used to calculate Lm_D which takes into account more information about the diffusion signal decay. The decline in FVC in this cohort appears to be correlated to the increase in mean Lm_D value (Figure 8.18). The outlier subject (circled in red in Figure 8.18) is of particular interest, as ADC and Lm_D maps after 6 months (Figure 8.16) demonstrated increased number of fibrotic regions in the base and apex of the lungs, and this resulted in a large increase in mean ADC and Lm_D. However, the associated small increase in FVC may be related to the large variability in longitudinal FVC measurements in IPF patients [314]. No significant change after 6 months in T_{LCO} or K_{CO} may suggest that DW-MRI metrics such as Lm_D are more sensitive; however, small patients numbers limit drawing wide-ranging conclusions from this study.

A concomitant significant decrease in red blood cell (RBC) and tissue plasma (TP) peak ratio (RBC/TP) from ^{129}Xe high resolution spectroscopy after 6 months was also observed

Figure 8.18: Plot of FVC (% predicted) and mean Lm_D change after 6 months in the IPF cohort. When all subjects are considered, no significant correlation is obtained. However, when the outlier subject (red circle) is excluded, a significant negative linear correlation is observed (r=-0.64, *P*=0.021).
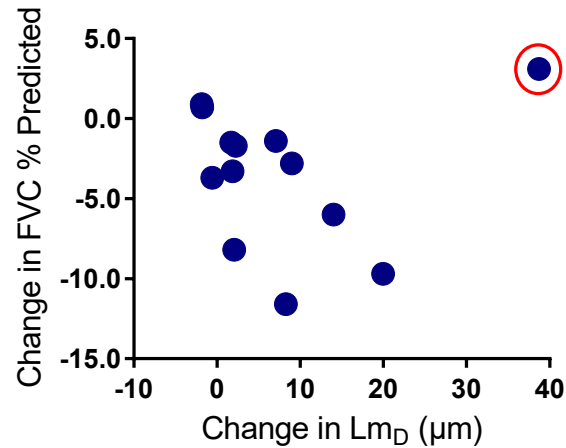
in the same IPF cohort [315]. RBC/TP ratio, representative of the relative amounts of dissolved ^{129}Xe in the RBC and TP compartments, was also significantly correlated with T_{LCO} and K_{CO} reflecting sensitivity to gas exchange efficiency of the lungs. However in this IPF cohort, mean Lm_D or ADC was not significantly correlated with RBC/TP ratio at baseline, and no correlation between the respective changes after 6 months was obtained. In a previous study ^{3}He ADC and ^{129}Xe spectroscopy-derived (CSSR) interstitial septal tissue thickness was found to be linearly correlated in healthy and interstitial lung disease patients [316]. The differences in patient populations could explain the absence of significant correlation in this IPF cohort. It is important to note that the two techniques are sensitive to different compartments of the lung gas exchange unit; where DW-MRI measures the acinar airspace, and ^{129}Xe spectroscopy measurements are made at the point of alveolar gas transfer. Therefore, more work is required to explore the possible similarities of these measurements and their representation of IPF disease progression.

^{129}Xe DW-MRI in IPF

With the limited supply of ^{3}He, currently there is an emphasis for the transition of hyperpolarised lung MRI research to the more cost-effective ^{129}Xe gas. To demonstrate the feasibility of longitudinal monitoring of lung microstructural changes in IPF patients, a subset of the cohort was imaged with ^{129}Xe DW-MRI in the same session as ^{3}He. To date, eight IPF patients have had same-session 3D ^{3}He and ^{129}Xe multiple b-value DW-MRI; ^{129}Xe DW-MRI was acquired as described in Section 6.3 with 550 ml ^{129}Xe, b = [0, 12, 20, 30] s/cm^2, and ^{129}Xe Δ = 8.5 ms. The mean ^{129}Xe ADC and Lm_D for this subset of the IPF cohort was 0.046 cm^2/s and 257 μm, respectively. Matching the trend observed in ^{3}He ADC, the mean ^{129}Xe ADC for IPF was higher than those previously reported for healthy subjects with both ^{129}Xe Δ = 5 (0.036 cm^2/s [113]) and 8.5 ms (0.030 cm^2/s, see Figure 6.10), but was smaller than reported values for COPD patients with emphysema (0.056 cm^2/s [113]).
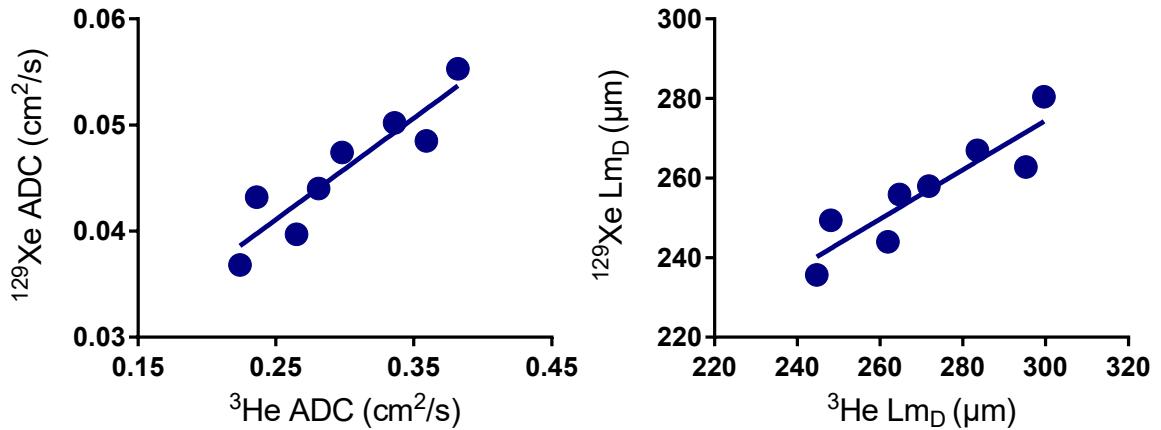
Figure 8.19: Statistically significant correlations between mean ^{3}He and ^{129}Xe ADC and Lm_D in eight IPF patients. Both lung microstructural metrics were significantly correlated with a Spearman's correlation coefficient r = 0.95, and $P = 0.001$.

Considering the same-day ^{3}He and ^{129}Xe DW-MRI metrics, a significant correlation (Spearman's r = 0.95, P=0.001) was observed between the two hyperpolarised gases for both whole lung mean ADC and Lm_D (Figure 8.19). The strong correlation between ^{3}He and ^{129}Xe ADC in IPF is in agreement with previous comparisons of ADC in a range of patients at 1.5 T [118] and 3 T [117]. A mean difference of 5.5% was obtained between ^{3}He and ^{129}Xe Lm_D; similar to the difference of 2.2% observed in Section 6.3 in subjects over a range of acinar length scales. Representative ADC and Lm_D maps with both nuclei are qualitatively similar in appearance, and elevated ADC and Lm_D fibrotic regions are visible with both ^{3}He and ^{129}Xe (Figure 8.20). These results suggest that the same microstructural changes, with respect to healthy normals, are detected with both ^{129}Xe and ^{3}He. However, more longitudinal ^{129}Xe data is required to determine if ^{129}Xe is equally sensitive to IPF disease progression.

8.2.5   Conclusions

In this first in vivo study of acinar microstructure measurements with hyperpolarised gas MRI in IPF, DW-MRI results with both ^{3}He and ^{129}Xe demonstrated an increase in ADC and Lm_D, representative of acinar airway enlargement. ^{3}He DW-MRI metrics were highly reproducible and correlated with clinically relevant measures of gas transfer factor and coefficient. In the absence of changes in T_{LCO} and K_{CO} after 6 months, longitudinal changes in Lm_D were detected, suggesting that hyperpolarised gas DW-MRI may be sensitive to longitudinal changes in lung microstructure in fibrotic lung disease. Whether the observed changes relate pathologically to bronchiolisation of terminal airways with honeycomb formation, traction bronchiectasis, or another pathological element of IPF is as yet unclear. Further work is needed to assess whether longitudinal changes in lung microstructure are evident in a larger population of deteriorating patients, before assessing the prognostic ability of this novel imaging modality in IPF and determining how this may differ in other forms of fibrotic lung disease.
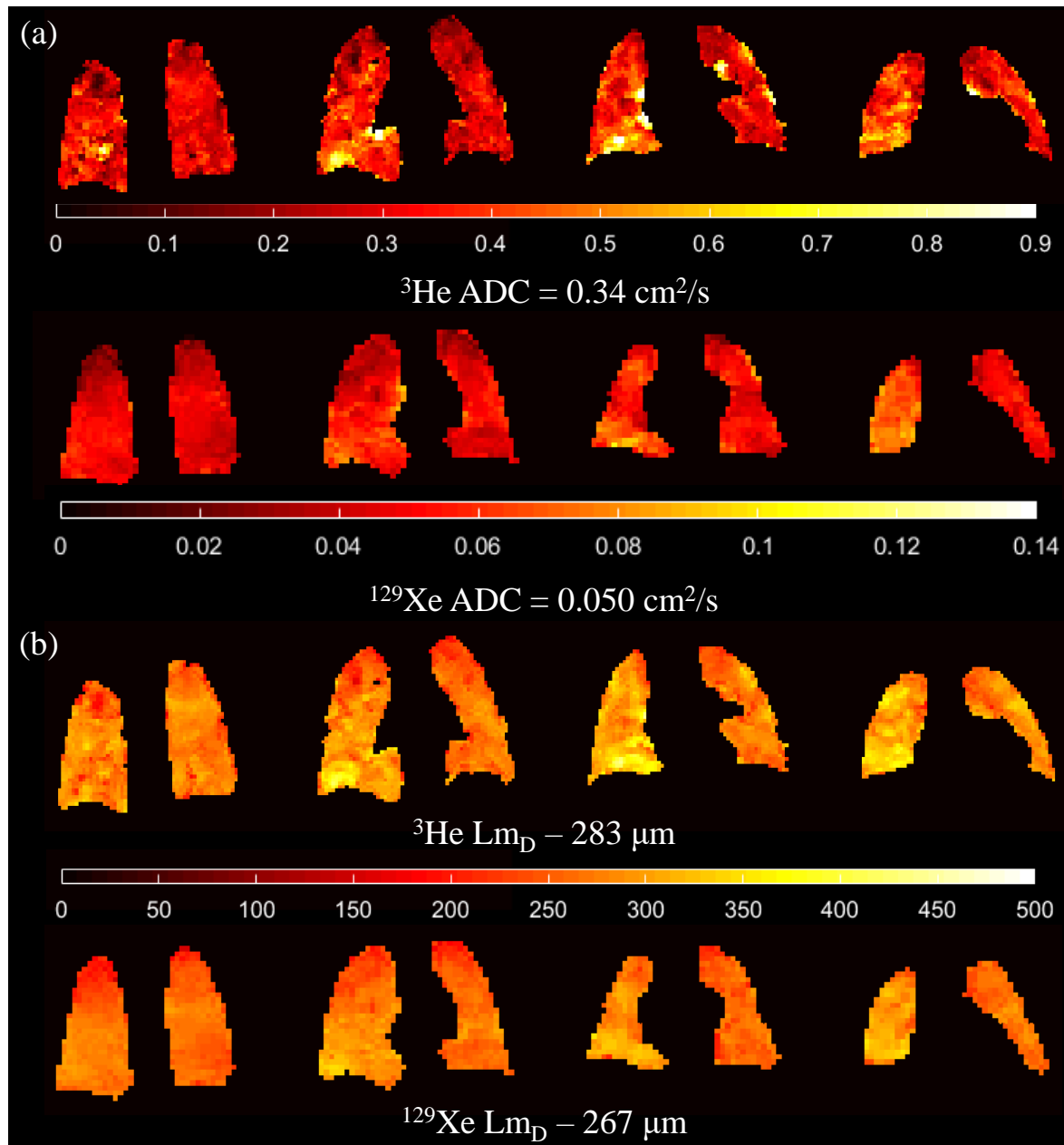
Figure 8.20: A representative IPF patient imaged with both ^{3}He and ^{129}Xe DW-MRI. Elevated regions of ADC (a) and Lm_D (b) corresponding to fibrosis can be observed with both ^{3}He and ^{129}Xe.

8.3 Exploring lung inflation mechanisms with 3D ^{3}He and ^{129}Xe whole lung morphometry mapping

8.3.1 Introduction

Alveolar dimensions change with lung inflation, however, there is currently no consensus on how this lung expansion occurs at the alveolar level. Greaves et al. [317] proposed five different possible lung inflation mechanisms (Figure 8.21): (A) isotropic (symmetrical) expansion; (B) decrease in alveolar depth ('cup to saucer'); (C) increase in alveolar depth ('saucer to cup'); (D) accordion-like expansion where the surface area does not change; (E) alveolar recruitment. The emergence of hyperpolarised gas diffusion-weighted (DW) MRI provides a non-invasive technique that is sensitive to changes in lung microstructure at the acinar level. With the mapping of the apparent diffusion coefficient (ADC), changes in lung inflation have been demonstrated to correspond in respective changes in ADC [103–105]. However, the ADC parameter, with its reported assumptions and limitations [104, 242, 244] (see Section 3.5.2), is reflective of changes in diffusion restriction and does not provide a true measurement of alveolar length scales.
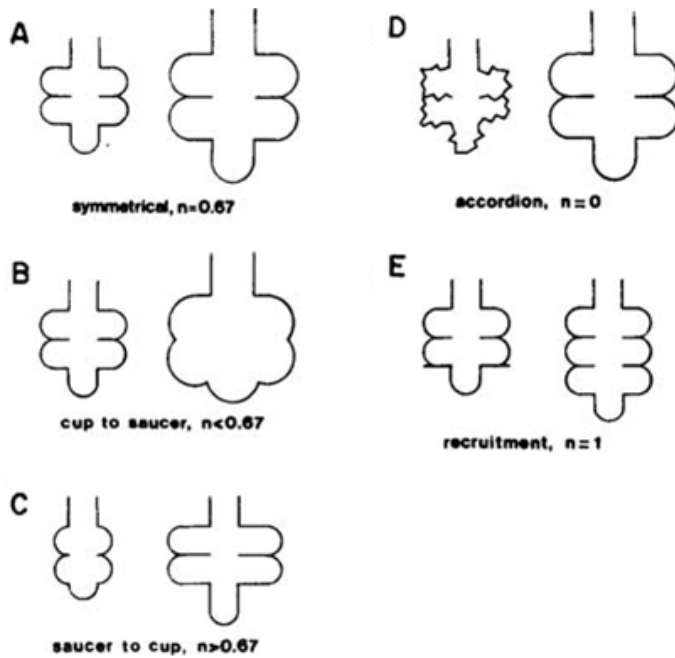
Figure 8.21: Diagrams of different possible alveolar expansion mechanisms proposed by Greaves et al. [317]. n represents the exponent on lung volume, and reflects how surface area changes ($S \propto V^n$). Adapted from Smaldone and Mitzner [318].

In vivo lung morphometry with a cylinder model and multiple b-value DW-MRI enables the derivation of non-invasive quantitative acinar geometrical parameters from the cylindrical geometry, and this technique has been used to explore inflation mechanisms [134]. In this feasibility study of healthy volunteers, a 143% increase in lung volume was accompanied by a 7% increase in alveolar duct radius (R), 21% decrease in alveolar duct depth (h), and 96% increase in the number of alveoli units (N_{tot}) (see Figure 3.26 for more details of the underlying

geometry of the cylinder model). These in vivo results suggested that a combination of alveolar recruitment and expansion of alveolar ducts occurs during lung expansion.

However, this study and previous ADC studies of lung inflation have used low resolution ^{3}He DW-MRI without whole lung coverage. The development of 3D ^{3}He and ^{129}Xe DW-MRI sequences in Chapters 5 and 6 has enabled high resolution whole lung morphometry maps to be obtained in a single breath-hold with both nuclei. These sequences were developed in conjunction with the stretched exponential model, an alternative gas diffusion model that is not based on an assumption of acinar airway geometry, that derives alveolar diffusive length scales (Lm_D) from the multiple b-value diffusion signal. The aim of this section was therefore to utilise 3D ^{3}He and ^{129}Xe multiple b-value DW-MRI and the stretched exponential model to investigate lung inflation mechanisms at different inflation states.

8.3.2   Methods

Five healthy volunteers were recruited and underwent 3D multiple b-value DW-MRI with both hyperpolarised ^{3}He and ^{129}Xe at two different lung inflation states (functional residual capacity + 1L (FRC+1L) and total lung capacity (TLC)). For the FRC+1L inflation state, volunteers inhaled a 1L mixture of hyperpolarised gas and N_2 at FRC. For the TLC inflation state, they performed the same manoeuvre and continued inhaling room air until TLC. All imaging acquisitions were performed on a 1.5 T GE HDx scanner with 3D SPGR ^{3}He and ^{129}Xe DW-MRI sequences and compressed sensing as described in Sections 5.3 and 6.3. Both 3D ^{3}He and ^{129}Xe was implemented with three-fold CS undersampling. A summary of relevant ^{3}He and ^{129}Xe DW imaging parameters is shown in Table 8.5.

Table 8.5: Summary of imaging parameters for 3D ^{3}He and ^{129}Xe DW-MRI sequences.

Imaging Parameters	^{3}He	^{129}Xe
Gas dose (ml)	250	700
Voxel size (mm^3)	$4.17 \times 4.17 \times 12$	$6.25 \times 6.25 \times 15$
TE/TR (ms)	4.2/6.0	14.0/17.3
Breath-hold (s)	15	21
b-values (s/cm^2)	[0, 1.6, 4.2, 7.2]	[0, 12, 20, 30]
Diffusion time (ms)	1.6	8.5
Diffusion gradient parameters (ms)	$\delta = 1.0, \tau = 0.3,$ gap = 0	$\delta = 2.3, \tau = 0.3,$ gap = 5.6

δ = gradient plateau time, τ = ramp time

Undersampled ^{3}He and ^{129}Xe DW-MRI datasets were reconstructed, and maps of ADC and stretched exponential model Lm_D and alpha (α) values were calculated for each acquisition as

described in Chapters 5 and 6. Each ^{3}He and ^{129}Xe dataset was also fitted to the ^{3}He-based cylinder model (see Sections 6.3.3) to derive lung morphometry parameters R, h, and alveoli density (N_a) (Section 3.5.2). The total number of alveoli (N_{tot}) was subsequently estimated by multiplying the mean N_a per voxel by the imaging lung volume (V_{tot}):

$$N_{tot} = \bar{N}_a \times V_{tot} \tag{8.2}$$

where V_{tot} is the product of the image voxel volume and the total number of ventilated voxels. V_{tot} derived from the diffusion-weighted imaging is comparable to the alveolar volume (V_A) measurement determined from PFTs, and represents the volume of ventilated alveolar units. Voxels with an alveoli density greater than 5×10^5 cm^{-3} appear to correspond to major airways in the maps of N_a, and were excluded from the calculated of N_{tot} and V_{tot}. Any statistical difference in lung morphometry parameters between lung inflation states was assessed with paired t-tests, and statistical significance was determined at the $P<0.05$ level.

The parameters R, h, and N_{tot} were derived to ascertain if the same lung expansion mechanism of alveolar recruitment and expansion, proposed by Hajari et al. [134], are observed. To determine if a similar trend can also be observed with the stretched exponential model, Lm_D results were compared to an isotropic expansion model based upon imaging lung volumes. FRC+1L and TLC volumes were utilised to estimate the expected lung volume expansion between the two inflation states. For an isotropic volume expansion model, this volume increase can be used to predict an Lm_D expansion value as follows:

$$Lm_D^{\text{TLC isotropic}} = (\% \text{ volume increase})^{1/3} \times Lm_D^{\text{FRC+1L}} \tag{8.3}$$

8.3.3 Results and Discussion

All ^{3}He and ^{129}Xe lung morphometry results for each volunteer at FRC+1L and TLC are summarised in Tables 8.6 and 8.7, respectively. A statistically significant difference between FRC+1L and TLC was observed for ADC (^{3}He $P=0.002$, ^{129}Xe $P=0.020$); Lm_D ($P=0.011$, $P=0.007$); α (^{3}He $P=0.018$); R ($P=0.039$, $P=0.005$); h (^{3}He $P=0.005$); N_{tot} ($P<0.001$, $P=0.010$). ^{129}Xe α ($P=0.101$) and h ($P=0.425$) was not significantly different between inflation states. On average, for ^{3}He DW-MRI, a 58.7% increase in imaging lung volume (V_{tot}) from FRC+1L to TLC results in a 18.9% increase in mean ADC, a 8.1% increase in Lm_D, a 2.3% decrease in α, a 6.5% increase in R, a 13.6% decrease in h, and a 38.6% increase in N_{tot}. While for ^{129}Xe, a 79.9% increase V_{tot} was observed leading to a 13.3% increase in mean ADC, a 10.5% increase in Lm_D, a 5.2% increase in α, a 14.9% increase in R, a 2.5% increase in h, and a 54.3% increase in N_{tot}.

Table 8.6: Summary of global mean ^{3}He ADC and lung morphometry results for five healthy volunteers imaged at lung inflation states of FRC+1L and TLC. Values are given as mean ($\pm$ standard deviation).

Subject	Inflation State	ADC (cm²/s)	Stretched exponential model		Cylinder model			
			Lm_D (µm)	Alpha (α)	R (µm)	h (µm)	N_{tot} (10⁶)	V_{tot} (L)
HV1	FRC+1L	0.182 ± 0.084	208 ± 30	0.827 ± 0.192	268 ± 68	124 ± 48	715 ± 348	4.27
	TLC	0.223 ± 0.080	236 ± 24	0.819 ± 0.164	304 ± 63	106 ± 83	1030 ± 564	7.85
HV2	FRC+1L	0.196 ± 0.077	224 ± 24	0.843 ± 0.158	293 ± 62	124 ± 80	593 ± 315	4.19
	TLC	0.242 ± 0.081	246 ± 24	0.815 ± 0.164	318 ± 61	95 ± 86	862 ± 474	7.36
HV3	FRC+1L	0.166 ± 0.068	205 ± 23	0.841 ± 0.155	267 ± 66	135 ± 80	638 ± 333	3.76
	TLC	0.191 ± 0.072	219 ± 22	0.832 ± 0.167	283 ± 69	124 ± 83	917 ± 509	6.01
HV4	FRC+1L	0.169 ± 0.065	210 ± 20	0.846 ± 0.148	274 ± 60	135 ± 73	774 ± 377	4.72
	TLC	0.193 ± 0.081	216 ± 23	0.815 ± 0.185	273 ± 74	117 ± 85	977 ± 550	6.01
HV5	FRC+1L	0.162 ± 0.064	205 ± 25	0.847 ± 0.157	271 ± 69	141 ± 76	621 ± 329	3.87
	TLC	0.193 ± 0.081	219 ± 24	0.831 ± 0.181	287 ± 72	128 ± 88	845 ± 496	5.77
Average	FRC+1L	0.175 ± 0.014	210 ± 8	0.841 ± 0.008	275 ± 11	132 ± 8	668 ± 74	4.16 ± 0.38
	TLC	0.208 ± 0.023	227 ± 13	0.822 ± 0.008	293 ± 18	114 ± 14	926 ± 78	6.60 ± 0.94
% Change (FRC+1L to TLC)		+18.9%	+8.1%	-2.3%	+6.5%	-13.6%	+38.6%	+58.7%

Table 8.7: Summary of global mean ^{129}Xe ADC and lung morphometry results for five healthy volunteers imaged at lung inflation states of FRC+1L and TLC. Values are given as mean (± standard deviation).

Subject	Inflation State	^{129}Xe diffusion-weighted MRI metrics						
		ADC (cm²/s)	Stretched exponential model		Cylinder model			
			Lm_D (µm)	Alpha (α)	R (µm)	h (µm)	N_{tot} (10^6)	V_{tot} (L)
HV1	FRC+1L	0.030 ± 0.010	204 ± 26	0.840 ± 0.164	271 ± 72	114 ± 77	733 ± 413	4.67
	TLC	0.037 ± 0.010	228 ± 21	0.846 ± 0.171	311 ± 71	117 ± 94	975 ± 598	7.56
HV2	FRC+1L	0.036 ± 0.013	218 ± 27	0.803 ± 0.220	291 ± 84	109 ± 99	623 ± 407	4.33
	TLC	0.041 ± 0.009	245 ± 22	0.856 ± 0.151	334 ± 69	104 ± 90	764 ± 458	7.12
HV3	FRC+1L	0.030 ± 0.012	199 ± 24	0.800 ± 0.235	258 ± 90	126 ± 98	581 ± 379	3.64
	TLC	0.031 ± 0.012	204 ± 23	0.803 ± 0.239	270 ± 89	128 ± 99	822 ± 546	5.39
HV4	FRC+1L	0.028 ± 0.015	188 ± 28	0.767 ± 0.271	237 ± 93	124 ± 97	396 ± 256	2.48
	TLC	0.030 ± 0.007	210 ± 17	0.880 ± 0.136	290 ± 74	144 ± 86	912 ± 573	6.19
HV5	FRC+1L	0.027 ± 0.013	189 ± 33	0.829 ± 0.215	255 ± 84	135 ± 94	465 ± 277	2.79
	TLC	0.033 ± 0.008	217 ± 20	0.866 ± 0.147	298 ± 73	134 ± 92	846 ± 538	5.92
Average	FRC+1L	0.030 ± 0.004	200 ± 12	0.808 ± 0.028	262 ± 20	122 ± 10	560 ± 133	3.58 ± 0.95
	TLC	0.034 ± 0.005	221 ± 16	0.850 ± 0.029	301 ± 24	125 ± 15	864 ± 82	6.44 ± 0.89
% Change (FRC+1L to TLC)		+13.3%	+10.5%	+5.2%	+14.9%	+2.5%	+54.3%	+79.9%

The increase in mean ADC observed between FRC+1L and TLC with both ^{3}He and ^{129}Xe is in agreement with previous studies [103–105, 134]. The increase in ^{3}He ADC (18.9%) matches the previously reported results (18.1%) at 1.5 T and with b-value = 1.6 s/cm^2 [104]. A strong linear correlation between ^{3}He and ^{129}Xe ADC has been reported previously suggesting that equivalent structural information is probed with both nuclei [117, 118]. Therefore, the smaller increase in ^{129}Xe ADC (13.3%) could be attributed to variability between scan sessions or effects related to differences in D_0 and diffusion regimes.

The changes to ^{3}He cylinder model lung morphometry parameters are very similar to the those observed previously (V_{tot}, +56.9%; R, +3.5%; h, -11.8%; N_{tot}, +40.2%) in a cohort of healthy volunteers from FRC+1L to TLC [134]. The ^{129}Xe cylinder model parameters all demonstrated a similar trend except for alveolar sleeve depth h, which was 2.5% larger at TLC, but not statistically different. It is likely the opposite trend with inflation observed between ^{3}He and ^{129}Xe h value may be related to intersubject scan variability. Nevertheless, the results with both nuclei suggests that lung expansion leads to alveolar duct expansion and alveolar recruitment; this is in agreement with previous studies with the cylinder model [134]. The derived total number of alveoli from the cylinder model is larger the reported average number estimated from histology (∼480 million) [12]. The larger estimated alveoli number obtained with DW-MRI could in part be related to partial volume effects leading to an over-estimation of the V_{tot} and subsequently N_{tot}.

Stretched exponential model Lm_D value increased from FRC+1L to TLC by 8.1% and 10.5% for ^{3}He and ^{129}Xe, respectively; which is similar to the increase in R values. For the FRC+1L inflation state, a mean difference of 3.5% (7.2 µm) was observed between ^{3}He and ^{129}Xe Lm_D values; similar to the 2.9% difference (Table 6.2) seen in the same healthy volunteers with four-fold undersampling of ^{129}Xe DW-MRI with an empirically-optimised ^{129}Xe diffusion time (see Section 6.3). A smaller difference between ^{3}He and ^{129}Xe of 2.9% (6.6 µm) was detected at TLC, and this improved matching may in part be explained by the fact that the TLC inflation state is more reproducible than FRC [319]. The heterogeneity index parameter (α) was significantly decreased with ^{3}He. This change of -2.3% matches the variation in α (∼2%) observed previously in healthy subjects between FRC+1L and TLC inflation states [141]. However, when compared to other lung morphometry parameters, the change in α is relatively small and suggests that α may be relatively constant with lung expansion.

In conjunction with the increase in ^{3}He and ^{129}Xe ADC and Lm_D values between inflation states, statistically significant differences in the posterior to anterior (P-A) gradients at the two inflation states were also observed (Figure 8.22). A significant decrease in P-A ADC of -0.003 cm^{2}s^{-1}cm^{-1} (P=0.006), and -0.001 cm^{2}s^{-1}cm^{-1} (P=0.001) was observed from FRC+1L to TLC volume for ^{3}He and ^{129}Xe, respectively. A significant decrease in Lm_D gradient was also observed for both ^{3}He and ^{129}Xe, -2.072 µm·cm^{-1} (P=0.005), and -2.316 µm·cm^{-1} (P=0.011), respectively.
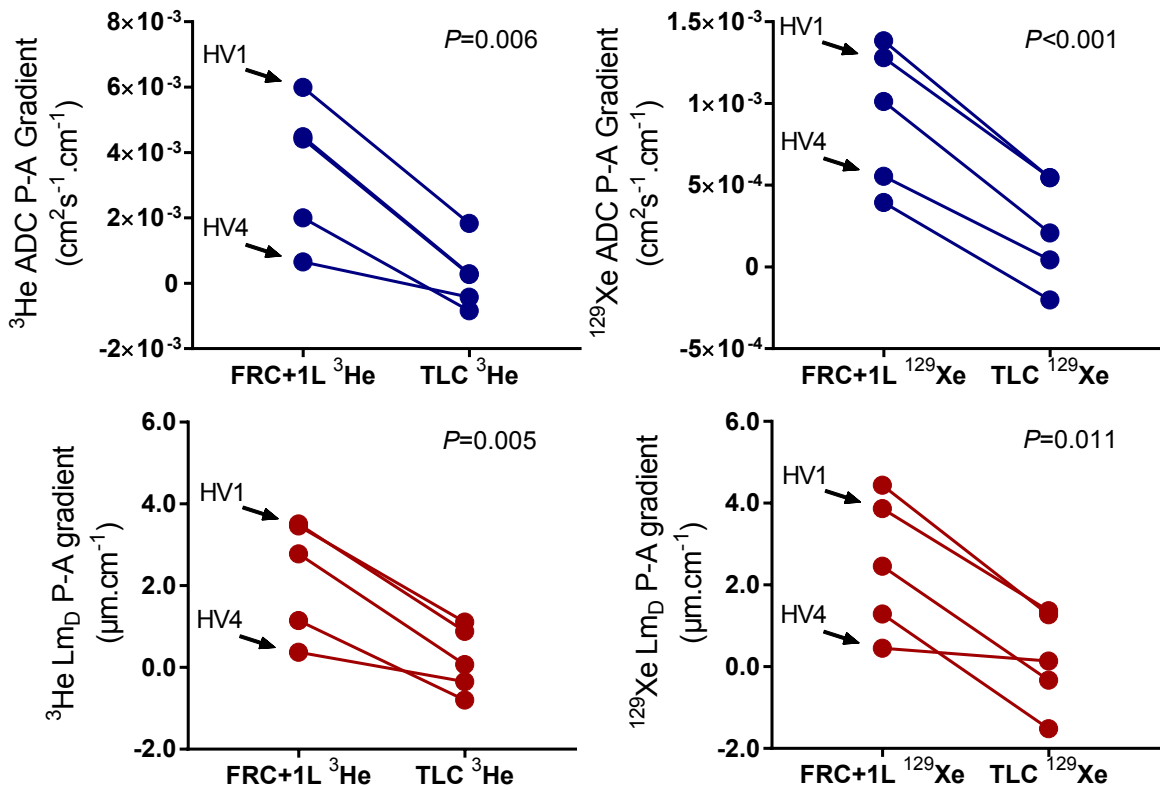
Figure 8.22: Changes in ADC and Lm_D posterior to anterior gradients between FRC+1L and TLC inflation states for the five healthy volunteers. HV1 and HV4 are highlighted, as representative examples of the two gradient trend groups.

The reduction in P-A gradient at TLC was observed previously with ^{3}He ADC mapping [105], and can be explained by the regional differences in pleural pressure leading to an uneven distribution of ventilation at FRC+1L that reduces when the lung fully expands [320]. The P-A gradients for the five healthy volunteers can be classified in two distinct groups with either small or large differences between FRC+1L and TLC. HV1 Lm_D data is shown in Figure 8.23a, where a large P-A gradient can be seen at FRC+1L; at TLC, this P-A gradient is reduced. HV4 (Figure 8.23b) in contrast, exhibits a small P-A gradient at FRC+1L and this gradient reduces slightly at TLC. These differences in P-A gradient between healthy volunteers could be the result of inter-subject variations in lung anatomy and body mass which may affect regional differences of lung ventilation.

Table 8.8 summarises imaging volume (V_{tot}) for each volunteer that was used to derive an isotropic predicted TLC Lm_D value for ^{3}He and ^{129}Xe. Each volunteer's predicted TLC ^{3}He and ^{129}Xe Lm_D value was larger than the experimentally measured TLC equivalent. These results suggest that a simple model of isotropic alveolar expansion does not fully explain the changes to alveolar dimensions during lung inflation. A possible explanation for the smaller mean Lm_D value is alveolar recruitment (Figure 8.21E), where previously closed alveoli become ventilated at TLC, thereby contributing to increased lung volume but not to
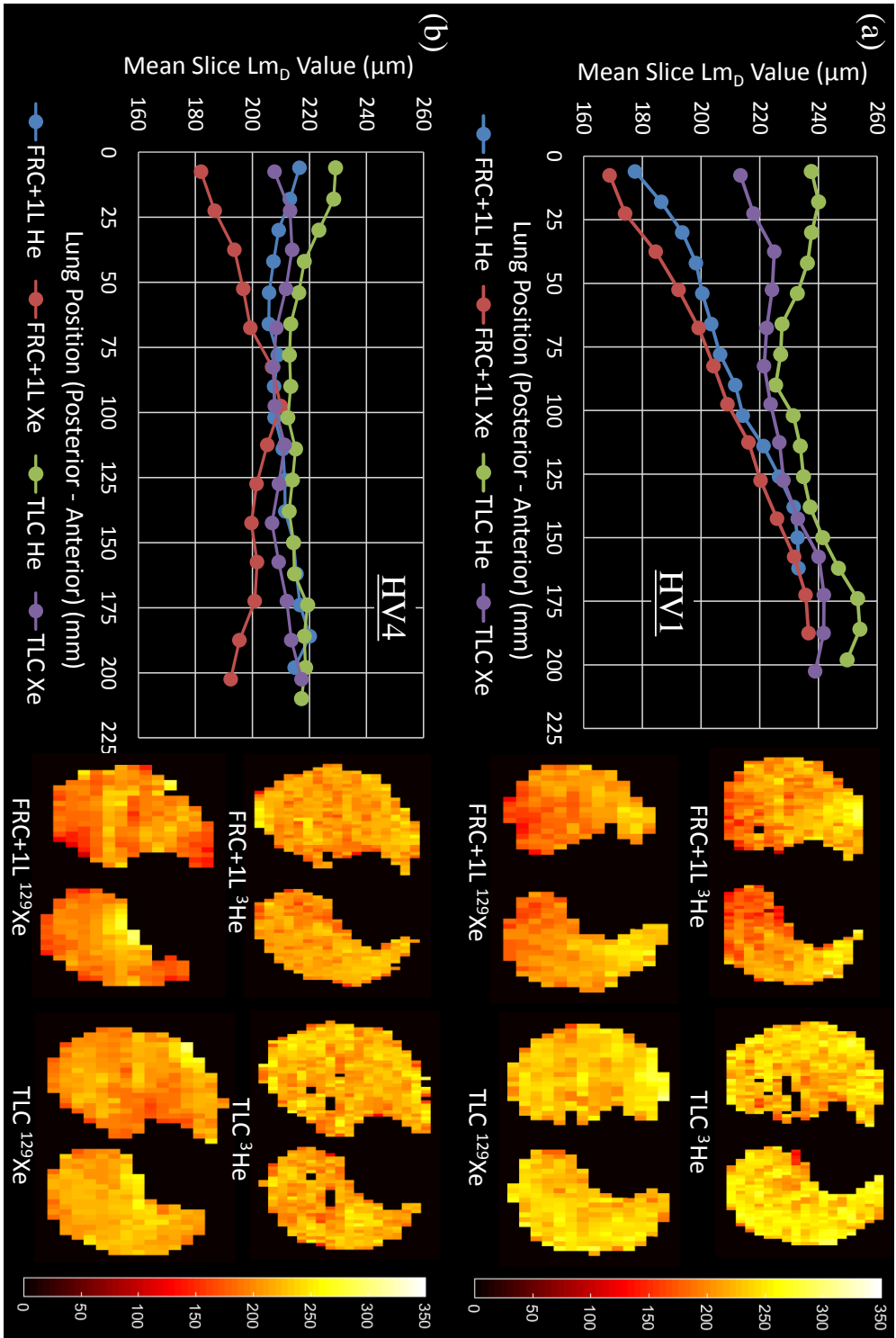
Figure 8.23: (a) Gravitational gradients of mean slice Lm_D values from posterior to anterior direction for ^{3}He and ^{129}Xe FRC+1L and TLC volumes with corresponding reconstructed axial Lm_D maps for HV1. (b) The respective ^{3}He and ^{129}Xe gravitational gradients and axial Lm_D maps for HV4.

mean Lm_D value. These results support the hypothesis of alveolar expansion and recruitment during lung inflation observed with the cylinder model lung morphometry parameters.

Table 8.8: Measured ^{3}He and ^{129}Xe TLC Lm_D values and predicted TLC Lm_D calculated from an isotropic expansion model using the imaging volume (V_{tot}) at each inflation state.

Subject	Nuclei	Imaging volume (V_{tot}) (L)			TLC Lm_D (µm)	
		FRC+1L	TLC	Scaling	Isotropic	Measured
HV1	^{3}He	4.27	7.85	1.23	255	236
	^{129}Xe	4.67	7.56	1.17	240	228
HV2	^{3}He	4.19	7.36	1.21	270	246
	^{129}Xe	4.33	7.12	1.18	257	245
HV3	^{3}He	3.76	6.01	1.17	240	219
	^{129}Xe	3.64	5.39	1.14	227	204
HV4	^{3}He	4.72	6.01	1.08	223	216
	^{129}Xe	2.48	6.19	1.36	255	210
HV5	^{3}He	3.87	5.77	1.14	234	219
	^{129}Xe	2.79	5.92	1.29	243	217

The accuracy of the scaling factor in the isotropic expansion model is dependent on the estimated V_{tot} of the FRC+1L and TLC datasets. With the relatively large effective slice thickness of ^{3}He (12 mm) and ^{129}Xe DW-MRI (15 mm), a more accurate estimation of V_{tot} could be achieved with a higher resolution ^{1}H SPGR dataset acquired in the same-breath as the hyperpolarised gas DW-MRI [181]. Body plethysmography is the standard pulmonary function test used to estimate lung volumes. However, in body plethysmography, FRC and TLC volumes are measured in the sitting posture, in contrast to MR imaging in supine. Previous studies have demonstrated the effect of posture on lung volumes; where the supine FRC and TLC volumes were approximately 30% and 5% smaller than the sitting volumes [321]. It is also important to note that body plethysmography provides a measurement of total lung volume (TLV); which in healthy volunteers is very similar to V_{tot} or VV% (96%) [117]. However, in obstructed patients, regions of the lung become unventilated and a difference in TLV and V_{tot} may be be observed. Therefore, while the estimated lung volume may be more accurate with body plethysmography, the differences in lung volume between postures alongside the potential mismatch of TLV and V_{tot} in obstructed patients, suggests that V_{tot} may be the most accurate estimation of lung volume for the derivation of the volume scaling factor.

The Lm_D results in the study confirm that lung inflation is not through isotropic alveolar expansion alone. One limitation of the stretched exponential model is that an estimate of alveoli numbers cannot be derived, therefore the hypothesis of alveolar recruitment cannot be investigated with this model. However, in a recent comparison of hyperpolarised gas ventilation imaging at different lung inflation in healthy volunteers, the quantitative metrics of

lung ventilation appear to support this alveolar recruitment hypothesis [319]. The coefficient of variation (CV), representative of the standard deviation of ventilation image voxel intensity, is a measurement of ventilation heterogeneity [190]. In Hughes et al. [319], the CV% of healthy volunteers was observed to increase at smaller lung inflation volumes (residual volume (RV)) and decreased with lung expansion. The increased CV% at RV, in conjunction with areas of unventilated lung visible in the dependent lung were suggested to be related to airway closure at small inflation states. While the decrease in CV% at TLC was associated with the opening of airways resulting in a more homogeneous ventilation signal intensity. These ventilation imaging results complement the diffusion-weighted imaging metrics and suggests alveolar recruitment plays a significant role during lung inflation.

The derivation of lung morphometry parameters from the cylinder and stretched exponential models were derived under the assumption that the free diffusion coefficient of ^{3}He (0.88 cm^2/s) or ^{129}Xe (0.14 cm^2/s) in the lungs stayed the same at the two lung inflation states. The concentration dependent diffusion coefficient $D_0(C)$ can be calculated as follows [322]:

$$\frac{1}{D_0(C)} = \frac{1 - C}{D_0(C \rightarrow 0)} + \frac{C}{D_0(C \rightarrow 1)} \tag{8.4}$$

where $D_0(C \rightarrow 0)$ is the free diffusion coefficient in air, and $D_0(C \rightarrow 1)$ is the self diffusion coefficient for either ^{3}He or ^{129}Xe (see Table 3.1). The ^{3}He and ^{129}Xe $D_0(C)$ were estimated from the respective V_{tot} (Table 8.8) and gas doses (Table 8.5). The average ^{3}He $D_0(C)$ for the five healthy volunteers at FRC+1L and TLC was 0.89 and 0.88 cm^2/s, respectively; while the average ^{129}Xe $D_0(C)$ was 0.11 and 0.12 cm^2/s, respectively. These results suggests that the assumed ^{129}Xe D_0 (0.14 cm2/s) may have been slightly over-estimated, and this may have a small effect on the derived ^{129}Xe lung morphometry metrics. However, the minimal difference in ^{129}Xe D_0 between FRC+1L and TLC indicates that any changes to lung morphometry metrics will be negligible between the lung inflation states.

8.3.4   Conclusion

This is the first study of lung inflation with 3D multiple b-value ^{3}He and ^{129}Xe DW-MRI in healthy volunteers. Good matching of Lm_D values and changes in the P-A gravitational gradient were observed between FRC+1L and TLC inflation states with both hyperpolarised gases. An increase in alveolar duct radius R and total number of alveoli N_{tot} were observed along with measured TLC Lm_D values that were smaller than predicted TLC values from an isotropic alveolar expansion model. These results suggests that a combination of both alveolar expansion and recruitment may occur during lung inflation. In this preliminary study, lung inflation mechanisms were explored in healthy volunteers only. Additional imaging in patients experienced with pulmonary diseases could be used to further explore if lung inflation mechanisms change in response to disease.

Chapter 9

Summary and further work

The focus of this thesis has been on the development and implementation of 3D hyperpolarised gas diffusion-weighted MRI techniques for measuring and modelling lung microstructure. This chapter presents a summary of the main research findings from each experimental chapter, and provides a brief overview along with preliminary results for some work in progress that builds upon the methods developed in this thesis.

9.1 Summary

In **Chapter 4**, a framework for lobar comparison of lung microstructure measurements derived from CT and ^{3}He DW-MRI in an asthmatic cohort was presented. CT lobar regions were used to guide the manual lobar segmentation of ^{3}He DW-MRI. Statistically significant linear correlations were obtained between ^{3}He DW-MRI lung microstructure metrics of ADC and Lm_D, and CT metrics in all lobar regions. Significant correlation suggested that the lung microstructure metrics from CT and DW-MRI are inter-related in asthmatic patients.

Compressed sensing was implemented in **Chapter 5** to facilitate the acquisition of 3D multiple b-value ^{3}He DW-MRI in a single breath-hold for whole lung morphometry mapping. An optimised three-fold undersampled k-space pattern was validated in healthy volunteers and COPD patients, and good agreement between CS-derived and fully-sampled whole lung morphometry maps indicates that CS undersampled ^{3}He DW-MRI is fit for clinical lung imaging studies. CS techniques were further implemented for the simultaneous acquisition of co-registered ^{3}He ventilation, ADC, Lm_D, and T_2^* maps to reduce the number of ^{3}He doses required in clinical imaging studies.

Chapter 6 builds upon the ^{3}He DW-MRI CS techniques to acquire whole lung morphometry maps with the more cost-effective ^{129}Xe isotope. An empirically-optimised ^{129}Xe diffusion time ($\Delta = 8.5$ ms) was derived and benchmarked against ^{3}He DW-MRI in healthy volunteers,

ex-smokers, and COPD patients. Strong agreement was demonstrated between [3]He and
[129]Xe lung morphometry values derived from both stretched exponential and cylinder models;
indicating that [129]Xe DW-MRI at [129]Xe $\Delta = 8.5$ ms is a viable alternative to [3]He for whole
lung morphometry mapping in clinical imaging studies.

Chapter 7 presents an in vivo comparison of the stretched exponential and cylinder theoretical
gas diffusion models in a range of patient groups with the newly developed 3D [3]He and [129]Xe
DW-MRI sequences. The mean diffusive length scale (Lm_D), derived from the stretched
exponential model, was related to cylinder model mean chord length (Lm) in a non-linear
power relationship; while the cylinder model mean alveolar diameter (L_{Alv}) demonstrated
excellent linear correlation with Lm_D. The results indicate that the two theoretical gas
diffusion models are inter-related and the distinct relationships are representative of different
sections of the acinar airway geometry measured during DW-MRI.

In **Chapter 8**, the implementation of [3]He and [129]Xe DW-MRI in three different investigations
of lung microstructure was demonstrated. First, [3]He DW-MRI was used in a longitudinal
study comparing children with mild cystic fibrosis and healthy controls at baseline and after
2 years. No significant difference in DW-MRI metrics was observed both at baseline between
the two groups, and after 2 years in mild CF despite increased ventilation heterogeneity.
This indicated that acinar microstructural changes do not accompany the observed increased
ventilation heterogeneity in early CF lung disease.

A cohort of idiopathic pulmonary fibrosis (IPF) patients were imaged with [3]He and [129]Xe DW-
MRI in a longitudinal study to investigate changes in DW-MRI metrics in IPF lung disease.
ADC and Lm_D were elevated in IPF, when compared to healthy subjects, and significantly
correlated with carbon monoxide gas transfer factor and coefficient. DW-MRI metrics were
also highly reproducible and Lm_D demonstrated significant increase after 6 months, suggesting
sensitivity to longitudinal changes in lung microstructure from fibrotic lung disease.

Finally, 3D [3]He and [129]Xe DW-MRI were acquired at two different lung volumes to investigate
lung inflation mechanisms at the acinar level. An increase in alveolar duct radius (R) and
total number of alveoli (N_{tot}) at TLC from the cylinder model was observed; while the
stretched exponential model Lm_D TLC measurements were smaller than the respective values
predicted with isotropic expansion. These results suggest that a combination of both alveolar
expansion and recruitment may occur during lung inflation.

In conclusion, compressed sensing has facilitated the acquisition 3D [3]He and [129]Xe DW-
MRI in a single breath-hold. These sequences allow for the derivation of 3D whole lung
morphometry mapping to validate quantitative gas diffusion models and investigate clinical
and physiological changes in acinar microstructure.

9.2 Further work

9.2.1 Multi-modality PRM

One of the main motivations for the development of 3D multiple b-value ^{3}He and ^{129}Xe DW-MRI sequences was the additional microstructural information that can be ascertained from 3D whole lung morphometry mapping. The framework developed in Chapter 4 for a lobar multi-modality comparison of CT and DW-MRI metrics of lung microstructure could be improved with the inclusion of 3D DW-MRI. Image registration of 3D CT and 3D DW-MRI would improve the accuracy of lobar region segmentations, and following registration, a more quantitative voxel-by-voxel comparison of lung microstructure metrics would be possible through a similar approach taken with the parametric response mapping (PRM) method [42, 258].

The feasibility of this is demonstrated in Figure 9.1 where an image registration methodology, adapted from Tahir et al. [262], was used to register CT and 3D ^{3}He DW-MRI from an IPF patient. 3D ^{3}He DW-MRI was up-sampled and registered to the same spatial domain of ^{3}He ventilation images acquired in the same patient; while inspiratory CT images were down-sampled and registered to the spatial domain of the ^{1}H anatomical images that were acquired in the same-breath as the ^{3}He ventilation images [181].
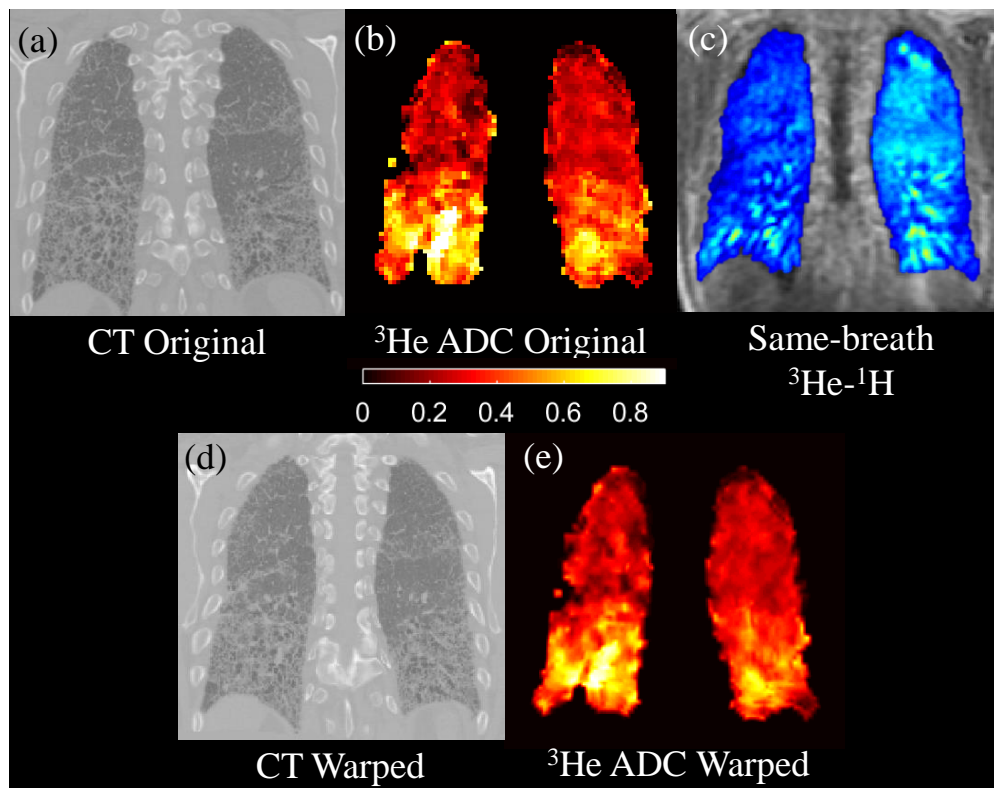
Figure 9.1: Multi-modality image registration framework. Inspiratory CT (a) and 3D ^{3}He ADC (b) maps are registered to the same spatial domain of same-breath ^{3}He ventilation and ^{1}H anatomical images (c). The warped CT image (d) and ^{3}He ADC map (e).

A multi-modality PRM was developed by combining the registered CT and ^{3}He ADC maps. For CT, a threshold of <-950 HU corresponds to the emphysema threshold of inspiratory CT (white pixels in Fig. 9.2a); while ADC thresholds of 0.25 (orange in Fig. 9.2b) and 0.35 cm^2/s (yellow in Fig. 9.2b) were selected corresponding to the reported mean ADC in older healthy never smokers [116], and IPF patients (see Section 8.2.3), respectively. These CT and ADC thresholds were defined to classify each co-registered image voxel: group 1 (green), CT>-950 HU and 0<ADC<0.25 cm^2/s; group 2 (yellow), CT>-950 HU and 0.25<ADC<0.35 cm^2/s; group 3 (red), CT>-950 HU and ADC>0.35 cm^2/s; group 4 (blue), CT$\leq$-950 HU and ADC>0.25 cm^2/s; group 5 (white), ADC = 0 (i.e. ventilation defects).
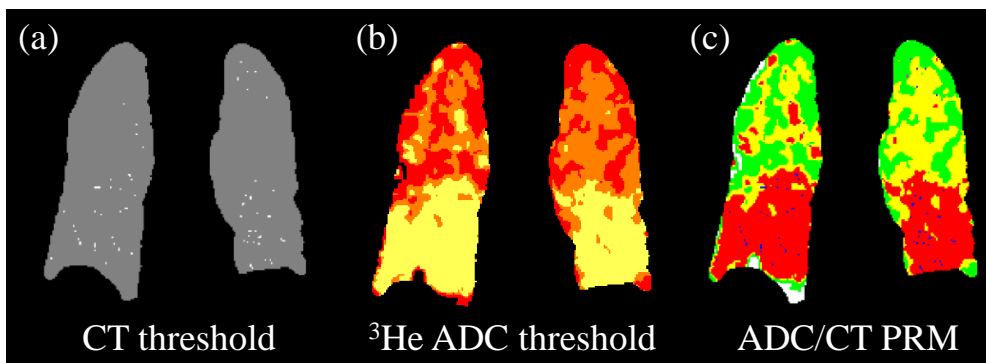
Figure 9.2: Multi-modality parametric response mapping. (a) Inspiratory CT map with emphysema threshold. (b) ^{3}He ADC map with thresholds for older healthy and IPF ADC values. (c) These threshold were used to produce a combined ADC and CT PRM.

In the example multi-modality PRM image in Figure 9.2c, the defined voxel thresholds appears to represent the expected IPF disease pattern. No areas of blue voxels, corresponding to emphysema in the PRM, are visible confirming that the observed elevated ADC voxels are related to fibrosis. The yellow and red thresholds, defined to separate mild and severe IPF regions, also appear to correspond well with the distribution of fibrotic regions in this IPF patient. The preliminary results are promising and demonstrate the feasibility of PRM with multi-modality imaging. Further work will be focused on defining optimal ADC or Lm_D thresholds to differentiate DW-MRI voxels in different patient groups and also including expiratory CT metrics, to extrapolate complementary lung microstructural information from multi-modality imaging.

9.2.2 Validation of theoretical gas diffusion models

Another area of future work is the validation of alveolar dimension estimates from the stretched exponential model in known geometries. Diffusion experiments in realistic acinar geometry phantoms derived from micro-CT images of lung samples could improve the validation of lung morphometry gas diffusion models. Phantoms with realistic acinar geometry derived from micro-CT images have been previously demonstrated [323, 324], where a 3D

rendering of micro-CT images of a lung tissue sample (Figure 9.3a) was used to segment a pulmonary acinus (Figure 9.3b) using a region growing algorithm with Simpleware ScanIP (Synopsys, Mountain View, USA). The segmented acinus was 3D-printed with stereolithography technology (TuskT, Materialise NV, Leuven, Belgium) to create 3D acinar phantom geometries at different volume scalings (Figure 9.3c). Finally, to verify the accuracy of 3D printed geometries, the phantoms were re-imaged with micro-CT and the internal geometry was segmented and finite element meshes (Figure 9.3d) were created to validate in vitro diffusion measurements through diffusion simulations.
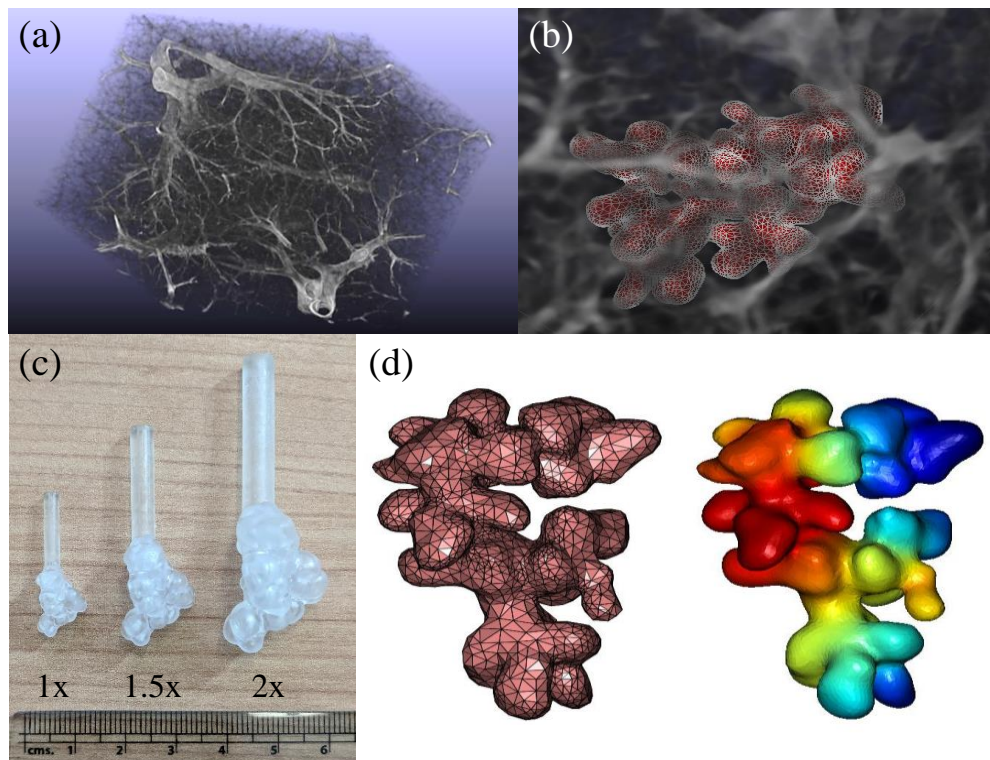
Figure 9.3: Realistic acinar geometry phantoms derived from micro-CT. (a) A 3D render of micro-CT images of an ex vivo lung tissue sample. (b) The acinus is segmented from micro-CT images. (c) 3D printing technology is then used to create acinus phantoms. (d) The phantoms were re-imaged with micro-CT to verify 3D printing quality and to validate in vitro diffusion measurements through finite element diffusion simulations.

Diffusion MR measurements can be obtained from these acinus phantoms using a modified 3D multiple b-value SPGR sequence that has no phase and readout gradients to allow for a free induction decay (FID) acquisition following bipolar diffusion gradients. An imaging sequence could also be possible in the larger phantom sizes, but SNR limitations may prevent imaging of the $1\times$ scale phantom. The finite element meshes generated from micro-CT of the acinus phantoms in Figure 9.3d will allow finite element simulations of gas diffusion to validate in vitro diffusion MR measurements. These realistic acinar geometry phantoms could also provide an opportunity to explore changes to acinar geometry through inflation and provide experimental validation to the in vivo results obtained in Section 8.3. In conjunction,

experiments in phantoms modified to reflect emphysema or fibrosis disease patterns could help improve the understanding of these disease processes.

9.2.3   Alternative accelerated acquisition strategies

The final potential area of future work is the development of different and complementary acceleration strategies for the acquisition of 3D multiple b-value diffusion-weighted MRI with hyperpolarised gases. Parallel imaging (see Section 3.4) with multiple-channel receiver coils has facilitated accelerated hyperpolarised gas MR imaging [174, 220, 221], and can be combined with compressed sensing techniques (e.g. ℓ_1-SPIRiT [325]) to improve the quality of reconstructed undersampled images. Non-Cartesian acquisitions, such as spiral [194] and radial [195] trajectories, offer an alternative method to accelerate hyperpolarised gas imaging. Recently, this has been demonstrated with the simultaneous interleaved acquisition of 3D isotropic ^{129}Xe images of the gas and dissolved phases with 3D radial imaging [308]. These alternative acceleration techniques could be translated to 3D hyperpolarised gas diffusion-weighted MRI, and provide an alternative to CS undersampling for 3D whole lung coverage diffusion-weighted MRI acquisitions.

Appendix A

List of publications

A.1 Publications arising from this thesis

Journal articles

- "3D diffusion-weighted ^{129}Xe MRI for whole lung morphometry". **H.-F. Chan**, N. J. Stewart, G. Norquay, G. J. Collier, J. M. Wild. *Magnetic Resonance in Medicine.* doi:10.1002/mrm.26960 (2017).

- "Whole lung morphometry with 3D multiple b-value hyperpolarized gas MRI and compressed sensing". **H.-F. Chan**, N. J. Stewart, J. Parra-Robles, G. J. Collier, J. M. Wild. *Magnetic Resonance in Medicine.* 77(5): 1916-1925 (2017).

Conference proceedings

- "Longitudinal monitoring of lung microstructure with HP gas diffusion-weighted MRI in mild cystic fibrosis children". **H.-F. Chan**, L. Smith, H. Marshall, et al. *Proceedings of the European Respiratory Society (ERS) Meeting, Milan, Italy, 2017.* Programme number: OA4399. (Oral presentation).

- "Comparison of in-vivo lung morphometry models from multiple b-value diffusion-weighted MRI in healthy controls, IPF and COPD patients". **H.-F. Chan**, J. Parra-Robles, G. J. Collier, J. M. Wild. *Proceedings of the European Respiratory Society (ERS) Meeting, Milan, Italy, 2017.* Programme number: OA4644. (Oral presentation).

- "3D Mapping of Whole Lung Morphometry with ^{129}Xe Diffusion-Weighted MRI and Compressed Sensing: Comparison with ^{3}He". **H.-F. Chan**, N. J. Stewart, J. Parra-Robles, G. J. Collier, J. M. Wild. *Proceedings of the International Society for Magnetic Resonance in Medicine (ISMRM) Meeting, Honolulu, Hawaii, USA, 2017.* Programme number: 2138. (Poster presentation).

- "Exploring Lung Inflation Mechanisms with 3D ^{3}He and ^{129}Xe Whole Lung Morphometry Mapping". **H.-F. Chan**, J. Parra-Robles, G. J. Collier, J. M. Wild. *Proceedings of the International Society for Magnetic Resonance in Medicine (ISMRM) Meeting, Honolulu, Hawaii, USA, 2017.* Programme number: 3315. (Poster presentation).

- "Hyperpolarised ^{3}He Diffusion-Weighted MRI in Mild Cystic Fibrosis Children and Age-Matched Healthy Controls". **H.-F. Chan**, G. J. Collier, L. Smith, et al. *Proceedings of the International Society for Magnetic Resonance in Medicine (ISMRM) Meeting, Honolulu, Hawaii, USA, 2017.* Programme number: 4903. (Poster presentation).

- "Comparison of In-Vivo Lung Morphometry Models from 3D Multiple b-value ^{3}He Diffusion-Weighted MRI". **H.-F. Chan**, J. Parra-Robles, G. J. Collier, J. M. Wild. *Proceedings of the International Society for Magnetic Resonance in Medicine (ISMRM) Meeting, Honolulu, Hawaii, USA, 2017.* Programme number: 876. (Oral & Poster presentation).

- "3D Whole Lung Morphometry Mapping with ^{129}Xe MRI and Compressed Sensing: Comparison with ^{3}He". **H.-F. Chan**, N. J. Stewart, G. J. Collier, J. M. Wild. *Proceedings of the British Chapter (BC) of the International Society for Magnetic Resonance in Medicine (ISMRM) Meeting, Leeds, United Kingdom, 2016.* (Oral presentation).

- "Whole Lung Morphometry with Hyperpolarised ^{3}He Gas Diffusion MRI - 3D Multiple b-Value Acquisition and Compressed Sensing". **H.-F. Chan**, N. J. Stewart, J. Parra-Robles, G. J. Collier, J. M. Wild. *Proceedings of the International Society for Magnetic Resonance in Medicine (ISMRM) Meeting, Singapore, 2016.* Programme number: 2925. (Poster presentation).

- "3D Multi-Parametric Acquisition of ^{3}He Lung Ventilation Images, Lung Diffusion Morphometry and T_2* Maps with Compressed Sensing". **H.-F. Chan**, N. J. Stewart, G. J. Collier, J. M. Wild. *Proceedings of the International Society for Magnetic Resonance in Medicine (ISMRM) Meeting, Singapore, 2016.* Programme number: 2928. (Poster presentation).

- "3D multiple b-value ADC acquisition for whole lung morphometry with hyperpolarised gas MRI and compressed sensing". **H.-F. Chan**, N. J. Stewart, J. Parra-Robles, G. J. Collier, J. M. Wild. *Proceedings of the European Society for Magnetic Resonance in Medicine and Biology (ESMRMB) Meeting, Edinburgh, United Kingdom, 2015.* Programme number: 135. (Oral presentation).

- "Lobar comparison of CT densitometry and ^{3}He diffusion MRI models of lung microstructure in asthmatics". **H.-F. Chan**, J. Parra-Robles, C. E. Brightling, W. Vos, J. M. Wild. *Proceedings of the European Respiratory Society (ERS) Meeting, Amsterdam, Netherlands, 2015.* Programme number: OA4991. (Oral presentation).

A.2 Other co-authored publications

Book chapter

- "Hyperpolarised Helium-3 (^{3}He) MRI: Physical Methods for Imaging Human Lung Function". J. M. Wild, N. J. Stewart, **H.-F. Chan**. *In Medical Radiology.* 1-29 (2017).

Journal articles

- "Comparison of ^{3}He and ^{129}Xe MRI for evaluation of lung microstructure and ventilation at 1.5 T". N. J. Stewart, **H.-F. Chan**, P. J. C. Hughes, et al. *Journal of Magnetic Resonance Imaging.* doi:10.1002/jmri.25992 (2018).

Conference proceedings

- "Rapid Acquisition of Hyperpolarized ^{129}Xe Lung MR Ventilation and Diffusion-Weighted Images with Compressed Sensing". G. J. Collier, **H.-F. Chan**, N. J. Stewart, et al. *Proceedings of the Hyperpolarised Noble Gases (PING) Meeting, Salt Lake City, Utah, USA, 2017.* (Poster presentation).

- "Hyperpolarised gas MRI demonstrates sub-clinical progression in IPF over 6 months". N. D. Weatherley, **H.-F. Chan**, N. J. Stewart, et al. *Proceedings of the European Respiratory Society (ERS) Meeting, Milan, Italy, 2017.* Programme number: OA4642. (Oral presentation).

- "Hyperpolarised gas ventilation MRI detects early lung ventilation heterogeneity in children with primary ciliary dyskinesia". N. West, L. Smith, **H.-F. Chan**, et al. *Proceedings of the European Respiratory Society (ERS) Meeting, Milan, Italy, 2017.* Programme number: PA3342. (Poster presentation).

- "Assessment of Acinar Destruction in Idiopathic Pulmonary Fibrosis with Hyperpolarised ^{3}He Gas Diffusion-Weighted MRI: Reproducibility of ADC Metrics and Correlation with Physiological Parameters of Disease Severity". N. D. Weatherley, **H.-F. Chan**, N. J. Stewart, et al. *Proceedings of the International Society for Magnetic Resonance in Medicine (ISMRM) Meeting, Honolulu, Hawaii, USA, 2017.* Programme number: 3328. (Poster presentation).

- "Double Tracer Gas Single Breath Washout (SBW) Lung Imaging with Hyperpolarized Xe-129 and He-3". F. C. Horn, G. J. Collier, **H.-F. Chan**, N. J. Stewart, L. Smith, J. M. Wild. *Proceedings of the International Society for Magnetic Resonance in Medicine (ISMRM) Meeting, Honolulu, Hawaii, USA, 2017.* Programme number: 2141. (Poster presentation).

- "Rapid Acquisition of Co-Registered 3D Xenon-129 and Proton Images of the Human Lung in a Single Breath-Hold Using Compressed Sensing". G. J. Collier, P. J. C. Hughes, F. C. Horn, **H.-F. Chan**, et al. *Proceedings of the International Society for Magnetic Resonance in Medicine (ISMRM) Meeting, Honolulu, Hawaii, USA, 2017.* Programme number: 2139. (Poster presentation).

- "Reproducibility and Methodological Considerations for Dissolved-Phase ^{129}Xe Spectroscopy in Patients with Idiopathic Pulmonary Fibrosis". N. J. Stewart, N. D. Weatherley, **H.-F. Chan**,

et al. *Proceedings of the International Society for Magnetic Resonance in Medicine (ISMRM) Meeting, Honolulu, Hawaii, USA, 2017.* Programme number: 2148. (Poster presentation).

- "Diffusion-weighted hyperpolarised gas MRI in idiopathic pulmonary fibrosis: Reproducibility and clinical significance". N. D. Weatherley, **H.-F. Chan**, N. J. Stewart, et al. *Proceedings of the European Respiratory Society (ERS) Meeting, London, United Kingdom, 2016.* Programme number: OA3504. (Oral presentation).

- "Comparison of ^{3}He and ^{129}Xe MRI for evaluation of lung microstructure and ventilation at 1.5 T". N. J. Stewart, **H.-F. Chan**, P. J. C. Hughes, et al. *Proceedings of the European Respiratory Society (ERS) Meeting, London, United Kingdom, 2016.* Programme number: PA743. (Poster presentation).

- "Regional phase III slope measurement using hyperpolarized gas MR imaging". F. C. Horn, G. J. Collier, **H.-F. Chan**, N. J. Stewart, J. M. Wild. *Proceedings of the European Respiratory Society (ERS) Meeting, London, United Kingdom, 2016.* Programme number: PA743. (Poster presentation).

- "Comparison of ^{3}He and ^{129}Xe MRI for Evaluation of Lung Microstructure and Ventilation in Healthy Volunteers and COPD Patients at 1.5 T". N. J. Stewart, **H.-F. Chan**, G. J. Collier, et al. *Proceedings of the International Society for Magnetic Resonance in Medicine (ISMRM) Meeting, Singapore, 2016.* Programme number: 979. (Oral presentation).

Bibliography

[1] Albert, M. S., Cates, G. D., Driehuys, B., Happer, W., Saam, B., Springer, C. S., and Wishnia, A. Biological magnetic resonance imaging using laser-polarized 129Xe. *Nature*, 370(6486):199–201, 1994.

[2] Ebert, M., Grossmann, T., Heil, W., Otten, E. W., Surkau, R., Thelen, M., Leduc, M., Bachert, P., Knopp, M. V., and Schad, L. R. Nuclear magnetic resonance imaging with hyperpolarised helium-3. *The Lancet*, 347(9011):1297–1299, 1996.

[3] MacFall, J. R., Charles, H. C., Black, R. D., Middleton, H., Swartz, J. C., Saam, B., Driehuys, B., Erickson, C., Happer, W., Cates, G. D., Johnson, G. A., and Ravin, C. E. Human lung air spaces: potential for MR imaging with hyperpolarized He-3. *Radiology*, 200(2):553–8, 1996.

[4] Mugler III, J. P., Driehuys, B., Brookeman, J. R., Cates, G. D., Berr, S. S., Bryant, R. G., Daniel, T. M., De Lange, E. E., Downs, J. H., Erickson, C. J., Happer, W., Hinton, D. P., Kassel, N. F., Maier, T., Phillips, C. D., Saam, B. T., Sauer, K. L., and Wagshul, M. E. MR imaging and spectroscopy using hyperpolarized 129Xe gas: Preliminary human results. *Magnetic Resonance in Medicine*, 37(6):809–815, 1997.

[5] Yablonskiy, D. A., Sukstanskii, A. L., Leawoods, J. C., Gierada, D. S., Bretthorst, G. L., Lefrak, S. S., Cooper, J. D., and Conradi, M. S. Quantitative in vivo assessment of lung microstructure at the alveolar level with hyperpolarized 3He diffusion MRI. *Proceedings of the National Academy of Sciences of the United States of America*, 99(5):3111–6, 2002.

[6] Yablonskiy, D. A., Sukstanskii, A. L., Woods, J. C., Gierada, D. S., Quirk, J. D., Hogg, J. C., Cooper, J. D., and Conradi, M. S. Quantification of lung microstructure with hyperpolarized 3He diffusion MRI. *Journal of Applied Physiology*, 107(4):1258–65, 2009.

[7] Weibel, E. R. What makes a good lung? *Swiss Medical Weekly*, 139(27-28):375–86, 2009.

[8] Wanger, J. *Pulmonary Function Testing: A Practical Approach*. Jones & Bartlett Learning, 2012.

[9] Weibel, E. R. *Morphometry of the human lung*. Springer, 1963.

[10] West, J. *Respiratory Physiology: The Essentials*. Wolters Kluwer Health/Lippincott Williams & Wilkins, 2012.

[11] Haefeli-Bleuer, B. and Weibel, E. R. Morphometry of the human pulmonary acinus. *Anatomical Record*, 220(4):401–14, 1988.

[12] Ochs, M., Nyengaard, J. R., Jung, A., Knudsen, L., Voigt, M., Wahlers, T., Richter, J., and Gundersen, H. J. The number of alveoli in the human lung. *American Journal of Respiratory and Critical Care Medicine*, 169(1):120–4, 2004.

[13] Ochs, M. A brief update on lung stereology. *Journal of Microscopy*, 222(Pt 3):188–200, 2006.

[14] Gehr, P., Bachofen, M., and Weibel, E. R. The normal human lung: ultrastructure and morphometric estimation of diffusion capacity. *Respiration Physiology*, 32(2):121–140, 1978.

[15] Schreider, J. P. and Raabe, O. G. Structure of the human respiratory acinus. *American Journal of Anatomy*, 162(3):221–232, 1981.

[16] Hsia, C. C., Hyde, D. M., Ochs, M., and Weibel, E. R. An official research policy statement of the American Thoracic Society/European Respiratory Society: standards for quantitative assessment of lung structure. *American Journal of Respiratory and Critical Care Medicine*, 181(4):394–418, 2010.

[17] Knudsen, L., Weibel, E. R., Gundersen, H. J., Weinstein, F. V., and Ochs, M. Assessment of air space size characteristics by intercept (chord) measurement: an accurate and efficient stereological approach. *Journal of Applied Physiology*, 108(2):412–21, 2010.

[18] Dunnill, M. S. Quantitative Methods in the Study of Pulmonary Pathology. *Thorax*, 17(4):320–328, 1962.

[19] Thurlbeck, W. M. Internal surface area and other measurements in emphysema. *Thorax*, 22(6):483–496, 1967.

[20] Knudson, R. J., Clark, D. F., Kennedy, T. C., and Knudson, D. E. Effect of aging alone on mechanical properties of the normal adult human lung. *Journal of Applied Physiology: Respiratory, Environmental and Exercise Physiology*, 43(6):1054–62, 1977.

[21] Heemskerk-Gerritsen, B. A., Dijkman, J. H., and Ten Have-Opbroek, A. A. Stereological methods: a new approach in the assessment of pulmonary emphysema. *Microscopy Research and Technique*, 34(6): 556–62, 1996.

[22] Wiebe, B. M. and Laursen, H. Lung morphometry by unbiased methods in emphysema: bronchial and blood vessel volume, alveolar surface area and capillary length. *Journal of Pathology, Microbiology and Immunology*, 106(6):651–6, 1998.

[23] Hou, R., Le, T., Murgu, S. D., Chen, Z., and Brenner, M. Recent advances in optical coherence tomography for the diagnoses of lung disorders. *Expert Review of Respiratory Medicine*, 5(5):711–24, 2011.

[24] Drexler, W. Ultrahigh-resolution optical coherence tomography. *Journal of Biomedical Optics*, 9(1): 47–74, 2004.

[25] Hanna, N., Saltzman, D., Mukai, D., Chen, Z., Sasse, S., Milliken, J., Guo, S., Jung, W., Colt, H., and Brenner, M. Two-dimensional and 3-dimensional optical coherence tomographic imaging of the airway, lung, and pleura. *Journal of Thoracic and Cardiovascular Surgery*, 129(3):615–22, 2005.

[26] Coxson, H. O., Quiney, B., Sin, D. D., Xing, L., McWilliams, A. M., Mayo, J. R., and Lam, S. Airway wall thickness assessed using computed tomography and optical coherence tomography. *American Journal of Respiratory and Critical Care Medicine*, 177(11):1201–6, 2008.

[27] McLaughlin, R. A., Yang, X., Quirk, B. C., Lorenser, D., Kirk, R. W., Noble, P. B., and Sampson, D. D. Static and dynamic imaging of alveoli using optical coherence tomography needle probes. *Journal of Applied Physiology*, 113(6):967–74, 2012.

[28] Hounsfield, G. N. Computerized transverse axial scanning (tomography): Part 1. Description of system. *The British Journal of Radiology*, 46(552):1016–1022, 1973.

[29] Cormack, A. Reconstruction of densities from their projections, with applications in radiological physics. *Physics in medicine and biology*, 18(2):195, 1973.

[30] Albert, J. M. Radiation risk from CT: implications for cancer screening. *American Journal of Roentgenology*, 201(1):W81–7, 2013.

[31] Goddard, P. R., Nicholson, E. M., Laszlo, G., and Watt, I. Computed tomography in pulmonary emphysema. *Clinical Radiology*, 33(4):379–387, 1982.

[32] Coxson, H. O. Computed tomography and monitoring of emphysema. *European Respiratory Journal*, 29 (6):1075–7, 2007.

[33] Hedlund, L. W., Vock, P., and Effmann, E. L. Evaluating Lung Density by Computed Tomography. *Seminars in Respiratory Medicine*, 5(01):76–88, 1983.

[34] Gevenois, P. A. and Yernault, J. C. Can computed tomography quantify pulmonary emphysema? *European Respiratory Journal*, 8(5):843–8, 1995.

[35] Gould, G. A., MacNee, W., McLean, A., Warren, P. M., Redpath, A., Best, J. J. K., Lamb, D., and Flenley, D. C. CT Measurements of Lung Density in Life Can Quantitate Distal Airspace Enlargement - An Essential Defining Feature of Human Emphysema. *American Review of Respiratory Disease*, 137(2): 380–392, 1988.

[36] Uppaluri, R., Mitsa, T., Sonka, M., Hoffman, E. A., and McLennan, G. Quantification of pulmonary emphysema from lung computed tomography images. *American Journal of Respiratory and Critical Care Medicine*, 156(1):248–54, 1997.

[37] Muller, N. L., Staples, C., Miller, R., and Abboud, R. "Density mask". An objective method to quantitate emphysema using computed tomography. *Chest*, 94(4):782, 1988.

[38] Dirksen, A., Dijkman, J. H., Madsen, F., Stoel, B., Hutchison, D. C., Ulrik, C. S., Skovgaard, L. T., Kok-Jensen, A., Rudolphus, A., Seersholm, N., Vrooman, H. A., Reiber, J. H., Hansen, N. C., Heckscher, T., Viskum, K., and Stolk, J. A randomized clinical trial of alpha(1)-antitrypsin augmentation therapy. *American Journal of Respiratory and Critical Care Medicine*, 160(5 Pt 1):1468–72, 1999.

[39] Jain, N., Covar, R. A., Gleason, M. C., Newell, J., J. D., Gelfand, E. W., and Spahn, J. D. Quantitative computed tomography detects peripheral airway disease in asthmatic children. *Pediatric Pulmonology*, 40(3):211–8, 2005.

[40] Coxson, H. O., Rogers, R. M., Whittall, K. P., D'Yachkova, Y., Pare, P. D., Sciurba, F. C., and Hogg, J. C. A quantification of the lung surface area in emphysema using computed tomography. *American Journal of Respiratory and Critical Care Medicine*, 159(3):851–6, 1999.

[41] Mishima, M., Hirai, T., Itoh, H., Nakano, Y., Sakai, H., Muro, S., Nishimura, K., Oku, Y., Chin, K., Ohi, M., Nakamura, T., Bates, J. H., Alencar, A. M., and Suki, B. Complexity of terminal airspace geometry assessed by lung computed tomography in normal subjects and patients with chronic obstructive pulmonary disease. *Proceedings of the National Academy of Sciences of the United States of America*, 96 (16):8829–34, 1999.

[42] Galban, C. J., Han, M. K., Boes, J. L., Chughtai, K. A., Meyer, C. R., Johnson, T. D., Galban, S., Rehemtulla, A., Kazerooni, E. A., Martinez, F. J., and Ross, B. D. Computed tomography-based biomarker provides unique signature for diagnosis of COPD phenotypes and disease progression. *Nature Medicine*, 18(11):1711–5, 2012.

[43] Hasegawa, M., Nasuhara, Y., Onodera, Y., Makita, H., Nagai, K., Fuke, S., Ito, Y., Betsuyaku, T., and Nishimura, M. Airflow Limitation and Airway Dimensions in Chronic Obstructive Pulmonary Disease. *American Journal of Respiratory and Critical Care Medicine*, 173(12):1309–1315, 2006.

[44] Bartholmai, B. J., Raghunath, S., Karwoski, R. A., Moua, T., Rajagopalan, S., Maldonado, F., Decker, P. A., and Robb, R. A. Quantitative computed tomography imaging of interstitial lung diseases. *Journal of Thoracic Imaging*, 28(5):298–307, 2013.

[45] Maldonado, F., Moua, T., Rajagopalan, S., Karwoski, R. A., Raghunath, S., Decker, P. A., Hartman, T. E., Bartholmai, B. J., Robb, R. A., and Ryu, J. H. Automated quantification of radiological patterns predicts survival in idiopathic pulmonary fibrosis. *European Respiratory Journal*, 43(1):204–12, 2014.

[46] Soejima, K., Yamaguchi, K., Kohda, E., Takeshita, K., Ito, Y., Mastubara, H., Oguma, T., Inoue, T., Okubo, Y., Amakawa, K., Tateno, H., and Shiomi, T. Longitudinal follow-up study of smoking-induced lung density changes by high-resolution computed tomography. *American Journal of Respiratory and Critical Care Medicine*, 161(4 Pt 1):1264–73, 2000.

[47] Madani, A., De Maertelaer, V., Zanen, J., and Gevenois, P. A. Pulmonary emphysema: radiation dose and section thickness at multidetector CT quantification–comparison with macroscopic and microscopic morphometry. *Radiology*, 243(1):250–7, 2007.

[48] Mishima, M., Itoh, H., Sakai, H., Nakano, Y., Muro, S., Hirai, T., Takubo, Y., Chin, K., Ohi, M., Nishimura, K., Yamaguchi, K., and Nakamura, T. Optimized Scanning Conditions of High Resolution CT in the Follow-Up of Pulmonary Emphysema. *Journal of Computer Assisted Tomography*, 23(3): 380–384, 1999.

[49] Knudson, R. J. Expiratory computed tomography for assessment of suspected pulmonary emphysema. *Chest*, 99(6):1357, 1991.

[50] Eda, S., Kubo, K., Fujimoto, K., Matsuzawa, Y., Sekiguchi, M., and Sakai, F. The relations between expiratory chest CT using helical CT and pulmonary function tests in emphysema. *American Journal of Respiratory and Critical Care Medicine*, 155(4):1290–1294, 1997.

[51] Gevenois, P. A., De Vuyst, P., de Maertelaer, V., Zanen, J., Jacobovitz, D., Cosio, M. G., and Yernault, J. C. Comparison of computed density and microscopic morphometry in pulmonary emphysema. *American Journal of Respiratory and Critical Care Medicine*, 154(1):187–192, 1996.

[52] King, G. G., Muller, N. L., and Pare, P. D. Evaluation of airways in obstructive pulmonary disease using high-resolution computed tomography. *American Journal of Respiratory and Critical Care Medicine*, 159(3):992–1004, 1999.

[53] Denny, E. and Schroter, R. C. A mathematical model for the morphology of the pulmonary acinus. *Journal of Biomechanical Engineering*, 118(2):210–5, 1996.

[54] Kitaoka, H., Tamura, S., and Takaki, R. A three-dimensional model of the human pulmonary acinus. *Journal of Applied Physiology*, 88(6):2260–8, 2000.

[55] Tawhai, M. H., Pullan, A. J., and Hunter, P. J. Generation of an Anatomically Based Three-Dimensional Model of the Conducting Airways. *Annals of Biomedical Engineering*, 28(7):793–802, 2000.

[56] Yamamoto, T., Kubo, M., Kawata, Y., Niki, N., Matsui, E., Ohamatsu, H., and Moriyama, N. Visualization and quantitative analysis of lung microstructure using micro CT images. In *Medical Imaging 2004: Physiology, Function, and Structure from Medical Images*, volume 5369, pages 431–438, 2004.

[57] Xiao, L., Sera, T., Koshiyama, K., and Wada, S. A semiautomatic segmentation algorithm for extracting the complete structure of acini from synchrotron micro-CT images. *Computational and Mathematical Methods in Medicine*, 2013:575086, 2013.

[58] Litzlbauer, H. D., Korbel, K., Kline, T. L., Jorgensen, S. M., Eaker, D. R., Bohle, R. M., Ritman, E. L., and Langheinrich, A. C. Synchrotron-based micro-CT imaging of the human lung acinus. *Anatomical Record*, 293(9):1607–14, 2010.

[59] Vasilescu, D. M., Gao, Z., Saha, P. K., Yin, L., Wang, G., Haefeli-Bleuer, B., Ochs, M., Weibel, E. R., and Hoffman, E. A. Assessment of morphometry of pulmonary acini in mouse lungs by nondestructive imaging using multiscale microcomputed tomography. *Proceedings of the National Academy of Sciences of the United States of America*, 109(42):17105–10, 2012.

[60] Vasilescu, D. M., Klinge, C., Knudsen, L., Yin, L., Wang, G., Weibel, E. R., Ochs, M., and Hoffman, E. A. Stereological assessment of mouse lung parenchyma via nondestructive, multiscale micro-CT imaging validated by light microscopic histology. *Journal of Applied Physiology*, 114(6):716–24, 2013.

[61] De Langhe, E., Vande Velde, G., Hostens, J., Himmelreich, U., Nemery, B., Luyten, F. P., Vanoirbeek, J., and Lories, R. J. Quantification of lung fibrosis and emphysema in mice using automated micro-computed tomography. *PLoS ONE*, 7(8):e43123, 2012.

[62] Parameswaran, H., Bartolak-Suki, E., Hamakawa, H., Majumdar, A., Allen, P. G., and Suki, B. Three-dimensional measurement of alveolar airspace volumes in normal and emphysematous lungs using micro-CT. *Journal of Applied Physiology*, 107(2):583–92, 2009.

[63] Kampschulte, M., Schneider, C. R., Litzlbauer, H. D., Tscholl, D., Schneider, C., Zeiner, C., Krombach, G. A., Ritman, E. L., Bohle, R. M., and Langheinrich, A. C. Quantitative 3D micro-CT imaging of human lung tissue. *Fortschr Rontgenstr*, 185(9):869–76, 2013.

[64] Watz, H., Breithecker, A., Rau, W. S., and Kriete, A. Micro-CT of the human lung: imaging of alveoli and virtual endoscopy of an alveolar duct in a normal lung and in a lung with centrilobular emphysema–initial observations. *Radiology*, 236(3):1053–8, 2005.

[65] Mai, C., Verleden, S. E., McDonough, J. E., Willems, S., De Wever, W., Coolen, J., Dubbeldam, A., Van Raemdonck, D. E., Verbeken, E. K., Verleden, G. M., Hogg, J. C., Vanaudenaerde, B. M., Wuyts, W. A., and Verschakelen, J. A. Thin-Section CT Features of Idiopathic Pulmonary Fibrosis Correlated with Micro-CT and Histologic Analysis. *Radiology*, 283(1):252–263, 2017.

[66] McDonough, J. E., Yuan, R., Suzuki, M., Seyednejad, N., Elliott, W. M., Sanchez, P. G., Wright, A. C., Gefter, W. B., Litzky, L., Coxson, H. O., Pare, P. D., Sin, D. D., Pierce, R. A., Woods, J. C., McWilliams, A. M., Mayo, J. R., Lam, S. C., Cooper, J. D., and Hogg, J. C. Small-airway obstruction and emphysema in chronic obstructive pulmonary disease. *New England Journal of Medicine*, 365(17): 1567–75, 2011.

[67] Hogg, J. C., McDonough, J. E., and Suzuki, M. Small Airway Obstruction in COPD. *Chest*, 143(5): 1436–1443, 2013.

[68] Tanabe, N., Vasilescu, D. M., McDonough, J. E., Kinose, D., Suzuki, M., Cooper, J. D., Pare, P. D., and Hogg, J. C. Micro-Computed Tomography Comparison of Preterminal Bronchioles in Centrilobular and Panlobular Emphysema. *American Journal of Respiratory and Critical Care Medicine*, 195(5):630–638, 2017.

[69] Boon, M., Verleden, S. E., Bosch, B., Lammertyn, E. J., McDonough, J. E., Mai, C., Verschakelen, J., Kemner-van de Corput, M., Tiddens, H. A., Proesmans, M., Vermeulen, F. L., Verbeken, E. K., Cooper, J., Van Raemdonck, D. E., Decramer, M., Verleden, G. M., Hogg, J. C., Dupont, L. J., Vanaudenaerde, B. M., and De Boeck, K. Morphometric Analysis of Explant Lungs in Cystic Fibrosis. *American Journal of Respiratory and Critical Care Medicine*, 193(5):516–26, 2016.

[70] Namati, E., Chon, D., Thiesse, J., Hoffman, E. A., de Ryk, J., Ross, A., and McLennan, G. In vivo micro-CT lung imaging via a computer-controlled intermittent iso-pressure breath hold (IIBH) technique. *Physics in Medicine and Biology*, 51(23):6061–75, 2006.

[71] Damadian, R. Tumor detection by nuclear magnetic resonance. *Science*, 171(3976):1151–3, 1971.

[72] Wild, J. M., Marshall, H., Bock, M., Schad, L. R., Jakob, P. M., Puderbach, M., Molinari, F., Van Beek, E. J., and Biederer, J. MRI of the lung (1/3): methods. *Insights Imaging*, 3(4):345–53, 2012.

[73] Hatabu, H., Alsop, D. C., Listerud, J., Bonnet, M., and Gefter, W. B. T2* and proton density measurement of normal human lung parenchyma using submillisecond echo time gradient echo magnetic resonance imaging. *European Journal of Radiology*, 29(3):245–252, 1999.

[74] Yu, J., Xue, Y., and Song, H. K. Comparison of lung T2* during free-breathing at 1.5 T and 3.0 T with ultrashort echo time imaging. *Magnetic Resonance in Medicine*, 66(1):248–54, 2011.

[75] Holverda, S., Theilmann, R. J., Sa, R. C., Arai, T. J., Hall, E. T., Dubowitz, D. J., Prisk, G. K., and Hopkins, S. R. Measuring lung water: ex vivo validation of multi-image gradient echo MRI. *Journal of Magnetic Resonance Imaging*, 34(1):220–4, 2011.

[76] Hopkins, S. R., Henderson, A. C., Levin, D. L., Yamada, K., Arai, T., Buxton, R. B., and Prisk, G. K. Vertical gradients in regional lung density and perfusion in the supine human lung: the Slinky effect. *Journal of Applied Physiology*, 103(1):240–8, 2007.

[77] Marshall, H. R., Prato, F. S., Deans, L., Theberge, J., Thompson, R. T., and Stodilka, R. Z. Variable lung density consideration in attenuation correction of whole-body PET/MRI. *Journal of Nuclear Medicine*, 53(6):977–84, 2012.

[78] Theilmann, R. J., Arai, T. J., Samiee, A., Dubowitz, D. J., Hopkins, S. R., Buxton, R. B., and Prisk, G. K. Quantitative MRI measurement of lung density must account for the change in T(2) (*) with lung inflation. *Journal of Magnetic Resonance Imaging*, 30(3):527–34, 2009.

[79] Zhang, W. J., Hubbard Cristinacce, P. L., Bondesson, E., Nordenmark, L. H., Young, S. S., Liu, Y. Z., Singh, D., Naish, J. H., and Parker, G. J. MR Quantitative Equilibrium Signal Mapping: A Reliable Alternative to CT in the Assessment of Emphysema in Patients with Chronic Obstructive Pulmonary Disease. *Radiology*, 275(2):579–88, 2015.

[80] Johnson, K. M., Fain, S. B., Schiebler, M. L., and Nagle, S. Optimized 3D ultrashort echo time pulmonary MRI. *Magnetic Resonance in Medicine*, 70(5):1241–50, 2013.

[81] Bergin, C. J., Pauly, J. M., and Macovski, A. Lung parenchyma: projection reconstruction MR imaging. *Radiology*, 179(3):777–81, 1991.

[82] Robson, M. D., Gatehouse, P. D., Bydder, M., and Bydder, G. M. Magnetic resonance: an introduction to ultrashort TE (UTE) imaging. *Journal of Computer Assisted Tomography*, 27(6):825–46, 2003.

[83] Lederlin, M. and Cremillieux, Y. Three-dimensional assessment of lung tissue density using a clinical ultrashort echo time at 3 tesla: A feasibility study in healthy subjects. *Journal of Magnetic Resonance Imaging*, 40(4):839–47, 2014.

[84] Ohno, Y., Koyama, H., Yoshikawa, T., Matsumoto, K., Takahashi, M., Van Cauteren, M., and Sugimura, K. T2* measurements of 3-T MRI with ultrashort TEs: capabilities of pulmonary function assessment and clinical stage classification in smokers. *AJR: American Journal of Roentgenology*, 197(2):W279–85, 2011.

[85] Ma, W., Sheikh, K., Svenningsen, S., Pike, D., Guo, F., Etemad-Rezai, R., Leipsic, J., Coxson, H. O., McCormack, D. G., and Parraga, G. Ultra-short echo-time pulmonary MRI: evaluation and reproducibility in COPD subjects with and without bronchiectasis. *Journal of Magnetic Resonance Imaging*, 41(5):1465–74, 2015.

[86] Higano, N. S., Hahn, A. D., Tkach, J. A., Cao, X., Walkup, L. L., Thomen, R. P., Merhar, S. L., Kingma, P. S., Fain, S. B., and Woods, J. C. Retrospective respiratory self-gating and removal of bulk motion in pulmonary UTE MRI of neonates and adults. *Magnetic Resonance in Medicine*, 77(3):1284–1295, 2017.

[87] Higano, N. S., Fleck, R. J., Spielberg, D. R., Walkup, L. L., Hahn, A. D., Thomen, R. P., Merhar, S. L., Kingma, P. S., Tkach, J. A., Fain, S. B., and Woods, J. C. Quantification of neonatal lung parenchymal density via ultrashort echo time MRI with comparison to CT. *Journal of Magnetic Resonance Imaging*, 2017.

[88] Kauczor, H. U., Surkau, R., and Roberts, T. MRI using hyperpolarized noble gases. *European Radiology*, 8(5):820–827, 1998.

[89] Chen, X. J., Moller, H. E., Chawla, M. S., Cofer, G. P., Driehuys, B., Hedlund, L. W., and Johnson, G. A. Spatially resolved measurements of hyperpolarized gas properties in the lung in vivo. Part I: diffusion coefficient. *Magnetic Resonance in Medicine*, 42(4):721–8, 1999.

[90] Mugler III, J. P., Brookeman, J. R., Knight-Scott, J., Maier, T., de Lange, E. E., and Bogorad, P. L. Regional Measurement of the 3He Diffusion Coefficient in the Human Lung. In *Proceedings of the International Society of Magnetic Resonance in Medicine*, volume 6, page 1906, 1998.

[91] Saam, B., Yablonskiy, D., Kodibagkar, V., Leawoods, J., Gierada, D., Cooper, J., Lefrak, S., and Conradi, M. MR imaging of diffusion of 3He gas in healthy and diseased lungs. *Magnetic Resonance in Medicine*, 44(2):174–179, 2000.

[92] Salerno, M., de Lange, E. E., Altes, T. A., Truwit, J. D., Brookeman, J. R., and Mugler, r., J. P. Emphysema: hyperpolarized helium 3 diffusion MR imaging of the lungs compared with spirometric indexes–initial experience. *Radiology*, 222(1):252–60, 2002.

[93] Diaz, S., Casselbrant, I., Piitulainen, E., Magnusson, P., Peterson, B., Wollmer, P., Leander, P., Ekberg, O., and Akeson, P. Validity of apparent diffusion coefficient hyperpolarized 3He-MRI using MSCT and pulmonary function tests as references. *European Journal of Radiology*, 71(2):257–63, 2009.

[94] Fain, S. B., Panth, S. R., Evans, M. D., Wentland, A. L., Holmes, J. H., Korosec, F. R., O'Brien, M. J., Fountaine, H., and Grist, T. M. Early emphysematous changes in asymptomatic smokers: detection with 3He MR imaging. *Radiology*, 239(3):875–83, 2006.

[95] van Beek, E. J., Dahmen, A. M., Stavngaard, T., Gast, K. K., Heussel, C. P., Krummenauer, F., Schmiedeskamp, J., Wild, J. M., Sogaard, L. V., Morbach, A. E., Schreiber, L. M., and Kauczor, H. U. Hyperpolarised 3He MRI versus HRCT in COPD and normal volunteers: PHIL trial. *European Respiratory Journal*, 34(6):1311–21, 2009.

[96] Woods, J. C., Choong, C. K., Yablonskiy, D. A., Bentley, J., Wong, J., Pierce, J. A., Cooper, J. D., Macklem, P. T., Conradi, M. S., and Hogg, J. C. Hyperpolarized 3He diffusion MRI and histology in pulmonary emphysema. *Magnetic Resonance in Medicine*, 56(6):1293–300, 2006.

[97] Gierada, D. S., Woods, J. C., Bierhals, A. J., Bartel, S. T., Ritter, J. H., Choong, C. K., Das, N. A., Hong, C., Pilgram, T. K., Chang, Y. V., Jacob, R. E., Hogg, J. C., Battafarano, R. J., Cooper, J. D., Meyers, B. F., Patterson, G. A., Yablonskiy, D. A., and Conradi, M. S. Effects of diffusion time on short-range hyperpolarized (3)He diffusivity measurements in emphysema. *Journal of Magnetic Resonance Imaging*, 30(4):801–8, 2009.

[98] Swift, A. J., Wild, J. M., Fichele, S., Woodhouse, N., Fleming, S., Waterhouse, J., Lawson, R. A., Paley, M. N., and Van Beek, E. J. Emphysematous changes and normal variation in smokers and COPD patients using diffusion 3He MRI. *European Journal of Radiology*, 54(3):352–8, 2005.

[99] Kirby, M., Heydarian, M., Wheatley, A., McCormack, D. G., and Parraga, G. Evaluating bronchodilator effects in chronic obstructive pulmonary disease using diffusion-weighted hyperpolarized helium-3 magnetic resonance imaging. *Journal of Applied Physiology*, 112(4):651–7, 2012.

[100] Fichele, S., Woodhouse, N., Swift, A. J., Said, Z., Paley, M. N., Kasuboski, L., Mills, G. H., van Beek, E. J., and Wild, J. M. MRI of helium-3 gas in healthy lungs: posture related variations of alveolar size. *Journal of Magnetic Resonance Imaging*, 20(2):331–5, 2004.

[101] Altes, T. A., Mata, J., de Lange, E. E., Brookeman, J. R., and Mugler, r., J. P. Assessment of lung development using hyperpolarized helium-3 diffusion MR imaging. *Journal of Magnetic Resonance Imaging*, 24(6):1277–83, 2006.

[102] Fain, S. B., Altes, T. A., Panth, S. R., Evans, M. D., Waters, B., Mugler Iii, J. P., Korosec, F. R., Grist, T. M., Silverman, M., Salerno, M., and Owers-Bradley, J. Detection of Age-Dependent Changes in Healthy Adult Lungs With Diffusion-Weighted 3He MRI. *Academic Radiology*, 12(11):1385–1393, 2005.

[103] Diaz, S., Casselbrant, I., Piitulainen, E., Pettersson, G., Magnusson, P., Peterson, B., Wollmer, P., Leander, P., Ekberg, O., and Akeson, P. Hyperpolarized 3He apparent diffusion coefficient MRI of the lung: reproducibility and volume dependency in healthy volunteers and patients with emphysema. *Journal of Magnetic Resonance Imaging*, 27(4):763–70, 2008.

[104] Parra-Robles, J., Ajraoui, S., Marshall, H., Deppe, M. H., Xu, X., and Wild, J. M. The influence of field strength on the apparent diffusion coefficient of 3He gas in human lungs. *Magnetic Resonance in Medicine*, 67(2):322–5, 2012.

[105] Halaweish, A. F., Hoffman, E. A., Thedens, D. R., Fuld, M. K., Sieren, J. P., and van Beek, E. J. Effect of lung inflation level on hyperpolarized 3He apparent diffusion coefficient measurements in never-smokers. *Radiology*, 268(2):572–80, 2013.

[106] Wang, C., Altes, T. A., Mugler, r., J. P., Miller, G. W., Ruppert, K., Mata, J. F., Cates, J., G. D., Borish, L., and de Lange, E. E. Assessment of the lung microstructure in patients with asthma using hyperpolarized 3He diffusion MRI at two time scales: comparison with healthy subjects and patients with COPD. *Journal of Magnetic Resonance Imaging*, 28(1):80–8, 2008.

[107] Mathew, L., Gaede, S., Wheatley, A., Etemad-Rezai, R., Rodrigues, G. B., and Parraga, G. Detection of longitudinal lung structural and functional changes after diagnosis of radiation-induced lung injury using hyperpolarized He3 magnetic resonance imaging. *Medical Physics*, 37(1):22–31, 2010.

[108] Bink, A., Hanisch, G., Karg, A., Vogel, A., Katsaros, K., Mayer, E., Gast, K. K., and Kauczor, H. U. Clinical aspects of the apparent diffusion coefficient in 3He MRI: results in healthy volunteers and patients after lung transplantation. *Journal of Magnetic Resonance Imaging*, 25(6):1152–8, 2007.

[109] Wild, J. M., Stewart, N. J., and Chan, H. F. Hyperpolarised Helium-3 (3He) MRI: Physical Methods for Imaging Human Lung Function. In *Medical Radiology*, pages 1–29. Springer Berlin Heidelberg, Berlin, Heidelberg, 2017.

[110] Shea, D. A. and Morgan, D. The helium-3 shortage: Supply, demand, and options for Congress. In *Congressional Research Service*, 2010.

[111] Mugler III, J. P., Mata, J. F., Wang, H.-T. J., Tobias, W. A., Cates, G. D., Christopher, J. M., Missel, J. L., Reish, A. G., Ruppert, K., Brookeman, J. R., and Hagspiel, K. D. The Apparent Diffusion Coefficient of Xe-129 in the Lung: Preliminary Human Results. In *Proceedings of the International Society of Magnetic Resonance in Medicine*, volume 11, page 769, 2004.

[112] Sindile, A., Muradian, I., Hrovat, M., Johnson, C., Hersman, F. W., and Patz, S. Human Pulmonary Diffusion Weighted Imaging at 0.2T with Hyperpolarized 129Xe. In *Proceedings of the International Society of Magnetic Resonance in Medicine*, volume 15, page 1290, 2007.

[113] Kaushik, S. S., Cleveland, Z. I., Cofer, G. P., Metz, G., Beaver, D., Nouls, J., Kraft, M., Auffermann, W., Wolber, J., McAdams, H. P., and Driehuys, B. Diffusion-weighted hyperpolarized 129Xe MRI in healthy volunteers and subjects with chronic obstructive pulmonary disease. *Magnetic Resonance in Medicine*, 65(4):1154–65, 2011.

[114] Matin, T. N., Rahman, N., Nickol, A. H., Chen, M., Xu, X., Stewart, N. J., Doel, T., Grau, V., Wild, J. M., and Gleeson, F. V. Chronic Obstructive Pulmonary Disease: Lobar Analysis with Hyperpolarized 129Xe MR Imaging. *Radiology*, 282(3):857–868, 2017.

[115] Thomen, R. P., Quirk, J. D., Roach, D., Egan-Rojas, T., Ruppert, K., Yusen, R. D., Altes, T. A., Yablonskiy, D. A., and Woods, J. C. Direct comparison of Xe diffusion measurements with quantitative histology in human lungs. *Magnetic Resonance in Medicine*, 77(1):265–272, 2017.

[116] Kirby, M., Ouriadov, A., Svenningsen, S., Owrangi, A., Wheatley, A., Etemad-Rezai, R., Santyr, G. E., McCormack, D. G., and Parraga, G. Hyperpolarized 3He and 129Xe magnetic resonance imaging apparent diffusion coefficients: physiological relevance in older never- and ex-smokers. *Physiological Reports*, 2(7), 2014.

[117] Kirby, M., Svenningsen, S., Owrangi, A., Wheatley, A., Farag, A., Ouriadov, A., Santyr, G. E., Etemad-Rezai, R., Coxson, H. O., McCormack, D. G., and Parraga, G. Hyperpolarized 3He and 129Xe MR imaging in healthy volunteers and patients with chronic obstructive pulmonary disease. *Radiology*, 265 (2):600–10, 2012.

[118] Stewart, N. J., Chan, H. F., Collier, G. J., Horn, F. C., Norquay, G., Parra-Robles, J., Yates, D. P., Collini, P., Lawson, R., Marshall, H., and Wild, J. M. Comparison of 3He and 129Xe MRI for Evaluation of Lung Microstructure and Ventilation in Healthy Volunteers and COPD Patients at 1.5 T. In *Proceedings of the International Society of Magnetic Resonance in Medicine*, volume 24, 2016.

[119] Deppe, M. H., Parra-Robles, J., Ajraoui, S., Parnell, S. R., Clemence, M., Schulte, R. F., and Wild, J. M. Susceptibility effects in hyperpolarized (3)He lung MRI at 1.5T and 3T. *Journal of Magnetic Resonance Imaging*, 30(2):418–23, 2009.

[120] Xu, X., Norquay, G., Parnell, S. R., Deppe, M. H., Ajraoui, S., Hashoian, R., Marshall, H., Griffiths, P. D., Parra-Robles, J., and Wild, J. M. Hyperpolarized 129Xe gas lung MRI-SNR and T2* comparisons at 1.5 T and 3 T. *Magnetic Resonance in Medicine*, 68(6):1900–4, 2012.

[121] Saam, B., Happer, W., and Middleton, H. Nuclear relaxation of 3He in the presence of O2. *Physical Review A*, 52(1):862–865, 1995.

[122] Owers-Bradley, J. R., Fichele, S., Bennattayalah, A., McGloin, C. J., Bowtell, R. W., Morgan, P. S., and Moody, A. R. MR tagging of human lungs using hyperpolarized 3He gas. *Journal of Magnetic Resonance Imaging*, 17(1):142–6, 2003.

[123] Woods, J. C., Yablonskiy, D. A., Choong, C. K., Chino, K., Pierce, J. A., Hogg, J. C., Bentley, J., Cooper, J. D., Conradi, M. S., and Macklem, P. T. Long-range diffusion of hyperpolarized 3He in explanted normal and emphysematous human lungs via magnetization tagging. *Journal of Applied Physiology*, 99(5):1992–7, 2005.

[124] Fichele, S., Paley, M. N., Woodhouse, N., Griffiths, P. D., van Beek, E. J., and Wild, J. M. Measurements and modeling of long range 3He diffusion in the lung using a "slice-washout" method. *Journal of Magnetic Resonance*, 174(1):28–33, 2005.

[125] Wang, C., Miller, G. W., Altes, T. A., de Lange, E. E., Cates, J., G. D., and Mugler, r., J. P. Time dependence of 3He diffusion in the human lung: measurement in the long-time regime using stimulated echoes. *Magnetic Resonance in Medicine*, 56(2):296–309, 2006.

[126] Wang, C., Altes, T. A., Mugler, r., J. P., De Lange, E. E., Ruppert, K., Hersman, W. F., Dregely, I. M., Ruset, I., Ketel, S., and Verbanck, S. Long-Time-Scale Hyperpolarized 3He and 129Xe Diffusion in Human Lungs: Experimental Measurements and Computer Simulation. In *Proceedings of the International Society of Magnetic Resonance in Medicine*, volume 18, page 2541, 2010.

[127] Conradi, M. S., Yablonskiy, D. A., Woods, J. C., Gierada, D. S., Bartel, S. E., Haywood, S. E., and Menard, C. The role of collateral paths in long-range diffusion of 3He in lungs. *Academic Radiology*, 15 (6):675–82, 2008.

[128] Sukstanskii, A. L. and Yablonskiy, D. A. In vivo lung morphometry with hyperpolarized 3He diffusion MRI: theoretical background. *Journal of Magnetic Resonance*, 190(2):200–10, 2008.

[129] Parra-Robles, J., Marshall, H., Hartley, R., Brightling, C. E., and Wild, J. Quantification of Lung Microstructure in Asthma Using a 3He Fractional Diffusion Approach. In *Proceedings of the International Society of Magnetic Resonance in Medicine*, volume 22, page 3529, 2014.

[130] Shanbhag, D. D., Altes, T. A., Miller, G. W., Mata, J. F., and Knight-Scott, J. q-Space analysis of lung morphometry in vivo with hyperpolarized 3He spectroscopy. *Journal of Magnetic Resonance Imaging*, 24(1):84–94, 2006.

[131] Quirk, J. D., Lutey, B. A., Gierada, D. S., Woods, J. C., Senior, R. M., Lefrak, S. S., Sukstanskii, A. L., Conradi, M. S., and Yablonskiy, D. A. In vivo detection of acinar microstructural changes in early emphysema with (3)He lung morphometry. *Radiology*, 260(3):866–74, 2011.

[132] Paulin, G. A., Svenningsen, S., Jobse, B. N., Mohan, S., Kirby, M., Lewis, J. F., and Parraga, G. Differences in hyperpolarized (3) He ventilation imaging after 4 years in adults with cystic fibrosis. *Journal of Magnetic Resonance Imaging*, 41(6):1701–7, 2015.

[133] Quirk, J. D., Sukstanskii, A. L., Woods, J. C., Lutey, B. A., Conradi, M. S., Gierada, D. S., Yusen, R. D., Castro, M., and Yablonskiy, D. A. Experimental evidence of age-related adaptive changes in human acinar airways. *Journal of Applied Physiology*, 120(2):159–65, 2016.

[134] Hajari, A. J., Yablonskiy, D. A., Sukstanskii, A. L., Quirk, J. D., Conradi, M. S., and Woods, J. C. Morphometric changes in the human pulmonary acinus during inflation. *Journal of Applied Physiology*, 112(6):937–43, 2012.

[135] Butler, J. P., Loring, S. H., Patz, S., Tsuda, A., Yablonskiy, D. A., and Mentzer, S. J. Evidence for adult lung growth in humans. *New England Journal of Medicine*, 367(3):244–7, 2012.

[136] Sukstanskii, A. L. and Yablonskiy, D. A. Lung morphometry with hyperpolarized 129Xe: theoretical background. *Magnetic Resonance in Medicine*, 67(3):856–66, 2012.

[137] Ruppert, K., Quirk, J. D., III, J. P. M., Altes, T. A., Wang, C., Miller, G. W., Ruset, I. C., Mata, J. F., Hersman, F. W., and Yablonskiy, D. A. Lung morphometry using hyperpolarized xenon-129: preliminary experience. In *Proceedings of the International Society of Magnetic Resonance in Medicine*, volume 20, page 3152, 2012.

[138] Ouriadov, A., Farag, A., Kirby, M., McCormack, D. G., Parraga, G., and Santyr, G. E. Lung morphometry using hyperpolarized (129) Xe apparent diffusion coefficient anisotropy in chronic obstructive pulmonary disease. *Magnetic Resonance in Medicine*, 70(6):1699–706, 2013.

[139] Ouriadov, A., Farag, A., Kirby, M., McCormack, D. G., Parraga, G., and Santyr, G. E. Pulmonary hyperpolarized Xe morphometry for mapping xenon gas concentrations and alveolar oxygen partial pressure: Proof-of-concept demonstration in healthy and COPD subjects. *Magnetic Resonance in Medicine*, 74(6):1726–1732, 2015.

[140] Parra-Robles, J., Ajraoui, S., and Wild, J. Modelling Non-Gaussian 3He Diffusion Signal Behaviour Using a Fractional Dynamics Approach. In *Proceedings of the International Society of Magnetic Resonance in Medicine*, volume 18, page 2538, 2010.

[141] Parra-Robles, J., Marshall, H., and Wild, J. M. Characterization of 3He Diffusion in Lungs Using a Stretched Exponential Model. In *Proceedings of the International Society of Magnetic Resonance in Medicine*, volume 21, page 820, 2013.

[142] Callaghan, P. T., Eccles, C. D., and Xia, Y. NMR microscopy of dynamic displacements: k-space and q-space imaging. *Journal of Physics E: Scientific Instruments*, 21(8):820–822, 1988.

[143] Narayanan, M., Owers-Bradley, J., Beardsmore, C. S., Mada, M., Ball, I., Garipov, R., Panesar, K. S., Kuehni, C. E., Spycher, B. D., Williams, S. E., and Silverman, M. Alveolarization continues during childhood and adolescence: new evidence from helium-3 magnetic resonance. *American Journal of Respiratory and Critical Care Medicine*, 185(2):186–91, 2012.

[144] Narayanan, M., Beardsmore, C. S., Owers-Bradley, J., Dogaru, C. M., Mada, M., Ball, I., Garipov, R. R., Kuehni, C. E., Spycher, B. D., and Silverman, M. Catch-up alveolarization in ex-preterm children: evidence from (3)He magnetic resonance. *American Journal of Respiratory and Critical Care Medicine*, 187(10):1104–9, 2013.

[145] O'Halloran, R. L., Holmes, J. H., Wu, Y. C., Alexander, A., and Fain, S. B. Helium-3 MR q-space imaging with radial acquisition and iterative highly constrained back-projection. *Magnetic Resonance in Medicine*, 63(1):41–50, 2010.

[146] Abragam, A. *The principles of nuclear magnetism.* Oxford university press, 1961.

[147] Callaghan, P. T. *Principles of nuclear magnetic resonance microscopy.* Oxford University Press on Demand, 1993.

[148] Haacke, E., Brown, R., Thompson, M., and Venkatesan, R. *Magnetic Resonance Imaging: Physical Principles and Sequence Design.* Wiley, 1999.

[149] Bernstein, M., King, K., and Zhou, X. *Handbook of MRI Pulse Sequences.* Elsevier Science, 2004.

[150] McRobbie, D. W., Moore, E. A., Graves, M. J., and Prince, M. R. *MRI from Picture to Proton.* Cambridge University Press, 2006.

[151] Rabi, I. I., Zacharias, J. R., Millman, S., and Kusch, P. A New Method of Measuring Nuclear Magnetic Moment. *Physical Review*, 53(4):318–318, 1938.

[152] Bloch, F. Nuclear Induction. *Physical Review*, 70(7-8):460–474, 1946.

[153] Purcell, E. M., Torrey, H. C., and Pound, R. V. Resonance Absorption by Nuclear Magnetic Moments in a Solid. *Physical Review*, 69(1-2):37–38, 1946.

[154] Lauterbur, P. C. Image Formation by Induced Local Interactions: Examples Employing Nuclear Magnetic Resonance. *Nature*, 242:190, 1973.

[155] Mansfield, P. and Grannell, P. K. "Diffraction" and microscopy in solids and liquids by NMR. *Physical Review B*, 12(9):3618–3634, 1975.

[156] Moller, H. E., Chen, X. J., Saam, B., Hagspiel, K. D., Johnson, G. A., Altes, T. A., de Lange, E. E., and Kauczor, H. U. MRI of the lungs using hyperpolarized noble gases. *Magnetic Resonance in Medicine*, 47 (6):1029–51, 2002.

[157] Miller, K. W., Reo, N. V., Schoot Uiterkamp, A. J., Stengle, D. P., Stengle, T. R., and Williamson, K. L. Xenon NMR: chemical shifts of a general anesthetic in common solvents, proteins, and membranes. *Proceedings of the National Academy of Sciences of the United States of America*, 78(8):4946–9, 1981.

[158] Seydoux, R., Diehl, P., Mazitov, R. K., and Jokisaari, J. Chemical-Shifts in Magnetic-Resonance of the 3He Nucleus in Liquid Solvents and Comparison with Other Noble Gases. *Journal of Magnetic Resonance, Series A*, 101(1):78–83, 1993.

[159] Wang, J. H. Self-Diffusion Coefficients of Water. *The Journal of Physical Chemistry*, 69(12):4412–4412, 1965.

[160] Weathersby, P. K. and Homer, L. D. Solubility of inert gases in biological fluids and tissues: a review. *Undersea Biomedical Research*, 7(4):277–96, 1980.

[161] Oros, A. M. and Shah, N. J. Hyperpolarized xenon in NMR and MRI. *Physics in Medicine & Biology*, 49(20):R105, 2004.

[162] Walker, T. G. and Happer, W. Spin-exchange optical pumping of noble-gas nuclei. *Reviews of Modern Physics*, 69(2):629–642, 1997.

[163] Colegrove, F. D., Schearer, L. D., and Walters, G. K. Polarization of 3He Gas by Optical Pumping. *Physical Review*, 132(6):2561–2572, 1963.

[164] Goodson, B. M. Nuclear magnetic resonance of laser-polarized noble gases in molecules, materials, and organisms. *Journal of Magnetic Resonance*, 155(2):157–216, 2002.

[165] Babcock, E., Nelson, I., Kadlecek, S., Driehuys, B., Anderson, L. W., Hersman, F. W., and Walker, T. G. Hybrid spin-exchange optical pumping of 3He. *Physical Review Letters*, 91(12):123003, 2003.

[166] Driehuys, B., Cates, G. D., Miron, E., Sauer, K., Walter, D. K., and Happer, W. High-volume production of laser-polarized 129Xe. *Applied Physics Letters*, 69(12):1668–1670, 1996.

[167] Norquay, G., Parnell, S. R., Xu, X., Parra-Robles, J., and Wild, J. M. Optimized production of hyperpolarized 129Xe at 2 bars for in vivo lung magnetic resonance imaging. *Journal of Applied Physics*, 113(4):044908, 2013.

[168] Mooney, K., Miller, G., Dolph, P., Tobias, W., Nelyubin, V., Singh, J., III, J. M., and Cates, G. A 3-liter capacity, hybrid spin-exchange 3He polarizer for medical imaging. In *Proceedings of the International Society of Magnetic Resonance in Medicine*, volume 17, page 2166, 2009.

[169] He, M., Robertson, S. H., Kaushik, S. S., Freeman, M. S., Virgincar, R. S., Davies, J., Stiles, J., Foster, W. M., McAdams, H. P., and Driehuys, B. Dose and pulse sequence considerations for hyperpolarized (129)Xe ventilation MRI. *Magnetic Resonance Imaging*, 33(7):877–85, 2015.

[170] Norquay, G., Collier, G. J., Rao, M., Maunder, A., Rodgers, O. I., Stewart, N. J., and Wild, J. M. Large-scale production of highly-polarized 129Xe. In *Proceedings of the International Society of Magnetic Resonance in Medicine*, volume 25, page 2140, 2017.

[171] Bidinosti, C. P., Choukeife, J., Tastevin, G., Vignaud, A., and Nacher, P. J. MRI of the lung using hyperpolarized 3He at very low magnetic field (3 mT). *Magnetic Resonance Materials in Physics, Biology and Medicine*, 16(6):255–8, 2004.

[172] Parraga, G., Ouriadov, A., Evans, A., McKay, S., Lam, W. W., Fenster, A., Etemad-Rezai, R., McCormack, D., and Santyr, G. Hyperpolarized 3He ventilation defects and apparent diffusion coefficients in chronic obstructive pulmonary disease: preliminary results at 3.0 Tesla. *Investigative Radiology*, 42 (6):384–91, 2007.

[173] De Zanche, N., Chhina, N., Teh, K., Randell, C., Pruessmann, K. P., and Wild, J. M. Asymmetric quadrature split birdcage coil for hyperpolarized 3He lung MRI at 1.5T. *Magnetic Resonance in Medicine*, 60(2):431–438, 2008.

[174] Deppe, M. H., Parra-Robles, J., Marshall, H., Lanz, T., and Wild, J. M. A flexible 32-channel receive array combined with a homogeneous transmit coil for human lung imaging with hyperpolarized 3He at 1.5 T. *Magnetic Resonance in Medicine*, 66(6):1788–97, 2011.

[175] Wild, J. M., Paley, M. N., Viallon, M., Schreiber, W. G., van Beek, E. J., and Griffiths, P. D. k-space filtering in 2D gradient-echo breath-hold hyperpolarized 3He MRI: spatial resolution and signal-to-noise ratio considerations. *Magnetic Resonance in Medicine*, 47(4):687–95, 2002.

[176] Zhao, L., Mulkern, R., Tseng, C. H., Williamson, D., Patz, S., Kraft, R., Walsworth, R. L., Jolesz, F. A., and Albert, M. S. Gradient-Echo Imaging Considerations for Hyperpolarized 129Xe MR. *Journal of Magnetic Resonance. Series B*, 113(2):179–83, 1996.

[177] Wild, J. M., Teh, K., Woodhouse, N., Paley, M. N., Fichele, S., de Zanche, N., and Kasuboski, L. Steady-state free precession with hyperpolarized 3He: experiments and theory. *Journal of Magnetic Resonance*, 183(1):13–24, 2006.

[178] Mugler III, J. P. and Altes, T. A. Hyperpolarized 129Xe MRI of the human lung. *Journal of Magnetic Resonance Imaging*, 37(2):313–31, 2013.

[179] Ruppert, K. Biomedical imaging with hyperpolarized noble gases. *Reports on Progress in Physics*, 77 (11):116701, 2014.

[180] Woodhouse, N., Wild, J. M., Paley, M. N., Fichele, S., Said, Z., Swift, A. J., and van Beek, E. J. Combined helium-3/proton magnetic resonance imaging measurement of ventilated lung volumes in smokers compared to never-smokers. *Journal of Magnetic Resonance Imaging*, 21(4):365–9, 2005.

[181] Horn, F. C., Tahir, B. A., Stewart, N. J., Collier, G. J., Norquay, G., Leung, G., Ireland, R. H., Parra-Robles, J., Marshall, H., and Wild, J. M. Lung ventilation volumetry with same-breath acquisition of hyperpolarized gas and proton MRI. *NMR in Biomedicine*, 27(12):1461–7, 2014.

[182] Mathew, L., Evans, A., Ouriadov, A., Etemad-Rezai, R., Fogel, R., Santyr, G., McCormack, D. G., and Parraga, G. Hyperpolarized 3He magnetic resonance imaging of chronic obstructive pulmonary disease: reproducibility at 3.0 tesla. *Academic Radiology*, 15(10):1298–311, 2008.

[183] Woodhouse, N., Wild, J. M., van Beek, E. J., Hoggard, N., Barker, N., and Taylor, C. J. Assessment of hyperpolarized 3He lung MRI for regional evaluation of interventional therapy: a pilot study in pediatric cystic fibrosis. *Journal of Magnetic Resonance Imaging*, 30(5):981–8, 2009.

[184] de Lange, E. E., Altes, T. A., Patrie, J. T., Gaare, J. D., Knake, J. J., Mugler, J. P., and Platts-Mills, T. A. Evaluation of Asthma With Hyperpolarized Helium-3 MRI: Correlation With Clinical Severity and Spirometry. *Chest*, 130(4):1055–1062, 2006.

[185] Kirby, M., Svenningsen, S., Ahmed, H., Wheatley, A., Etemad-Rezai, R., Paterson, N. A. M., and Parraga, G. Quantitative Evaluation of Hyperpolarized Helium-3 Magnetic Resonance Imaging of Lung Function Variability in Cystic Fibrosis. *Academic Radiology*, 18(8):1006–1013, 2011.

[186] Mathew, L., Kirby, M., Etemad-Rezai, R., Wheatley, A., McCormack, D. G., and Parraga, G. Hyperpolarized 3He magnetic resonance imaging: Preliminary evaluation of phenotyping potential in chronic obstructive pulmonary disease. *European Journal of Radiology*, 79(1):140–146, 2011.

[187] Kirby, M., Mathew, L., Heydarian, M., Etemad-Rezai, R., McCormack, D. G., and Parraga, G. Chronic obstructive pulmonary disease: quantification of bronchodilator effects by using hyperpolarized (3)He MR imaging. *Radiology*, 261(1):283–92, 2011.

[188] Kirby, M., Mathew, L., Wheatley, A., Santyr, G. E., McCormack, D. G., and Parraga, G. Chronic obstructive pulmonary disease: longitudinal hyperpolarized (3)He MR imaging. *Radiology*, 256(1):280–9, 2010.

[189] Smith, L., Marshall, H., Aldag, I., Horn, F., Collier, G., Hughes, D., West, N., Horsley, A., Taylor, C. J., and Wild, J. M. Longitudinal Assessment of Children with Mild CF Using Hyperpolarised Gas Lung MRI and LCI. *American Journal of Respiratory and Critical Care Medicine*, 2017.

[190] Tzeng, Y. S., Lutchen, K., and Albert, M. The difference in ventilation heterogeneity between asthmatic and healthy subjects quantified using hyperpolarized 3He MRI. *Journal of Applied Physiology*, 106(3): 813–22, 2009.

[191] Svenningsen, S., Kirby, M., Starr, D., Leary, D., Wheatley, A., Maksym, G. N., McCormack, D. G., and Parraga, G. Hyperpolarized (3) He and (129) Xe MRI: differences in asthma before bronchodilation. *Journal of Magnetic Resonance Imaging*, 38(6):1521–30, 2013.

[192] He, M., Driehuys, B., Que, L. G., and Huang, Y. T. Using Hyperpolarized 129Xe MRI to Quantify the Pulmonary Ventilation Distribution. *Academic Radiology*, 23(12):1521–1531, 2016.

[193] Kirby, M., Svenningsen, S., Kanhere, N., Owrangi, A., Wheatley, A., Coxson, H. O., Santyr, G. E., Paterson, N. A., McCormack, D. G., and Parraga, G. Pulmonary ventilation visualized using hyperpolarized helium-3 and xenon-129 magnetic resonance imaging: differences in COPD and relationship to emphysema. *Journal of Applied Physiology*, 114(6):707–15, 2013.

[194] Salerno, M., Altes, T. A., Brookeman, J. R., de Lange, E. E., and Mugler, r., J. P. Dynamic spiral MRI of pulmonary gas flow using hyperpolarized (3)He: preliminary studies in healthy and diseased lungs. *Magnetic Resonance in Medicine*, 46(4):667–77, 2001.

[195] Wild, J. M., Paley, M. N., Kasuboski, L., Swift, A., Fichele, S., Woodhouse, N., Griffiths, P. D., and van Beek, E. J. Dynamic radial projection MRI of inhaled hyperpolarized 3He gas. *Magnetic Resonance in Medicine*, 49(6):991–7, 2003.

[196] Koumellis, P., van Beek, E. J., Woodhouse, N., Fichele, S., Swift, A. J., Paley, M. N., Hill, C., Taylor, C. J., and Wild, J. M. Quantitative analysis of regional airways obstruction using dynamic hyperpolarized 3He MRI-preliminary results in children with cystic fibrosis. *Journal of Magnetic Resonance Imaging*, 22(3):420–6, 2005.

[197] de Rochefort, L., Maitre, X., Fodil, R., Vial, L., Louis, B., Isabey, D., Croce, C., Darrasse, L., Apiou, G., Caillibotte, G., Bittoun, J., and Durand, E. Phase-contrast velocimetry with hyperpolarized 3He for in vitro and in vivo characterization of airflow. *Magnetic Resonance in Medicine*, 55(6):1318–25, 2006.

[198] Collier, G. J. and Wild, J. M. In vivo measurement of gas flow in human airways with hyperpolarized gas MRI and compressed sensing. *Magnetic Resonance in Medicine*, 73(6):2255–61, 2015.

[199] Deninger, A. J., Mansson, S., Petersson, J. S., Pettersson, G., Magnusson, P., Svensson, J., Fridlund, B., Hansson, G., Erjefeldt, I., Wollmer, P., and Golman, K. Quantitative measurement of regional lung ventilation using 3He MRI. *Magnetic Resonance in Medicine*, 48(2):223–32, 2002.

[200] Horn, F. C., Deppe, M. H., Marshall, H., Parra-Robles, J., and Wild, J. M. Quantification of regional fractional ventilation in human subjects by measurement of hyperpolarized 3He washout with 2D and 3D MRI. *Journal of Applied Physiology*, 116(2):129–39, 2014.

[201] Hamedani, H., Kadlecek, S., Xin, Y., Siddiqui, S., Gatens, H., Naji, J., Ishii, M., Cereda, M., Rossman, M., and Rizi, R. A hybrid multibreath wash-in wash-out lung function quantification scheme in human subjects using hyperpolarized (3) He MRI for simultaneous assessment of specific ventilation, alveolar oxygen tension, oxygen uptake, and air trapping. *Magnetic Resonance in Medicine*, 78(2):611–624, 2017.

[202] Deninger, A. J., Eberle, B., Ebert, M., Grossmann, T., Heil, W., Kauczor, H., Lauer, L., Markstaller, K., Otten, E., Schmiedeskamp, J., Schreiber, W., Surkau, R., Thelen, M., and Weiler, N. Quantification of regional intrapulmonary oxygen partial pressure evolution during apnea by (3)He MRI. *Journal of Magnetic Resonance*, 141(2):207–16, 1999.

[203] Wild, J. M., Fichele, S., Woodhouse, N., Paley, M. N., Kasuboski, L., and van Beek, E. J. 3D volume-localized pO2 measurement in the human lung with 3He MRI. *Magnetic Resonance in Medicine*, 53(5): 1055–64, 2005.

[204] Marshall, H., Parra-Robles, J., Deppe, M. H., Lipson, D. A., Lawson, R., and Wild, J. M. (3)He pO2 mapping is limited by delayed-ventilation and diffusion in chronic obstructive pulmonary disease. *Magnetic Resonance in Medicine*, 71(3):1172–8, 2014.

[205] Patz, S., Hersman, F. W., Muradian, I., Hrovat, M. I., Ruset, I. C., Ketel, S., Jacobson, F., Topulos, G. P., Hatabu, H., and Butler, J. P. Hyperpolarized (129)Xe MRI: a viable functional lung imaging modality? *European Journal of Radiology*, 64(3):335–44, 2007.

[206] Jameson, C. J., Jameson, A. K., and Hwang, J. K. Nuclear spin relaxation by intermolecular magnetic dipole coupling in the gas phase.129Xe in oxygen. *The Journal of Chemical Physics*, 89(7):4074–4081, 1988.

[207] Tsai, C.-M. and Nishimura, D. G. Reduced aliasing artifacts using variable-densityk-space sampling trajectories. *Magnetic Resonance in Medicine*, 43(3):452–458, 2000.

[208] Greiser, A. and von Kienlin, M. Efficient k-space sampling by density-weighted phase-encoding. *Magnetic Resonance in Medicine*, 50(6):1266–75, 2003.

[209] Hu, X. and Parrish, T. Reduction of field of view for dynamic imaging. *Magnetic Resonance in Medicine*, 31(6):691–694, 1994.

[210] Scheffler, K. and Hennig, J. Reduced circular field-of-view imaging. *Magnetic Resonance in Medicine*, 40(3):474–480, 1998.

[211] Sodickson, D. K. and Manning, W. J. Simultaneous acquisition of spatial harmonics (SMASH): Fast imaging with radiofrequency coil arrays. *Magnetic Resonance in Medicine*, 38(4):591–603, 1997.

[212] Pruessmann, K. P., Weiger, M., Scheidegger, M. B., and Boesiger, P. SENSE: Sensitivity encoding for fast MRI. *Magnetic Resonance in Medicine*, 42(5):952–962, 1999.

[213] Griswold, M. A., Jakob, P. M., Heidemann, R. M., Nittka, M., Jellus, V., Wang, J., Kiefer, B., and Haase, A. Generalized autocalibrating partially parallel acquisitions (GRAPPA). *Magnetic Resonance in Medicine*, 47(6):1202–10, 2002.

[214] McGibney, G., Smith, M. R., Nichols, S. T., and Crawley, A. Quantitative evaluation of several partial fourier reconstruction algorithms used in mri. *Magnetic Resonance in Medicine*, 30(1):51–59, 1993.

[215] Korosec, F. R., Frayne, R., Grist, T. M., and Mistretta, C. A. Time-resolved contrast-enhanced 3D MR angiography. *Magnetic Resonance in Medicine*, 36(3):345–351, 1996.

[216] Madore, B., Glover, G. H., and Pelc, N. J. Unaliasing by Fourier-encoding the overlaps using the temporal dimension (UNFOLD), applied to cardiac imaging and fMRI. *Magnetic Resonance in Medicine*, 42(5):813–828, 1999.

[217] Tsao, J., Boesiger, P., and Pruessmann, K. P. k-t BLAST and k-t SENSE: Dynamic MRI with high frame rate exploiting spatiotemporal correlations. *Magnetic Resonance in Medicine*, 50(5):1031–1042, 2003.

[218] Noll, D. C., Nishimura, D. G., and Macovski, A. Homodyne detection in magnetic resonance imaging. *IEEE Transactions on Medical Imaging*, 10(2):154–63, 1991.

[219] Haacke, E. M., Lindskogj, E. D., and Lin, W. A fast, iterative, partial-fourier technique capable of local phase recovery. *Journal of Magnetic Resonance (1969)*, 92(1):126–145, 1991.

[220] Lee, R. F., Johnson, G., Grossman, R. I., Stoeckel, B., Trampel, R., and McGuinness, G. Advantages of parallel imaging in conjunction with hyperpolarized helium–a new approach to MRI of the lung. *Magnetic Resonance in Medicine*, 55(5):1132–41, 2006.

[221] Meise, F. M., Rivoire, J., Terekhov, M., Wiggins, G. C., Keil, B., Karpuk, S., Salhi, Z., Wald, L. L., and Schreiber, L. M. Design and evaluation of a 32-channel phased-array coil for lung imaging with hyperpolarized 3-helium. *Magnetic Resonance in Medicine*, 63(2):456–64, 2010.

[222] Taubman, D. S. and Marcellin, M. W. *JPEG 2000: Image Compression Fundamentals, Standards and Practice.* Kluwer Academic Publishers, 2001.

[223] CandÃs, E. J., Romberg, J. K., and Tao, T. Stable signal recovery from incomplete and inaccurate measurements. *Communications on Pure and Applied Mathematics*, 59(8):1207–1223, 2006.

[224] Donoho, D. L. Compressed sensing. *IEEE Transactions on Information Theory*, 52(4):1289–1306, 2006.

[225] Lustig, M., Donoho, D., and Pauly, J. M. Sparse MRI: The application of compressed sensing for rapid MR imaging. *Magnetic Resonance in Medicine*, 58(6):1182–95, 2007.

[226] Vitanis, V., Gamper, U., Boesiger, P., and Kozerke, S. 1143 Compressed sensing cardiac perfusion imaging: feasibility and comparison to k-t BLAST. *Journal of Cardiovascular Magnetic Resonance*, 10 (Suppl 1):A268, 2008.

[227] Ji, J. and Lang, T. Dynamic MRI with compressed sensing imaging using temporal correlations. In *2008 5th IEEE International Symposium on Biomedical Imaging: From Nano to Macro*, pages 1613–1616, 2008.

[228] Milles, J., Versluis, M. J., Webb, A. G., and Reiber, J. H. C. Quantitative evaluation of Compressed Sensing in MRI: Application to 7T time-of-flight angiography. In *10th IEEE International Conference on Information Technology and Applications in Biomedicine*, pages 1–4, 2010.

[229] Hong, J. and Jong Chul, Y. Performance evaluation of accelerated functional MRI acquisition using compressed sensing. In *2009 IEEE International Symposium on Biomedical Imaging: From Nano to Macro*, pages 702–705, 2009.

[230] Lustig, M., Donoho, D. L., Santos, J. M., and Pauly, J. M. Compressed Sensing MRI. *IEEE Signal Processing Magazine*, 25(2):72–82, 2008.

[231] Candes, E. J., Romberg, J., and Tao, T. Robust uncertainty principles: exact signal reconstruction from highly incomplete frequency information. *IEEE Transactions on Information Theory*, 52(2):489–509, 2006.

[232] Davenport, M. A., Duarte, M. F., Eldar, Y. C., and Kutyniok, G. Introduction to compressed sensing. In Kutyniok, G. and Eldar, Y. C., editors, *Compressed Sensing: Theory and Applications*, pages 1–64. Cambridge University Press, Cambridge, 2012.

[233] Mallat, S. G. and Zhifeng, Z. Matching pursuits with time-frequency dictionaries. *IEEE Transactions on Signal Processing*, 41(12):3397–3415, 1993.

[234] Blumensath, T. and Davies, M. E. Iterative hard thresholding for compressed sensing. *Applied and Computational Harmonic Analysis*, 27(3):265–274, 2009.

[235] Daubechies, I., Defrise, M., and De Mol, C. An iterative thresholding algorithm for linear inverse problems with a sparsity constraint. *Communications on Pure and Applied Mathematics*, 57(11):1413–1457, 2004.

[236] Stejskal, E. O. and Tanner, J. E. Spin Diffusion Measurements: Spin Echoes in the Presence of a Time-Dependent Field Gradient. *The Journal of Chemical Physics*, 42(1):288, 1965.

[237] Torrey, H. C. Bloch Equations with Diffusion Terms. *Physical Review*, 104(3):563–565, 1956.

[238] Hayden, M. E., Archibald, G., Gilbert, K. M., and Lei, C. Restricted diffusion within a single pore. *Journal of Magnetic Resonance*, 169(2):313–22, 2004.

[239] Parra-Robles, J., Ajraoui, S., Deppe, M. H., Parnell, S. R., and Wild, J. M. Experimental investigation and numerical simulation of 3He gas diffusion in simple geometries: implications for analytical models of 3He MR lung morphometry. *Journal of Magnetic Resonance*, 204(2):228–38, 2010.

[240] Hurlimann, M. D., Helmer, K. G., Deswiet, T. M., and Sen, P. N. Spin Echoes in a Constant Gradient and in the Presence of Simple Restriction. *Journal of Magnetic Resonance, Series A*, 113(2):260–264, 1995.

[241] Saam, B., Drukker, N., and Happer, W. Edge enhancement observed with hyperpolarized 3He. *Chemical Physics Letters*, 263(3-4):481–487, 1996.

[242] Fichele, S., Paley, M. N., Woodhouse, N., Griffiths, P. D., van Beek, E. J., and Wild, J. M. Investigating 3He diffusion NMR in the lungs using finite difference simulations and in vivo PGSE experiments. *Journal of Magnetic Resonance*, 167(1):1–11, 2004.

[243] Komlosi, P., Altes, T. A., Qing, K., Mooney, K. E., Miller, G. W., Mata, J. F., de Lange, E. E., Tobias, W. A., Cates, J., G. D., Brookeman, J. R., and Mugler III, J. P. Regional anisotropy of airspace orientation in the lung as assessed with hyperpolarized helium-3 diffusion MRI. *Journal of Magnetic Resonance Imaging*, 42(6):1777–82, 2015.

[244] Ajraoui, S., Parra-Robles, J., Deppe, M., Teh, K., Parnell, S., Owers-Bradley, J., and Wild, J. Experimental investigation of non-gaussian diffusion in hyperpolarized 3He MRI of lungs. In *Proceedings of the International Society of Magnetic Resonance in Medicine*, volume 17, page 2178, 2009.

[245] Parra-Robles, J. and Wild, J. M. The influence of lung airways branching structure and diffusion time on measurements and models of short-range 3He gas MR diffusion. *Journal of Magnetic Resonance*, 225: 102–13, 2012.

[246] Perez-Sanchez, J. M., Rodriguez, I., and Ruiz-Cabello, J. Random walk simulation of the MRI apparent diffusion coefficient in a geometrical model of the acinar tree. *Biophysical Journal*, 97(2):656–64, 2009.

[247] Grebenkov, D. S., Guillot, G., and Sapoval, B. Restricted diffusion in a model acinar labyrinth by NMR: theoretical and numerical results. *Journal of Magnetic Resonance*, 184(1):143–56, 2007.

[248] Habib, D., Grebenkov, D., and Guillot, G. Gas diffusion in a pulmonary acinus model: experiments with hyperpolarized helium-3. *Magnetic Resonance Imaging*, 26(8):1101–13, 2008.

[249] Fichele, S., Paley, M. N., Woodhouse, N., Griffiths, P. D., Van Beek, E. J., and Wild, J. M. Finite-difference simulations of 3He diffusion in 3D alveolar ducts: comparison with the "cylinder model". *Magnetic Resonance in Medicine*, 52(4):917–20, 2004.

[250] Yablonskiy, D. A., Sukstanskii, A. L., and Quirk, J. D. Diffusion lung imaging with hyperpolarized gas MRI. *NMR in Biomedicine*, 2015.

[251] Callaghan, P. T., Jolley, K. W., and Lelievre, J. Diffusion of water in the endosperm tissue of wheat grains as studied by pulsed field gradient nuclear magnetic resonance. *Biophysical Journal*, 28(1):133–141, 1979.

[252] Sukstanskii, A. L., Conradi, M. S., and Yablonskiy, D. A. (3)He lung morphometry technique: accuracy analysis and pulse sequence optimization. *Journal of Magnetic Resonance*, 207(2):234–41, 2010.

[253] Berberan-Santos, M. N., Bodunov, E. N., and Valeur, B. Mathematical functions for the analysis of luminescence decays with underlying distributions 1. Kohlrausch decay function (stretched exponential). *Chemical Physics*, 315(1-2):171–182, 2005.

[254] Newman, K. B., Lynch, D. A., Newman, L. S., Ellegood, D., and Newell, J. D. Quantitative Computed Tomography Detects Air Trapping due to Asthma. *Chest*, 106(1):105–109, 1994.

[255] Busacker, A., Newell, J., J. D., Keefe, T., Hoffman, E. A., Granroth, J. C., Castro, M., Fain, S., and Wenzel, S. A multivariate analysis of risk factors for the air-trapping asthmatic phenotype as measured by quantitative CT analysis. *Chest*, 135(1):48–56, 2009.

[256] Aysola, R. S., Hoffman, E. A., Gierada, D., Wenzel, S., Cook-Granroth, J., Tarsi, J., Zheng, J., Schechtman, K. B., Ramkumar, T. P., Cochran, R., Xueping, E., Christie, C., Newell, J., Fain, S., Altes, T. A., and Castro, M. Airway remodeling measured by multidetector CT is increased in severe asthma and correlates with pathology. *Chest*, 134(6):1183–91, 2008.

[257] Choi, S., Hoffman, E. A., Wenzel, S. E., Castro, M., Fain, S. B., Jarjour, N. N., Schiebler, M. L., Chen, K., and Lin, C. L. Quantitative assessment of multiscale structural and functional alterations in asthmatic populations. *Journal of Applied Physiology*, 118(10):1286–98, 2015.

[258] Capaldi, D. P., Zha, N., Guo, F., Pike, D., McCormack, D. G., Kirby, M., and Parraga, G. Pulmonary Imaging Biomarkers of Gas Trapping and Emphysema in COPD: (3)He MR Imaging and CT Parametric Response Maps. *Radiology*, 279(2):597–608, 2016.

[259] Verschakelen, J. A., Van fraeyenhoven, L., Laureys, G., Demedts, M., and Baert, A. L. Differences in CT density between dependent and nondependent portions of the lung: influence of lung volume. *AJR: American Journal of Roentgenology*, 161(4):713–7, 1993.

[260] Evans, A., McCormack, D., Ouriadov, A., Etemad-Rezai, R., Santyr, G., and Parraga, G. Anatomical distribution of 3He apparent diffusion coefficients in severe chronic obstructive pulmonary disease. *Journal of Magnetic Resonance Imaging*, 26(6):1537–47, 2007.

[261] Hartley, R. A., Barker, B. L., Newby, C., Pakkal, M., Baldi, S., Kajekar, R., Kay, R., Laurencin, M., Marshall, R. P., Sousa, A. R., Parmar, H., Siddiqui, S., Gupta, S., and Brightling, C. E. Relationship between lung function and quantitative computed tomographic parameters of airway remodeling, air trapping, and emphysema in patients with asthma and chronic obstructive pulmonary disease: A single-center study. *Journal of Allergy and Clinical Immunology*, 137(5):1413–1422, 2016.

[262] Tahir, B. A., Swift, A. J., Marshall, H., Parra-Robles, J., Hatton, M. Q., Hartley, R., Kay, R., Brightling, C. E., Vos, W., Wild, J. M., and Ireland, R. H. A method for quantitative analysis of regional lung ventilation using deformable image registration of CT and hybrid hyperpolarized gas/(1)H MRI. *Physics in Medicine and Biology*, 59(23):7267–77, 2014.

[263] Altes, T. A., Powers, P. L., Knight-Scott, J., Rakes, G., Platts-Mills, T. A., de Lange, E. E., Alford, B. A., Mugler, r., J. P., and Brookeman, J. R. Hyperpolarized 3He MR lung ventilation imaging in asthmatics: preliminary findings. *Journal of Magnetic Resonance Imaging*, 13(3):378–84, 2001.

[264] Ajraoui, S., Lee, K. J., Deppe, M. H., Parnell, S. R., Parra-Robles, J., and Wild, J. M. Compressed sensing in hyperpolarized 3He lung MRI. *Magnetic Resonance in Medicine*, 63(4):1059–69, 2010.

[265] Qing, K., Altes, T. A., Tustison, N. J., Feng, X., Chen, X., Mata, J. F., Miller, G. W., de Lange, E. E., Tobias, W. A., Cates, J., G. D., Brookeman, J. R., and Mugler, r., J. P. Rapid acquisition of helium-3 and proton three-dimensional image sets of the human lung in a single breath-hold using compressed sensing. *Magnetic Resonance in Medicine*, 74(4):1110–5, 2015.

[266] Ajraoui, S., Parra-Robles, J., and Wild, J. M. Incorporation of prior knowledge in compressed sensing for faster acquisition of hyperpolarized gas images. *Magnetic Resonance in Medicine*, 69(2):360–9, 2013.

[267] Ajraoui, S., Parra-Robles, J., Marshall, H., Deppe, M. H., Clemence, M., and Wild, J. M. Acquisition of (3)He ventilation images, ADC, T(2)* and B(1) maps in a single scan with compressed sensing. *NMR in Biomedicine*, 25(1):44–51, 2012.

[268] Wild, J. M., Woodhouse, N., Paley, M. N., Fichele, S., Said, Z., Kasuboski, L., and van Beek, E. J. Comparison between 2D and 3D gradient-echo sequences for MRI of human lung ventilation with hyperpolarized 3He. *Magnetic Resonance in Medicine*, 52(3):673–8, 2004.

[269] Chang, Y. V., Quirk, J. D., and Yablonskiy, D. A. In vivo lung morphometry with accelerated hyperpolarized (3) He diffusion MRI: a preliminary study. *Magnetic Resonance in Medicine*, 73(4): 1609–14, 2015.

[270] O'Halloran, R. L., Holmes, J. H., Altes, T. A., Salerno, M., and Fain, S. B. The effects of SNR on ADC measurements in diffusion-weighted hyperpolarized He-3 MRI. *Journal of Magnetic Resonance*, 185(1): 42–9, 2007.

[271] Sukstanskii, A. L., Bretthorst, G. L., Chang, Y. V., Conradi, M. S., and Yablonskiy, D. A. How accurately can the parameters from a model of anisotropic 3He gas diffusion in lung acinar airways be estimated? Bayesian view. *Journal of Magnetic Resonance*, 184(1):62–71, 2007.

[272] Gudbjartsson, H. and Patz, S. The rician distribution of noisy mri data. *Magnetic Resonance in Medicine*, 34(6):910–914, 1995.

[273] Chen, X. J., Moller, H. E., Chawla, M. S., Cofer, G. P., Driehuys, B., Hedlund, L. W., MacFall, J. R., and Johnson, G. A. Spatially resolved measurements of hyperpolarized gas properties in the lung in vivo. Part II:T?2. *Magnetic Resonance in Medicine*, 42(4):729–737, 1999.

[274] Vignaud, A., Maitre, X., Guillot, G., Durand, E., de Rochefort, L., Robert, P., Vives, V., Santus, R., and Darrasse, L. Magnetic susceptibility matching at the air-tissue interface in rat lung by using a superparamagnetic intravascular contrast agent: influence on transverse relaxation time of hyperpolarized helium-3. *Magnetic Resonance in Medicine*, 54(1):28–33, 2005.

[275] de Rochefort, L., Vignaud, A., Maitre, X., Guillot, G., Darrasse, L., Bittoun, J., and Durand, E. Influence of lung filling on T2* values in human at 1.5 T with hyperpolarised 3He. In *Proceedings of the International Society of Magnetic Resonance in Medicine*, volume 11, page 2724, 2004.

[276] Ajraoui, S., Ireland, R., Lee, K., Woodhouse, N., and Wild, J. Anatomical trends in coregistered ADC and T2* maps of 3He gas in the lungs of healthy normals. In *Proceedings of the International Society of Magnetic Resonance in Medicine*, volume 16, page 2652, 2008.

[277] Wild, J. M., Woodhouse, N., and Teh, K. Single-scan acquisition of registered hyperpolarized (3)He ventilation and ADC images using a hybrid 2D gradient-echo sequence. *Magnetic Resonance in Medicine*, 57(6):1185–9, 2007.

[278] Bock, M. Simultaneous T2* and diffusion measurements with3He. *Magnetic Resonance in Medicine*, 38 (6):890–895, 1997.

[279] Hughes, P. J. C., Horn, F. C., Collier, G. J., Biancardi, A., Marshall, H., and Wild, J. M. Spatial fuzzy c-means thresholding for semiautomated calculation of percentage lung ventilated volume from hyperpolarized gas and 1 H MRI. *Journal of Magnetic Resonance Imaging*, 2017.

[280] Imai, H., Kimura, A., Hori, Y., Iguchi, S., Kitao, T., Okubo, E., Ito, T., Matsuzaki, T., and Fujiwara, H. Hyperpolarized 129Xe lung MRI in spontaneously breathing mice with respiratory gated fast imaging and its application to pulmonary functional imaging. *NMR in Biomedicine*, 24(10):1343–52, 2011.

[281] Collier, G. J., Hughes, P. J., Horn, F. C., Chan, H. F., Norquay, G., Stewart, N. J., and Wild, J. M. Rapid Acquisition of Co-Registered 3D Xenon-129 and Proton Images of the Human Lung in a Single Breath-Hold Using Compressed Sensing. In *Proceedings of the International Society of Magnetic Resonance in Medicine*, volume 25, 2017.

[282] Quirk, J. D., Chang, Y. V., and Yablonskiy, D. A. In vivo lung morphometry with hyperpolarized (3) He diffusion MRI: reproducibility and the role of diffusion-sensitizing gradient direction. *Magnetic Resonance in Medicine*, 73(3):1252–7, 2015.

[283] Ouriadov, A., Lessard, E., Sheikh, K., Parraga, G., and Canadian Respiratory Research, N. Pulmonary MRI morphometry modeling of airspace enlargement in chronic obstructive pulmonary disease and alpha-1 antitrypsin deficiency. *Magnetic Resonance in Medicine*, 79(1):439–448, 2018.

[284] Mercer, R. R., Russell, M. L., and Crapo, J. D. Alveolar septal structure in different species. *Journal of Applied Physiology*, 77(3):1060–6, 1994.

[285] O'Sullivan, B. P. and Freedman, S. D. Cystic fibrosis. *The Lancet*, 373(9678):1891–1904, 2009.

[286] Marshall, H., Horsley, A., Taylor, C. J., Smith, L., Hughes, D., Horn, F. C., Swift, A. J., Parra-Robles, J., Hughes, P. J., Norquay, G., Stewart, N. J., Collier, G. J., Teare, D., Cunningham, S., Aldag, I., and Wild, J. M. Detection of early subclinical lung disease in children with cystic fibrosis by lung ventilation imaging with hyperpolarised gas MRI. *Thorax*, 72(8):760–762, 2017.

[287] van Beek, E. J., Hill, C., Woodhouse, N., Fichele, S., Fleming, S., Howe, B., Bott, S., Wild, J. M., and Taylor, C. J. Assessment of lung disease in children with cystic fibrosis using hyperpolarized 3-Helium MRI: comparison with Shwachman score, Chrispin-Norman score and spirometry. *European Radiology*, 17(4):1018–24, 2007.

[288] McMahon, C. J., Dodd, J. D., Hill, C., Woodhouse, N., Wild, J. M., Fichele, S., Gallagher, C. G., Skehan, S. J., van Beek, E. J., and Masterson, J. B. Hyperpolarized 3helium magnetic resonance ventilation imaging of the lung in cystic fibrosis: comparison with high resolution CT and spirometry. *European Radiology*, 16(11):2483–90, 2006.

[289] O'Sullivan, B., Couch, M., Roche, J. P., Walvick, R., Zheng, S., Baker, D., Johnson, M., Botfield, M., and Albert, M. S. Assessment of repeatability of hyperpolarized gas MR ventilation functional imaging in cystic fibrosis. *Academic Radiology*, 21(12):1524–9, 2014.

[290] Mentore, K., Froh, D. K., de Lange, E. E., Brookeman, J. R., Paget-Brown, A. O., and Altes, T. A. Hyperpolarized HHe 3 MRI of the lung in cystic fibrosis: assessment at baseline and after bronchodilator and airway clearance treatment. *Academic Radiology*, 12(11):1423–9, 2005.

[291] Altes, T. A., Johnson, M., Fidler, M., Botfield, M., Tustison, N. J., Leiva-Salinas, C., de Lange, E. E., Froh, D., and Mugler, r., J. P. Use of hyperpolarized helium-3 MRI to assess response to ivacaftor treatment in patients with cystic fibrosis. *Journal of Cystic Fibrosis*, 16(2):267–274, 2017.

[292] Walkup, L. L., Thomen, R. P., Akinyi, T. G., Watters, E., Ruppert, K., Clancy, J. P., Woods, J. C., and Cleveland, Z. I. Feasibility, tolerability and safety of pediatric hyperpolarized (129)Xe magnetic resonance imaging in healthy volunteers and children with cystic fibrosis. *Pediatric Radiology*, 46(12): 1651–1662, 2016.

[293] Thomen, R. P., Walkup, L. L., Roach, D. J., Cleveland, Z. I., Clancy, J. P., and Woods, J. C. Hyperpolarized (129)Xe for investigation of mild cystic fibrosis lung disease in pediatric patients. *Journal of Cystic Fibrosis*, 16(2):275–282, 2017.

[294] Smith, L. J., Macleod, K. A., Collier, G. J., Horn, F. C., Sheridan, H., Aldag, I., Taylor, C. J., Cunningham, S., Wild, J. M., and Horsley, A. Supine posture changes lung volumes and increases ventilation heterogeneity in cystic fibrosis. *PLoS ONE*, 12(11):e0188275, 2017.

[295] Thurlbeck, W. M. Postnatal human lung growth. *Thorax*, 37(8):564–571, 1982.

[296] Verbanck, S., Schuermans, D., Van Muylem, A., Paiva, M., Noppen, M., and Vincken, W. Ventilation distribution during histamine provocation. *Journal of Applied Physiology*, 83(6):1907–1916, 1997.

[297] Verbanck, S., Schuermans, D., Van Muylem, A., Melot, C., Noppen, M., Vincken, W., and Paiva, M. Conductive and acinar lung-zone contributions to ventilation inhomogeneity in COPD. *American Journal of Respiratory and Critical Care Medicine*, 157(5 Pt 1):1573–7, 1998.

[298] Horsley, A. R., Macleod, K. A., Robson, A. G., Lenney, J., Bell, N. J., Cunningham, S., Greening, A. P., Gustafsson, P. M., and Innes, J. A. Effects of cystic fibrosis lung disease on gas mixing indices derived from alveolar slope analysis. *Respiratory Physiology and Neurobiology*, 162(3):197–203, 2008.

[299] Gonem, S., Hardy, S., Buhl, N., Hartley, R., Soares, M., Kay, R., Costanza, R., Gustafsson, P., Brightling, C. E., Owers-Bradley, J., and Siddiqui, S. Characterization of acinar airspace involvement in asthmatic patients by using inert gas washout and hyperpolarized helium magnetic resonance. *Journal of Allergy and Clinical Immunology*, 2015.

[300] Kirby, M., Villemaire, L., Ahmed, H., Paterson, N. A., McCormack, D. G., Lewis, J. F., and Parraga, G. Diffusion-Weighted Hyperpolarized Helium-3 Magnetic Resonance Imaging In Adult Cystic Fibrosis. In *American Thoracic Society International Conference*, page A2072, 2013.

[301] Gross, T. J. and Hunninghake, G. W. Idiopathic pulmonary fibrosis. *New England Journal of Medicine*, 345(7):517–25, 2001.

[302] Noble, P. W., Albera, C., Bradford, W. Z., Costabel, U., Glassberg, M. K., Kardatzke, D., King, T. E., Lancaster, L., Sahn, S. A., Szwarcberg, J., Valeyre, D., and du Bois, R. M. Pirfenidone in patients with idiopathic pulmonary fibrosis (CAPACITY): two randomised trials. *The Lancet*, 377(9779):1760–1769, 2011.

[303] Richeldi, L., du Bois, R. M., Raghu, G., Azuma, A., Brown, K. K., Costabel, U., Cottin, V., Flaherty, K. R., Hansell, D. M., Inoue, Y., Kim, D. S., Kolb, M., Nicholson, A. G., Noble, P. W., Selman, M., Taniguchi, H., Brun, M., Le Maulf, F., Girard, M., Stowasser, S., Schlenker-Herceg, R., Disse, B., Collard, H. R., and Investigators, I. T. Efficacy and safety of nintedanib in idiopathic pulmonary fibrosis. *New England Journal of Medicine*, 370(22):2071–82, 2014.

[304] Maher, T. M. Disease stratification in idiopathic pulmonary fibrosis: the dawn of a new era? *European Respiratory Journal*, 43(5):1233–6, 2014.

[305] Patz, S., Muradyan, I., Hrovat, M. I., Dabaghyan, M., Washko, G. R., Hatabu, H., and Butler, J. P. Diffusion of hyperpolarized 129Xe in the lung: a simplified model of 129Xe septal uptake and experimental results. *New Journal of Physics*, 13(1):015009, 2011.

[306] Stewart, N. J., Leung, G., Norquay, G., Marshall, H., Parra-Robles, J., Murphy, P. S., Schulte, R. F., Elliot, C., Condliffe, R., Griffiths, P. D., Kiely, D. G., Whyte, M. K., Wolber, J., and Wild, J. M. Experimental validation of the hyperpolarized 129 Xe chemical shift saturation recovery technique in healthy volunteers and subjects with interstitial lung disease. *Magnetic Resonance in Medicine*, 74(1): 196–207, 2015.

[307] Kaushik, S. S., Freeman, M. S., Yoon, S. W., Liljeroth, M. G., Stiles, J. V., Roos, J. E., Foster, W., Rackley, C. R., McAdams, H. P., and Driehuys, B. Measuring diffusion limitation with a perfusion-limited gas–hyperpolarized 129Xe gas-transfer spectroscopy in patients with idiopathic pulmonary fibrosis. *Journal of Applied Physiology*, 117(6):577–85, 2014.

[308] Kaushik, S. S., Robertson, S. H., Freeman, M. S., He, M., Kelly, K. T., Roos, J. E., Rackley, C. R., Foster, W. M., McAdams, H. P., and Driehuys, B. Single-breath clinical imaging of hyperpolarized (129)Xe in the airspaces, barrier, and red blood cells using an interleaved 3D radial 1-point Dixon acquisition. *Magnetic Resonance in Medicine*, 75(4):1434–43, 2016.

[309] Wang, J. M., Robertson, S. H., Wang, Z., He, M., Virgincar, R. S., Schrank, G. M., Smigla, R. M., O'Riordan, T. G., Sundy, J., Ebner, L., Rackley, C. R., McAdams, P., and Driehuys, B. Using hyperpolarized 129Xe MRI to quantify regional gas transfer in idiopathic pulmonary fibrosis. *Thorax*, 73 (1):21–28, 2018.

[310] Stephen, M. J., Emami, K., Woodburn, J. M., Chia, E., Kadlecek, S., Zhu, J., Pickup, S., Ishii, M., Rizi, R. R., and Rossman, M. Quantitative assessment of lung ventilation and microstructure in an animal model of idiopathic pulmonary fibrosis using hyperpolarized gas MRI. *Academic Radiology*, 17 (11):1433–43, 2010.

[311] Morbach, A. E., Gast, K. K., Schmiedeskamp, J., Dahmen, A., Herweling, A., Heussel, C. P., Kauczor, H. U., and Schreiber, W. G. Diffusion-weighted MRI of the lung with hyperpolarized helium-3: a study of reproducibility. *Journal of Magnetic Resonance Imaging*, 21(6):765–74, 2005.

[312] Pellegrino, R., Viegi, G., Brusasco, V., Crapo, R. O., Burgos, F., Casaburi, R., Coates, A., van der Grinten, C. P., Gustafsson, P., Hankinson, J., Jensen, R., Johnson, D. C., MacIntyre, N., McKay, R., Miller, M. R., Navajas, D., Pedersen, O. F., and Wanger, J. Interpretative strategies for lung function tests. *European Respiratory Journal*, 26(5):948–68, 2005.

[313] Jacob, J., Bartholmai, B. J., Rajagopalan, S., Kokosi, M., Maher, T. M., Nair, A., Karwoski, R., Renzoni, E., Walsh, S. L. F., Hansell, D. M., and Wells, A. U. Functional and prognostic effects when emphysema complicates idiopathic pulmonary fibrosis. *European Respiratory Journal*, 50(1), 2017.

[314] Nathan, S. D., Albera, C., Bradford, W. Z., Costabel, U., du Bois, R. M., Fagan, E. A., Fishman, R. S., Glaspole, I., Glassberg, M. K., Glasscock, K. F., King, J., T. E., Lancaster, L., Lederer, D. J., Lin, Z., Pereira, C. A., Swigris, J. J., Valeyre, D., Noble, P. W., and Wells, A. U. Effect of continued treatment with pirfenidone following clinically meaningful declines in forced vital capacity: analysis of data from three phase 3 trials in patients with idiopathic pulmonary fibrosis. *Thorax*, 71(5):429–35, 2016.

[315] Weatherley, N. D., Chan, H. F., Stewart, N. J., Norquay, G., Rao, M., Collier, G. J., Austin, M., Smith, L. J., Renshaw, S. A., Bianchi, S., and Wild, J. M. Hyperpolarised gas MRI demonstrates sub-clinical progression in IPF over 6 months. In *European Respiratory Society Congress*, page OA4642, 2017.

[316] Stewart, N. J., Norquay, G., Parra-Robles, J., Marshall, H., Leung, G., Murphy, P. S., Schulte, R. F., Elliot, C. A., Condliffe, R., Billings, C. G., Smith, I., Griffiths, P. D., Wolber, J., Whyte, M. K., Kiely, D. G., and Wild, J. M. Assessment of lung microstructure in ILD with 3He and 129Xe MRI. In *European Respiratory Society Congress*, page OA2945, 2015.

[317] Greaves, I. A., Hildebrandt, J., and Hoppin, F. G. Micromechanics of the Lung. In *Comprehensive Physiology*. John Wiley & Sons, Inc., 2011.

[318] Smaldone, G. C. and Mitzner, W. Viewpoint: unresolved mysteries. *Journal of Applied Physiology*, 113 (12):1945–7, 2012.

[319] Hughes, P. J., Smith, L., Horn, F. C., Biancardi, A., Stewart, N. J., Norquay, G., Collier, G. J., and Wild, J. M. Assessment of Lung Inflation State on the Repeatability of Hyperpolarized Gas Ventilation MRI. In *Proceedings of the International Society of Magnetic Resonance in Medicine*, volume 25, page 2145, 2017.

[320] Milic-Emili, J., Henderson, J., Dolovich, M., Trop, D., and Kaneko, K. Regional distribution of inspired gas in the lung. *Journal of Applied Physiology: Respiratory, Environmental and Exercise Physiology*, 21 (3):749–759, 1966.

[321] Moreno, F. and Lyons, H. A. Effect of body posture on lung volumes. *Journal of Applied Physiology*, 16 (1):27–29, 1961.

[322] Yablonskiy, D. A., Sukstanskii, A. L., Quirk, J. D., Woods, J. C., and Conradi, M. S. Probing lung microstructure with hyperpolarized noble gas diffusion MRI: theoretical models and experimental results. *Magnetic Resonance in Medicine*, 71(2):486–505, 2014.

[323] Parra-Robles, J., Vasilescu, D., Hogg, J., and Wild, J. Modelling of 3He gas diffusion in realistic 3D models of human acinar airways obtained from micro-CT images. In *European Respiratory Society Congress*, page P4972, 2014.

[324] Parra-Robles, J., Veeckmans, B., Rao, M., Hogg, J. C., and Wild, J. M. Hyperpolarized gas MR diffusion simulations and experiments in realistic 3D models and phantoms of human acinar airways. In *Proceedings of the International Society of Magnetic Resonance in Medicine*, volume 23, page 160, 2015.

[325] Murphy, M., Alley, M., Demmel, J., Keutzer, K., Vasanawala, S., and Lustig, M. Fast l(1)-SPIRiT compressed sensing parallel imaging MRI: scalable parallel implementation and clinically feasible runtime. *IEEE Trans Med Imaging*, 31(6):1250–62, 2012.